ANALYSIS OF RESONANT CONVERTERS

Thesis by

Vatché Vorpérian

In Partial Fulfillment of the Requirements

for the Degree of

Doctor of Philosophy

California Institute of Technology

Pasadena, California

1984

(Submitted May 21, 1984)

to my parents

ACKNOWLEDGMENTS

I wish to thank my advisor, Professor Slobodan Ćuk, for accepting me into the Power Electronics Group at Caltech and for the kind support that he and Professor R.D. Middlebrook provided during the course of this work.

I appreciate the financial support of the California Institute of Technology by way of Graduate Teaching Assistantship, the Office of Naval Research and the Naval Ocean System Center by way of Graduate Research Assistantship. Also, I thank the International Business Machines Corporation for their generous support during my last year at Caltech by way of their Graduate Fellowship Program.

Finally, I wish to thank my friends who made my stay an enjoyable and productive experience.

ABSTRACT

The load parameter, Q, and the ratio of the switching frequency to the resonant frequency, F_s / F_0, characterize the operation of resonant converters. An accurate dc analysis of the series and parallel resonant converters is given in terms of these parameters whereby the conversion ratio, peak stresses, and diode conduction time are determined. An exact and systematic method of small-signal analysis is given whereby the control-to-output transfer function, audio susceptibility, and input impedance are determined at a given operating point. In addition, simple and approximate transfer functions are obtained under high-Q assumption.

TABLE OF CONTENTS

CHAPTER 1

INTRODUCTION

In the past two decades resonant converters have gained importance owing to certain advantages of switching sinusoidal voltages and currents. The principal motivation behind the development of these converters has been their ability, when operating properly, to provide natural turn-off for the switching devices. This minimizes turn-off losses and facilitates the implementation of thyristor switches which are indispensable at power levels greater than 50kW. Operation at higher frequencies is another desirable feature in power-processing circuits because smaller filters can be used and consequently higher power densities can be attained. When field-effect or bipolar transistors are used at lower or moderate power levels, resonant converters can operate at higher frequencies with greater ease than PWM square-wave converters.

Although, undoubtedly, the turn-on and turn-off switching stresses are far less in resonant converters than in PWM converters, the total switching losses may *not* necessarily be less in comparison, because the ratio of peak resonant current to the average input current is generally *higher* in resonant converters than in PWM converters. It is *not* possible to compare the efficiencies of resonant and PWM converters in general, and if such comparisons are made, they should be interpreted with caution. Therefore, to help the engineer understand and design these converters, an accurate analysis of their operation must be given. Whereas for PWM

converters numerous methods of analysis exist, to date only limited dc analysis of resonant converters has been given while their small-signal analysis has not even been touched. The purpose of this thesis is to provide an accurate analysis of resonant converters and characterize their operation in terms of two *simple* and *relevant* parameters: the load parameter Q and the control parameter F_s / F_0, which is the ratio of switching frequency to the resonant frequency. A block diagram that follows from this characterization is shown in Fig. 1.1a.

In Chapters 2 and 3 the dc analysis of the series and the parallel resonant converters is given. The conversion ratio characteristics, peak stress levels, output-network switching time, and diode conduction time are determined in terms of Q and F_s / F_0. A systematic method of small-signal analysis of resonant converters is outlined in detail in Chapter 4. In this analysis the system equations are linearized at the operating point, determined from dc analysis, assuming small-signal perturbations in the switching frequency and the input voltage. A block diagram representing the small-signal perturbations is shown in Fig. 1.1b. The results of the analysis are determined numerically because of the occurrence of exponential matrices which are difficult to determine in expression form. In Chapter 5 simple and approximate transfer functions are obtained for high-Q approximation.

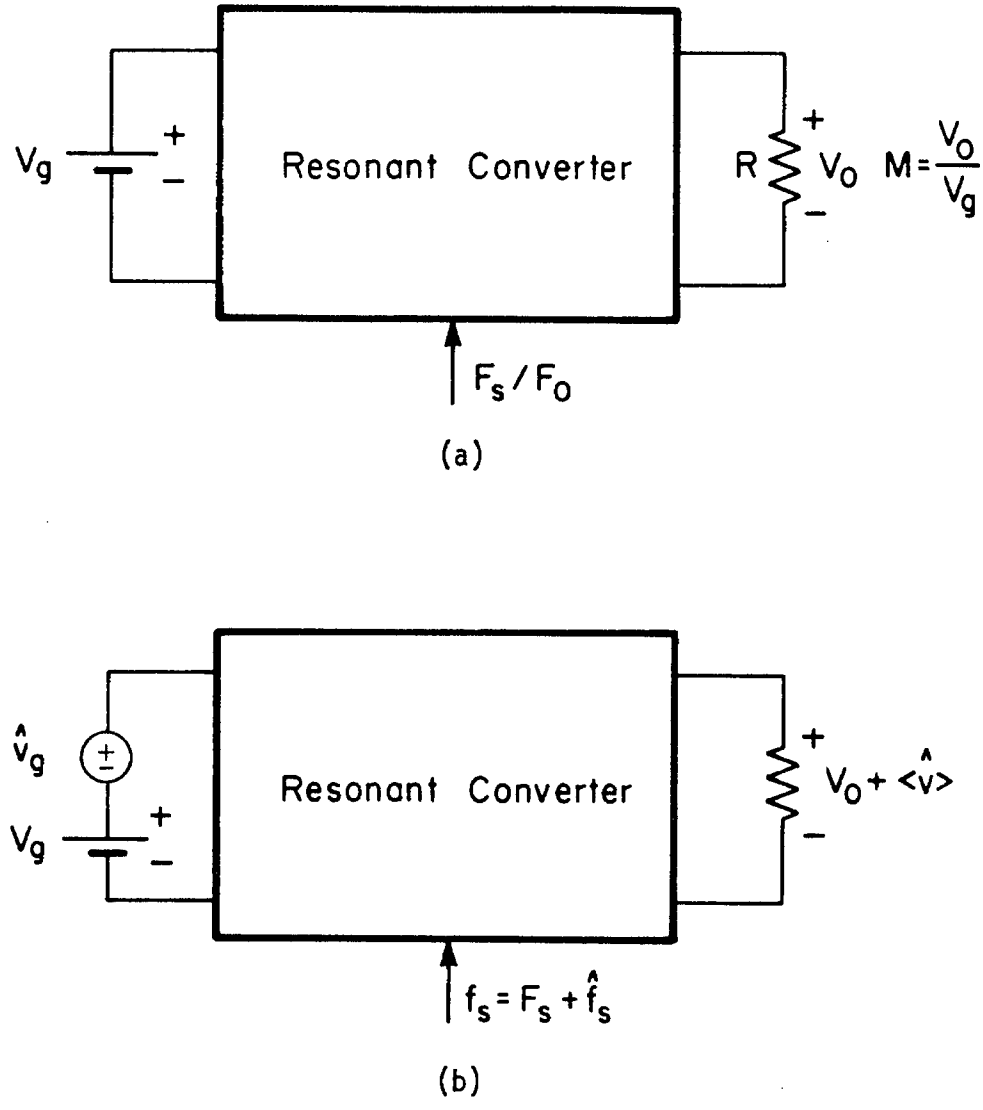

Fig. 1.1 a) Block diagram of resonant converters and b) perturbations in input voltage and switching frequency.

CHAPTER 2

DC ANALYSIS OF THE PARALLEL RESONANT CONVERTER

2.1 Introduction

In this chapter the steady-state operation and the dc analysis of the parallel resonant converter are discussed. The basic operation is reviewed in Sec. 2.2. The dc analysis is presented in Sec. 2.3 where first a thorough treatment of the conversion ratio characteristics is given in terms of the normalized load and control parameters. Other steady-state quantities such as diode conduction time, output-network switching time, and the initial state variables at the beginning of the switching interval are determined. Maximum stress levels such as the peak capacitor voltage and the peak inductor current are determined as well. Proper selection of the the range of the normalized load and control parameters for optimum operation is discussed. In Sec. 2.4, the efficiency and the conversion ratio are discussed in the presence of such nonidealities as parasitic resistances and semiconductor voltage drops. Experimental results given in Sec. 2.5 are in good agreement with the theoretical predictions.

2.2 Operation

The parallel resonant converter with two different methods of voltage excitation is shown in Fig. 2.1a and b. In Fig. 2.1a the capacitors C_∞ serve as voltage dividers and are assumed to be much larger than the resonant capacitor, C_0, i.e., $C_\infty \gg C_0$. The parallel combination of the transistors and the diodes forms bidirectional switches which operate at fifty percent duty ratio to generate a symmetrical square voltage waveform V_T across the resonant circuit. For the converter in Fig. 2.1a the peak value, V_g, of the square wave is equal to half the input voltage whereas for the converter in Fig. 2.1b the peak value is equal to the input voltage. The ideal circuit is shown in Fig. 2.1c. The switching times T_s' and T_s are shown in Fig. 2.1 and are defined as follows

$$T_s' = \text{Switching interval}$$

$$F_s = 1/T_s' = \text{Switching frequency}$$

$$T_s = T_s'/2$$

The resonant frequency is defined as

$$F_0 = \frac{1}{2\pi\sqrt{L_0 C_0}} \tag{2.1}$$

The voltage across the resonant capacitor is rectified and applied to a low-pass filter from which the output voltage is obtained. By analogy to linear circuits it is clear that the output voltage can be controlled by changing the ratio of the switching frequency to the resonant frequency. This is shown in Fig. 2.2 where the converter is represented by a block

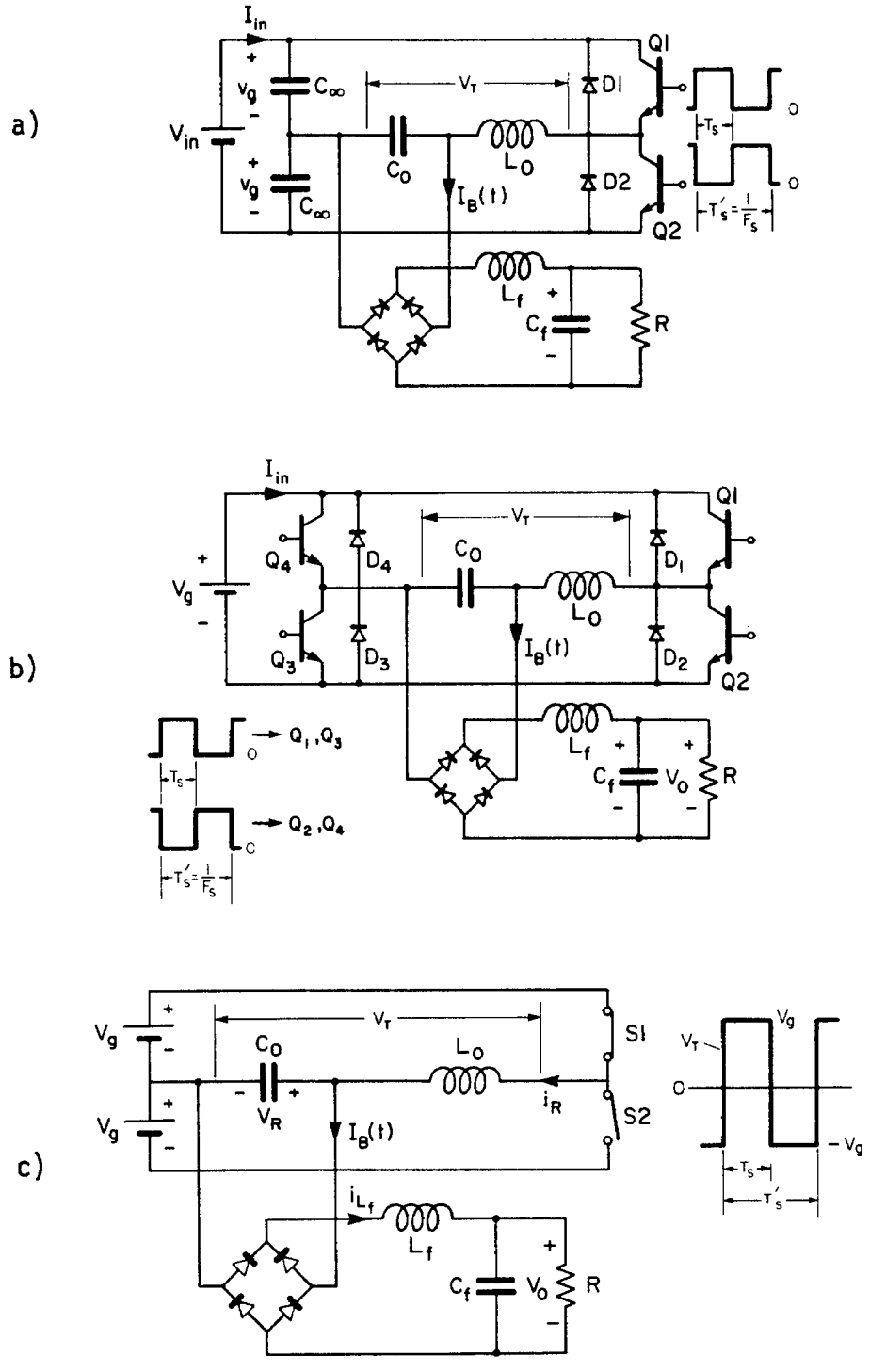

Fig. 2.1 The parallel resonant converter with two different methods of excitation a) and b), and ideal equivalent circuit c).

diagram with an input voltage V_g, an output voltage V_0 across a load R, and a control parameter F_s/F_0. In the following section the conversion ratio characteristics, $M = V_0/V_g$, will be determined for continuous conduction mode operation and for the range of the control parameter $F_s/F_0 > .5$.

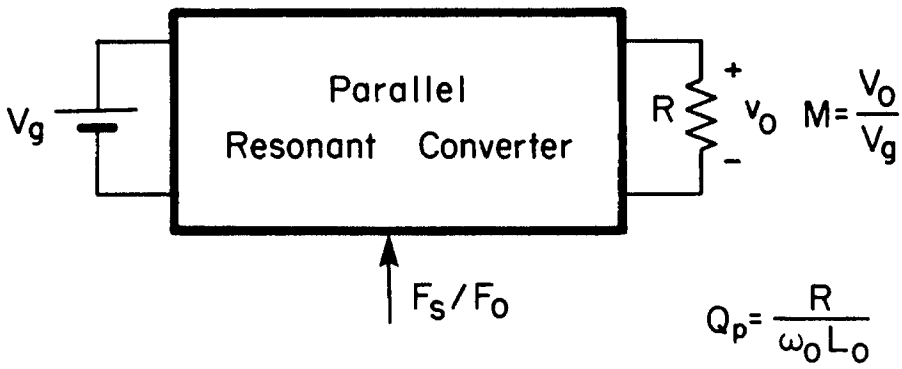

Fig. 2.2 Block diagram of the parallel resonant converter.

2.3 Analysis

The basic operation of the parallel resonant converter is discussed in [1,2,3]. The analysis given in [3] is strictly an iterative computational method whereby the circuit equations are solved numerically cycle by cycle until the initial conditions converge. No attempt is made in [3] to determine neither the initial conditions nor the conversion ratio for a given load R and control parameter F_s/F_0. The analysis given in this section begins with the determination of the conversion ratio characteristics and the initial conditions for a given F_s/F_0 and normalized load parameter, Q_p, defined by

$$Q_p = \frac{R}{\omega_0 L_0} \tag{2.2}$$

The waveforms during a complete switching interval are shown in Fig. 2.3. Since the operation of the circuit is symmetrical over an entire switching interval T_s', the analysis is performed over half the switching interval T_s. It is assumed that the output filter inductor, L_f, is much larger than the resonant inductor, L_0, so that the output filter section can be represented by a current source $I_0 = V_0/R$. Because of the output rectifiers, as the voltage across the resonant capacitor changes sign at $t = T_a$, the output network, or the current source I_0, switches polarity. This results in two switched networks over half the switching interval, T_s, as shown in Fig. 2.4.

According to Fig. 2.4a, the equations for the resonant capacitor voltage, $V_R(t)$, and the resonant inductor current, $I_R(t)$, for the time interval $0 < t < T_a$ are given by

$$I_R(t) = \left[\frac{V_0}{R} + I_R(0)\right]\cos\omega_0 t + \frac{1}{\omega_0 L_0}\left[V_g - V_R(0)\right]\sin\omega_0 t - \frac{V_0}{R} \tag{2.3a}$$

$$V_R(t) = -\left[V_g - V_R(0)\right]\cos\omega_0 t + \omega_0 L_0\left[\frac{V_0}{R} + I_R(0)\right]\sin\omega_0 t + V_g \tag{2.3b}$$

According to Fig. 2.4b, the equations for $T_a < t < T_s$ are

$$I_R(t) = \left[I_R(T_a) - \frac{V_0}{R}\right]\cos\omega_0(t - T_a) + \frac{V_g}{\omega_0 L_0}\sin\omega_0(t - T_a) + \frac{V_0}{R} \tag{2.4a}$$

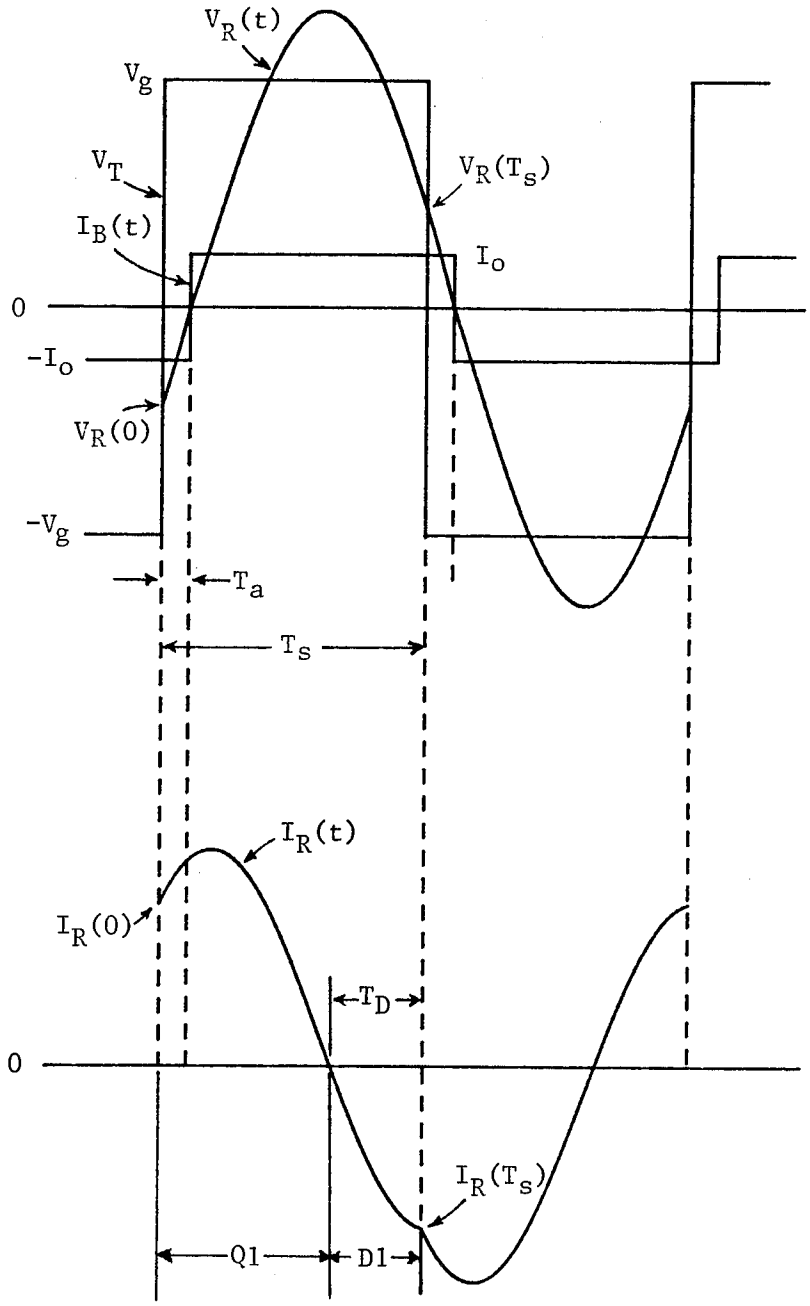

Fig. 2.3 Voltage and current waveforms of the parallel resonant converter.

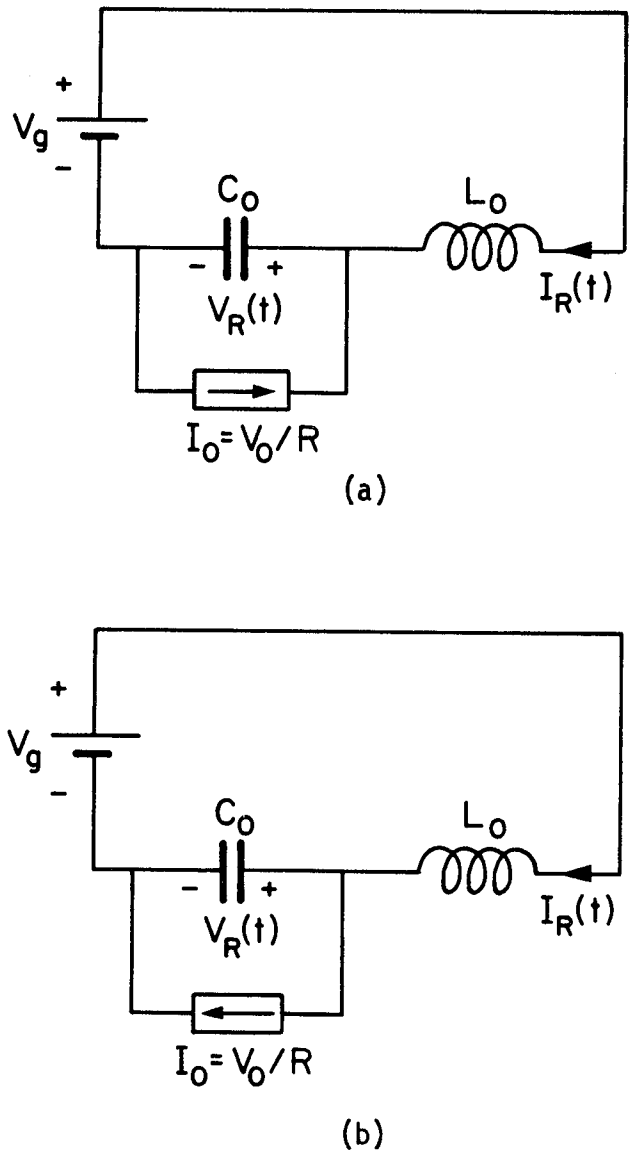

Fig. 2.4 The two switched networks of the parallel resonant converter during half the switching interval T_s. a) $0 < t < T_a$ and b) $T_a < t < T_s$

$$V_R(t) = -V_g\cos\omega_0(t-T_a) + \omega_0 L_0\left[I_R(T_a) - \frac{V_0}{R}\right]\sin\omega_0(t-T_a) + V_g \quad (2.4b)$$

When Eqs. (2.3) and Eqs. (2.4) are matched at $t = T_a$ and cyclic stability required, i.e., $I_R(T_s) = -I_R(0)$ and $V_R(T_s) = -V_R(0)$, the following two equations are obtained

$$\frac{V_R(0)}{V_g}\sin\omega_0 T_a\cos(\gamma-\omega_0 T_a) - \frac{I_R(0)R}{Q_p V_g}\left[1+\cos\omega_0 T_a\cos(\gamma-\omega_0 T_a)\right]$$

$$-\frac{M}{Q_p}\left[1+\cos(\gamma-\omega_0 T_a)(\cos\omega_0 T_a-2)\right] = \sin\omega_0 T_a\cos(\gamma-\omega_0 T_a)+\sin(\gamma-\omega_0 T_a) \quad (2.5a)$$

$$\frac{V_R(0)}{V_g}\left[\sin\omega_0 T_a\sin(\gamma-\omega_0 T_a)-1\right] - \frac{I_R(0)R}{V_g Q_p}\cos\omega_0 T_a\sin(\gamma-\omega_0 T_a)$$

$$-\frac{M}{Q_p}\left[\cos\omega_0 T_a-2\right]\sin(\gamma-\omega_0 T_a) = 1+\sin\omega_0 T_a\sin(\gamma-\omega_0 T_a)-\cos(\gamma-\omega_0 T_a) \quad (2.5b)$$

The requirement $V_R(T_a) = 0$ in Eq. (2.3a) gives

$$\frac{V_R(0)}{V_g}\cos\omega_0 T_a + \frac{I_R(0)R}{V_g Q_p}\sin\omega_0 T_a + \frac{M}{Q_p}\sin\omega_0 T_a = \cos\omega_0 T_a - 1 \quad (2.5c)$$

where

$$\gamma = \pi\frac{F_0}{F_s} \quad (2.6)$$

Eqs. (2.5) are three equations in which the three unknowns $I_R(0)$, $V_R(0)$, and M can be solved for :

$$I_R(0) = \frac{1+\cos\gamma-2\cos(\gamma-\omega_0 T_a)+2\cos\omega_0 T_a[\cos(\gamma-\omega_0 T_a)-1]}{\omega_0 L_0 \sin\gamma} V_g \tag{2.7a}$$

$$V_R(0) = \frac{\sin(\gamma-2\omega_0 T_a)+\sin\omega_0 T_a-\sin(\gamma-\omega_0 T_a)}{\sin\gamma} V_g \tag{2.7b}$$

$$M = \frac{\cos(\gamma-\omega_0 T_a)+\cos\omega_0 T_a-1-\cos\gamma}{\sin\gamma} Q_p \tag{2.7c}$$

The unknown time T_a in Eqs. (2.7) is determined by equating input and output powers. The input power is given by

$$P_{in} = \frac{1}{T_s}\int_0^{T_s} V_g I_R(t)\ dt \tag{2.8}$$

and the output power is given by

$$P_{out} = \frac{1}{T_s}\int_0^{T_s} V_R(t) I_B(t)\ dt \tag{2.9}$$

where

$$I_B(t) = \begin{cases} -\dfrac{V_0}{R} & 0 < t < T_a \\ \dfrac{V_0}{R} & T_a < t < T_s \end{cases} \tag{2.10}$$

When the integration is performed and P_{in} is set equal to P_{out} an implicit equation of the form $G_p(\gamma, Q_p, T_a) = 0$ is obtained from which the time T_a can be determined for a given Q_p and γ :

$$G_p(\gamma, Q_p, T_a) = \cos(\gamma - \omega_0 T_a)\left[\sin^2\omega_0 T_a + \cos 2\omega_0 T_a\right]$$

$$+ \sin\omega_0 T_a\left[\sin\gamma - \sin(\gamma - 2\omega_0 T_a)\right] + (\gamma - 2\omega_0 T_a)\sin\gamma - 2\cos\omega_0 T_a$$

$$+ Q_p\gamma\left[1 + \cos\gamma - \cos\omega_0 T_a - \cos(\gamma - \omega_0 T_a)\right] = 0 \qquad (2.11)$$

Once T_a is determined, the conversion ratio M and the initial conditions are determined from Eqs. (2.7). A plot of M vs. F_s/F_0 for different values of Q_p is shown in Fig. 2.5.

It can be seen from Fig. 2.5 that for a given Q_p the maximum value of the conversion ratio M_{max} and the control parameter $(F_s/F_0)_{max}$ at which the maximum occurs depend on the value of Q_p. A plot of $(F_s/F_0)_{max}$ and M_{max} vs. Q_p is shown in Fig. 2.6. The maximum value of M for large Q_p is approximately given by

$$M_{max} \approx Q_p \qquad (2.12)$$

Figure 2.5 reveals that in order to achieve significant control over the conversion ratio M with a reasonable change in the control parameter, Q_p should be selected larger than two or three. For instance, if $Q_p = 1$, then even a large variation of F_s/F_0 produces very little change in M, which clearly is not suitable for control purposes. Also, according to Fig. 2.5, when Q_p is selected large and the converter is operated away from the resonant peaks, the conversion ratio characteristics are less sensitive to changes in the load R. Therefore, only when operating away from the resonant peaks with Q_p larger than two or three , can the parallel resonant converter be somewhat considered as a voltage-fed converter.

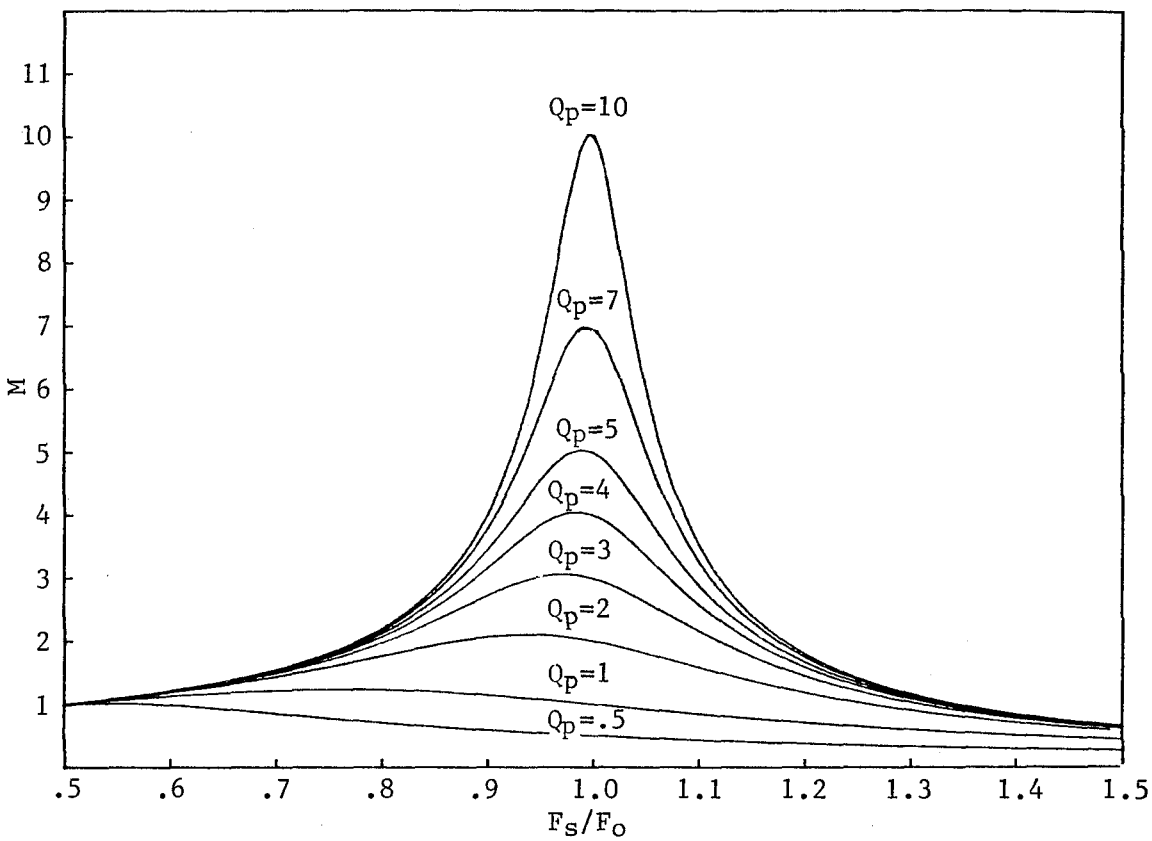

Fig. 2.5 Conversion ratio characteristics of the parallel resonant converter in continuous conduction mode.

For a given design application, the range of the control parameter F_s/F_0 can be selected either above or below $(F_s/F_0)_{max}$. It is advantageous, however, to operate this converter below $(F_s/F_0)_{max}$ because the transistor stops conducting as the resonant current, or the collector current, passes through zero. This eliminates problems of turn-off and makes it very attractive for SCR applications. Actually, for a given Q_p, the critical value of the control parameter $(F_s/F_0)_{zc}$ below which this natural turn-off occurs is slightly less than $(F_s/F_0)_{max}$ and is plotted in Fig. 2.6. This is illustrated in Fig. 2.7 where it is shown how the shape of the resonant current changes as F_s/F_0 is swept through $(F_s/F_0)_{zc}$. When the converter is operating below $(F_s/F_0)_{zc}$, as shown in Fig 2.7a, the transistor conducts first because the resonant current at the beginning of the switching interval is positive, i.e., $I_R(0)>0$. As the collector current passes through zero the parallel diode begins to conduct for a duration T_D. When using SCRs, it is important to know this diode conduction time T_D in order to allow sufficient turn-off time for the SCR. When operating exactly at the critical value $(F_s/F_0)_{zc}$, the transistors turn on and off at zero current and the parallel diodes never conduct. When operating above $(F_s/F_0)_{zc}$, as shown in Fig. 2.7c, the diodes conduct first because $I_R(0)$ is negative. As the diode current passes through zero, the transistor in parallel with it starts to conduct and is switched off while still in conduction. Therefore, this range of operation is not suitable for SCR applications. $(F_s/F_0)_{zc}$ is determined numerically by requiring $I_R(0) = 0$ for a given Q_p.

The diode conduction time T_D, shown in Fig. 2.7a, is now determined. The resonant current passes through zero at $t = T_z$ in the interval $T_a < t < T_s$ as shown in Fig. 2.7a. Therefore, Eq. (2.4a) is set equal

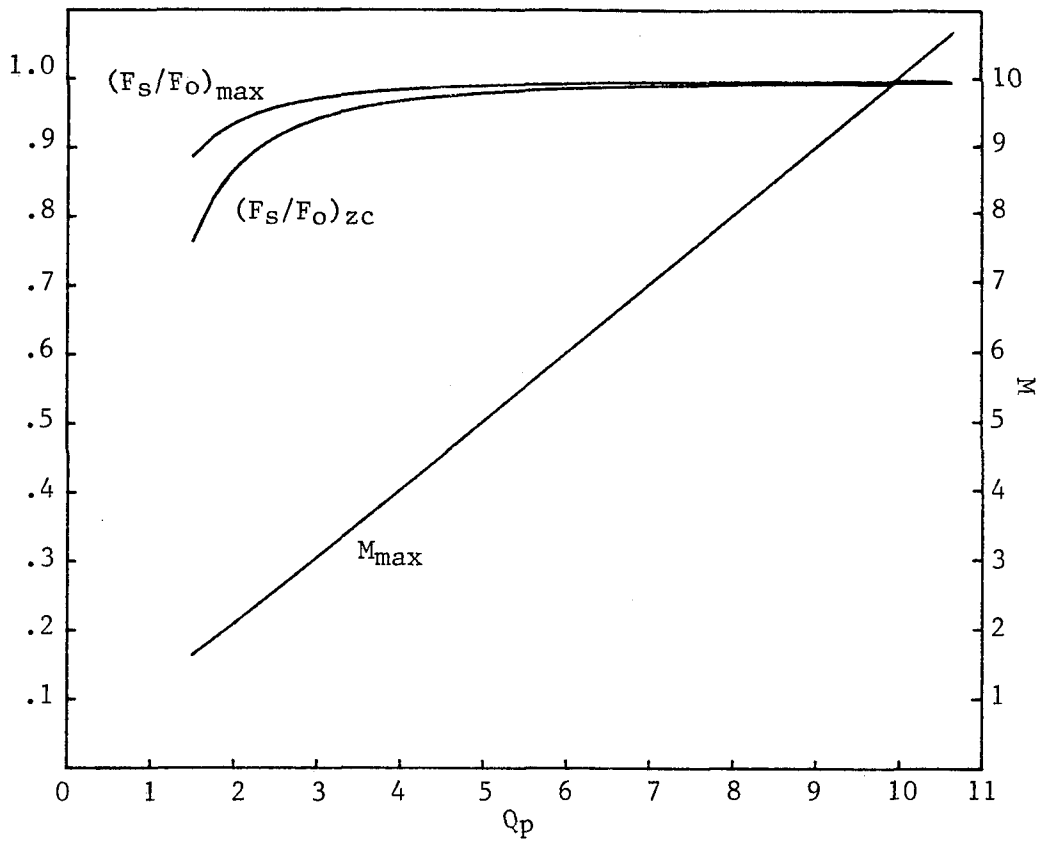

Fig. 2.6 The critical control parameters $(F_s/F_0)_{max}$ and $(F_s/F_0)_{zc}$ and the maximum value of M vs. Q_p. Note that M_{max} is almost linearly related to Q_p.

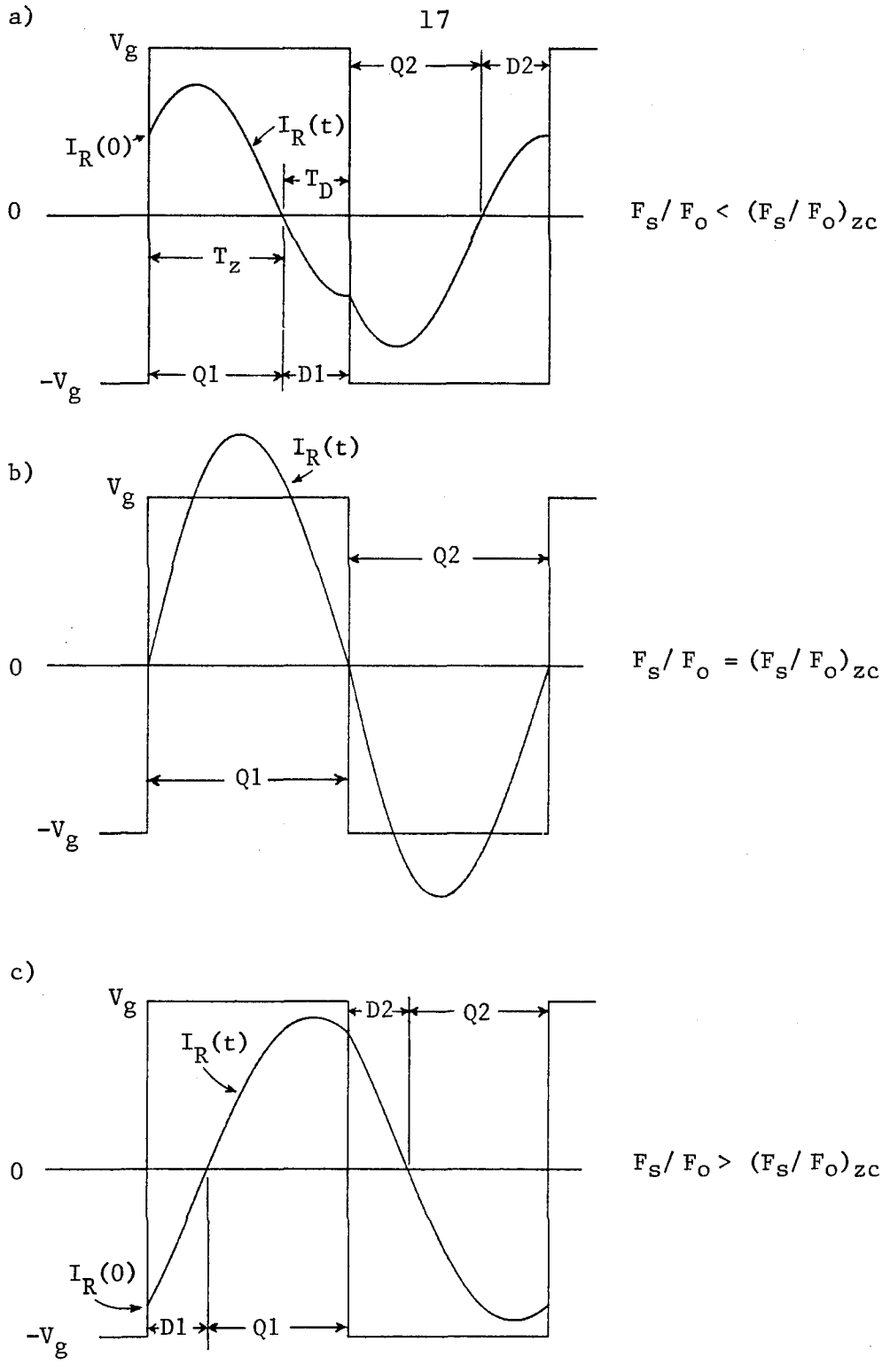

Fig. 2.7 Explanation of the change in the shape of the resonant current as F_s/F_0 is swept through $(F_s/F_0)_{zc}$. a) $F_s/F_0 < (F_s/F_0)_{zc}$ b) $F_s/F_0 = (F_s/F_0)_{zc}$ c) $F_s/F_0 > (F_s/F_0)_{zc}$.

to zero for $t = T_z$ and is written here as Eq. (2.13) after multiplying it out by $\omega_0 L_0 / V_g$

$$\left[I_R(T_a) \frac{\omega_0 L_0}{V_g} - \frac{M}{Q_p} \right] \cos\omega_0(T_z - T_a) + \sin\omega_0(T_z - T_a) + \frac{M}{Q_p} = 0 \qquad (2.13)$$

The angle $\omega_0\alpha$ is defined as follows

$$\tan(\omega_0\alpha) = I_R(T_a) \frac{\omega_0 L_0}{V_g} - \frac{M}{Q_p} \qquad (2.14)$$

which when manipulated further gives

$$\tan(\omega_0\alpha) = \frac{1 + \cos\gamma - 2\cos\omega_0 T_a}{\sin\gamma} \qquad (2.15)$$

Substitution of Eq. (2.15) in Eq. (2.13) gives

$$\frac{M}{Q_p} \cos(\omega_0\alpha) + \sin\omega_0(T_z - T_a + \alpha) = 0 \qquad (2.16)$$

From Eq. (2.16) the diode conduction time $T_D = T_s - T_z$ is obtained

$$\omega_0 T_D = \gamma - \pi + \omega_0(\alpha - T_a) - \sin^{-1}\left(\frac{M}{Q_p} \cos(\omega_0\alpha) \right) \qquad (2.17)$$

Therefore, for a given Q_p and γ, the time T_D is determined from Eq. (2.17) where T_a, M and α are determined from Eqs. (2.11), (2.7c) and (2.15) respectively. The normalized conduction time or the conduction angle vs. F_s / F_0 is plotted in Fig 2.8 for different values of Q_p. It can be seen from Figs. 2.6 and 2.8 that if Q_p is selected small, the useful range of the control parameter $.5 < F_s / F_0 < (F_s / F_0)_{zc}$ gets smaller. For all practical purposes then it is desirable to design the parallel converter with a minimum Q_p no

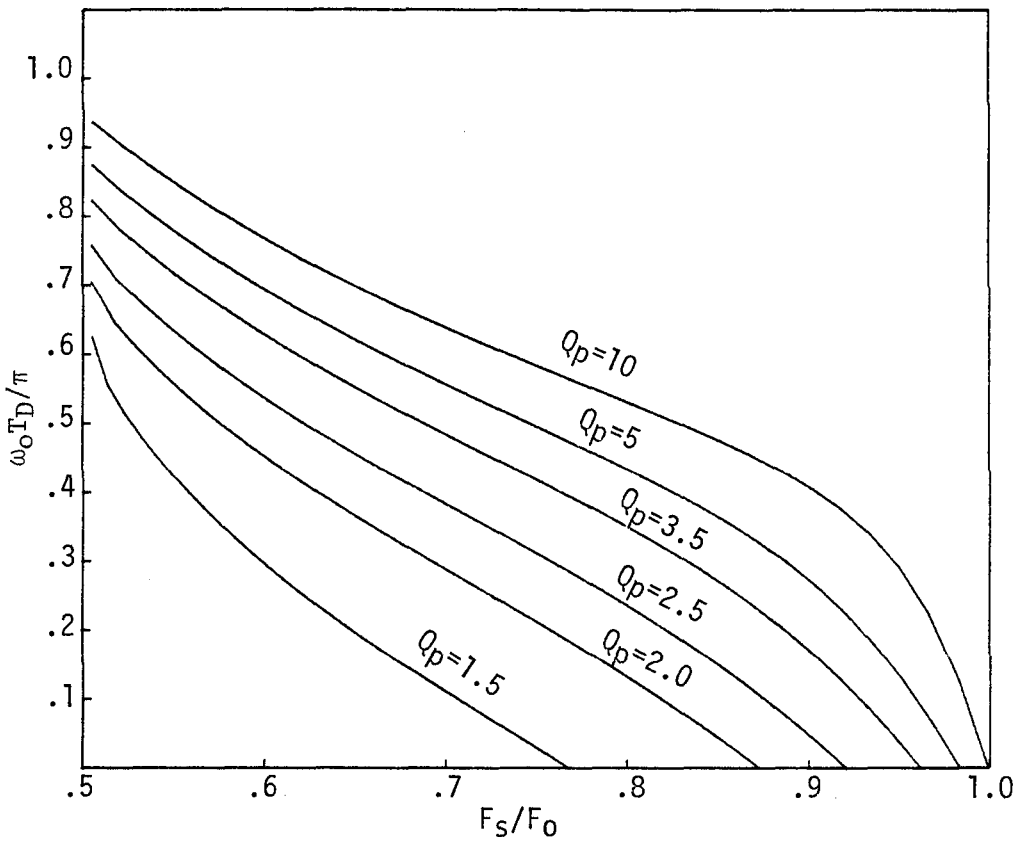

Fig. 2.8 Diode conduction angle characteristics of the parallel resonant converter.

less than two or three. The condition at $(F_s/F_0)_{zc}$ corresponds to $\omega_0 T_D = 0$.

A review of the linear parallel resonant circuit shown in Fig. 2.9a will now be given to show its similarity to the corresponding resonant converter. The transfer function characteristics of the linear circuit for different values of Q_p are shown in Fig. 2.9b. A comparison of these transfer function characteristics and the conversion ratio characteristics of the parallel converter shown in Fig. 2.5 shows that the peak of the characteristics and its position in both cases depend on Q_p. Furthermore, for large Q_p, the peak is approximately equal to Q_p and occurs approximately at resonance. For the parallel converter this is shown in Fig. 2.6 where it can be seen that $(F_s/F_0)_{max}$ approaches unity for large Q_p and M_{max} is approximately equal to Q_p.

The critical value of the control parameter $(F_s/F_0)_{zc}$ for the parallel converter can be likened to the critical value $\omega_c/\omega_0 = \sqrt{1-1/Q_p^2}$ of the linear resonant circuit for which the input impedance is real. For the linear circuit when the input impedance is real, the input voltage and the input current are in phase. Figures 2.9c and d show the similarity of the voltage and current relationship of the linear circuit at ω_c/ω_0 and the converter at $(F_s/F_0)_{zc}$; in both cases the voltage and current are of the same sign. For large values of Q_p, both ω_c/ω_0 of the linear circuit and $(F_s/F_0)_{zc}$ of the parallel converter tend to unity.

For proper component selection, the peak stress levels must be determined. First, the peak capacitor voltage and its dependence on Q_p and F_s/F_0 is determined. The variation of the capacitor voltage with F_s/F_0 is shown in Fig. 2.10. For a given Q_p, as the control parameter is

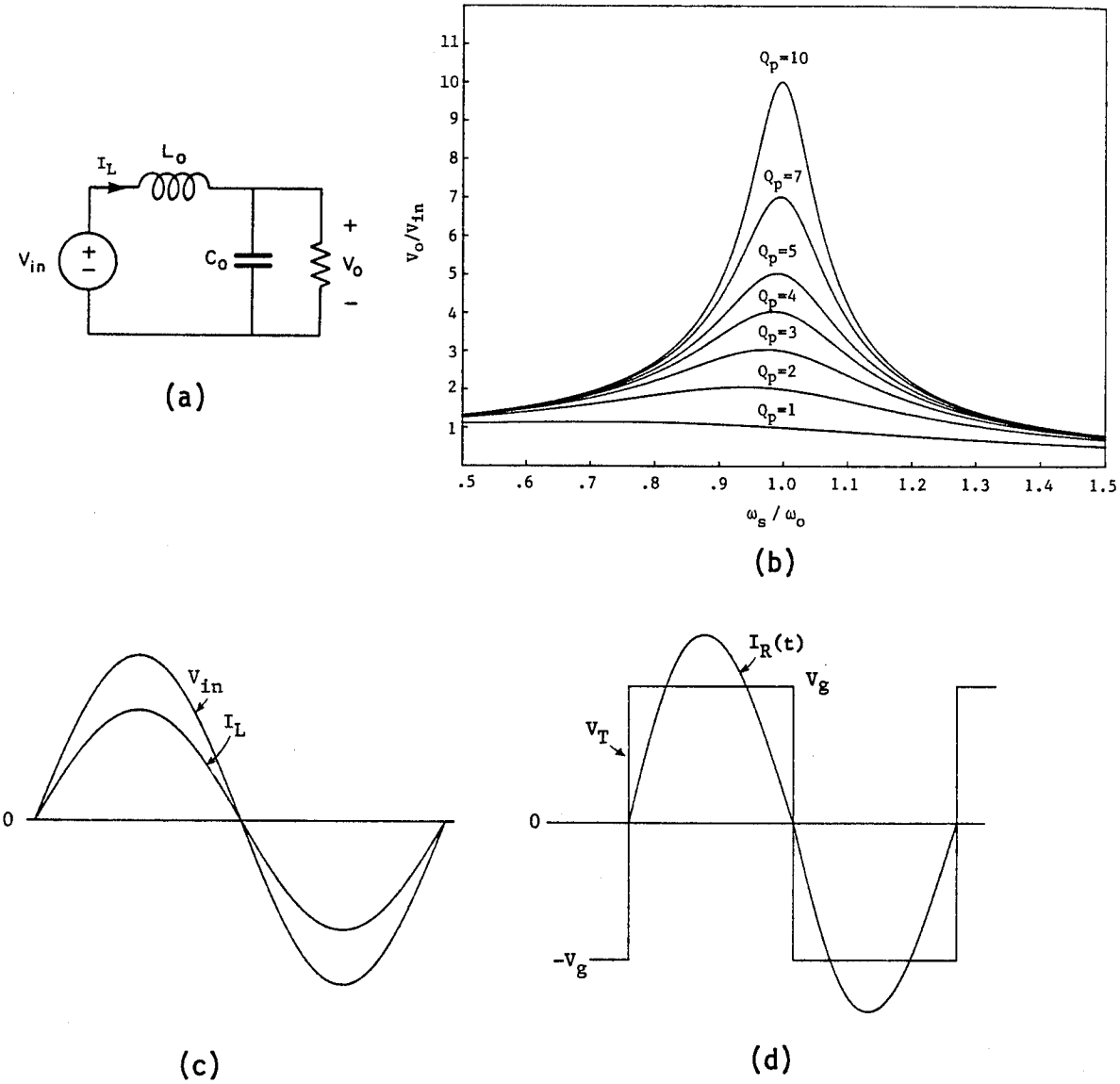

Fig. 2.9 a) The linear parallel resonant circuit and b) the magnitude of its transfer function characteristics. c) Input voltage and current relationships for the linear circuit at $\omega_c/\omega_0 = \sqrt{1-1/Q_p^2}$ *and d) for the converter at* $F_s/F_0 = (F_s/F_0)_{zc}$.

swept through $(F_s/F_0)_{max}$, the peak of the capacitor voltage shifts from the interval $T_a < t < T_s$ to the interval $0 < t < T_a$. Therefore, depending on which range F_s/F_0 falls in, the peak capacitor voltage is determined either from Eq. (2.3b) or Eq. (2.4b). First, the range $F_s/F_0 < (F_s/F_0)_{max}$ is considered where the peak capacitor voltage occurs in the interval $T_a < t < T_s$. The capacitor voltage in the interval $T_a < t < T_s$ is given by Eq. (2.4b) which after some manipulation is rewritten here as Eq. (2.18)

$$\frac{V_R(t)}{V_g} = -\cos\omega_0(t-T_a) + \left[I_R(T_a)\frac{\omega_0 L_0}{V_g} - \frac{M}{Q_p}\right]\sin\omega_0(t-T_a) + 1 \qquad (2.18)$$

Substitution of Eq. (2.14) in Eq. (2.18) gives

$$\frac{V_R(t)}{V_g} = 1 - \sec(\omega_0\alpha)\cos\omega_0(t-T_a+\alpha) \qquad (2.19)$$

From Eq. (2.19) it is clear that the peak capacitor voltage V_{peak} is given by

$$\frac{V_{peak}}{V_g} = 1 + |\sec(\omega_0\alpha)| \qquad F_s/F_0 < (F_s/F_0)_{max} \qquad (2.20)$$

When the converter is operating in the range of the control parameter $F_s/F_0 > (F_s/F_0)_{max}$, the peak occurs in the interval $0 < t < T_a$ in which case the capacitor voltage is given by Eq. (2.3b) which, after multiplying out by $\omega_0 L_0/V_g$, is rewritten here as Eq. (2.21)

$$\frac{V_R(t)}{V_g} = \left[\frac{V_R(0)}{V_g} - 1\right]\cos\omega_0 t + \left[\frac{M}{Q_p} + \omega_0 L_0 \frac{I_R(0)}{V_g}\right]\sin\omega_0 t + 1 \qquad (2.21)$$

The angle $\omega_0\beta$ is defined as

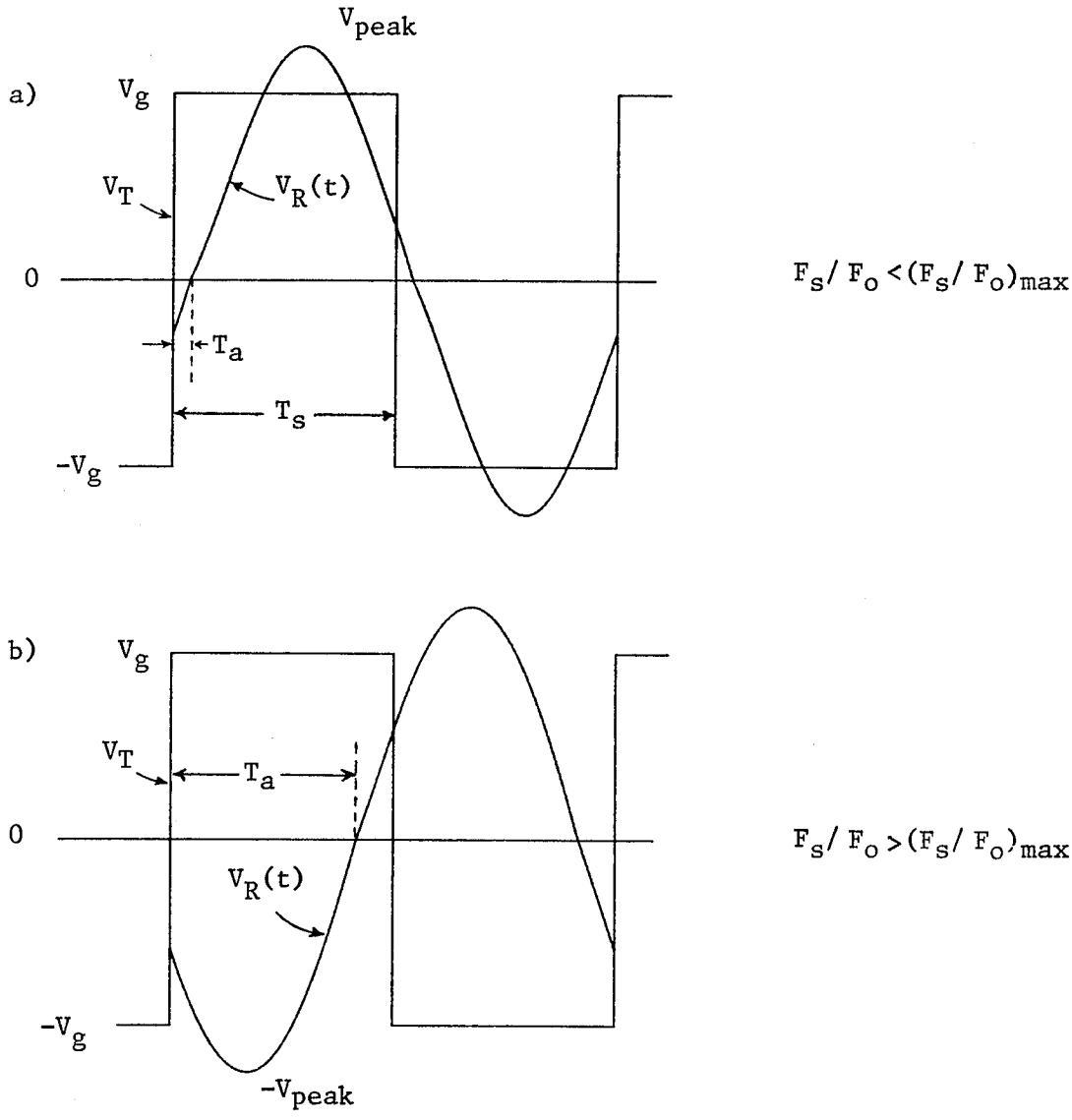

Fig. 2.10 Explanation of the shift in the peak capacitor voltage from a) the interval $T_a < t < T_s$ to b) to the interval $0 < t < T_a$, as the control parameter is swept through $(F_s/F_0)_{max}$.

$$\tan(\omega_0\beta) = \frac{M/Q_p + \omega_0 L_0 I_R(0)/V_g}{V_R(0)/V_g - 1} \tag{2.22}$$

where $I_R(0)$ and $V_R(0)$ are given by Eqs. (2.7a) and (2.7b) respectively. When Eq. (2.22) is substituted in Eq. (2.21), the following equation is obtained

$$\frac{V_R(t)}{V_g} = \sec(\omega_0\beta)\left[\frac{V_R(0)}{V_g} - 1\right]\cos\omega_0(t-\beta) + 1 \tag{2.23}$$

Since the capacitor voltage in this interval is negative, it can be seen from Eq. (2.23) that V_{peak} is given by

$$\frac{V_{peak}}{V_g} = -1 + \left|\sec(\omega_0\beta)\left[\frac{V_R(0)}{V_g} - 1\right]\right| \qquad F_s/F_0 > (F_s/F_0)_{max} \tag{2.24}$$

The results are summarized in the following equation

$$\frac{V_{peak}}{V_g} = \begin{cases} 1 + |\sec(\omega_0\alpha)| & ; \quad F_s/F_0 < (F_s/F_0)_{max} \\ -1 + \left|\sec(\omega_0\beta)\left[\frac{V_R(0)}{V_g} - 1\right]\right| & ; \quad F_s/F_0 > (F_s/F_0)_{max} \end{cases} \tag{2.25}$$

A plot of the normalized peak resonant capacitor voltage vs. F_s/F_0 for different values of Q_p is shown in Fig. 2.11. These characteristics are very similar to the conversion ratio characteristics because the output voltage is equal to the average rectified resonant capacitor voltage.

The variation of the resonant inductor current, $I_R(t)$, with the control parameter is slightly different from that of the capacitor voltage, $V_R(t)$. The peak of $I_R(t)$, shown in Fig. 2.12a, occurs in the time interval $T_a < t < T_s$ and is given by the maximum value of Eq. (2.4a). As the control

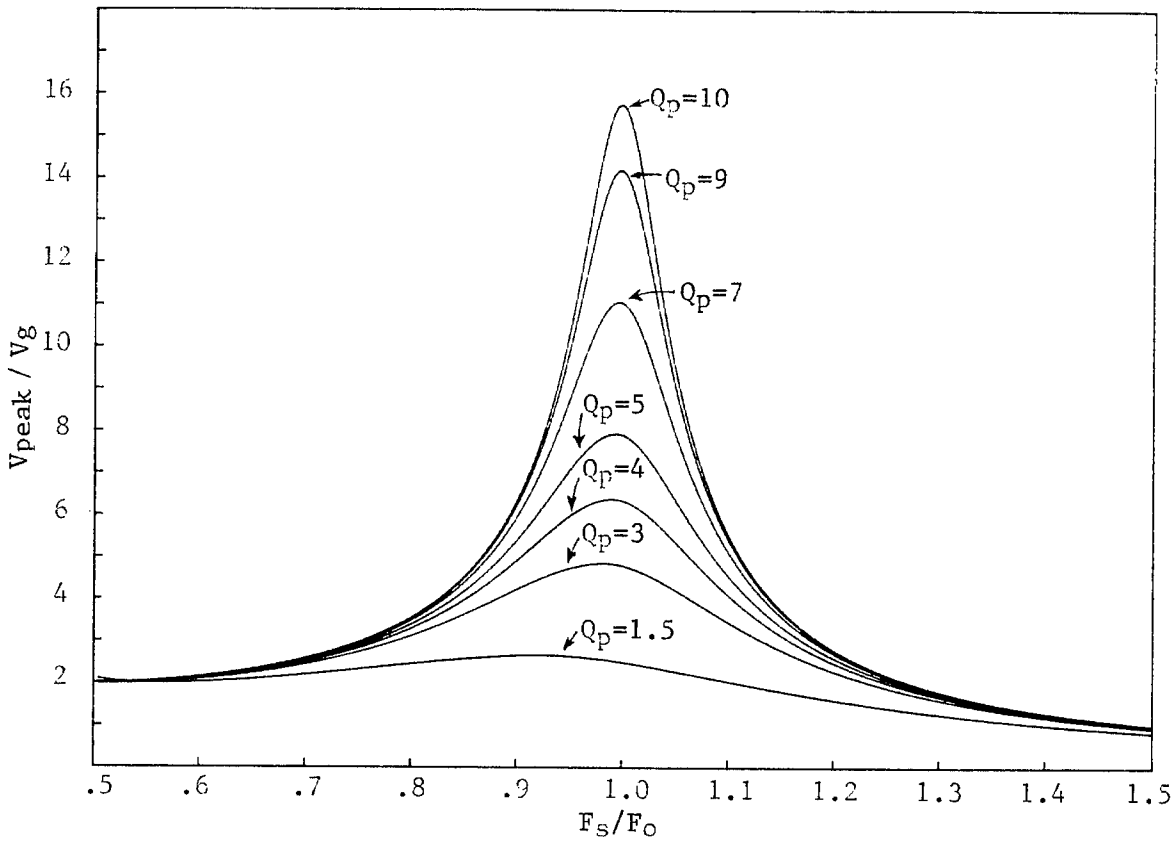

Fig. 2.11 Normalized peak resonant capacitor voltage characteristics of the parallel resonant converter.

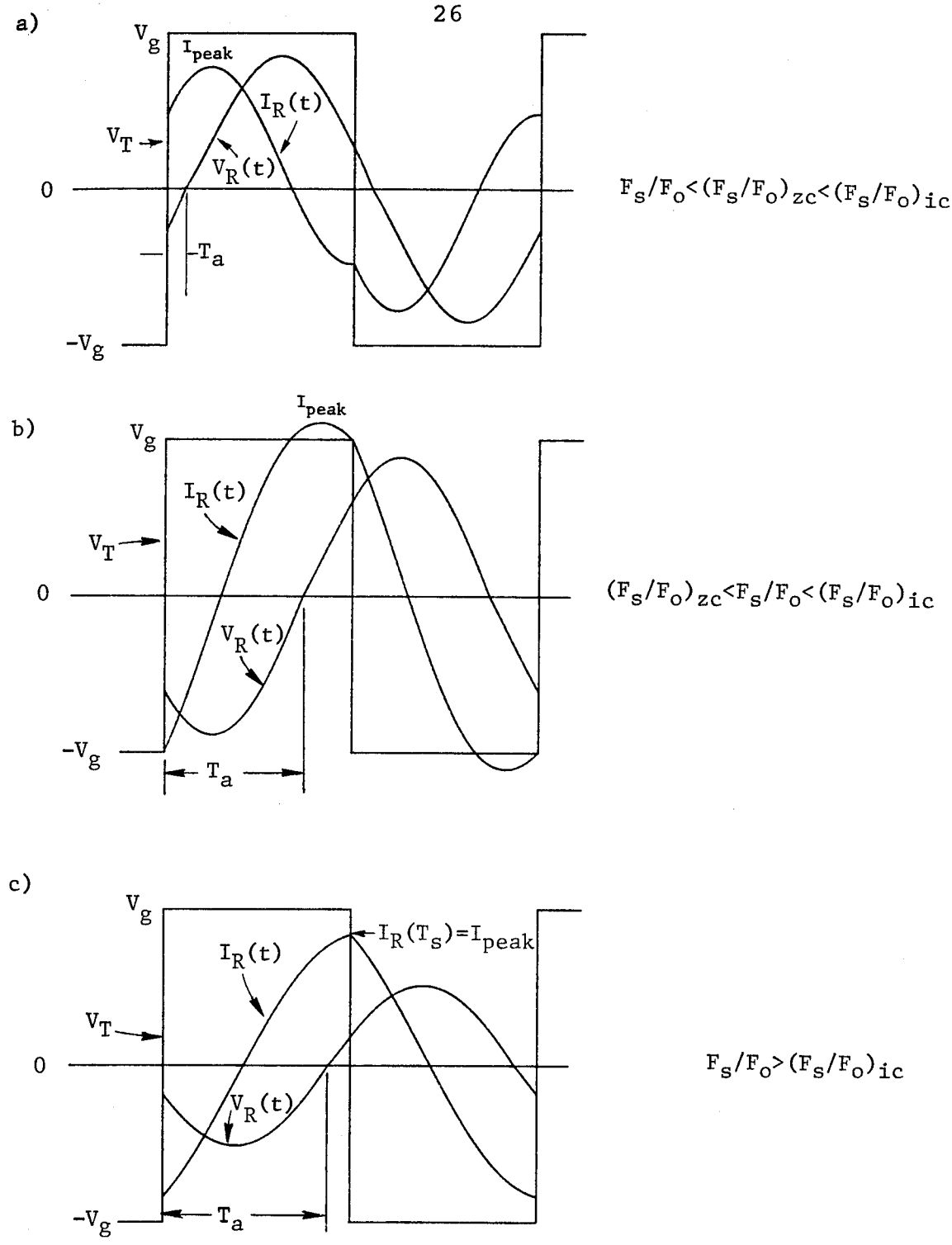

Fig. 2.12 Explanation of the change in the peak resonant current as F_s/F_0 is swept through $(F_s/F_0)_{ic}$. a) and b) For $F_s/F_0<(F_s/F_0)_{ic}$ the peak is given by the maximum value of the resonant current in the interval $T_a<t<T_s$ and c) for $F_s/F_0>(F_s/F_0)_{ic}$ the peak is given by $I_R(T_s)$.

parameter is swept through some critical value $(F_s/F_0)_{ic}$, the maximum value of Eq. (2.4a) does not occur because the time interval $T_a < t < T_s$ is not long enough. Consequently, when the converter is operating above $(F_s/F_0)_{ic}$, as shown in Fig. 2.12b, the peak is given by the value of the resonant current at the end of the switching time T_s, i.e., $I_{peak} = I_R(T_s) = -I_R(0)$. First, operation in the range $F_s/F_0 < (F_s/F_0)_{ic}$ is considered for which the peak inductor current is determined from Eq. (2.4a) which, after multiplying out by $\omega_0 L_0/V_g$, is rewritten here as Eq. (2.28)

$$I_R(t)\frac{\omega_0 L_0}{V_g} = \left[I_R(T_a)\frac{\omega_0 L_0}{V_g} - \frac{M}{Q_p}\right]\cos\omega_0(t-T_a) + \sin\omega_0(t-T_a) + \frac{M}{Q_p} \quad (2.28)$$

Substitution of Eq. (2.14) in Eq. (2.28) gives

$$I_R(t)\frac{\omega_0 L_0}{V_g} = \frac{M}{Q_p} + \sec(\omega_0\alpha)\sin\omega_0(t-T_a+\alpha) \quad (2.29)$$

The maximum value of $I_R(t)$ in Eq. (2.29) is

$$I_{peak}\frac{\omega_0 L_0}{V_g} = \frac{M}{Q_p} + |\sec\omega_0\alpha| \qquad F_s/F_0 < (F_s/F_0)_{ic} \quad (2.30)$$

As explained earlier, for $F_s/F_0 > (F_s/F_0)_{ic}$, the peak is given by $I_R(T_s) = -I_R(0)$. The normalized peak resonant current can be summarized by the following equation

$$I_{peak}\frac{\omega_0 L_0}{V_g}=\begin{cases}\dfrac{M}{Q_p}+|\sec(\omega_0\alpha)| & F_s/F_0<(F_s/F_0)_{ic}\\ -I_R(0)\ \ (\text{Eq. (2.7a)}) & F_s/F_0>(F_s/F_0)_{ic}\end{cases}\qquad(2.31)$$

The normalized peak resonant inductor current vs. F_s/F_0 for different values of Q_p is plotted in Fig. 2.13. According to Fig. 2.13, an interesting feature of the peak resonant current is that, in a certain range below resonance depending on Q_p, it decreases with increasing Q_p. This of course is expected because, as explained earlier, in this range of operation the converter behaves like a voltage-fed converter. Consequently, as the output power decreases the peak current decreases while on the other hand the peak capacitor voltage, like the output voltage, remains mostly unaffected. Also, a comparison of the peak current below and above resonance shows that, for the same conversion ratio, the peak current below resonance is less than the peak current above resonance.

The critical control parameter $(F_s/F_0)_{ic}$ is determined numerically and is plotted in Fig. 2.14. A comparison of Figs. 2.14 and 2.6 reveals the following important relation

$$(F_s/F_0)_{zc} < (F_s/F_0)_{\max} < (F_s/F_0)_{ic}\qquad(2.32)$$

According to the inequality in Eq. (2.32), when the converter is operating in the more useful range of the control parameter, $.5<F_s/F_0<(F_s/F_0)_{zc}$, where natural turn-off of the transistors occur, the peak capacitor voltage and peak inductor current can be summarized by the following equation

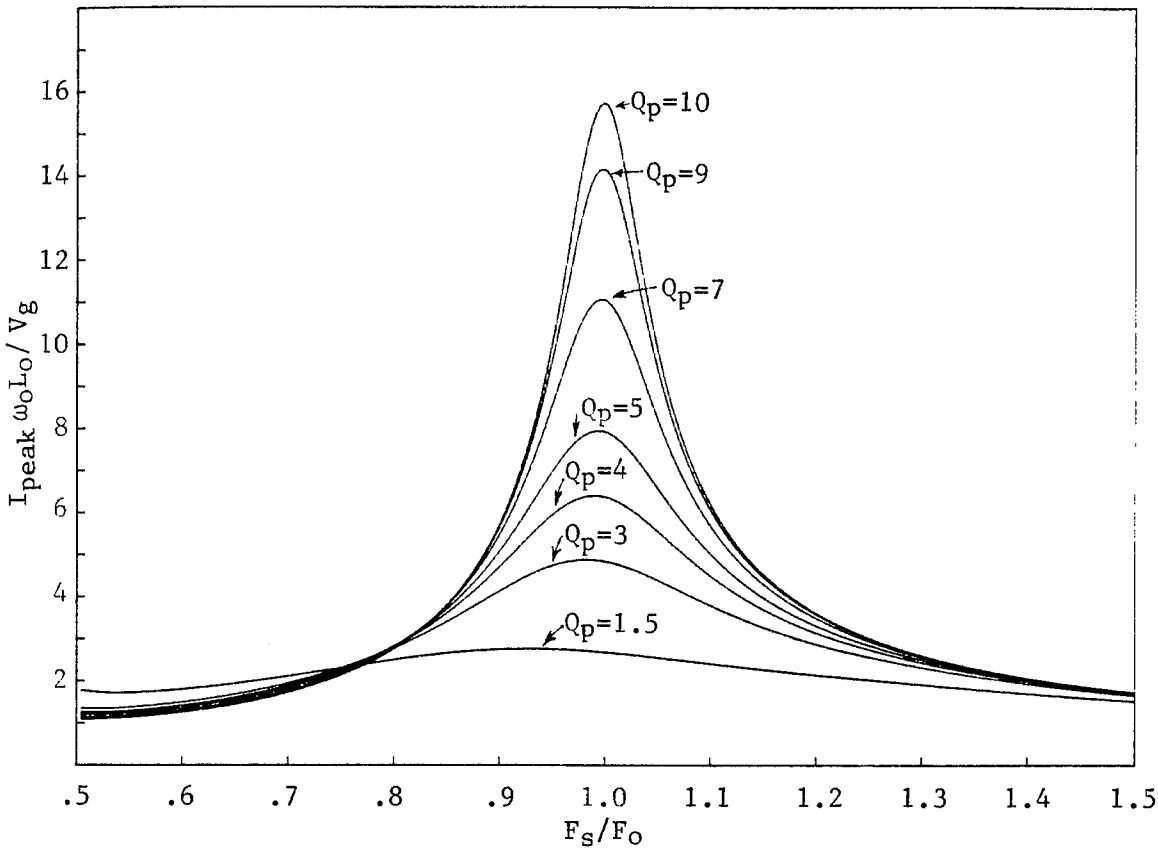

Fig. 2.13 Normalized peak resonant inductor current characteristics of the parallel resonant converter.

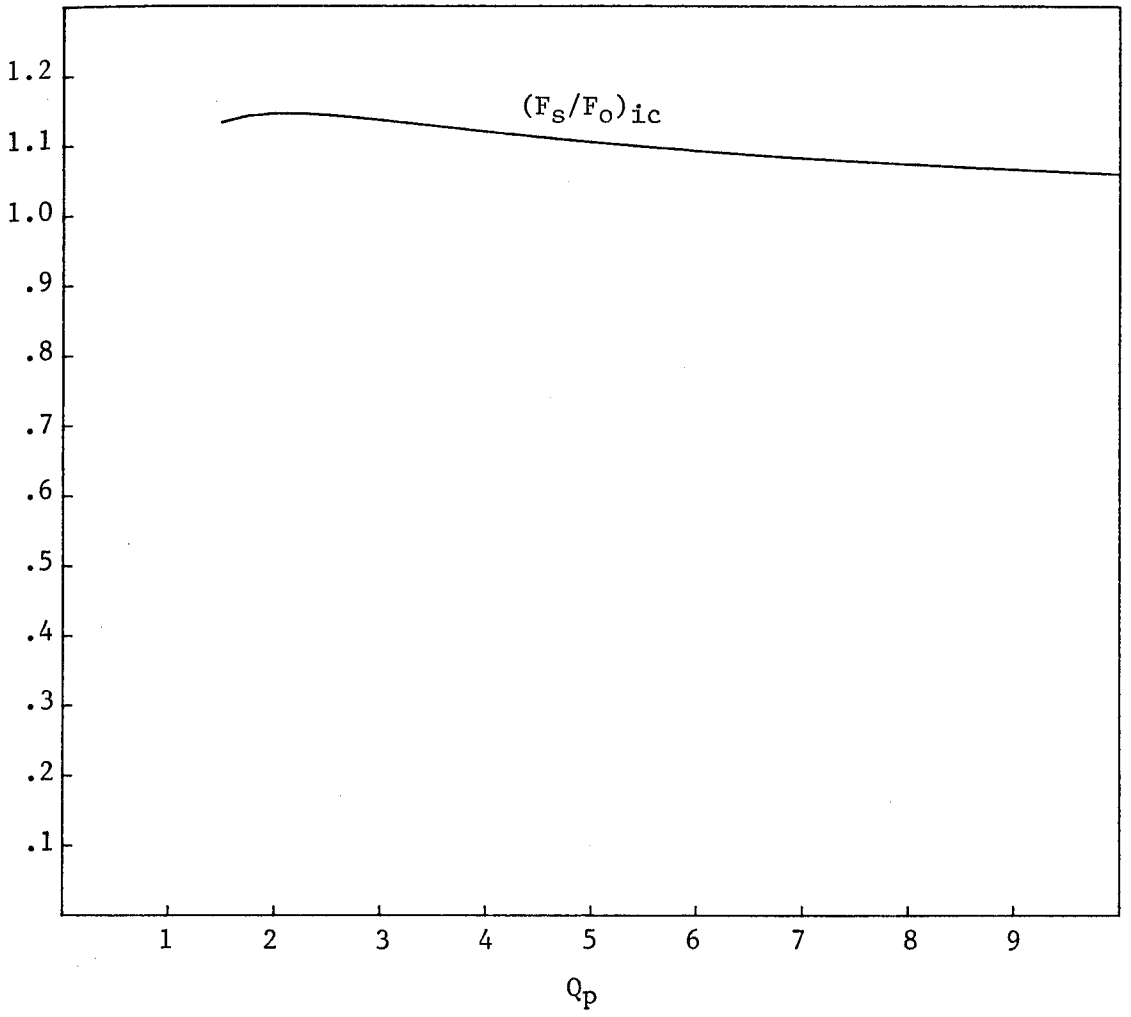

Fig. 2.14 Critical value of the control parameter $(F_s/F_0)_{ic}$ vs. Q_p.

$$1/2 \leq F_s/F_0 \leq (F_s/F_0)_{zc} \begin{cases} \dfrac{V_{peak}}{V_g} = 1 + |\sec(\omega_0 \alpha)| \\ I_{peak}\ \dfrac{\omega_0 L_0}{V_g} = \dfrac{M}{Q_p} + |\sec(\omega_0 \alpha)| \end{cases} \quad \text{(2.33a-b)}$$

2.4 Nonidealities

In Sec. 2.3 the analysis was carried out with the assumption that all the active and passive devices were ideal. Nonidealities, such as parasitic resistances of the resonant inductor and capacitor and the output filter inductor, as well as the voltage drops in the active components, are considered in this section. These parasitics introduce losses which deteriorate the efficiency of the converter. The losses due to parasitic resistances and voltage drops in the semiconductors are considered separately to show the contribution of each loss mechanism to the efficiency. Since these parasitics are small and do not affect the main operation of the converter, the results of the analysis given in Sec. 2.3 are modified slightly in this section by introduction of fudge factors.

The first nonideality to be considered is the voltage drop V_{BD} in the output rectifiers. The two different methods of output rectification are shown in Fig. 2.15 where the isolation transformer is assumed to be ideal and of unity turns ratio. In Fig. 2.16a the output network is reflected to the primary side of the transformer and the voltage drop in the rectifiers is separated and represented by a voltage source V_{BD} in series with an ideal diode. The voltage source, V_{BD}, is either equal to one diode voltage drop, V_D, or two diode voltage drops, $2V_D$, depending on the method of

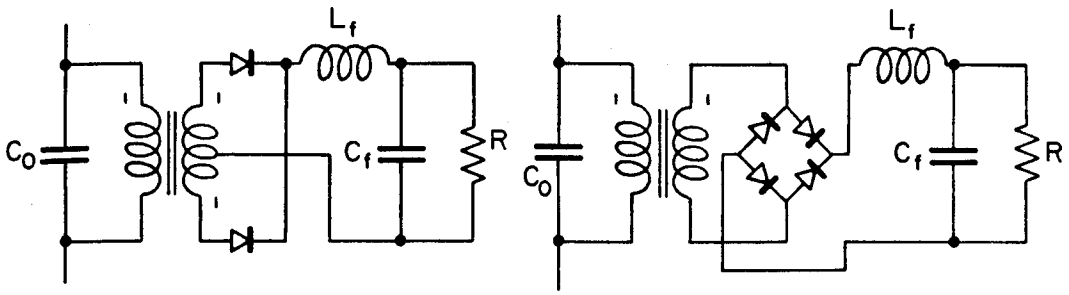

Fig. 2.15 Two methods of implementing the isolation transformer in the parallel resonant converter. a) center-tapped and b) full-bridge.

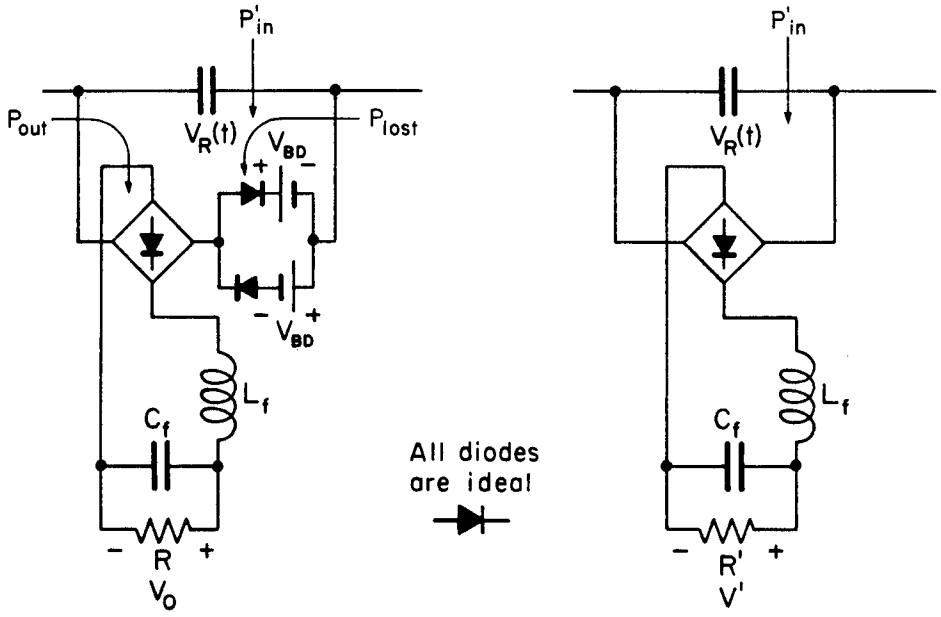

Fig. 2.16 a) Nonideal circuit with voltage drop V_{BD} in the output rectifiers and b) ideal circuit that delivers the same power P_{in}' as the nonideal circuit in a).

rectification

$$V_{BD} = \begin{cases} V_D & \text{center-tapped} \\ 2V_D & \text{full-bridge} \end{cases}$$

The power flow is shown in Fig. 2.16a where P_{Lost} represents losses in the diode voltage drops and P_{out} represents the power delivered to the load. The input power is given by

$$P_{in}' = P_{out} + P_{Lost} \tag{2.34}$$

P_{in}' is given by Eq. (2.9) and rewritten here as Eq. (2.35)

$$P_{in}' = \frac{1}{T_s}\int_0^{T_s} V_R(t)\, I_B(t)\, dt \tag{2.35}$$

It is clear that in the absence of losses $P_{in}'=P_{out}$. Equation (2.11) was obtained by equating input and output powers. In the absence of rectifier losses, the power delivered at the terminals of the resonant capacitor is equal to the output power. In the presence of these losses the power, P_{in}', delivered at the terminals of the resonant capacitor must be correctly accounted for. In what follows, an ideal circuit, such as the one shown in Fig. 2.16b, will be determined which has the same power, P_{in}', delivered at the terminals of the resonant capacitor as the nonideal circuit in Fig. 2.16a, and to which the same analysis given in Sec. 2.3 can be applied. First, the power P_{in}' in Fig. 2.16a is considered which is equal to the sum of the power lost in the rectifiers and the power delivered to the load

$$P_{in}' = V_{BD}I_0 + V_0I_0 \quad ; \quad I_0 = \frac{V_0}{R} \tag{2.36}$$

According to Fig. 2.16a the output voltage V_0 is equal to the average rectified capacitor voltage $<|V_R(t)|>$ less V_{BD}

$$V_0 = <|V_R(t)|> - V_{BD} \tag{2.37}$$

where

$$<|V_R(t)|> = \frac{1}{T_s}\int_0^{T_s} |V_R(t)|\, dt \tag{2.38}$$

substitution of Eq. (2.37) in Eq. (2.36) gives

$$P_{in}' = \frac{<|V_R(t)|>^2}{R}\left[1 - \frac{V_{BD}}{<|V_R(t)|>}\right] \tag{2.39}$$

Now let

$$V' = <|V_R(t)|> \tag{2.40}$$

$$M' = \frac{V'}{V_g} \tag{2.41}$$

$$R' = \frac{R}{1-\frac{V_{BD}}{M'V_g}} \tag{2.42}$$

Equation (2.39) can now be written as

$$P_{in}' = \frac{V'^2}{R'} \tag{2.43}$$

Equations (2.40) through (2.43) are satisfied by the ideal circuit shown in

Fig. 2.16b which has a conversion ratio M' and a load R'. According to Eq. (2.42) the normalized load parameter, Q_p', of this ideal circuit is related to the original Q_p of the nonideal circuit by

$$Q_p' = \frac{Q_p}{1 - \frac{V_{BD}}{M' V_g}} \tag{2.44}$$

The results of the analysis given in Sec. 2.3 will now be applied to the ideal circuit in Fig. 2.16b. First, the conversion ratio M' is considered which according to Eq. (2.7c) is given by

$$M' = \frac{\cos(\gamma - \omega_0 T_a) + \cos\omega_0 T_a - 1 - \cos\gamma}{\sin\gamma} Q_p' \tag{2.45}$$

Substitution of Eq. (2.44) in Eq. (2.45) gives

$$M' = \frac{\cos(\gamma - \omega_0 T_a) + \cos\omega_0 T_a - 1 - \cos\gamma}{\sin\gamma} Q_p + \frac{V_{BD}}{V_g} \tag{2.46}$$

Next, the implicit Equation (2.11), from which $\omega_0 T_a$ is determined, is modified. The last line in Eq. (2.11) can be seen to be equal to $-M\gamma\sin\gamma$. Now, when M is substituted by M' a new implicit equation $G_p'(\gamma, Q_p, T_a)$ is obtained which is related to $G_p(\gamma, Q_p, T_a)$ by the following equation

$$G_p'(\gamma, Q_p, T_a) = G_p(\gamma, Q_p, T_a) - \gamma\sin\gamma \frac{V_{BD}}{V_g} = 0 \tag{2.47}$$

Once $\omega_0 T_a$ is determined from Eq. (2.47) for a given Q_p and γ, the conversion ratio M' can be determined from Eq. (2.46). The actual conversion ratio M_a of the nonideal circuit can now be obtained from Eq. (2.37) as follows

$$M_a = \frac{V_0}{V_g} = M' - \frac{V_{BD}}{V_g} \tag{2.48}$$

According to Eqs. (2.46) and (2.48), the conversion ratio of the nonideal circuit M_a is still given by Eq. (2.7c), but the angle $\omega_0 T_a$ is now determined from the modified implicit equation given by Eq. (2.47).

The efficiency of the converter due to losses in the output rectifiers is considered next. This efficiency η_R due to rectifier losses is easily seen to be given by

$$\eta_R = \frac{1}{\frac{V_{BD}}{V_0} + 1} \tag{2.49}$$

The first thing to note from Eq. (2.49) is that, just as in the case of PWM converters, the efficiency deteriorates for lower output voltages. According to Eq. (2.48), substitution of V_0 in Eq. (2.49) gives another expression for the efficiency η_R

$$\eta_R = 1 - \frac{V_{BD}}{M' V_g} \tag{2.50}$$

The actual gain can now be written as

$$M_a = \eta_R M' \tag{2.51}$$

The efficiency η_R vs. F_s / F_0 is plotted in Fig. 2.17 for two different values of V_{BD} / V_g. The efficiency is seen to be higher near resonance where the conversion ratio is higher. These curves do not suggest that the converter should be operated near the resonant peak; all they show is the behavior of η_R in open loop operation. For a closed loop regulator with a

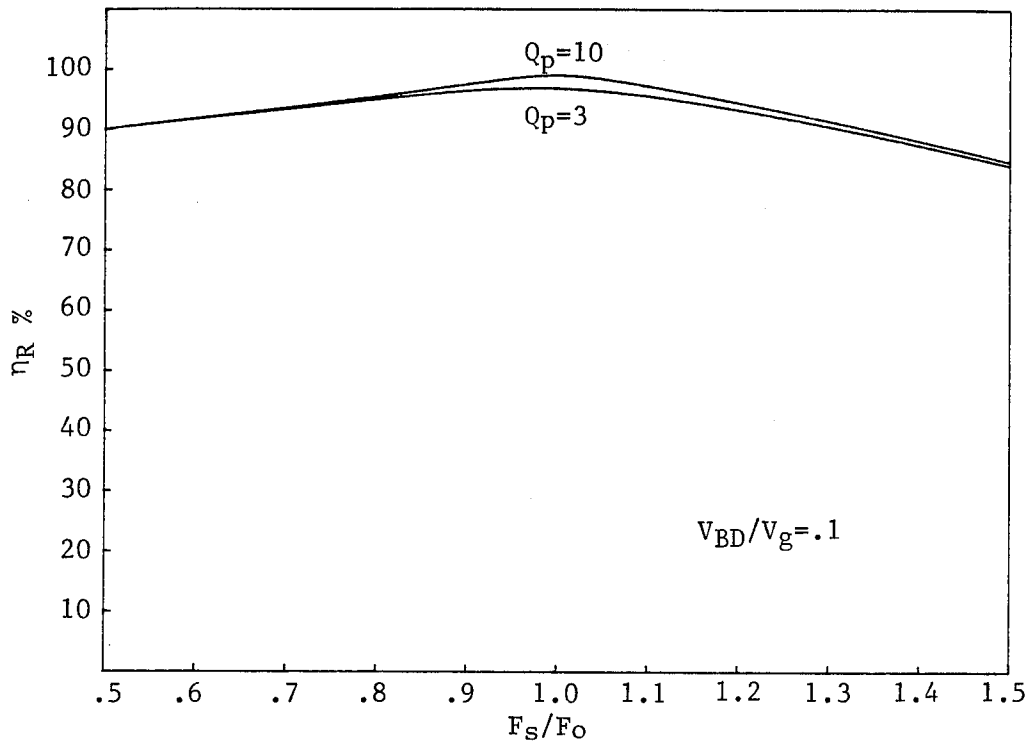

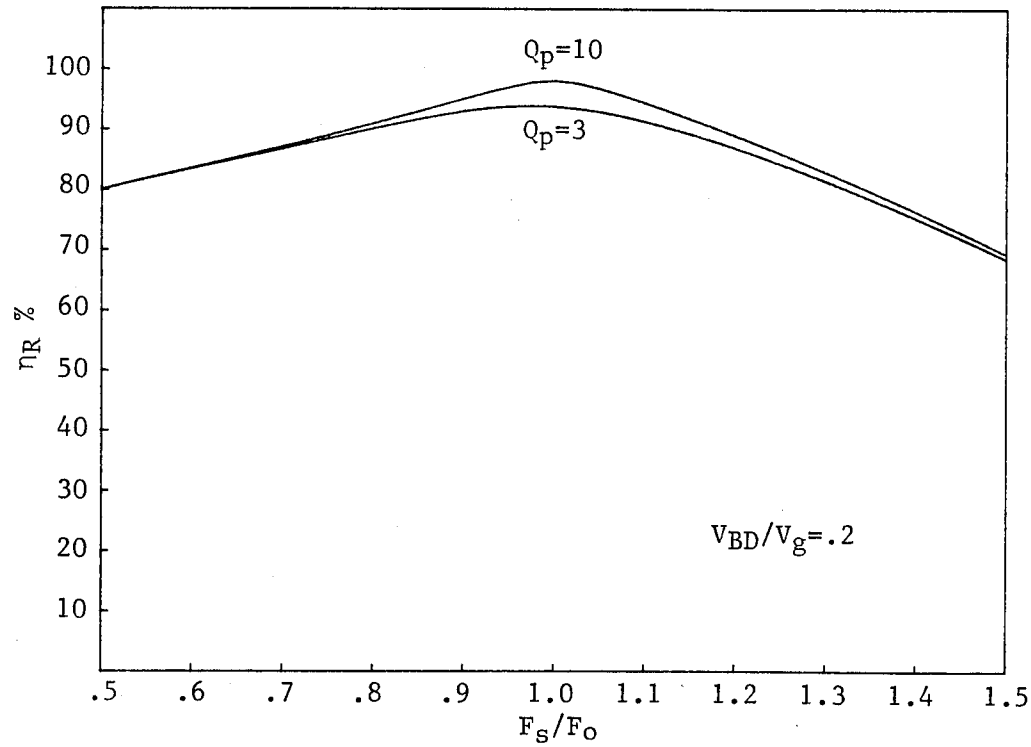

Fig. 2.17 a-b) Efficiency of the parallel resonant converter due to losses in the output rectifiers for two different ratios of V_{BD}/V_g.

fixed output voltage, η_R is given by Eq. (2.49).

The losses in the switches are now considered briefly. These switches can be realized by implementing BJTs, FETs [1,2], or SCRs [3]. In all these cases the voltage drop during forward conduction, V_{FS}, is different from the voltage drop during reverse conduction, V_{RS}. The losses in the switches are given by

$$P_{Lost} = \frac{1}{T_s}\left[V_{FS}\int_0^{T_z}|I_R(t)|dt + V_{RS}\int_{T_z}^{T_s}|I_R(t)|dt\right] \tag{2.52}$$

where T_z is the zero-crossing time of $I_R(t)$. In Eq. (2.52), the resonant current, $I_R(t)$, must be determined taking into account the voltage drops V_{FS} and V_{RS}. Such an analysis would be rather complicated, however, if V_{FS} and V_{RS} are small compared to V_g, which is generally the case for most applications, $I_R(t)$ in Eq. (2.52) can be determined assuming ideal switches. Therefore, for thermal design, the losses can be estimated according to Eq. (2.52), in which $I_R(t)$ is determined assuming ideal switches. Experimental results given in Sec. 2.5 are in good agreement with the predicted results assuming ideal switches.

The losses in the parasitic resistances are considered next. The losses in the esr of the output filter capacitor are not considered because in the dc analysis given in Sec. 2.3 the current in the output filter inductor was assumed to be free of ripple. The input power is given by

$$P_{in} = V_{in}I_{in} \tag{2.53}$$

where I_{in} is the average input current shown in Fig. 2.1a and b. The

output power, in the presence of parasitics, is given by

$$P_{out} = \eta_p P_{in} = V_0 I_0 \tag{2.54}$$

According to Eq. (2.53) and (2.34), the efficiency due to the parasitics is given by

$$\eta_p = \frac{V_0}{V_{in}} \frac{I_0}{I_{in}} \tag{2.55}$$

It will be assumed now that in the presence of these parasitics, the current conversion ratio I_{in} / I_0 remains unaffected and is still given by the ideal voltage conversion ratio. Therefore, the actual conversion ratio, $M_a = V_0 / V_{in}$, of the converter in Fig. 2.1a, according to Eq. (2.55) is now given by

$$M_a = \eta_p \frac{M}{2} \tag{2.56a}$$

and for the converter in Fig. 2.1b, M_a is given by

$$M_a = \eta_p M \tag{2.56b}$$

The results given in Eqs. (2.56) hold for PWM converters as well. The actual conversion ratio for PWM converters in the presence of parasitics is derived by the method of state-space averaging [4]. It was shown in [4] that the current conversion ratio remains unaffected in the presence of parasitic resistances and that the actual conversion ratio is given by the product of the efficiency and the ideal conversion ratio. Since for resonant converters the steady-state results are not as easily obtained, rather than deriving it, the current conversion ratio is *assumed* to remain unchanged. The power

lost in the parasitic resistances is given by

$$P_{Lost} = I_r^2 r_{L_o} + I_c^2 r_{C_o} + I_0^2 r_{L_f} \tag{2.57}$$

where r_{L_o}, r_{C_o} and r_{L_f} are the parasitic resistances of the resonant inductor, resonant capacitor and output filter inductor respectively. The currents I_r and I_c are the rms values of the resonant inductor and capacitor currents determined in Appendix A. The efficiency is now given by

$$\eta_p = \frac{1}{1 + \frac{I_r^2}{I_0^2}\frac{r_{L_o}}{R} + \frac{I_c^2}{I_0^2}\frac{r_{C_o}}{R} + \frac{r_{L_f}}{R}} \tag{2.58}$$

As before, it will be assumed that the ratios I_r / I_0 and I_c / I_0 remain unchanged in the presence of parasitics. Consequently, the rms values are determined from the expressions derived in Sec. 2.3. The following normalized loss parameters are defined

$$Q_l = \frac{\omega_0 L_0}{r_{L_o}} \;,\; Q_c = \frac{\omega_0 L_0}{r_{C_o}} \;,\; Q_f = \frac{\omega_0 L_0}{r_{L_f}} \tag{2.59}$$

The efficiency due to the parasitics can be written now as

$$\eta_p = \frac{1}{\frac{Q_p}{M^2}\left[\frac{B_r}{Q_l} + \frac{B_c}{Q_c}\right] + \frac{1}{Q_f Q_p} + 1} \tag{2.60}$$

The constants B_r and B_c are determined in Appendix A. According to Eq. (2.60) it can be seen that the efficiency due to the parasitics in the

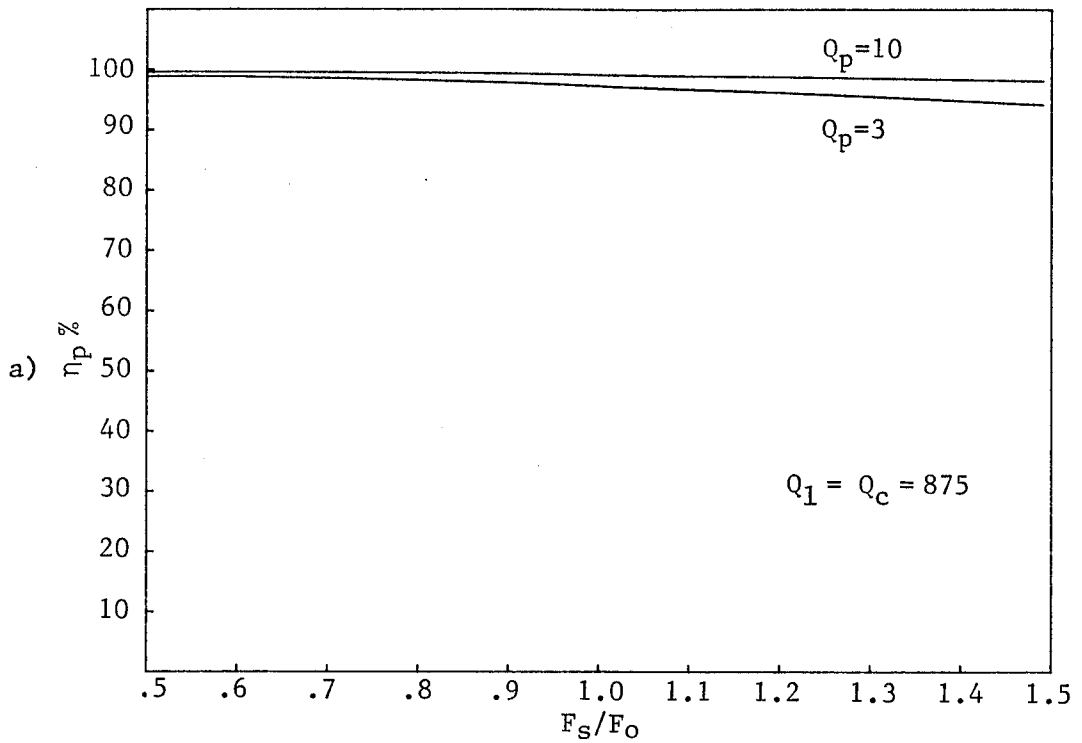

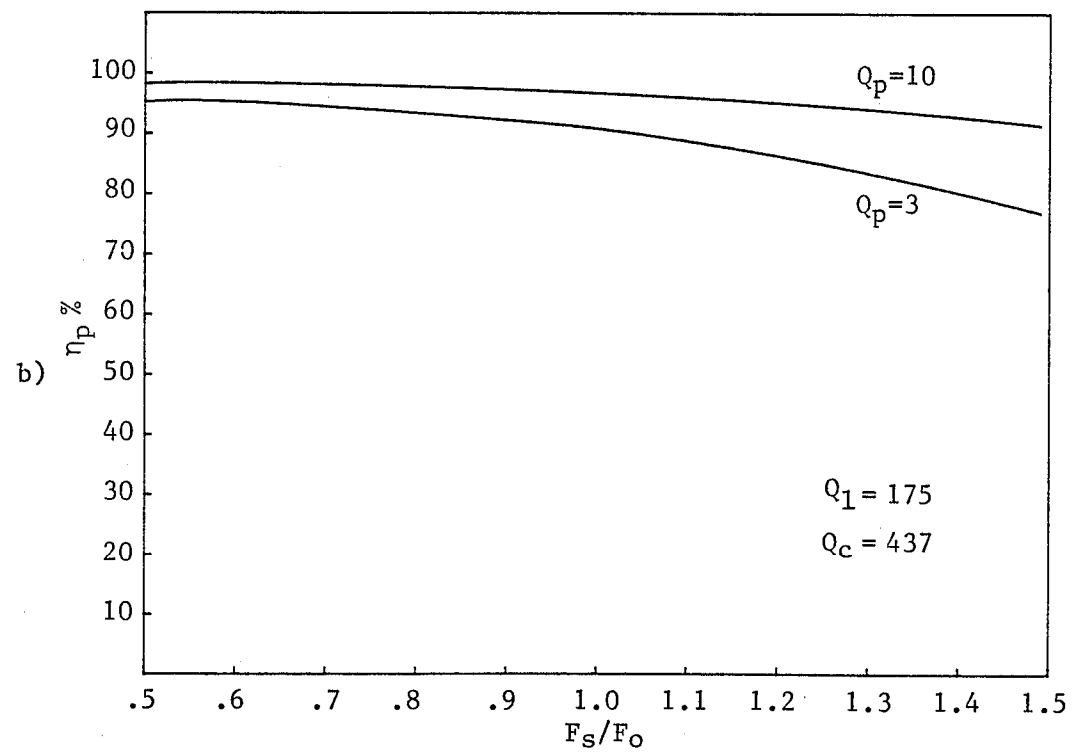

Fig. 2.18 Efficiency of the parallel resonant converter due to losses in the parasitic resistances. a) $Q_l = Q_c = 875$ and b) $Q_l = 175$ $Q_c = 437$.

resonant capacitor and inductor depend on the operating point whereas the efficiency due to the parasitic resistance in the output filter inductor does not. In Fig. 2.18 the efficiency vs. F_s/F_0 is plotted for two different values of Q_p, Q_l, and Q_c assuming $r_{L_f}=0$. It can be seen that the efficiency deteriorates for increasing Q_p and F_s/F_0. Clearly the efficiency deteriorates for small Q_l and large Q_c as can be seen by comparing Fig. 2.19a and b. It can also be seen that the efficiency is higher in the important range of the control parameter $.5<F_s/F_0<(F_s/F_0)_{zc}$ determined earlier in Sec. 2.3.

2.5 Experimental Results

The experimental circuit used to verify the conversion ratio characteristics is shown in Fig. 2.19. The circuit values are

$$L_0=49\mu\text{H} \qquad C_0=.1\mu\text{F} \qquad V_g=12\text{V} \tag{2.61}$$

The experimental and predicted results are shown in Fig. 2.20. The predicted characteristics are obtained considering only the diode voltage drops using Eqs. (2.46) through (2.48). The experimental and the predicted results are in good agreement except near the peaks. This discrepancy owes to the fact that the analysis for the nonideal circuit is not exact. An exact analysis with all the parasitic losses (including core losses) would result in better agreement near the peaks, but since it is desirable to operate the converter away from the peaks, such a tedious analysis would be unnecessary.

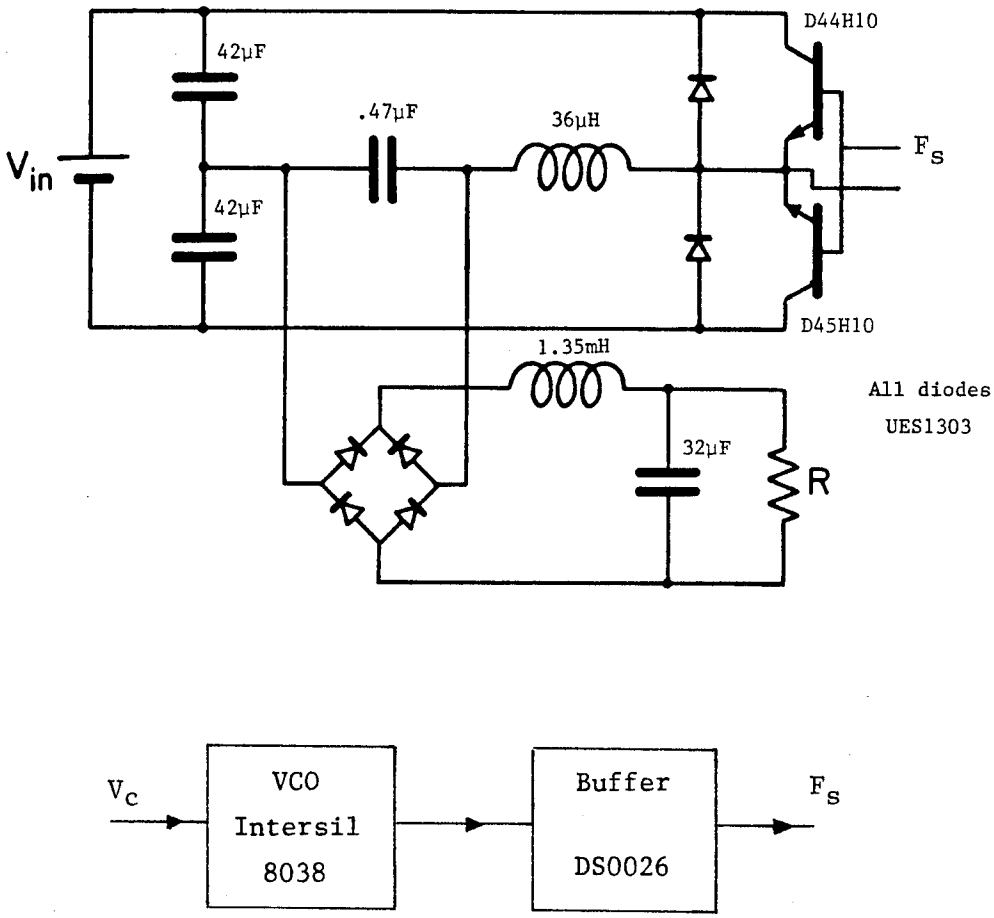

Fig. 2.19 Experimental circuit for the parallel resonant converter

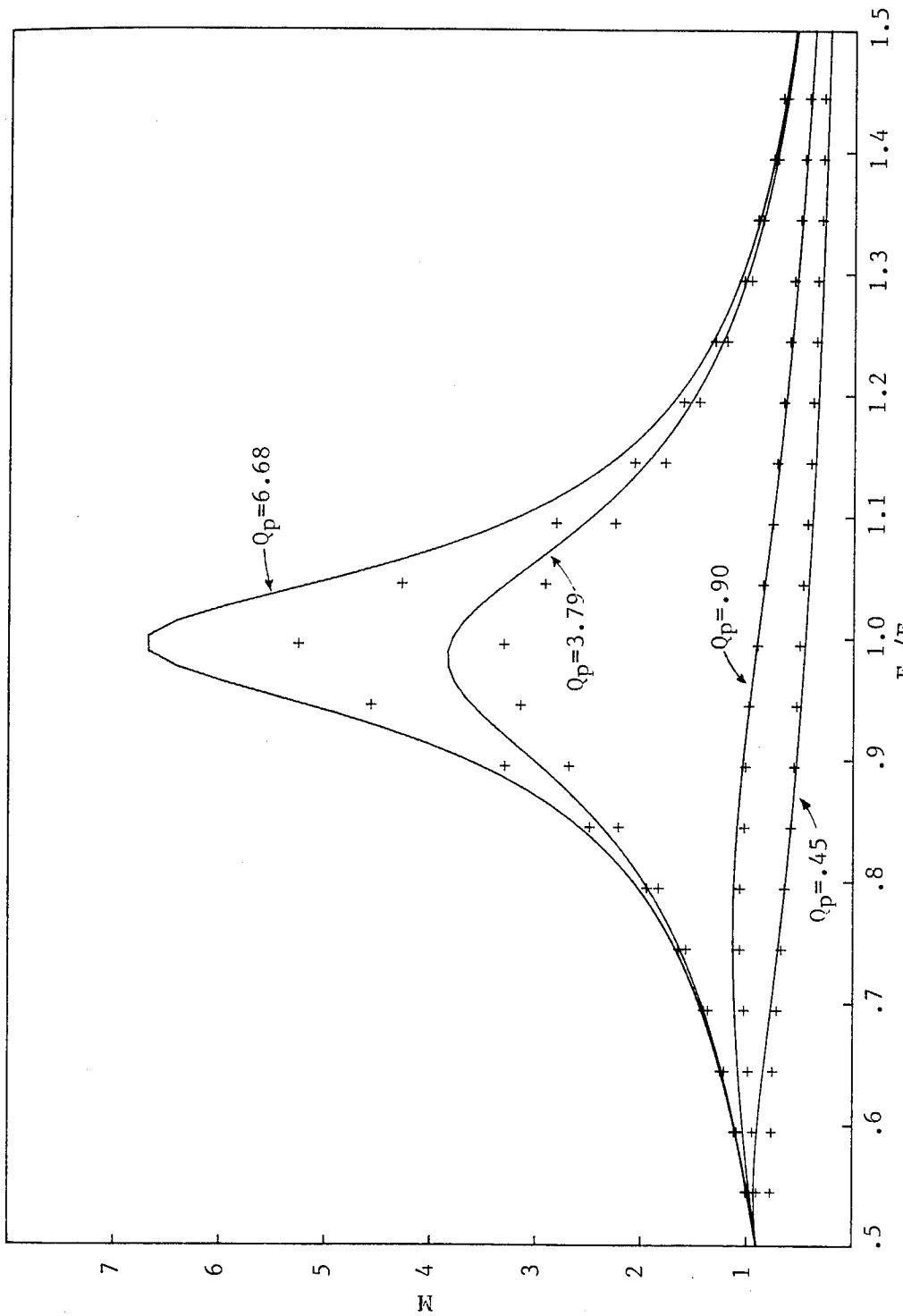

Fig. 2.20 Experimental and predicted results of the conversion ratio characteristics of the parallel resonant converter.
$L_0 = 49\mu H$ $C_0 = .1\mu F$ $V_g = 12V$.

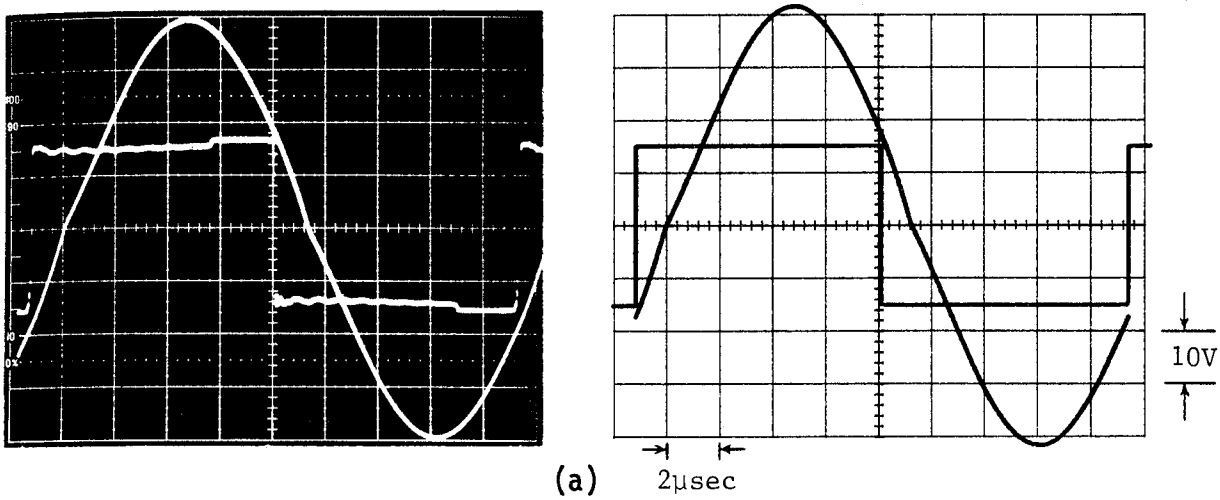

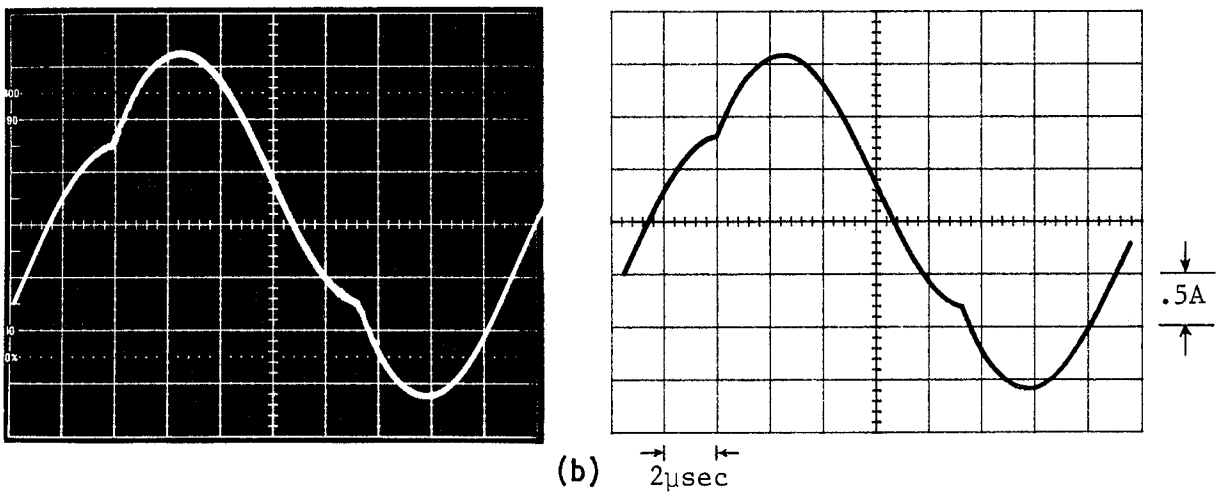

Fig. 2.21 Experimentally measured waveforms, left, and predicted waveforms, right, of the parallel resonant converter. a) Resonant capacitor voltage $V_R(t)$ and excitation voltage V_T, and b) resonant inductor current $I_R(t)$. $L_0 = 49\mu H$, $C_0 = .1\mu F$, $Q_p = 2.95$, $F_s / F_0 = .75$, and $V_g = 15V$.

Figure 2.21 shows experimental and predicted voltage and current waveforms for the following circuit values

$$Q_p = 2.95 \quad F_s/F_0 = .75 \quad C_0 = .1\mu F \quad L_0 = 49\mu H \quad V_g = 15V$$

The following table summarizes the results relevant to Fig. 2.23

	Predicted	Measured
V_{peak}	41.4V	40V
I_{peak}	1.57A	1.6A
T_D	2.58μsec	2.5μsec
T_a	1.14μsec	1.3μsec

2.6 Conclusion

In this chapter the parallel resonant converter is first described as a black box with a control signal F_s/F_0, input voltage source V_g, and an output connected across a load R. The output voltage is controlled by changing the ratio of switching frequency to the resonant frequency, F_s/F_0. The conversion ratio characteristics are determined for continuous conduction mode in terms of the normalized load parameter, Q_p, and control parameter, F_s/F_0. Only the range of the control parameter $F_s/F_0 > .5$ is considered. The peak resonant voltage and current characteristics are determined likewise in terms of Q_p and F_s/F_0.

The critical value of the control parameter $(F_s/F_0)_{zc}$, below which natural turn-off of the switches occurs, is determined in terms of Q_p. It is shown that $(F_s/F_0)_{zc}$ tends to unity for large Q_p. The diode conduction time, T_D, in the range $.5 < F_s/F_0 < (F_s/F_0)_{zc}$, which is an important design

parameter when SCRs are used, is determined in terms of Q_p and F_s/F_0.

The efficiency in the presence of parasitic resistances is discussed and it is shown that the efficiency decreases for increasing F_s/F_0.

According to the conversion ratio, diode conduction time and efficiency characteristics it is shown that it is best to operate this converter below resonance and away from the peak with a Q_p no less than two or three. This will insure higher efficiency and minimum sensitivity of the conversion ratio to variations in the load.

CHAPTER 3

DC ANALYSIS OF THE SERIES RESONANT CONVERTER

3.1 Introduction

This chapter discusses the steady-state operation and the dc analysis of the series resonant converter. After a brief review of the basic operation in Sec. 3.2, the analysis is presented in Sec. 3.3 and Sec. 3.4. In Sec. 3.3 the analysis in the range $F_s/F_0 \geq 1/2$ is given, and in Sec. 3.4 a general analysis is given in the entire range $0 \leq F_s/F_0 \leq \infty$. The various modes of operation in discontinuous and continuous conduction are identified, and the conversion ratio for each mode of operation is determined in terms of the normalized load parameter, Q_s, and the control parameter F_s/F_0. The boundaries between the various modes of operation are determined in terms of Q_s and F_s/F_0 as well. It is shown that certain types of discontinuous conduction modes should be avoided because the conversion ratio for such modes is insensitive to the control parameter. For example, in the range $1/2 \leq F_s/F_0 \leq 1$ a simple equation is given for the proper selection of Q_s in order to avoid the occurrence of dcm. Other steady-state quantities such as peak stress levels and diode conduction time are determined as well. Nonidealities due to the parasitic resistances and rectifier voltage drops are considered in Sec. 3.5. The experimental results given in Sec. 3.6 are in good agreement with the predictions.

3.2 Operation

The series resonant converter was first introduced by Schwarz [5]. The major drawback of the converter described in [5] is that its conversion ratio is fixed. The converter shown in Fig. 3.1a, which has an adjustable conversion ratio, was introduced later by Schwarz [6]. The reason for the drawback of the converter described in [5] is the absence of the diodes $D1$ and $D2$ shown in Fig. 3.1a. It is shown in the next section that in the absence of $D1$ and $D2$, the converter is forced to operate in a certain discontinuous conduction mode for which the conversion ratio is uncontrollable and fixed at unity. Other methods of exciting this converter are shown in Fig. 3.1b-d. All these converters are equivalent to the ideal circuit shown in Fig. 3.1e. Switches $S1$ and $S2$ operate at fifty percent duty ratio and generate a symmetrical square waveform, V_T, of amplitude V_g across the resonant circuit. For the converters in Fig. 3.1a-c, V_g is equal to $V_{in}/2$, whereas for the converter in Fig. 3.1d V_g is equal to V_{in}. In Fig. 3.1a the capacitors $C_0/2$ serve as resonant capacitors as well as voltage dividers whereas in Fig. 3.1b the capacitors C_∞ serve only as voltage dividers and are much larger than the C_0, i.e., $C_\infty \gg C_0$. The switching times T_s and T_s', shown Figs. 3.1, are defined as before

$$T_s' = \text{Switching interval}$$

$$F_s = \frac{1}{T_s'} = \text{Switching frequency}$$

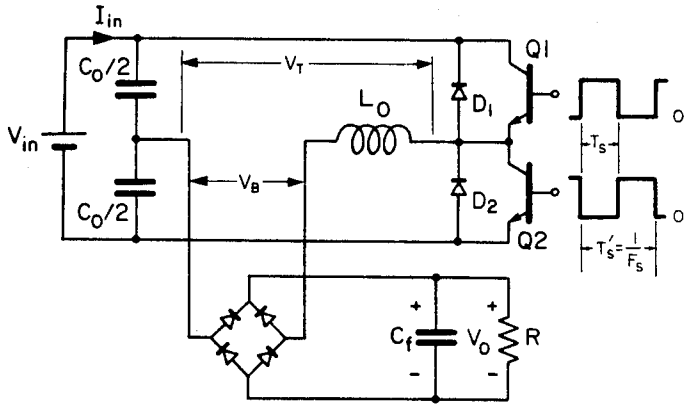
I_{in}
$C_o/2$
V_{in}
$C_o/2$
V_T
V_B
L_o
D_1
D_2
Q1
Q2
T_s
$T_s' = \frac{1}{F_s}$
C_f
V_o
R

(a)

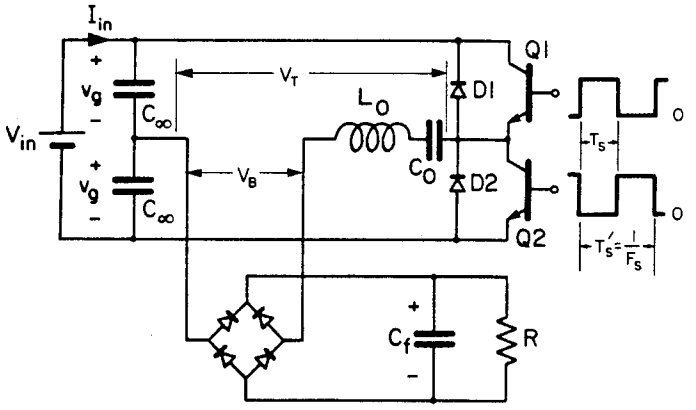
I_{in}
V_{in}
v_g
C_∞
v_g
C_∞
V_T
V_B
L_o
C_o
D1
D2
Q1
Q2
T_s
$T_s' = \frac{1}{F_s}$
C_f
R

(b)

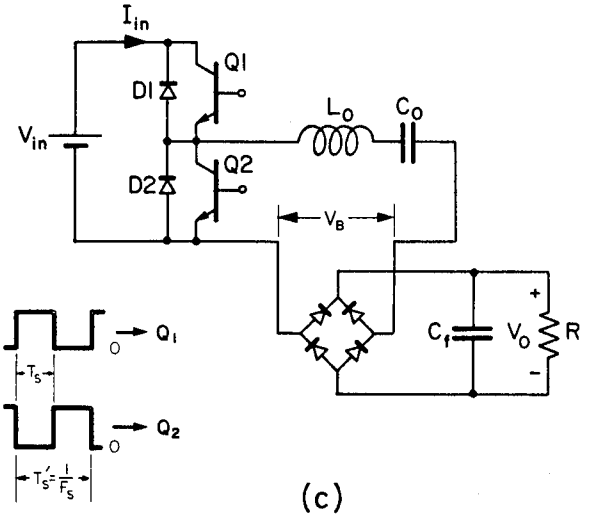
I_{in}
V_{in}
D1
D2
Q1
Q2
L_o
C_o
V_B
C_f
V_o
R
Q_1
Q_2
T_s
$T_s' = \frac{1}{F_s}$

(c)

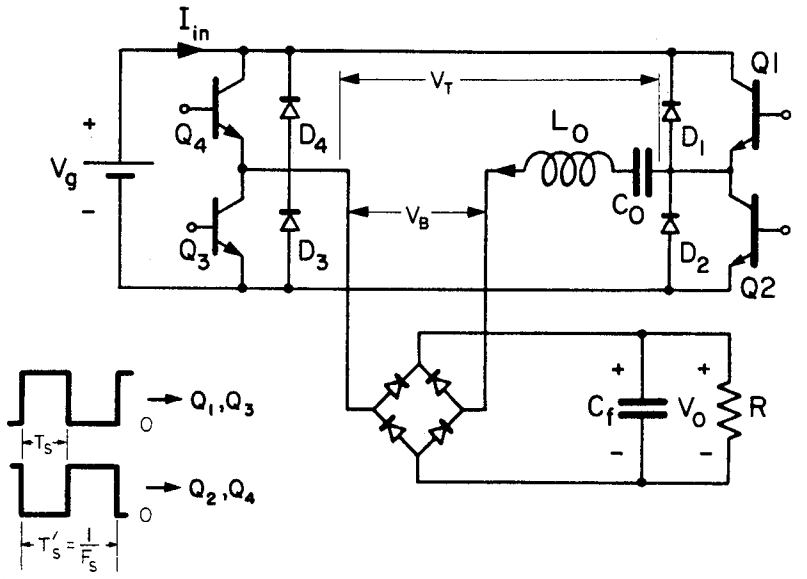

(d)

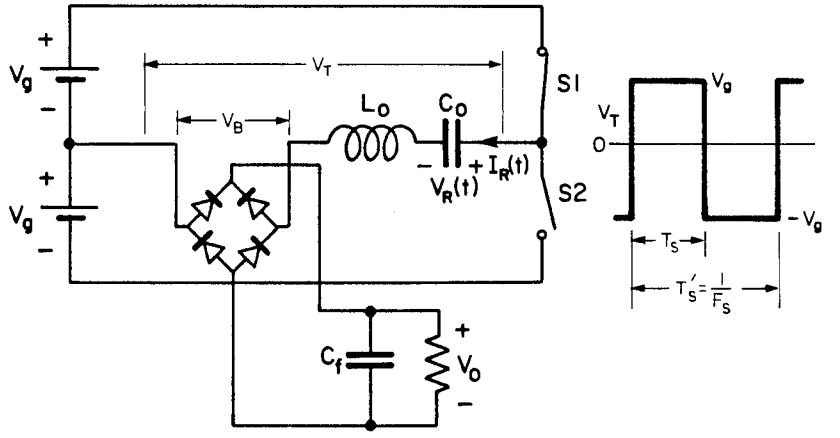

(e)

Fig. 3.1 a-d) The series resonant converter with various methods of excitation and e) the ideal equivalent circuit.

$$T_s = \frac{T_s'}{2}$$

The resonant frequency is defined as

$$F_0 = \frac{1}{2\pi\sqrt{L_0 C_0}} \tag{3.1}$$

The normalized load parameter is given by

$$Q_s = \frac{\omega_0 L_0}{R} \tag{3.2}$$

The constant K is defined as

$$K = \frac{Q_s \gamma}{2} \tag{3.3}$$

where

$$\gamma = \pi \frac{F_0}{F_s} \tag{3.4}$$

The resonant current, $I_R(t)$, is rectified and applied to a low-pass filter from which the output voltage is obtained. It is then clear, by analogy to linear circuits, that the output voltage can be regulated by controlling the ratio of the switching frequency to the resonant frequency, F_s / F_0. The same block diagram given for the parallel converter is repeated here for the series resonant converter in Fig. 3.2.

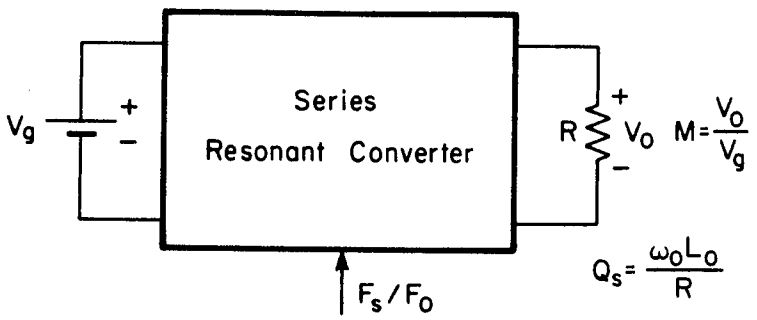

Fig. 3.2 Block diagram of the series resonant converter.

3.3 Analysis: $F_s / F_0 \geq 1/2$

The analysis of the series resonant converter for the range of the control parameter $F_s/F_0 \geq 1/2$ is divided into two parts; below resonance, $1/2 \leq F_s/F_0 \leq 1$, and above resonance, $F_s/F_0 \geq 1$. First the range $1/2 \leq F_s/F_0 \leq 1$ is discussed.

3.3.1 $1/2 \leq F_s/F_0 \leq 1$

According to Fig. 3.2 the analysis in this section begins by the determination of the conversion ratio, M, in terms of Q_s and F_s/F_0 in continuous and discontinuous conduction modes. The analyses given in [6] and [7] have considered the operation of this converter in terms of the diode conduction angle, $\omega_0 T_D$ and have *not* explicitly determined the conversion ratio nor the occurrence of *discontinuous conduction mode* (dcm) in the range $1/2 \leq F_s/F_0 \leq 1$.

The voltage and current waveforms in continuous conduction mode (ccm) are shown in Fig. 3.3. In this range, the resonant current at the beginning of the switching interval is always positive, i.e., $I_R(0) \geq 0$. This means that the transistor always conducts first and thereafter, as the collector current passes through zero, the parallel diode begins to conduct for a duration $\omega_0 T_D$. This natural turn-off is very attractive for SCR applications. For the parallel converter it was shown that the range of the control parameter in which natural turn-off occurs is load dependent. In the case of the series resonant converter this range is given by $1/2 \leq F_s/F_0 \leq 1$ and is independent of the load.

As in the case of the parallel converter, owing to the symmetry of operation over an entire switching interval, the analysis is carried out over half the switching interval, T_s. It is assumed that the output filter capacitor, C_f, is much larger than C_0 so that the output section can be represented by a voltage source V_0. As the resonant current changes sign at $t = T_a$, the output section, or the voltage source V_0, switches polarity because of the output rectifier bridge. This results in two switched networks over the interval T_s as shown in Fig. 3.4.

According to Fig. 3.4a, the equations for $I_R(t)$ and $V_R(t)$ in the interval $0 \leq t \leq T_a$ are given by

$$I_R(t) = I_R(0)\cos\omega_0 t + \omega_0 C_0 \left[V_g - V_0 - V_R(0)\right]\sin\omega_0 t \qquad (3.5a)$$

$$V_R(t) = -\left[V_g - V_0 - V_R(0)\right]\cos\omega_0 t + \frac{I_R(0)}{\omega_0 C_0}\sin\omega_0 t + V_g - V_0 \qquad (3.5b)$$

According to Fig. 3.4b, the equations in the interval $T_a \leq t \leq T_s$ are

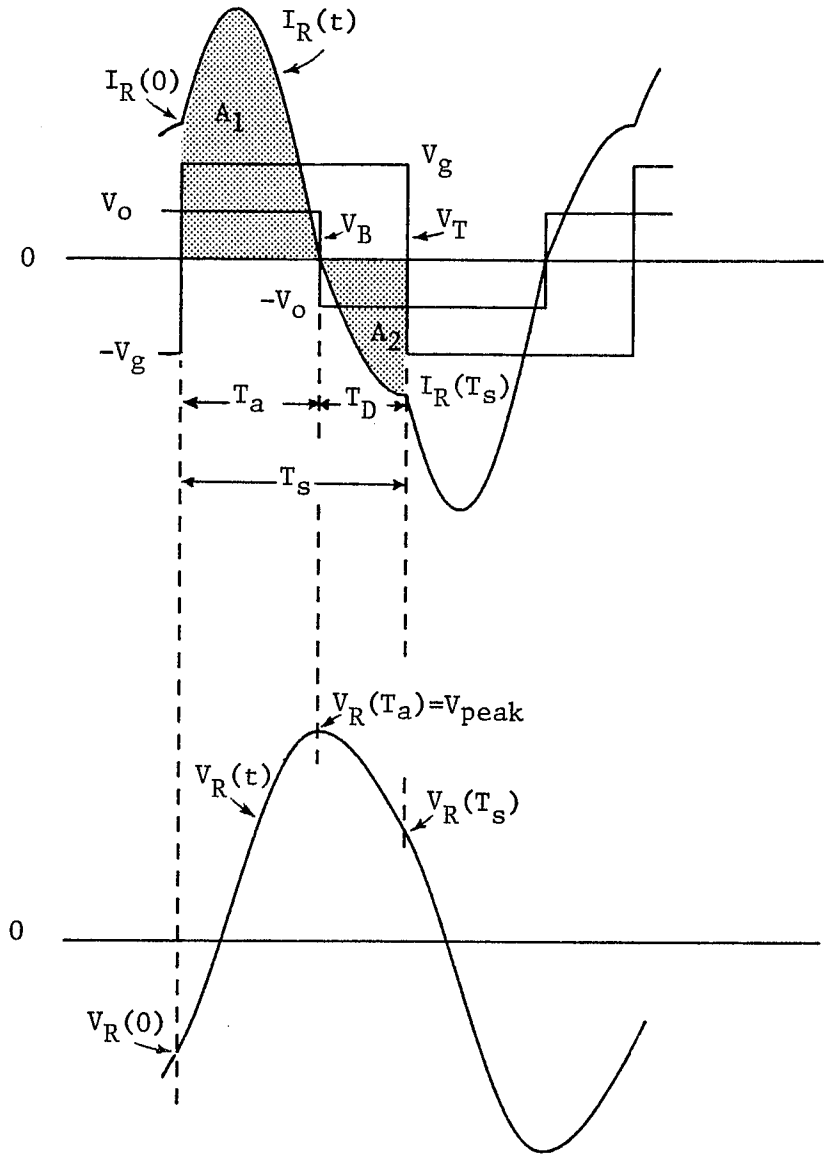

Fig. 3.3 Voltage and current waveforms of the series resonant converter when operating in continuous conduction mode and in the range $1/2 \leq F_s / F_0 \leq 1$.

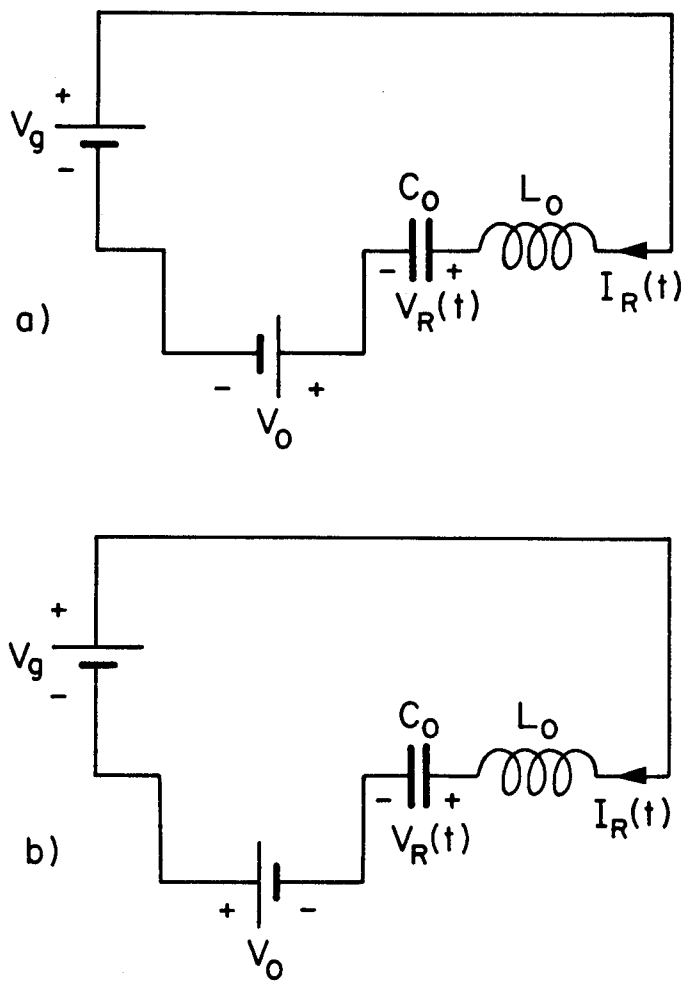

Fig. 3.4 The two switched networks of the series resonant converter during half the switching interval T_s when operating in the range $1/2 \leq F_s/F_0 \leq 1$. a) $0 \leq t \leq T_a$ and b) $T_a \leq t \leq T_s$. For operation in the range $F_s/F_0 \geq 1$, the sequence is switched around.

$$I_R(t) = \omega_0 C_0 \left[V_g + V_0 - V_R(T_a) \right] \sin\omega_0 (t - T_a) \tag{3.6a}$$

$$V_R(t) = -\left[V_g + V_0 - V_R(T_a) \right] \cos\omega_0 (t - T_a) + V_g + V_0 \tag{3.6b}$$

For the series resonant converter, the initial conditions $V_R(0)$ and $I_R(0)$ can be easily determined by the following simple approach which is also given in [6]. The input power to the the circuit is given by

$$P_{in} = \frac{V_g}{T_s} \left[\int_0^{T_a} I_R(t)dt + \int_{T_a}^{T_s} I_R(t)dt \right] = \frac{V_g}{T_s} (A_1 - A_2) \tag{3.7}$$

where A_1 and A_2 are the areas under the resonant current waveform shown in Fig. 3.3. The output power is given by

$$P_{out} = \frac{V_0}{T_s} \left[\int_0^{T_a} I_R(t)dt - \int_{T_a}^{T_s} I_R(t)dt \right] = \frac{V_0}{T_s} (A_1 + A_2) \tag{3.8}$$

The requirement $P_{in} = P_{out}$ gives

$$M = \frac{V_0}{V_g} = \frac{A_1 - A_2}{A_1 + A_2} \tag{3.9}$$

Since A_1 and A_2 are positive, it follows immediately that M cannot exceed unity

$$M \leq 1 \tag{3.10}$$

According to Fig. 3.3, the peak-to-peak capacitor voltage is given by

$$2V_{peak} = 2V_R(T_a) = \frac{1}{C_0} (A_1 + A_2) \tag{3.11}$$

Also, the output voltage is given by the average rectified resonant current

multiplied by the load R

$$V_0 = R\frac{1}{T_s}\int_0^{T_s}|I_R(t)|dt = \frac{R}{T_s}(A_1+A_2) \tag{3.12}$$

Substitution of Eq. (3.12) in Eq. (3.11) gives

$$V_R(T_a) = V_{peak} = \frac{T_s V_0}{2RC_0} = MKV_g \tag{3.13}$$

where K is given by Eq. (3.3). The initial capacitor voltage $V_R(0)$ can be expressed as

$$V_R(0) = V_{peak} - \frac{1}{C_0}\int_0^{T_a} I_R(T_a)dt = V_{peak} - \frac{A_1}{C_0} \tag{3.14}$$

which after some manipulation, gives

$$V_R(0) = -M^2KV_g \tag{3.15}$$

The requirement $I_R(T_a)=0$ in Eq. (3.5a) gives

$$I_R(0) = -\omega_0 C_0 V_g\left[1-M+M^2K\right]\tan\omega_0 T_a \tag{3.16}$$

When cyclic stability conditions are required, i.e., $I_R(0)=-I_R(T_s)$ and $V_R(0)=-V_R(T_s)$, the following two equations are obtained

$$\tan\omega_0 T_a = \frac{1+M-MK}{1-M+M^2K}\sin(\gamma-\omega_0 T_a) \tag{3.17}$$

$$\cos(\gamma-\omega_0 T_a) = \frac{1+M-M^2K}{1+M-MK} \tag{3.18}$$

In Appendix B.1 Eqs. (3.17) and (3.18) are solved simultaneously and an

implicit equation of the form $G_s(M,Q_s,\gamma)=0$ is obtained from which M can be determined for a given Q_s and F_s/F_0. This is given by

$$G_s(M,Q_s,\gamma) = \frac{1-M+M^2K}{M(K+1)-1}\cos\gamma$$

$$-\frac{\sqrt{(1-M^2)(MK-2)MK}}{M(K+1)-1}\sin\gamma$$

$$+\frac{1+M-M^2K}{1+M(1-K)} = 0 \qquad (3.19)$$

Also, the angle $\omega_0 T_a$ is shown to be given by

$$\cos\omega_0 T_a = \frac{1-M+M^2K}{1-M(K+1)} \qquad (3.20)$$

A plot of the conversion ratio characteristics in ccm is shown in Fig. 3.5. These characteristics are obtained by solving $G_s(M,Q_s,\gamma)=0$ numerically for each Q_s and for values of F_s/F_0 ranging from $1/2$ to 1. As expected, according to (3.10), the maximum value of M for any Q_s does not exceed unity. The characteristics for $Q_s \geq 4/\pi$ are seen to extend over the entire range $1/2 \leq F_s/F_0 \leq 1$ while those corresponding to $Q_s \leq 4/\pi$ are restricted to a narrower range of F_s/F_0. For example, for $Q_s = 3/\pi$ the characteristics for ccm are restricted to the range $1/2 \leq F_s/F_0 \leq 3/4$. This means that for $Q_s = 3/\pi$ the real solutions of Eq. (3.19) are restricted to this range and that no real roots exist in the range $3/4 \leq F_s/F_0 \leq 1$. This restricted range of F_s/F_0 will now be determined analytically and it will be shown that outside this range the converter operates in dcm.

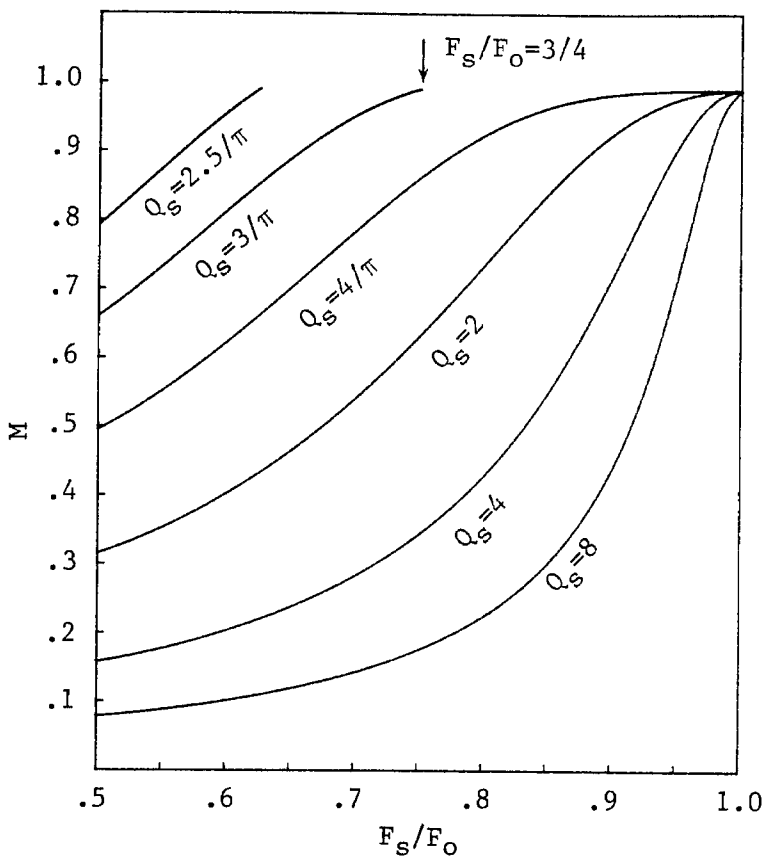

Fig. 3.5 Conversion ratio characteristics of the series resonant converter when operating in continuous conduction mode and in the range $1/2 \leq F_s / F_0 \leq 1$.

Since $M \leq 1$, an examination of the radical in Eq. (3.19) reveals that

$$MK \geq 2 \tag{3.21}$$

which can be written as

$$\frac{F_s}{F_0} \leq \frac{MQ_s\pi}{4} \tag{3.22}$$

According to (3.22), the range of F_s/F_0 in which Eq. (3.19) admits a real solution is given by

$$\frac{1}{2} \leq \frac{F_s}{F_0} \leq \frac{MQ_s\pi}{4} \tag{3.23}$$

Since the maximum value of M is unity, the upper bound in (3.23) can be written as

$$\frac{1}{2} \leq \frac{F_s}{F_0} \leq \frac{Q_s\pi}{4} \tag{3.24}$$

A comparison of (3.24) to $1/2 \leq F_s/F_0 \leq 1$ shows that for $Q_s \geq 4/\pi$ Eq. (3.19) has a real root M in the entire range $1/2 \leq F_s/F_0 \leq 1$, whereas for $Q_s \leq 4/\pi$ this range is restricted to (3.24). This then explains the characteristics shown in Fig. 3.5. For the example of $Q_s = 3/\pi$, (3.24) gives $1/2 \leq F_s/F_0 \leq 3/4$.

In order to complete Fig. 5, the characteristics for $Q_s \leq 4/\pi$ outside the range given in (3.24) is now determined. From the preceding discussion and Fig 3.5, M reaches unity for $Q_s \leq 4/\pi$ below resonance at $F_s/F_0 = Q_s\pi/4$. According to Eq. (3.9) unity gain implies $A_2 = 0$. The only

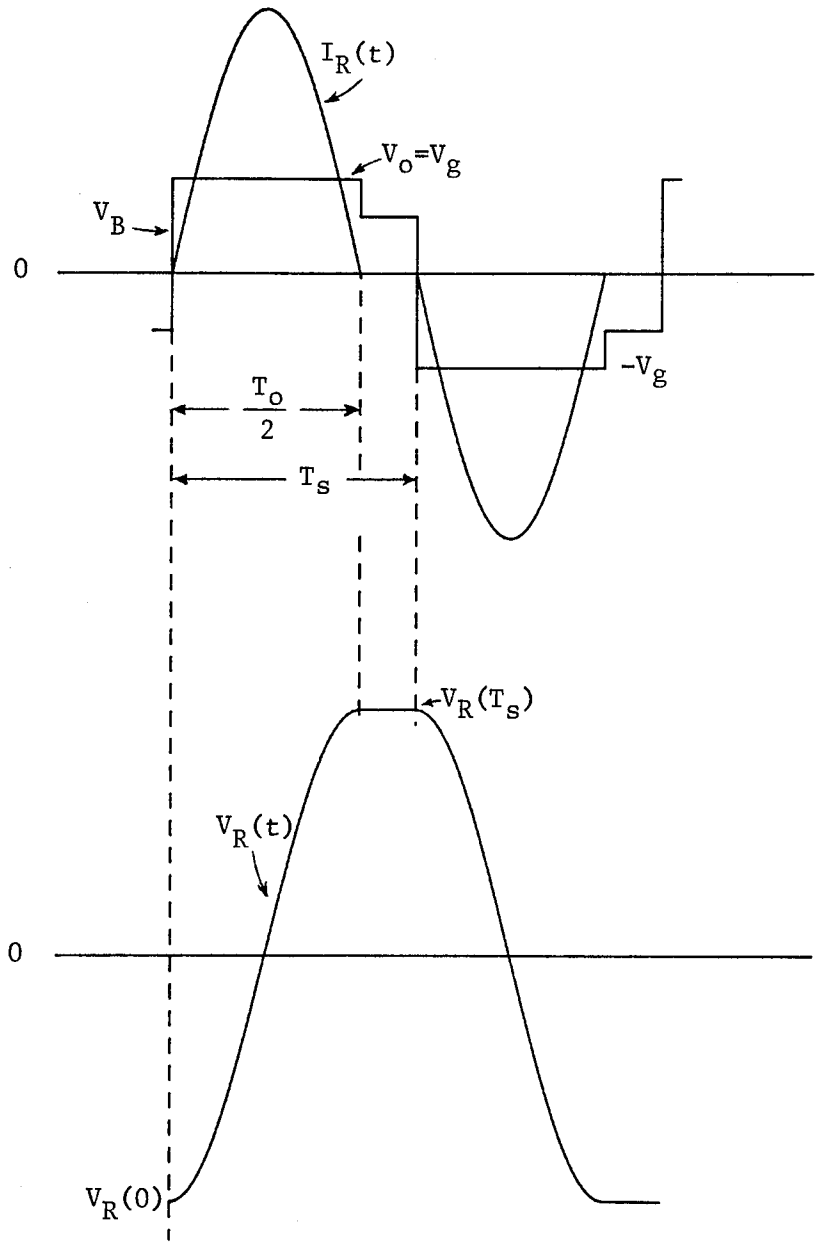

Fig. 3.6 Voltage and current waveforms of series resonant converter when operating in discontinuous conduction mode and in the range $1/2 \leq F_s/F_0 \leq 1$. *Note that during* $T_s - nT_0/2$, *the voltage at the input side of the bridge,* V_B, *is less than the output voltage.*

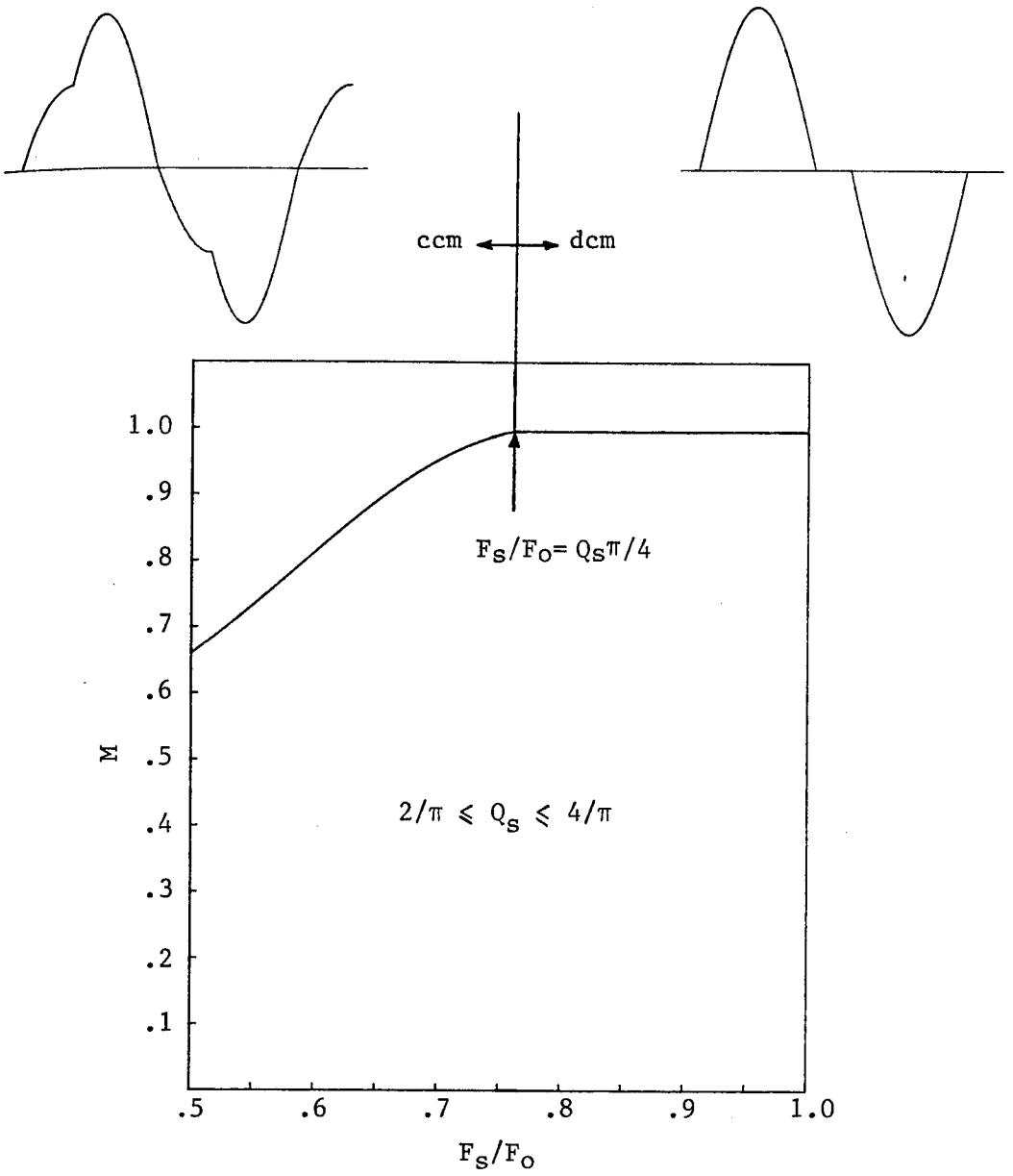

Fig. 3.7 A typical conversion ratio characteristics curve of the series resonant converter for $2/\pi \leq Q_s \leq 4/\pi$ when operating in the range $1/2 \leq F_s/F_0 \leq 1$. For such values of Q_s, the operating mode changes from continuous to discontinuous at $F_s/F_0 = Q_s\pi/4$.

way this can happen below resonance is for the current in the interval $T_a \le t \le T_s$ to be zero as shown in Fig. 3.6. This means that for such values of Q_s the converter enters dcm at $F_s/F_0 = Q_s\pi/4$. As F_s/F_0 is increased beyond $Q_s\pi/4$, the converter remains in dcm with M fixed at unity. This is illustrated in Fig 3.7. The combined characteristics in continuous and discontinuous conduction modes are shown in Fig. 3.8. These characteristics show that this converter is not well suited for applications that require very large load changes. This has been a known fact since the introduction of this converter, because of its apparent current fed nature. It is shown now that this is true only under certain conditions. A plot of the normalized output current, which is given by $I_0\omega_0 L_0 / V_g$, vs. F_s/F_0 for different values of Q_s is shown in Fig. 3.9. These characteristics are obtained by multiplying M by Q_s. Now, it can be seen from Fig. 3.9 that only for Q_s greater than three or four and away from resonance does the converter behave like a current fed converter. For a given Q_s the modes of operation in the range $1/2 \le F_s/F_0 \le 1$ can be summarized as follows

$$Q_s \ge \frac{4}{\pi} \quad \text{ccm in} \quad \frac{1}{2} \le \frac{F_s}{F_0} \le 1 \tag{3.25a}$$

$$Q_s \le \frac{4}{\pi} \begin{cases} \text{ccm in} & \dfrac{1}{2} \le \dfrac{F_s}{F_0} \le \dfrac{Q_s\pi}{4} \\ \text{dcm in} & \dfrac{Q_s\pi}{4} \le \dfrac{F_s}{F_0} \le 1 \end{cases} \tag{3.25b-c}$$

$$Q_s \le \frac{2}{\pi} \quad \text{dcm in} \quad \frac{1}{2} \le \frac{F_s}{F_0} \le 1 \tag{3.25d}$$

Condition (3.25d) follows immediately from (3.24) whence it can be seen

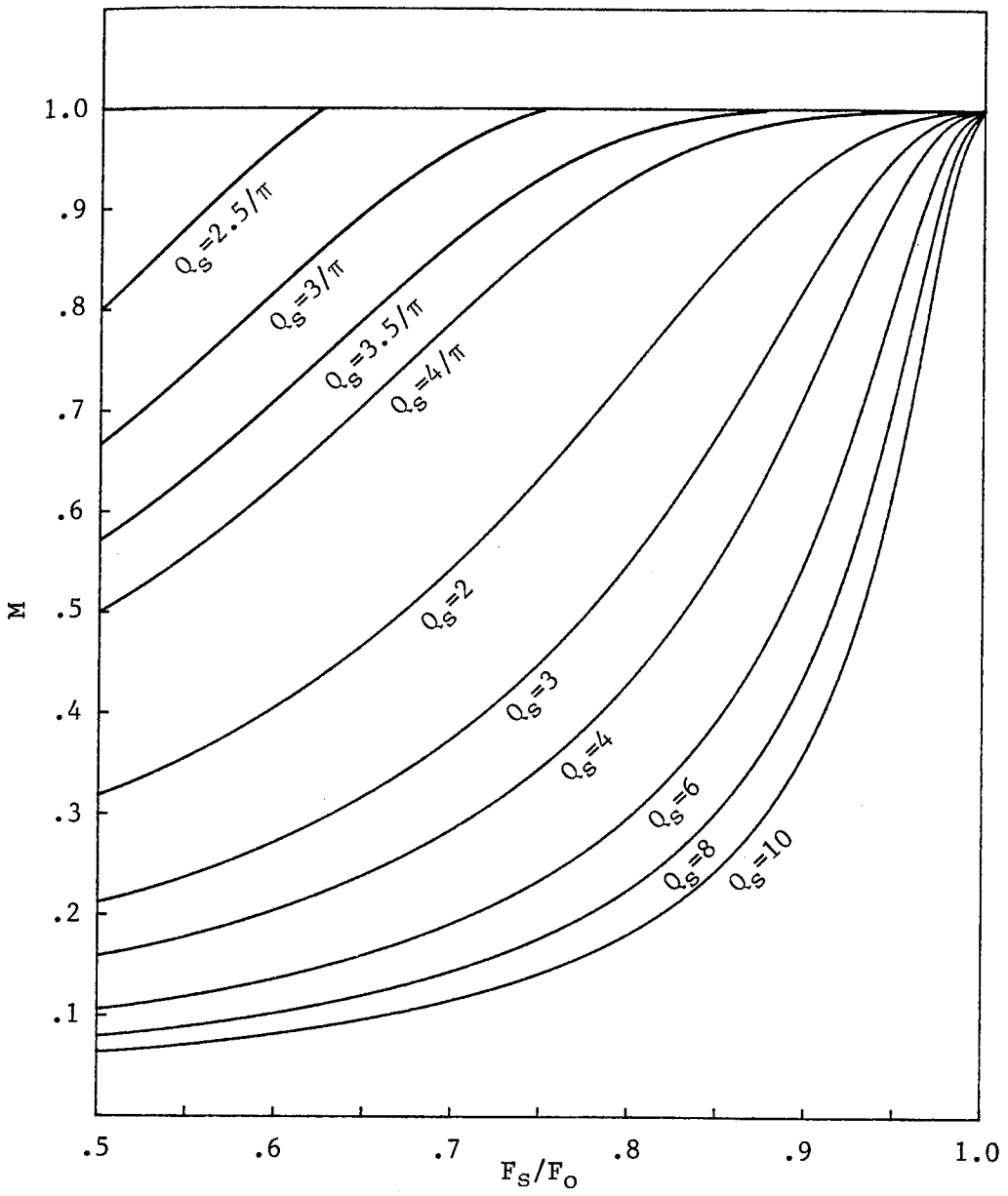

Fig. 3.8 Combined conversion ratio characteristics of the series resonant converter in continuous and discontinuous conduction modes and in the range $1/2 \leq F_s / F_0 \leq 1$.

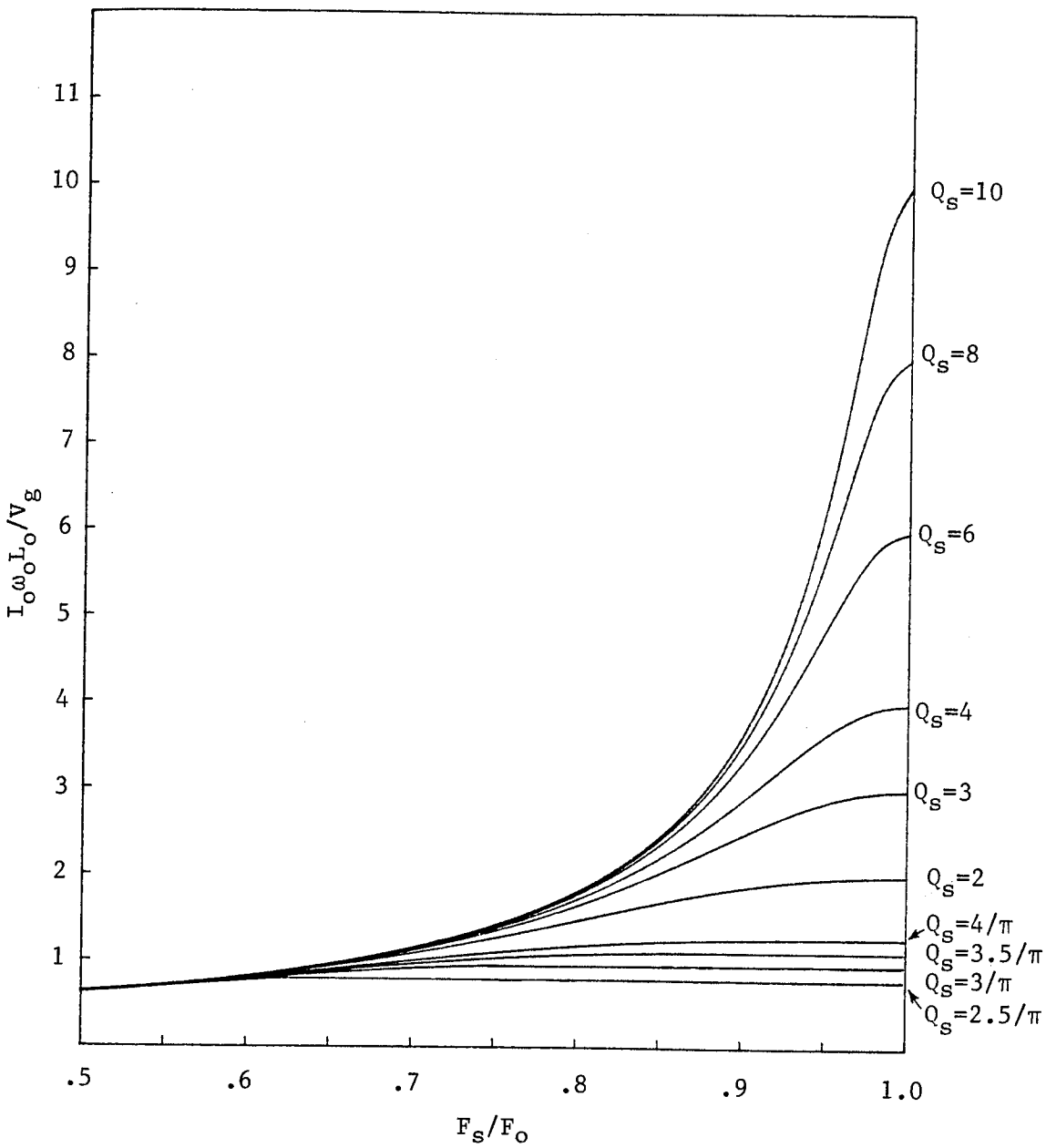

Fig. 3.9 Normalized average output current characteristics of the series resonant converter in continuous and discontinuous conduction modes and in the range $1/2 \leq F_s / F_0 \leq 1$.

that for $Q_s = 2/\pi$ the upper and lower bounds of ccm coincide. Alternately, the boundary between dcm and ccm as a function of Q_s for a given F_s/F_0 in the range $1/2 \le F_s/F_0 \le 1$, can be given as follows

$$1/2 \le F_s/F_0 \le 1 \begin{cases} Q_s \le \dfrac{4}{\pi}\dfrac{F_s}{F_0} & \text{dcm} \\ Q_s \ge \dfrac{4}{\pi}\dfrac{F_s}{F_0} & \text{ccm} \end{cases} \qquad (3.26a\text{-}b)$$

It is quite clear that dcm should be avoided if a controllable output is desired. This completes the discussion on the determination of M in both modes of operation. In what follows a physical reason for the occurrence of dcm is given.

According to Fig. 3.6 and Eqs. (3.5) and (3.6), the voltages and the currents in dcm are given by

$$I_R(t) = -\omega_0 C_0 V_R(0) \sin\omega_0 t \qquad V_R(t) = V_R(0)\cos\omega_0 t \qquad 0 \le t \le T_a \qquad (3.27)$$

$$I_R(t) = 0 \qquad V_R(t) = -V_R(0) \qquad T_a \le t \le T_s \qquad (3.28)$$

The output voltage, which in this case is equal to the input voltage, is given by

$$V_0 = V_g = R\frac{1}{T_s}\int_0^{T_s} |I_R(t)|\,dt = -\frac{2}{\pi Q_s}\frac{F_s}{F_0}V_R(0) \qquad (3.29)$$

In the time interval $T_a \le t \le T_s$ the net voltage at the input side of the bridge, V_B, is given by

$$V_B = V_R(T_s) - V_g = V_0\left[\frac{Q_s\pi}{2}\frac{F_0}{F_s} - 1\right] \tag{3.30}$$

The range of F_s/F_0 in which dcm occurs is given by (3.25c) from which it can be easily shown that

$$\frac{Q_s\pi}{2}\frac{F_0}{F_s} - 1 \leq 1 \tag{3.31}$$

which according to Eq. (3.30), implies that the voltage at the input side of the bridge is less than the output voltage. This means that in the interval $T_a \leq t \leq T_s$ the bridge becomes reverse biased and the diodes $D1$ and $D2$ do not conduct. The occurrence of this discontinuous conduction was never explained in [6] or [7] where it was assumed that the diodes $D1$ and $D2$ always remain in conduction. It should be clear now that if these diodes are removed the converter will always be forced to operate in dcm with M fixed at unity as in the case of the converter described in [5].

For proper component selection, the peak stress levels must be determined. According to Fig. 3.3 the peak of the resonant current occurs in the interval $0 \leq t \leq T_a$ during which the resonant current is given by Eq. (3.5a). When $V_R(0)$ and $I_R(0)$, given by Eqs. (3.15) and (3.16) respectively, are substituted in Eq. (3.5a), the following is obtained

$$I_R(t) = \omega_0 C_0 V_g \frac{1 - M + M^2K}{\cos\omega_0 T_a}\sin\omega_0(t - T_a) \tag{3.32}$$

Substitution of $\cos\omega_0 T_a$ from Eq. (3.20) in Eq. (3.32) gives (after taking the positive value $|1-M(K+1)| = M(K+1)-1$)

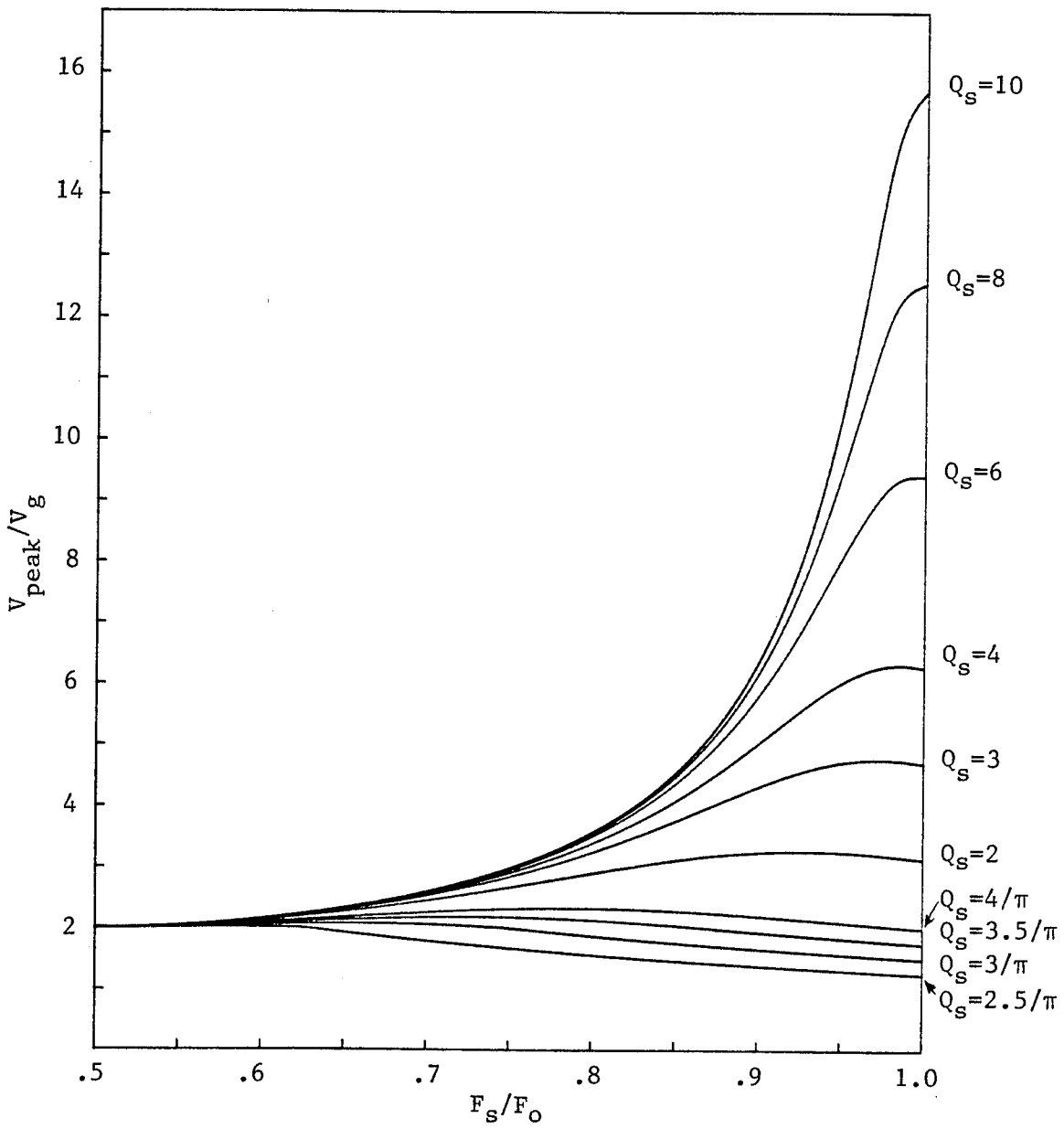

Fig. 3.10 Normalized peak resonant capacitor voltage characteristics of the series resonant converter in continuous and discontinuous conduction modes and in the range $1/2 \leq F_s / F_0 \leq 1$.

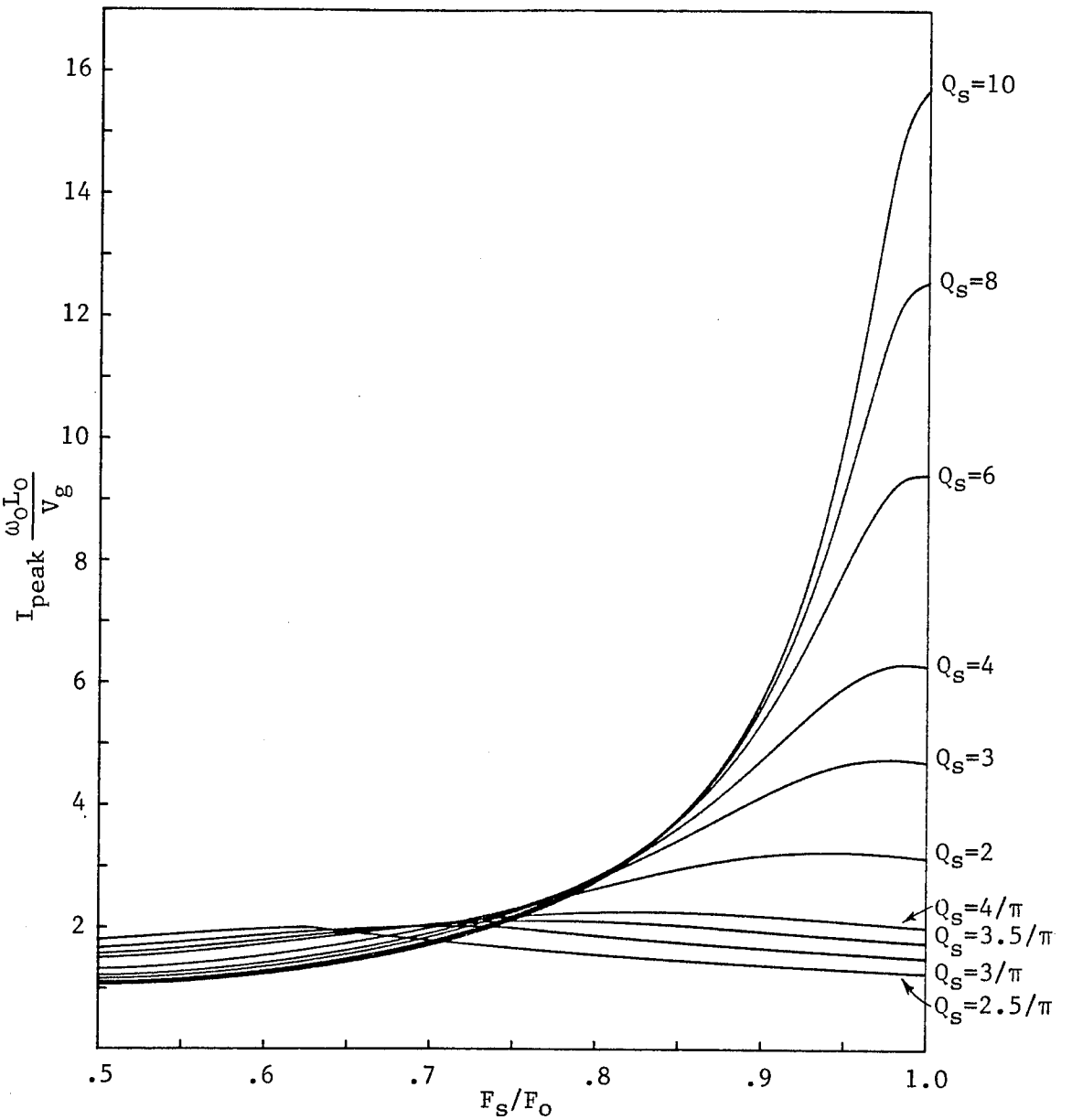

Fig. 3.11 Normalized peak resonant inductor current characteristics of the series resonant converter in continuous and discontinuous conduction modes and in the range $1/2 \leq F_s/F_0 \leq 1$.

$$I_{peak} = \omega_0 C_0 V_g \left[M(K+1) - 1 \right] \tag{3.33}$$

$$V_{peak} = MKV_g \tag{3.34}$$

where the peak capacitor voltage, given earlier in Eq. (3.13), is repeated here in Eq. (3.34).

For completeness, the peak stress levels in dcm are given now. From Eqs. (3.27) and (3.29) these are easily given by

$$I_{peak} = \omega_0 C_0 K V_g \tag{3.35}$$

$$V_{peak} = KV_g \tag{3.36}$$

It can be seen that the peak stress levels in dcm can be obtained from their corresponding expressions in ccm by letting $M=1$ in Eqs. (3.33) and (3.34). This, of course, is expected because at the boundary between dcm and ccm both expressions should match. Plots of V_{peak} and I_{peak} in continuous and discontinuous conduction mode are shown in Figs. 3.10 and 3.11 respectively.

When SCRs are used, it is important to know the diode conduction time, T_D, shown in Fig. 3.3, in order to allow sufficient time for the SCR to turn off. This angle according to Eq. (3.18) is given by

$$\omega_0 T_D = \gamma - \omega_0 T_a = \cos^{-1}\left[\frac{1 + M - M^2 K}{1 + M(1-K)} \right] \tag{3.37}$$

This is plotted in Fig 3.12. The characteristics for $Q_s \leq 4/\pi$ terminate at $F_s/F_0 = Q_s \pi/4$ because, as explained earlier, for such values of Q_s the converter operates in dcm in the range $Q_s \pi/4 \leq F_s/F_0 \leq 1$.

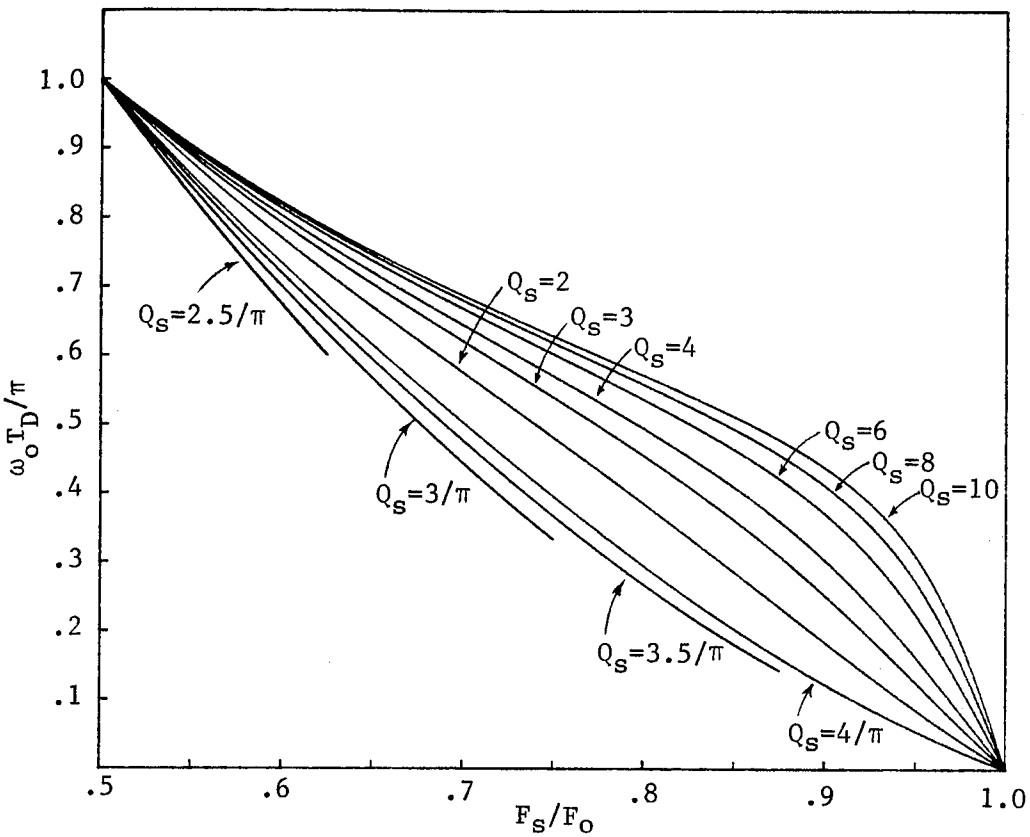

Fig. 3.12 Diode conduction angle characteristics of the series resonant converter in the range $1/2 \leq F_s/F_0 \leq 1$. *Note that for* $Q_s \leq 4/\pi$ *the curves terminate at* $F_s/F_0 = Q_s\pi/4$ *as the converter enters discontinuous conduction mode.*

3.3.2 $F_s/F_0 \geq 1$

The voltage and current waveforms in the range $F_s/F_0 \geq 1$ are shown in Fig. 3.13. In this range the diode $D1$ conducts first because $I_R(0)$ is always negative. As the resonant current passes through zero at $t = T_a$ the transistor enters conduction and is switched off at $t = T_s$ while still in conduction. Therefore, this range of operation is not very suitable for SCR applications since natural turn-off does not occur. It is clear that discontinuous conduction cannot occur in this range because $T_s \leq T_0/2$.

The analysis is similar to the analysis given earlier for the range $1/2 \leq F_s/F_0 \leq 1$. In this section only the final results are given. The details of the analysis are given in Appendix B.2. The implicit equation from which M is obtained is given by

$$G_s(M,Q_s,\gamma) = \frac{1+M+M^2K}{M(K+1)+1}\cos\gamma + \frac{\sqrt{(1-M^2)(MK+2)MK}}{M(K+1)+1}\sin\gamma - \frac{1-M-M^2K}{1-M(1-K)} = 0 \qquad (3.38)$$

The conversion ratio characteristics are shown in Fig. 3.14 along with the characteristics in the range $1/2 \leq F_s/F_0 \leq 1$. It was shown earlier for $Q_s \leq 4/\pi$ that the converter operates in dcm in the range $Q_s\pi/4 \leq F_s/F_0 \leq 1$. For such values of Q_s, the converter once again enters ccm when excited above resonance.

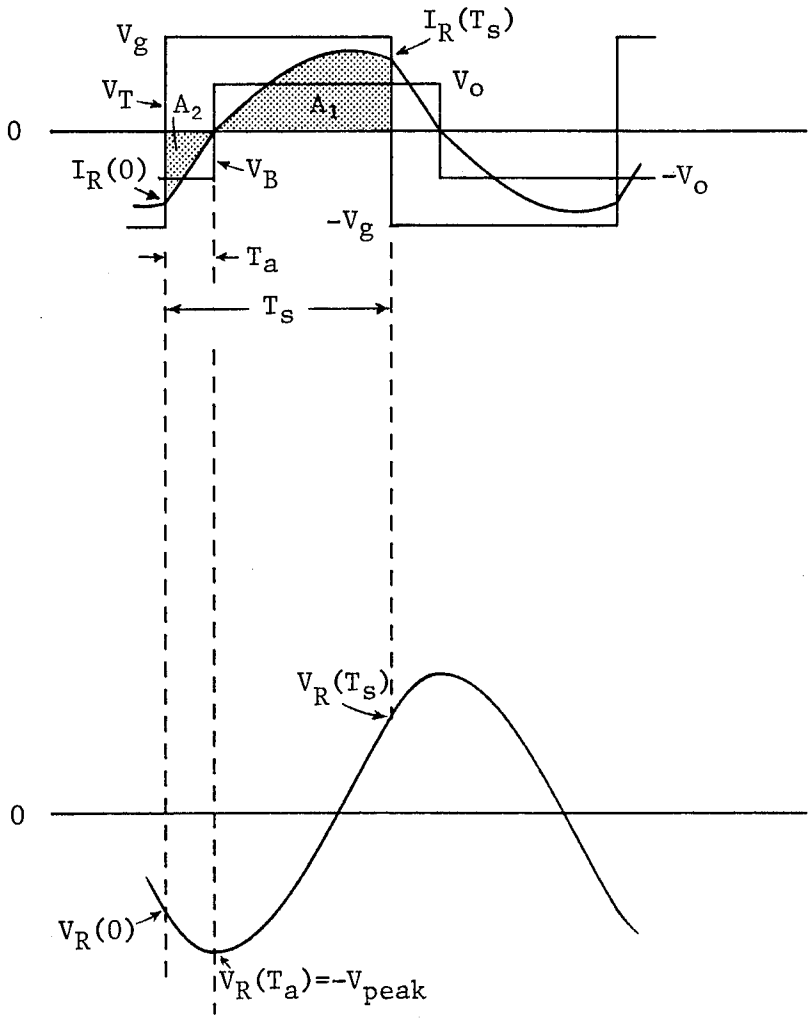

Fig. 3.13 Voltage and current waveforms of the series resonant converter when operating in the range $F_s / F_0 \geq 1$.

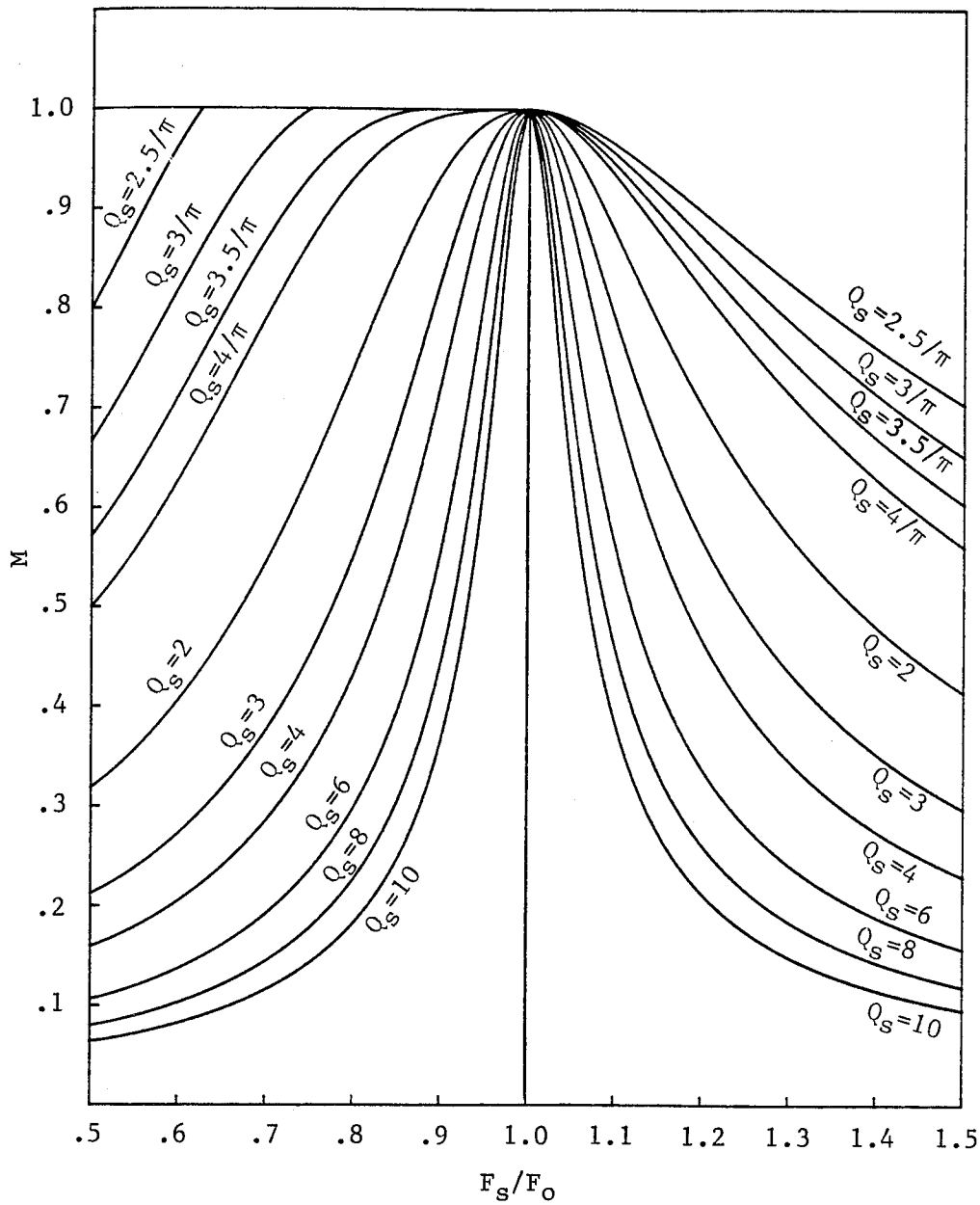

Fig. 3.14 Conversion ratio characteristics of the series resonant converter in the range $F_s/F_0 \geq 1/2$.

The output-network switching time, or the diode conduction time, is given by

$$\cos\omega_0 T_a = \frac{1+M+M^2K}{M(K+1)+1} \tag{3.39}$$

The voltages and currents for $0 \le t \le T_a$ are given by

$$I_R(t) = \omega_0 C_0 V_g \left[1+M(K+1)\right] \sin\omega_0(t-T_a) \tag{3.40a}$$

$$V_R(t) = -V_g \left[1+M(K+1)\right] \cos\omega_0(t-T_a) + V_g(M+1) \tag{3.40b}$$

and for $T_a \le t \le T_s$ are given by

$$I_R(t) = \omega_0 C_0 V_g \left[1-M+MK\right] \sin\omega_0(t-T_a) \tag{3.41a}$$

$$V_R(t) = -V_g \left[1-M+MK\right] \cos\omega_0(t-T_a) + V_g(1-M) \tag{3.41b}$$

The initial values $I_R(0)$ and $V_R(0)$ are given by

$$V_R(0) = -M^2 K V_g \tag{3.42}$$

$$I_R(0) = -\omega_0 C_0 V_g \sqrt{(1-M^2)MK(MK+2)} \tag{3.43}$$

The peak stress levels are given by

$$V_{peak} = MKV_g \tag{3.44}$$

$$I_{peak} = \begin{cases} \omega_0 C_0 V_g \left[1-M+MK\right] & ; \quad 1-M+M^2K \le 0 \\ \omega_0 C_0 V_g \sqrt{(1-M^2)MK(MK+2)} & ; \quad 1-M+M^2K \ge 0 \end{cases} \tag{3.45a-b}$$

The peak value value of the resonant current is either given by the maximum value of $I_R(t)$ or by $I_R(T_s)$ depending on whether this maximum

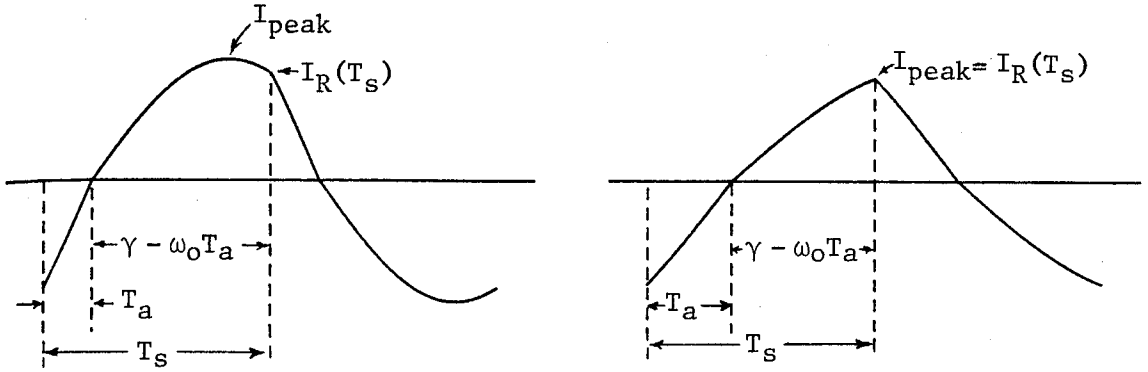

Fig. 3.15 Explanation of the change in the peak resonant current when the series resonant converter is operating in the range $F_s / F_0 \geq 1$. *a) when* $\gamma - \omega_0 T_a \geq \pi/2$, I_{peak} *is given by the maximum value of* $I_R(t)$ *in the interval* $T_a \leq t \leq T_s$. *b) When* $\gamma - \omega_0 T_a \leq \pi/2$, *the maximum value of* $I_R(t)$ *cannot occur and* $I_{peak} = I_R(T_s)$.

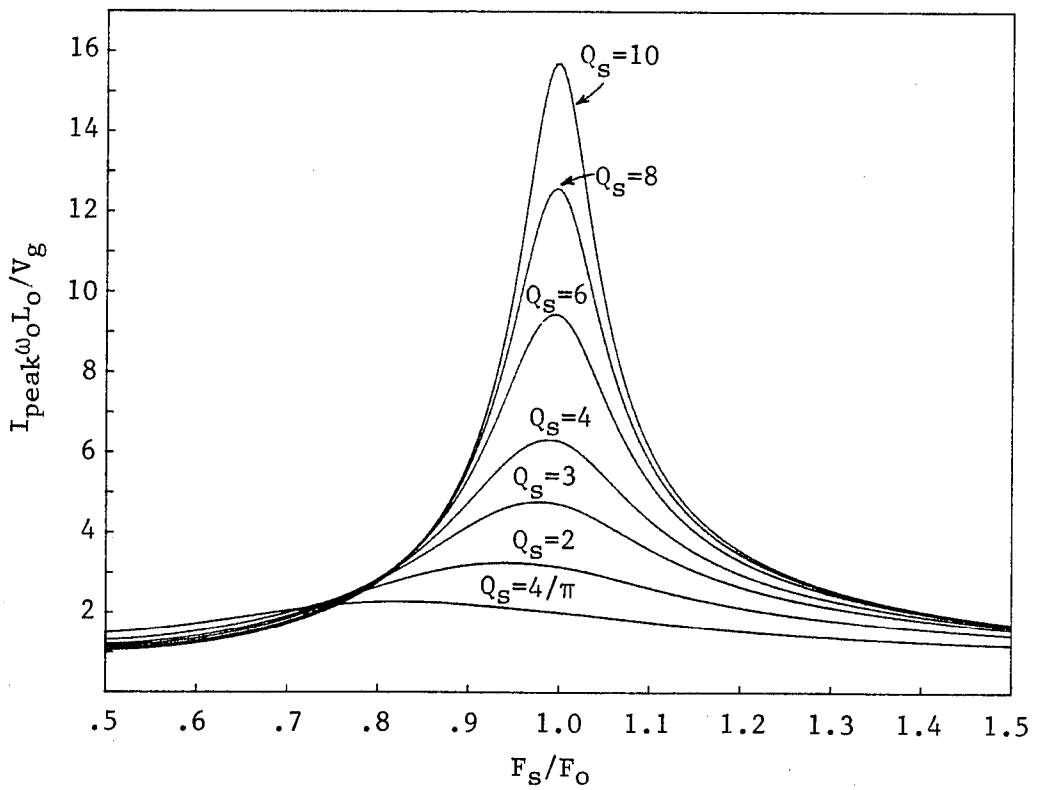

Fig. 3.16 Normalized peak resonant inductor current characteristics of the series resonant converter in the range $F_s / F_0 \geq 1/2$.

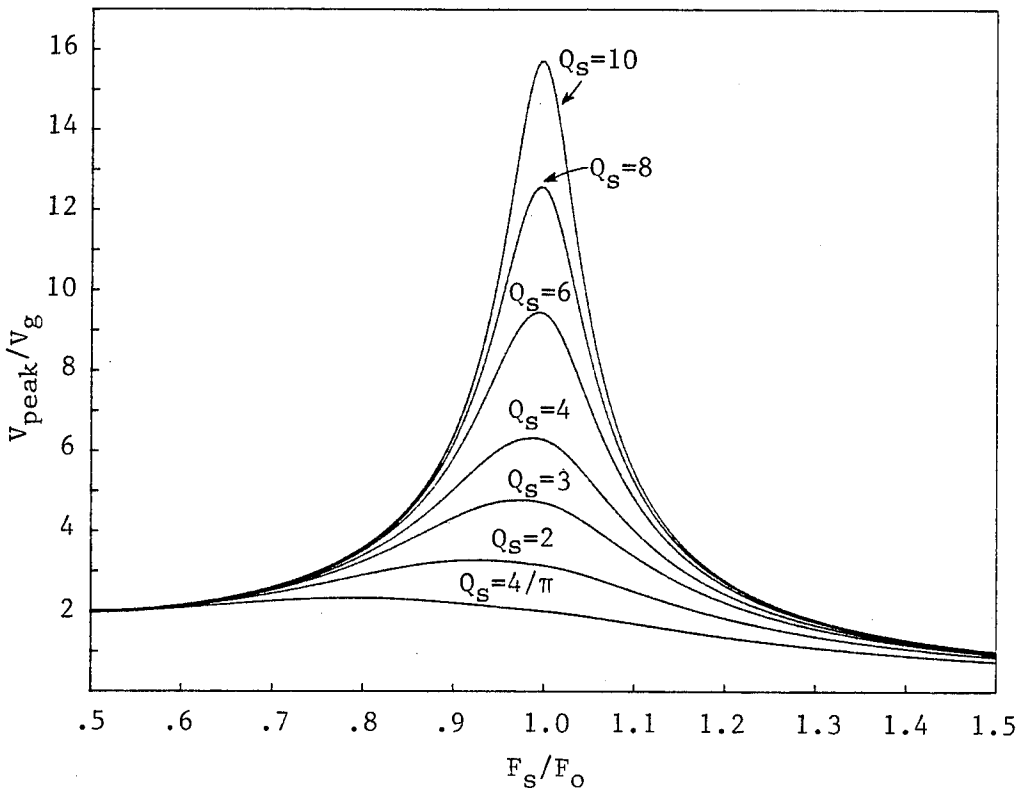

Fig. 3.17 Normalized peak resonant capacitor voltage characteristics of the series resonant converter in the range $F_s/F_0 \geq 1/2$.

can occur or not in the interval $T_a \leq t \leq T_s$ as shown in Fig. 3.15. The boundary between these two cases, according to Fig. 3.15, is determined by $\gamma - \omega_0 T_a = \pi/2$. From Appendix B.2 we have

$$\cos(\gamma - \omega_0 T_a) = \frac{1 - M - M^2 K}{1 - M(1-K)} \tag{3.46}$$

If $\gamma - \omega_0 T_a \geq \pi/2$, then the numerator in Eq. (3.46) is negative (since the denominator is always positive) and the peak is given by Eq. (3.45a), otherwise it is given by Eq. (3.45b). The peak current and voltage characteristics are plotted in Figs. 3.16 and 3.17 respectively.

3.4 General Analysis

In this section the operation of the series resonant converter is given in the entire range $0 < F_s/F_0 < \infty$. The general discontinuous and continuous conduction modes are identified, and the conversion ratio for each mode of operation is determined. The various modes of conduction are discussed first before the details of the analysis are given.

In Fig. 3.1e the switches $S1$ and $S2$ operate alternately at fifty percent duty ratio and for a duration T_s. In the following analysis, first, it is assumed that at no time $S1$ and $S2$ open simultaneously. Later, this restriction is removed in Sec. 3.4.7. Assume then that a turn-on pulse of duration T_s is applied to $Q1$ and simultaneously a similar turn-off pulse is applied to $Q2$ as shown in Fig. 3.1. Depending upon the duration of T_s and load conditions, $Q1$ and $D1$ may conduct alternately for the entire duration of the turn-on pulse, T_s, as may be the case for ccm, or only during a portion of T_s, as may be the case for dcm. For example, in Sec. 3.3.1 it

was shown that when the converter operates in ccm in the range $1/2 \leq F_s/F_0 \leq 1$, $Q1$ and $D1$ each conduct once in sequence during T_s, but in dcm only $Q1$ conducts for a duration $T_0/2$ while during the remaining time, $T_s - T_0/2$, $D1$ does not conduct. In the range $F_s/F_0 \leq 1/2$ since T_s may be many times larger than $T_0/2$, $Q1$ and $D1$ may conduct several times during T_s. This will be investigated presently.

There are two general types of dcm. These are shown in Fig. 3.18a and 3.18b whence it can be seen that the resonant current, $I_R(t)$, ceases to flow after completing n *complete* half-cycles each of duration $T_0/2$. During the remaining time, $T_s - nT_0/2$, neither $D1$ nor $Q1$ conduct even though $Q1$ is still on. The reason for this discontinuity in the resonant current is that, under certain load conditions, the output bridge becomes reversed biased during the time interval $T_s - nT_0/2$. In the previous section this was explained for the particular type of dcm that occurs in the range $1/2 \leq F_s/F_0 \leq 1$.

The two different types of dcm are shown in Figs. 3.18a and 3.18b. Each type corresponds to whether the number of conduction cycles, n, is even or odd, and is appropriately called *odd* or *even type n* dcm. The reason for this distinction becomes clear when the conversion ratio for each type of dcm is determined in the next section. Clearly, when n is specified explicitly, the words even or odd become redundant, i.e., *type* 3 dcm instead of *odd type* 3 dcm.

From Fig. 3.18a or b it can be easily seen that if the converter is operating in type n dcm (odd or even), then

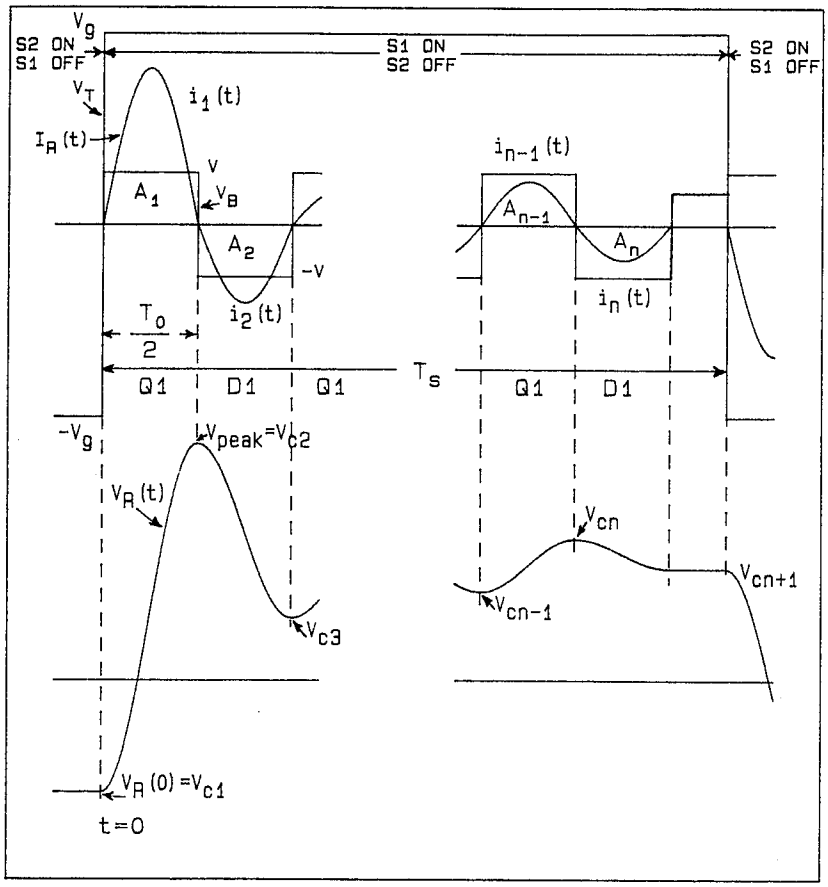

Fig. 3.18a Voltage and current waveforms of the series resonant converter in the general even type n discontinuous conduction mode.

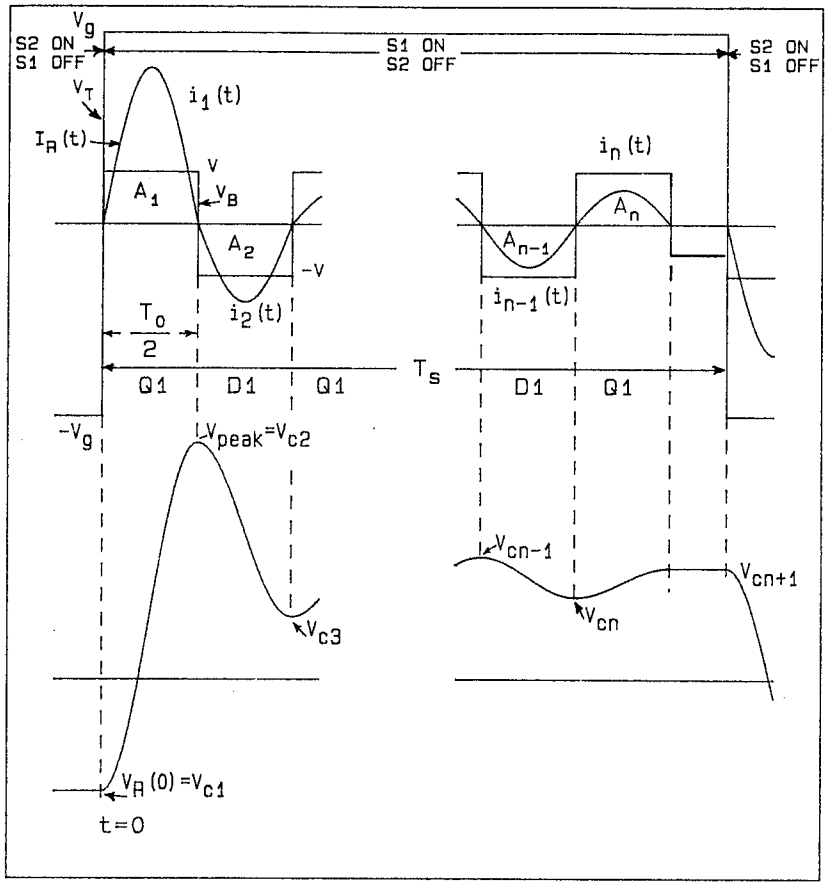

Fig. 3.18b Voltage and current waveforms of the series resonant converter in the general odd type n discontinuous conduction mode.

$$T_s \geq \frac{nT_0}{2} \quad \text{or} \quad 0 \leq \frac{F_s}{F_0} \leq \frac{1}{n} \tag{3.47}$$

The range of the control parameter given in (3.47) is only a sufficient condition for the occurrence of type n dcm. For a given Q_s, a necessary and sufficient condition for the occurrence of type n dcm is given by

$$0 < C_2(Q_s,n) \leq \frac{F_s}{F_0} \leq C_1(Q_s,n) \leq \frac{1}{n} \tag{3.48}$$

where $C_1(Q_s,n)$ and $C_2(Q_s,n)$ are determined in Sec. 3.4.3.

In continuous conduction mode the resonant current never ceases to flow. According to Fig. 3.19a and b there are two different types of ccm depending on whether $I_R(0)$ is positive or negative at the beginning of the switching cycle when $S1$ is closed. In Fig. 3.19a since $I_R(0)>0$, $Q1$ conducts first for a duration T_a after which $D1$ and $Q1$ conduct alternately for n *complete* half-cycles, each of duration $T_0/2$, and after which $D1$ conducts for a duration $T_D=T_s-nT_0/2-T_a$ until $S1$ is opened and $S2$ is closed. Cyclic stability requires that if $Q1$ conducts first then $D1$ conducts last, which implies that the number of half-cycles n, denoted by $i_1(t)$ through $i_n(t)$ in Fig. 3.19, must either be even or zero. This type of ccm is therefore appropriately called *+type n* ccm, where the positive sign refers to the fact that $I_R(0)$ is positive, and n refers to the conducted number of complete half-cycles. It can be seen from Fig. 3.19a that n = 0 corresponds to the case of ccm in the range $1/2 \leq F_s/F_0 \leq 1$ discussed in Sec. 3.3.1. According to Fig. 3.20a if the converter is operating in +type n ccm, then

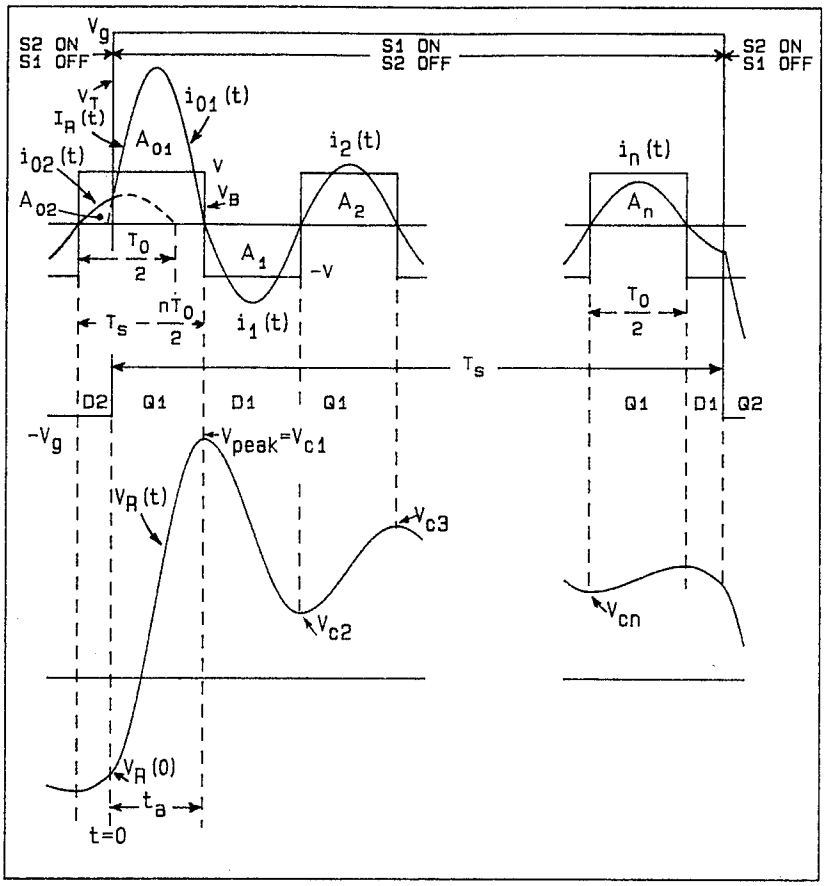

Fig. 3.19a Voltage and current waveforms of the series resonant converter in the general +type n continuous conduction mode.

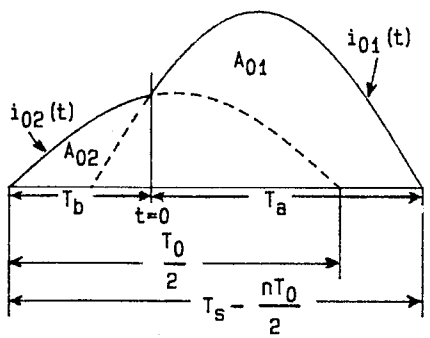

Fig. 3.20a Expanded view of the currents $i_{01}(t)$ and $i_{02}(t)$ in Fig. 3.19a.

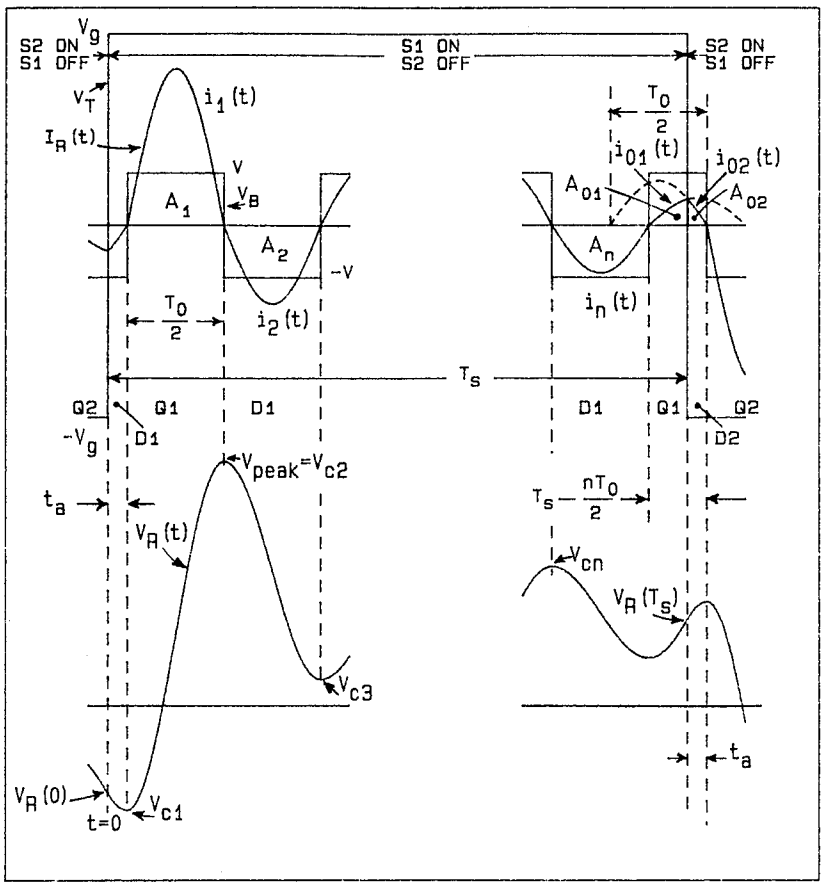

Fig. 3.19b Voltage and current waveforms of the series resonant converter in the general –type n continuous conduction mode.

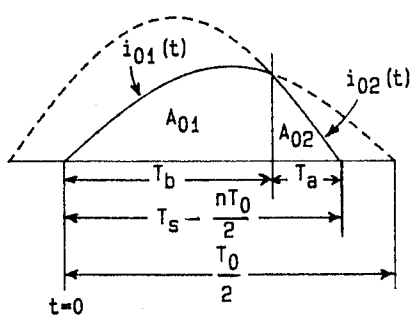

Fig. 3.20b Expanded view of the currents $i_{01}(t)$ and $i_{02}(t)$ in Fig. 3.19b.

$$\frac{T_0}{2} \leq T_s - \frac{nT_0}{2} \leq T_0 \quad \text{or} \quad \frac{1}{n+2} \leq \frac{F_s}{F_0} \leq \frac{1}{n+1} \tag{3.49}$$

The range of the control parameter given in (3.49) is only a sufficient condition for the occurrence of +type n ccm. For a given Q_s a necessary and sufficient condition for the occurrence of this type of ccm is given by

$$\frac{1}{n+2} \leq \frac{F_s}{F_0} \leq B_1(Q_s,n) \leq \frac{1}{n+1} \tag{3.50}$$

where $B_1(Q_s,n)$ is determined in Sec. 3.4.6.

The other type of ccm, which is called *–type n* ccm, is shown in Fig. 3.19b. In this case it can be seen that $I_R(0)$ is negative so that $D1$ conducts first for a duration T_a, after which $Q1$ and $D1$ conduct alternately for n complete half-cycles and after which $Q1$ conducts for a duration $T_D = T_s - nT_0/2 - T_a$ until $S1$ is opened and $S2$ is closed. At $t = T_s$, when $Q1$ is switched off and $Q2$ is switched on, $D2$ conducts first and the current is diverted from $Q1$ to $D2$. As before, n can only be even or zero. It can be easily seen that n = 0 corresponds to the case of ccm in the range $F_s/F_0 \geq 1$ discussed previously. According to Fig. 3.20b, it can be seen that if the converter is operating in this type of ccm then

$$0 \leq T_s - \frac{nT_0}{2} \leq \frac{T_0}{2} \quad \text{or} \quad \frac{1}{n+1} \leq \frac{F_s}{F_0} \leq \frac{1}{n} \tag{3.51}$$

As before, the range of the control parameter in (3.51) is only a sufficient condition for the occurrence for this type of ccm. A necessary and sufficient condition for the occurrence of –type n ccm is given by

$$\frac{1}{n+1} \leq \frac{F_s}{F_0} \leq B_2(Q_s,n) \leq \frac{1}{n} \tag{3.52}$$

where $B_2(Q_s,n)$ is determined in Sec. 3.4.6.

The results of the previous discussion are summarized in the following table.

Mode	Conduction Sequence	Frequency Interval
even type n dcm	Q1 D1 .... Q1 D1	$0 < C_2(Q_s,n) \leq \frac{F_s}{F_0} \leq C_1(Q_s,n) \leq \frac{1}{n}$ n even
	n complete half-cycles	
odd type n dcm	Q1 D1 .... Q1 D1 Q1	$0 < C_2(Q_s,n) \leq \frac{F_s}{F_0} \leq C_1(Q_s,n) \leq \frac{1}{n}$ n odd
+type n ccm	Q1 D1 Q1 .... D1 Q1 D1	$\frac{1}{n+2} \leq \frac{F_s}{F_0} \leq B_1(Q_s,n) \leq \frac{1}{n+1}$
	n complete half-cycles	n=0,2,4,...even
−type n ccm	D1 Q1 D1 .... Q1 D1 Q1	$\frac{1}{n+1} \leq \frac{F_s}{F_0} \leq B_2(Q_s,n) \leq \frac{1}{n}$

3.4.1 Even Type n dcm

The voltage and current waveforms for even type n dcm are shown in Fig. 3.18a. The current $i_m(t)$ is easily determined

$$i_m(t) = \omega_0 C_0 \left[V_g + (-1)^m V_0 - V_{cm} \right] \sin\omega_0 t \tag{3.53}$$

In Eq. (3.53) V_{cm} is the value of $V_R(t)$ at the beginning of each complete half-cycle, and the time reference is taken at the beginning of each cycle,

$i_m(t)$. The area, A_m, under the current $i_m(t)$ is given by

$$A_m = \int_0^{T_0/2} |i_m(t)|\,dt = 2C_0\left[V_g + (-1)^m V_0 - V_{cm}\right](-1)^{m+1} \tag{3.54}$$

The average output current can be expressed in terms of A_m

$$I_0 = \frac{V_0}{R} = \frac{1}{T_s}\int_0^{T_s} |I_R(t)|\,dt = \frac{1}{T_s}\sum_{m=1}^{n} A_m \tag{3.55}$$

which gives

$$\sum_{m=1}^{n} A_m = 2C_0 V_0 K \tag{3.56}$$

The input and output powers are given by

$$\frac{1}{T_s}\int_0^{T_s} I_R(t)\,V_g\,dt = \frac{V_g}{T_s}\sum_{m=1}^{n} A_m(-1)^{m+1} \tag{3.57}$$

$$\frac{1}{T_s}\int_0^{T_s} |I_R(t)|\,V_0\,dt = \frac{V_0}{T_s}\sum_{m=1}^{n} A_m \tag{3.58}$$

Substitution of Eq. (3.56) in (3.58) and the requirement $P_{in} = P_{out}$ gives

$$M = \frac{\sum_{m=1}^{n} A_m(-1)^{m+1}}{2C_0 V_0 K} \tag{3.59}$$

According to Fig. 3.18a the peak-to-peak capacitor voltage, $2V_{peak}$, is given by

$$-2V_{peak}C_0 = -A_2 + A_3 - A_4 + \cdots - A_n - A_1 + (A_1 - A_1)$$

$$= \sum_{m=1}^{n} A_m(-1)^{m+1} - 2A_1 \tag{3.60}$$

and $V_R(0)$, or V_{c1}, is given by

$$V_{c1} = V_{peak} - \frac{A_1}{C_0} = -\frac{1}{2C_0}\sum_{m=1}^{n} A_m(-1)^{m+1} = -MKV_0 \tag{3.61}$$

In Eq. (3.61) the last equality is obtained by using Eq. (3.59). In Eq. (3.54) V_{cm} is unknown except for m = 1, however, by successive application of

$$V_{cm} = V_{cm-1} + (-1)^m \frac{A_{m-1}}{C_0} \tag{3.62}$$

a recursive expression for A_m is obtained in Appendix B.3 given by

$$A_m = 2C_0V_g\left[1 - (2m-1)M + M^2K\right] \tag{3.63}$$

When Eq. (3.63) is substituted in (3.59), the summation for even n gives (Appendix B.3)

$$M = \frac{n}{K} = \frac{2n}{Q_s\pi}\frac{F_s}{F_0} \tag{3.64}$$

which is a *linear* function of the load R and the control parameter. Equation (3.64) also gives for the normalized average output current

$$I_0\frac{\omega_0 L_0}{V_g} = 2\frac{n}{\pi}\frac{F_s}{F_0} \tag{3.65}$$

which is independent of the load R. Therefore, when the series resonant converter is operating in an even type dcm, it acts as a *true current-fed*

converter.

The peak stress levels, determined in Appendix B.3, are given by

$$V_{peak} = V_g \left[2 - \frac{2n}{K} + \frac{n^2}{K} \right] \tag{3.66}$$

$$I_{peak} = \omega_0 C_0 V_g \left[1 - \frac{n}{K} + \frac{n^2}{K} \right] \tag{3.67}$$

3.4.2 Odd type n dcm

The only difference here is that n is odd in Eq. (3.59). In Appendix B.3 it is shown that for n odd M is given by

$$M = \frac{1}{n} \tag{3.68}$$

which implies that when the converter is operating in an odd type dcm the conversion ratio is *insensitive* to F_s/F_0 and R. The special case for $n=1$ was discussed earlier. Clearly this mode of operation should be avoided since the output in this mode is uncontrollable.

The peak stress levels are given by

$$V_{peak} = V_g \left[2 - \frac{2}{n} + \frac{K}{n^2} \right] \tag{3.69}$$

$$I_{peak} = \omega_0 C_0 V_g \left[1 - \frac{1}{n} + \frac{K}{n^2} \right] \tag{3.70}$$

3.4.3 Boundary between two Discontinuous Conduction Modes

Assume that the converter is operating in even type m dcm. The conversion ratio according to Eq. (3.64) is given by

$$M = \frac{2m}{\pi Q_s} \frac{F_s}{F_0} \tag{3.71}$$

and is plotted in Fig. 3.21 for three different cases. These are straight lines through the origin with slope $2m/\pi Q_s$. The conversion ratios for odd type (m−1) and odd type (m+1) dcm, given by Eq. (3.68), are also plotted in Fig. 3.21. Since a sufficient condition for type m dcm to occur is that $F_s/F_0 \leq 1/m$, Eq. (3.71) is valid in a region to the left of $F_s/F_0 = 1/m$ on the M vs. F_s/F_0 plot. In case I, as the switching frequency is increased, M increases linearly until the converter enters odd type (m−1) dcm at $(F_s/F_0)_c$. If F_s/F_0 is increased further , say up to $(F_s/F_0)_d$, M will stay at a fixed value of $1/(m-1)$ because of operation in odd type (m−1) dcm. (To complete the discussion for all $F_s/F_0 \geq (F_s/F_0)_c$, we need to know results from operation in ccm given in the next section, but for the present discussion we need only consider the results obtained for dcm). If F_s/F_0 on the other hand is decreased, M will decrease linearly until the converter enters odd type (m+1) dcm at $(F_s/F_0)_b$. If F_s/F_0 is decreased further, say down to $(F_s/F_0)_a$, M will remain at a fixed value of $1/(m+1)$. Therefore, Case I represents an even type m dcm that is bounded between odd type (m−1) and type (m+1) dcm. Case II on the other hand, which corresponds to a larger value of Q_s than case I, represents an even type m dcm that is bounded between odd type (m+1) dcm and +type (m−2) ccm. To understand this, we simply determine which of the two general types of

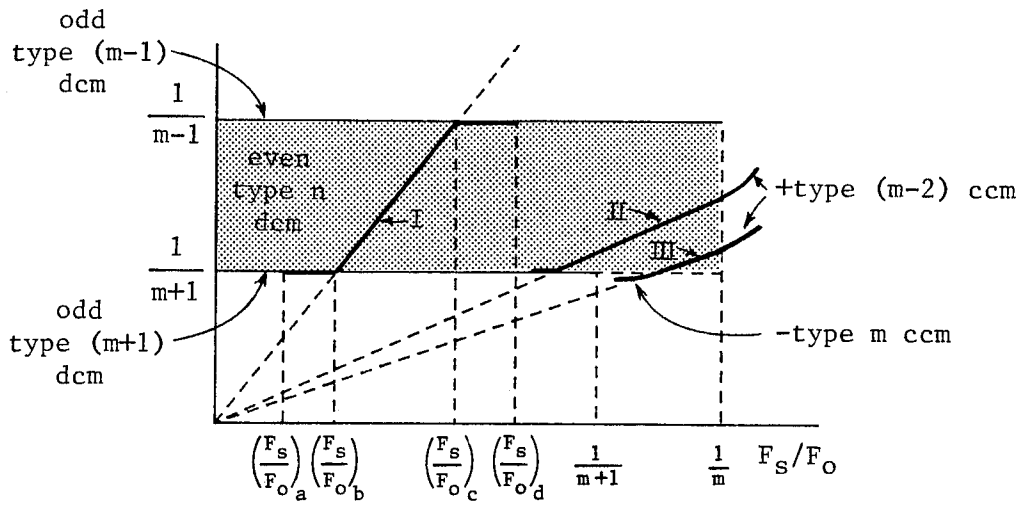

Fig. 3.21 Boundaries of even type n discontinuous conduction mode.

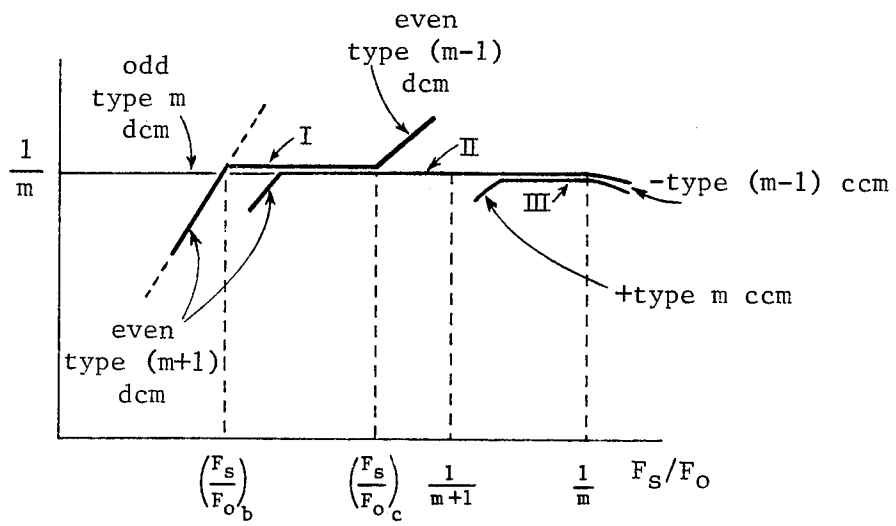

Fig. 3.22 Boundaries of odd type n discontinuous conduction mode.

ccm has a lower bound given by the reciprocal of an even integer. An inspection of (3.50) and (3.52), in both of which n can only be even or zero, reveals that only the lower bound of +type n ccm, given by 1/(n+2), can correspond to 1/m. This implies that n=m−2 and the continuous conduction mode in question is +type (m−2). The third case represents an even type m dcm that is bounded between −type m ccm and +type (m−2) ccm. In this case as F_s/F_0 is decreased, the converter enters −type m ccm in the range $1/(m+1) \le F_s/F_0 \le 1/m$ when $M = 1/(n+1)$. The reason how this happens is given in Sec. 3.4.6 where the boundaries between dcm and ccm are determined.

The lower bound $C_2(Q_s,n)$ in (3.48) can now be easily determined. From Fig. 3.21 it can be seen that at the lower bound $M = 1/(m+1)$ which according to Eq. (3.71) gives

$$C_2(Q_s,m) = \frac{\pi Q_s}{2m(m+1)} \tag{3.72}$$

Also, according to Fig. 3.21 a necessary condition for this type of dcm to occur is that $C_2(Q_s,n) \le 1/m$ which gives

$$Q_s \le \frac{2(m-1)}{\pi} \tag{3.73}$$

This last condition covers all three cases in Fig. 3.21. The upper bound in case I can be easily determined by setting $M = 1/(m-1)$ which according to Eq. (3.71) gives

$$(F_s/F_0)_c = \frac{Q_s\pi}{2m(m-1)} \tag{3.74}$$

The condition on Q_s for case I to occur is obtained by requiring $(F_s/F_0)_c \leq 1/m$ which from (3.74) gives

$$Q_s \leq \frac{2(m-1)}{\pi} \tag{3.75}$$

According to Eqs. (3.73), (3.74), and (3.75) the upper bound $C_1(Q_s,n)$ in (3.48) is given by

$$C_1(Q_s,m) = \begin{cases} \dfrac{Q_s\pi}{2m(m-1)} & ; \quad Q_s \leq \dfrac{2(m-1)}{\pi} \\ \dfrac{1}{m} & ; \quad \dfrac{2(m-1)}{\pi} \leq Q_s \leq \dfrac{2(m+1)}{\pi} \end{cases} \tag{3.76a-b}$$

A complete description of the conditions on Q_s for this mode to occur and the range of F_s/F_0 in which it can occur can be summarized by the following

$$\textit{type } m \text{ dcm} \begin{cases} \dfrac{Q_s\pi}{2m(m+1)} \leq \dfrac{F_s}{F_0} \leq \dfrac{Q_s\pi}{2m(m-1)} & ; \quad Q_s \leq \dfrac{2(m-1)}{\pi} \\ \dfrac{Q_s\pi}{2m(m+1)} \leq \dfrac{F_s}{F_0} \leq \dfrac{1}{m} & ; \quad \dfrac{2(m-1)}{\pi} \leq Q_s \leq \dfrac{2(m+1)}{\pi} \end{cases} \tag{3.77a-b}$$

Alternately for a given $F_s/F_0 \leq 1/m$ the range of Q_s in which even type m dcm can occur is easily determined from Eqs. (3.72) and (3.74)

$$\frac{2m(m-1)}{\pi}\frac{F_s}{F_0} \le Q_s \le \frac{2m(m+1)}{\pi}\frac{F_s}{F_0} \quad ; \quad \frac{F_s}{F_0} \le \frac{1}{m} \tag{3.78}$$

In odd type m dcm the conversion ratio according to Eq. (3.68) is constant. This is shown in Fig. 3.22 by a straight line parallel to the F_s/F_0 axis and extending to $F_s/F_0 = 1/m$. There are three cases to be considered as shown in Fig. 3.22. In the first case the value of Q_s is such that as F_s/F_0 is increased the converter enters even type (m−1) dcm at $(F_s/F_0)_c$, and when decreased the converter enters even type (m+1) dcm at $(F_s/F_0)_b$. For the second and third cases, as F_s/F_0 is increased the converter enters −type (m−1) ccm at $F_s/F_0 = 1/m$, and when decreased, the converter enters even type (m+1) dcm in the second case and +type (m−1) ccm in the third case. The boundary between odd type m dcm and +type (m−1) ccm in the third case is discussed in Sec. 3.4.6 where it is shown that at this boundary K is equal to m(m+1) just like at the boundary between even type (m+1) dcm and odd type m dcm in the first two cases. Proceeding exactly as before, we can determine the conditions on Q_s for the occurrence of odd type m dcm. The results obtained are identical to the results obtained for even type m dcm given by Eqs. (3.77) and (3.78). Therefore, these equations give a complete analytic description of odd and even types of discontinuous conduction mode.

The boundaries between even and odd type discontinuous conduction modes can be put together as shown in Fig. 3.23. The conversion ratio characteristics for even type type m dcm, which are linear functions of F_s/F_0, are confined to the shaded areas, and the characteristics for odd type m dcm, which are insensitive to F_s/F_0, are

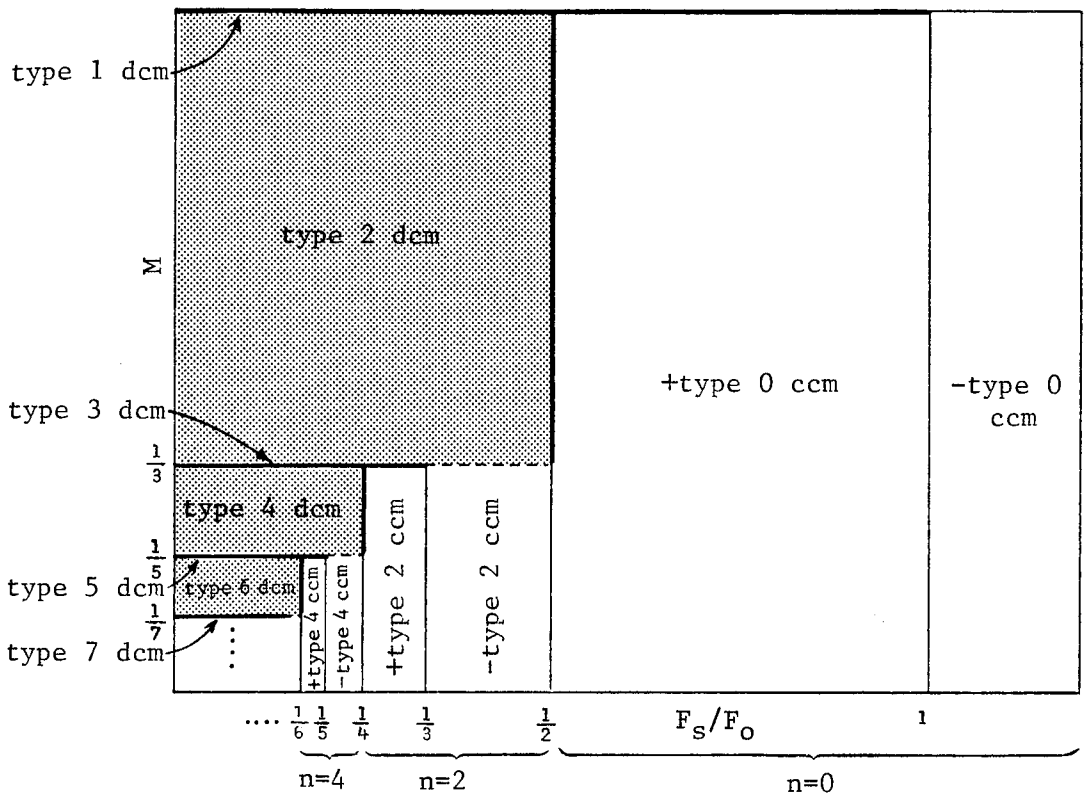

Fig. 3.23 Boundaries of odd and even type n discontinuous conduction modes in the entire range $0 \leq F_s / F_0 \leq \infty$. *The characteristics for even type discontinuous conduction modes are confined to the shaded areas, whereas the characteristics for odd type discontinuous conduction mode are confined to straight lines parallel to the* F_s / F_0 *axis. The characteristics for continuous conduction mode are confined to the unshaded areas.*

confined to lines parallel to the F_s/F_0 axis. The areas, to which the conversion ratio characteristics of the various continuous conduction modes are confined, can be easily identified by using (3.50) and (3.52). In Fig. 3.23 examples are given for n=0, 2 and 4 which correspond to $1/2 \leq F_s/F_0 \leq 1$ and $F_s/F_0 \geq 1$, $1/4 \leq F_s/F_0 \leq 1/3$ and $1/3 \leq F_s/F_0 \leq 1/2$, and $1/6 \leq F_s/F_0 \leq 1/5$ and $1/5 \leq F_s/F_0 \leq 1/4$ respectively. Note that the subdivision of F_s/F_0 axis according to (3.50) and (3.52) is only with respect to the continuous conduction modes. For example, the proper way to refer to the range $1/4 \leq F_s/F_0 \leq 1/3$ with respect to ccm is

$$\frac{1}{n+2} \leq \frac{F_s}{F_0} \leq \frac{1}{n+1} \quad ; \quad n=2$$

and *not* $1/(n+1) \leq F_s/F_0 \leq 1/n$ in which n=3. Therefore, investigation of the possibility of occurrence of ccm in an arbitrary range requires proper splitting of the arbitrary range. For example, a range such as $.4 \leq F_s/F_0 \leq .75$ is split into $.4 \leq F_s/F_0 \leq 1/2$ and $1/2 \leq F_s/F_0 \leq .75$. The first range belongs to $1/(n+1) \leq F_s/F_0 \leq 1/n$ for n=2, and consequently only –type 2 ccm can occur in this range, whereas the second range belongs to $1/(n+2) \leq F_s/F_0 \leq 1/(n+1)$ for n=0, and only +type 0 ccm can occur in the second range.

This completes the discussion on the boundaries between two general discontinuous conduction modes. The boundaries between discontinuous and continuous conduction in the ranges $1/(n+2) \leq F_s/F_0 \leq 1/(n+1)$ and $1/(n+1) \leq F_s/F_0 \leq 1/n$ are determined in Sec. 3.4.6.

3.4.4 +type n ccm

In this section the most important steps for the determination of M are given. The details of the analysis are given in Appendix B.4. The voltage and current waveforms are shown in Fig. 3.19a. As before, the expression of the output voltage in terms of the areas under the resonant current is given by

$$V_0 = I_0 R = \frac{R}{T_s}(A_{01} + A_{02} + \sum_{m=1}^{n} A_m) \tag{3.79}$$

When the input and output powers are set equal, an expression for M in terms of these areas is obtained which is given by

$$M = \frac{A_{01} - A_{02} + \sum_{m=1}^{n} A_m(-1)^m}{A_{01} + A_{02} + \sum_{m=1}^{n} A_m} \tag{3.80}$$

The current $i_m(t)$ is given by

$$i_m(t) = \omega_0 C_0 \left[V_g + V_0(-1)^{m+1} - V_{cm} \right] \sin\omega_0 t \tag{3.81}$$

In Eq. (3.81) V_{cm} is the initial capacitor voltage at the beginning of each complete half-cycle, $i_m(t)$, and the time origin is taken at the beginning of each cycle. The recursive relation for A_m is determined to be

$$A_m = 2C_0 \left[V_{c1} - (2m-1)V_0 - V_g \right] \tag{3.82}$$

and the summation in Eq. (3.80) is obtained for even n

$$\sum_{m=1}^{n} A_m(-1)^m = -2nC_0V_0 \tag{3.83}$$

The currents $i_{01}(t)$ and $i_{02}(t)$, which are shown in detail in Fig. 3.20a, are given by

$$i_{01}(t) = \omega_0 C_0 V_g \frac{1-M+M^2K}{\cos\omega_0 T_a} \sin(\omega_0 t - \omega_0 T_a) \tag{3.84}$$

$$i_{02}(t) = \omega_0 C_0 V_g \frac{M^2K-M-1}{\cos(\gamma-\omega_0 T_a)} \sin(\omega_0 t - \omega_0 T_a + \gamma) \tag{3.85}$$

The corresponding areas A_{01} and A_{02} are given by

$$A_{01} = C_0 V_g \left[1-M+M^2K\right]\left[1-\sec\omega_0 T_a\right] \tag{3.86}$$

$$A_{02} = C_0 V_g \left[M^2K-M-1\right]\left[\sec(\gamma-\omega_0 T_a)-1\right] \tag{3.87}$$

Substitution of Eqs. (3.83), (3.86) and (3.87) in (3.80) and the requirement $i_{01}(0)=i_{02}(0)$ give two simultaneous trigonometric equations in $\omega_0 T_a$ which when solved together give

$$G_{s+}(M,Q_s,\gamma,n) = (n+1)\frac{1-M+M^2K}{1-M(n+1)^2-MK}\cos\gamma$$

$$-\frac{\sqrt{[MK+n][M^2(n+1)^2-1][n+2-MK]}}{1-M(n+1)^2-MK}\sin\gamma$$

$$+\frac{M^2K-M-1}{1+M(n+1)^2-MK}(n+1) = 0 \tag{3.88}$$

Equation (3.88) is the implicit equation, which when solved numerically, gives the value of M for a given Q_s and F_s/F_0.

The peak stress levels are given by

$$V_{peak} = V_g\left[1+\mathrm{n}M+\frac{MK-1}{\mathrm{n}+1}\right] \tag{3.89}$$

$$I_{peak} = \frac{\omega_0 C_0 V_g}{\mathrm{n}+1}\left[M(\mathrm{n}+1)^2+MK-1\right] \tag{3.90}$$

3.4.5 –type n ccm

A similar analysis, given in Appendix B.5, for this mode of operation gives

$$G_{s-}(M,Q_s,\gamma,\mathrm{n}) = (\mathrm{n}+1)\frac{1+M+M^2K}{1+M(\mathrm{n}+1)^2+MK}\cos\gamma$$

$$+\frac{\sqrt{[MK-\mathrm{n}][1-M^2(\mathrm{n}+1)^2][\mathrm{n}+2+MK]}}{1+M(\mathrm{n}+1)^2+MK}\sin\gamma$$

$$-\frac{1-M-M^2K}{1-M(\mathrm{n}+1)^2+MK}(\mathrm{n}+1) = 0 \tag{3.91}$$

which is another implicit equation which must be solved numerically. It can be seen that

$$G_{s+}(M,Q_s,\gamma,\mathrm{n}) = G_{s-}(-M,-Q_s,-\gamma,\mathrm{n}) \tag{3.92}$$

The peak stress levels for $\mathrm{n}\neq 0$ are given by

$$V_{peak} = V_g\left[1-3M+\frac{1+M(n+1)^2+MK}{n+1}\right] \qquad n=2,4,6..... \tag{3.93}$$

$$I_{peak} = \frac{\omega_0 C_0 V_g}{n+1}[1+M(n^2-1+K)] \qquad n=2,4,6..... \tag{3.94}$$

For n=0 the peak stress levels are given in Sec. 3.3.2. The reason the results for n=0 are different from the results for $n\neq 0$ can be seen from Fig. 3.19b. For –type n ccm V_{peak} occurs at the end of $i_1(t)$ which for n=0 does not exist and consequently V_{peak} is given by Eq. (3.44) of Sec. 3.3.2. The same reason applies for I_{peak}, and consequently for n=0 I_{peak} is given by Eq. (3.45a-b).

Before the conversion ratio characteristics are plotted for the two general types of ccm, the boundaries between continuous and discontinuous conductions mode will be determined.

3.4.6 Boundaries between Discontinuous and Continuous Conduction Mode

For –type n ccm to occur in the interval $1/(n+1)\leq F_s/F_0<1/n$, an examination of the radical in Eq. (3.91) reveals that

$$MK \geq n \qquad \text{and} \qquad M \leq \frac{1}{n+1} \tag{3.95}$$

Therefore, the maximum value for –type n ccm is 1/(n+1). This explains the boundary line between –type n ccm and even type n dcm in the interval $1/(n+1)\leq F_s/F_0\leq 1/n$ which in Fig. 3.23 is shown by dashed lines for n=2 and 6. As explained earlier, in the range $F_s/F_0\geq 1$, which corresponds to n=0, dcm cannot occur. This is consistent with the

nomenclature, since such a dcm would have to be called type 0 dcm which implies that the resonant current is zero all the time which corresponds to no load conditions. According to (3.95) it can be seen that

$$K \geq n(n+1) \tag{3.96}$$

which implies

$$Q_s \geq \frac{F_s}{F_0}\frac{2n(n+1)}{\pi} \quad \text{or} \quad \frac{F_s}{F_0} \leq \frac{Q_s\pi}{2n(n+1)} \tag{3.97}$$

The first inequality in (3.97) gives the condition on Q_s for –type n ccm to occur which can be rewritten as

$$\frac{1}{n+1} \leq \frac{F_s}{F_0} \leq \frac{1}{n} \begin{cases} Q_s \leq \dfrac{F_s}{F_0}\dfrac{2n(n+1)}{\pi} & \text{dcm} \\ Q_s \geq \dfrac{F_s}{F_0}\dfrac{2n(n+1)}{\pi} & \textit{–type } n \text{ ccm} \end{cases} \tag{3.98a-b}$$

For example, $F_s/F_0 = .4$ falls in the interval $1/3 \leq F_s/F_0 \leq 1/2$, which corresponds to n=2. Therefore, according to (3.98) for $Q_s \geq (.4)12/\pi$, the converter operates in –type 2 ccm at $F_s/F_0 = .4$, otherwise it operates in dcm.

A comparison of (3.97) and the necessary and sufficient condition for the occurrence of –type n ccm given by (3.52) shows that

$$B_2(Q_s,n) = \begin{cases} \dfrac{Q_s\pi}{2n(n+1)} & ; \quad \dfrac{2n}{\pi} \leq Q_s \leq \dfrac{2(n+1)}{\pi} \\ \dfrac{1}{n} & ; \quad Q_s \geq \dfrac{2(n+1)}{\pi} \end{cases} \tag{3.99a-b}$$

An examination of the radical in Eq. (3.88) reveals that, for +type n ccm to occur in the interval $1/(n+2) \le F_s/F_0 < 1/(n+1)$, the following must be true

$$MK \ge n+2 \quad \text{and} \quad M \le \frac{1}{n+1} \tag{3.100}$$

Therefore, as in the case of –type n ccm, the maximum value of M for +type n ccm is $1/(n+1)$. This explains the boundary line between +type n ccm and odd type (n+1) dcm in the range $1/(n+2) \le F_s/F_0 \le 1/(n+1)$ as shown in Fig. 3.23. According to (3.100) it can be seen that

$$K \ge (n+1)(n+2) \tag{3.101}$$

which implies that

$$Q_s \ge \frac{F_s}{F_0}\frac{2(n+1)(n+2)}{\pi} \quad \text{or} \quad \frac{F_s}{F_0} \le \frac{Q_s \pi}{2(n+1)(n+2)} \tag{3.102}$$

The first inequality in (3.102) gives the condition on Q_s for +type n ccm to occur in the range $1/(n+2) < F_s/F_0 < 1/(n+1)$, which can be rewritten as

$$\frac{1}{n+2} \le \frac{F_s}{F_0} \le \frac{1}{n+1} \begin{cases} Q_s \le \dfrac{2(n+1)(n+2)}{\pi}\dfrac{F_s}{F_0} & \text{dcm} \\ Q_s \ge \dfrac{2(n+1)(n+2)}{\pi}\dfrac{F_s}{F_0} & \textit{+type } n \text{ ccm} \end{cases} \tag{3.103a-b}$$

For example, $F_s/F_0 = .3$ falls in the interval $1/4 \le F_s/F_0 \le 1/3$, which corresponds to n=2 in the range $1/(n+2) \le F_s/F_0 \le 1/(n+1)$. Therefore, according to (3.103) for $Q_s \ge (.3)24/\pi$ the converter operates in +type 2 ccm at $F_s/F_0 = .3$, otherwise it operates in dcm.

A comparison of (3.103a-b) and the necessary and sufficient condition for the occurrence of +type n ccm given in (3.50) shows that

$$B_1(Q_s,n) = \begin{cases} \dfrac{Q_s}{2(n+1)(n+2)} & ; \quad \dfrac{2(n+1)}{\pi} \le Q_s \le \dfrac{2(n+2)}{\pi} \\ \dfrac{1}{n+1} & ; \quad Q_s \ge \dfrac{2(n+2)}{\pi} \end{cases} \qquad (3.104a\text{-}b)$$

For a given F_s/F_0 the boundary between discontinuous and conduction modes can be determined as a function of Q_s either from (3.98) or (3.103) depending on which range F_s/F_0 falls in. To complete this discussion, the boundary between dcm and ccm for a given Q_s as a function of F_s/F_0 is determined next.

Consider now two adjacent cases of ccm corresponding to n and n−2. According to $B_1(Q_s,n-2)$ in (3.104b) if $Q_s \ge 2n/\pi$ the converter operates in +type (n−2) ccm in the entire range $1/n \le F_s/F_0 \le 1/(n-1)$. Also, according to $B_2(Q_s,n-2)$ in (3.99b) the converter operates in −type (n−2) ccm in the range $1/(n-1) \le F_s/F_0 < 1/(n-2)$. In fact, for $Q_s \ge 2n/\pi$ ccm occurs for all $F_s/F_0 \ge 1/n$, because the conditions for ccm according to $B_1(Q_s,n-m)$ in Eq. (3.104b) and $B_2(Q_s,n-m)$ in Eq. (3.99b) − for m even − is met by $Q_s \ge 2n/\pi$. Consider now two adjacent cases of ccm corresponding to n and n+2. If $Q_s \le 2(n+1)/\pi$ then according to $B_1(Q_s,n)$ in (3.104b), the converter operates in dcm in the range $1/(n+2) \le F_s/F_0 \le 1/(n+1)$. Also, according to $B_2(Q_s,n+2)$ in Eq. (3.99a) the converter operates in dcm in the range $1/(n+3) \le F_s/F_0 < 1/(n+2)$ since $Q_s \le 2(n+1)/\pi$ satisfies the condition $Q_s \le 2(n+2)/\pi$. In fact, the converter will be in dcm for all $F_s/F_0 \le 1/(n+1)$, since the condition for dcm

according to $B_1(Q_s,n+m)$ in (3.104a) and $B_2(Q_s,n+m)$ in Eq. (3.99a) – for m even – is satisfied by $Q_s \leq 2(n+1)/\pi$. The preceding discussion can be summarized by the following

$$\frac{2n}{\pi} \leq Q_s \leq \frac{2(n+1)}{\pi} \begin{cases} \dfrac{F_s}{F_0} \leq \dfrac{1}{n+1} & \text{dcm} \\ \dfrac{1}{n+1} \leq \dfrac{F_s}{F_0} \leq \dfrac{Q_s\pi}{2n(n+1)} & \textit{-type } n \text{ ccm} \\ \dfrac{Q_s\pi}{2n(n+1)} \leq \dfrac{F_s}{F_0} \leq \dfrac{1}{n} & \text{even } \textit{type } n \text{ dcm} \\ \dfrac{F_s}{F_0} \geq \dfrac{1}{n} & \text{ccm} \end{cases} \tag{3.105a-d}$$

A similar discussion gives

$$\frac{2(n+1)}{\pi} \leq Q_s \leq \frac{2(n+2)}{\pi} \begin{cases} \dfrac{F_s}{F_0} \geq \dfrac{1}{n+1} & \text{ccm} \\ \dfrac{Q_s\pi}{2(n+1)(n+2)} \leq \dfrac{F_s}{F_0} \leq \dfrac{1}{n+1} & \text{odd } \textit{type } (n+1) \text{ dcm} \\ \dfrac{1}{n+2} \leq \dfrac{F_s}{F_0} \leq \dfrac{Q_s\pi}{2(n+1)(n+2)} & \textit{+type } n \text{ ccm} \\ \dfrac{F_s}{F_0} \leq \dfrac{1}{n+2} & \text{dcm} \end{cases} \tag{3.106a-d}$$

Therefore, for a given Q_s the boundaries between dcm and ccm are determined as a function of F_s/F_0 either from (3.105) or (3.106) depending on which range Q_s falls in. For example if $Q_s = 4$ then of the following two ranges

$$n+2 \geq \frac{Q_s\pi}{2} \geq n+1 \qquad (n \text{ even}) \tag{3.107}$$

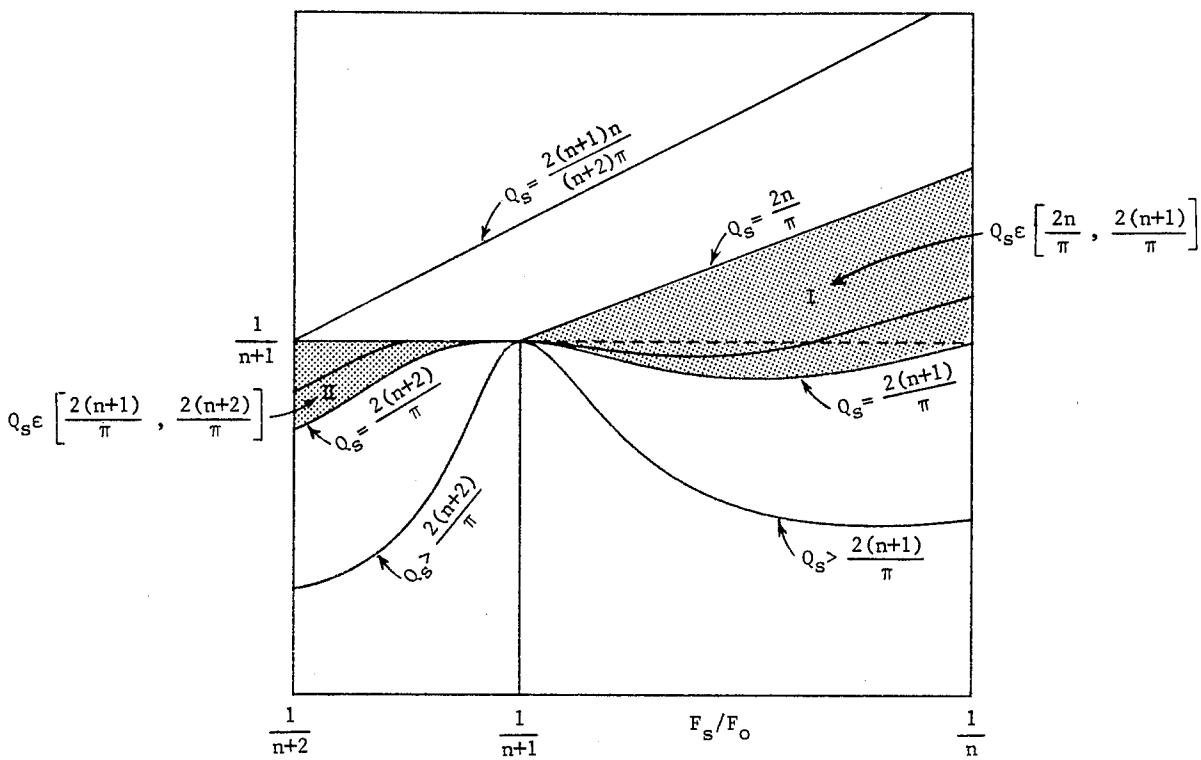

Fig. 3.24 Conversion ratio characteristics of +type n continuous conduction mode in the range $1/(n+2) \leq F_s/F_0 \leq 1/(n+1)$ *and −type n continuous conduction mode in the range* $1/(n+1) \leq F_s/F_0 \leq 1/n$. *The boundary between +type n ccm and odd type* $(n+1)$ *dcm is at the line* $M = 1/(n+1)$, *and the boundary between −type n ccm and even type n dcm is at the dotted line* $M = 1/(n+1)$. *The shaded regions I and II correspond to values of* Q_s *in* (3.105) *and* (3.106) *respectively.*

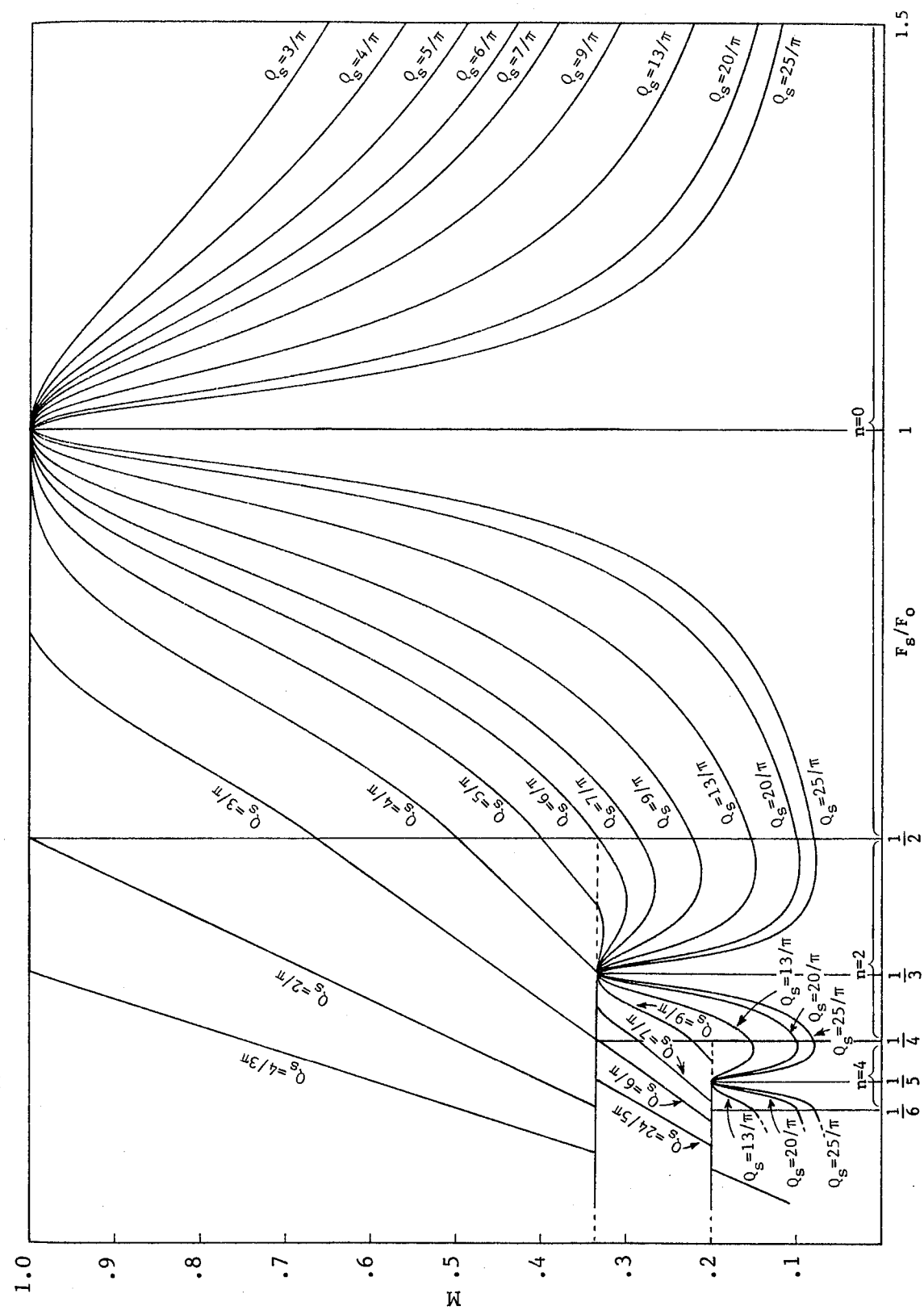

Fig. 3.25 General conversion ratio characteristics of the series resonant converter in the entire range $0 \leq F_s / F_0 \leq \infty$.

$$n+1 \geq \frac{Q_s \pi}{2} \geq n \qquad \text{(n even)} \tag{3.108}$$

only (3.108) is satisfied for n=6, and the boundaries as a function of F_s/F_0 are given by (3.101). On the other hand if $Q_s = 2$, then only (3.107) is satisfied for n=2, and the boundaries as a function of F_s/F_0 are given by (3.106).

The general boundaries between dcm and ccm for a given even n are shown in Fig. 3.24. The characteristics corresponding to the two ranges of Q_s given by (3.105) and (3.106) are shown in the shaded regions I and II respectively.

The general conversion ratio characteristics are plotted in Fig. 3.25 for n=0, 2, and 4. It can be seen that these characteristics admit multiple resonant peaks at $F_s/F_0 = 1, 1/3, 1/5 \ldots 1/(n+1)$ with corresponding values of $M = 1, 1/3, 1/5 \ldots$ at the peaks.

3.4.7 Operation in the Special Case When Q1 and Q2 Are Switched Off Simultaneously

Until now the switches $S1$ and $S2$ were allowed to conduct for the entire duration of T_s. If conduction is inhibited by switching off $Q1$ and $Q2$ before the end of T_s, then the converter can operate only in a finite number of continuous and discontinuous conduction modes. To illustrate this, consider the operation of this circuit when SCRs are used which are fired only once during T_s. In this case, when the circuit is excited in the range $F_s/F_0 \leq 1/2$, the switches $S1$ and $S2$ conduct only *once* during the forward and reverse directions. Consequently, the only allowed modes of operation in the range $F_s/F_0 \leq 1/2$ are type 1 dcm and type 2 dcm. In the

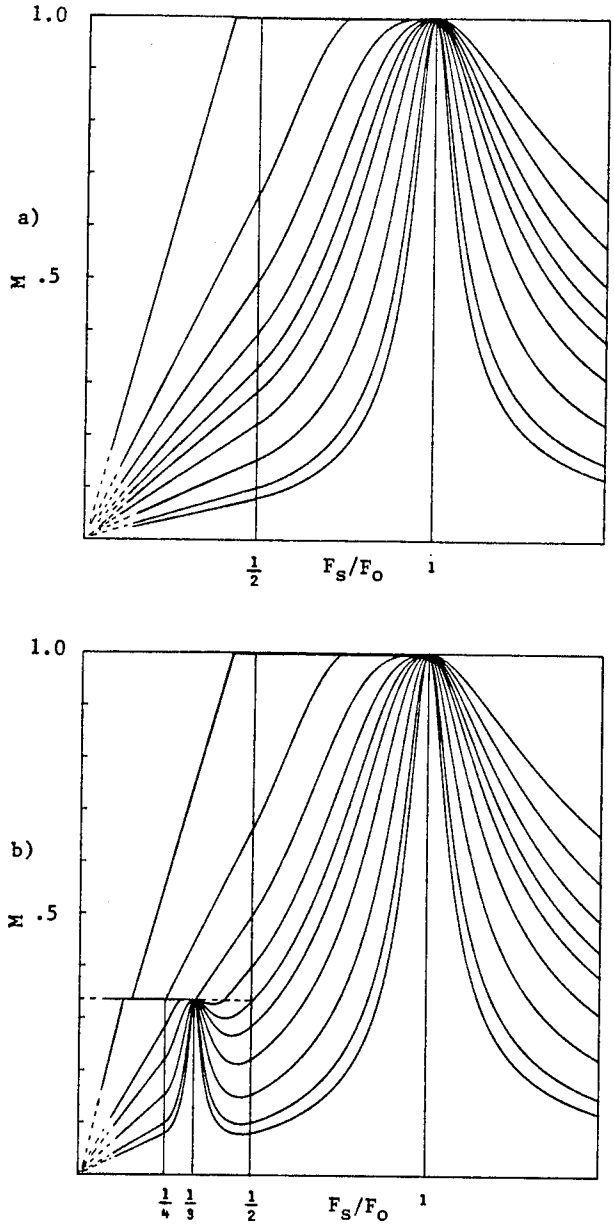

Fig. 3.26 a) Conversion ratio characteristics of the series resonant converter when SCRs are used or when Q1 and Q2 are allowed to conduct only once during T_s. b) The same characteristics when Q1 and Q2 are allowed to conduct at most twice during T_s. In the first case only one resonant peak at $F_s/F_0=1$ occures whereas in the second case only two resonant peaks, at $F_s/F_0=1$ and $F_s/F_0=1/3$, occur. In general if Q1 and Q2 are allowed to conduct only j number of times, only j resonant peaks occur.

range $F_s/F_0 \geq 1/2$ the operation remains unaffected since, as before, in this range $S1$ and $S2$ conduct only once as restricted by the switching time T_s. The conversion ratio characteristics for this case are shown in Fig. 3.26a where it can be seen that in the range $F_s/F_0 \leq 1/2$ only those characteristics corresponding to type 1 and type 2 dcm are present. In the range $F_s/F_0 \geq 1/2$ the characteristics remain unchanged. Also, since no other mode occurs in the range $F_s/F_0 \leq 1/2$, the lower bound of type 2 dcm is now zero instead of $C_2(Q_s,2) = Q_s\pi/12$ as required by (3.48) and (3.72).

In general, $Q1$ and $Q2$ can be made to conduct at most j number of times. In Fig 3.26b the characteristics for $j=2$ are shown. In this case the maximum allowed discontinuity is type 4 dcm and consequently $C_2(Q_s,4) = 0$. The M for type 2 dcm is now confined, as in the general case, between $M = 1$ and $M = 1/3$ because of the occurrence of type 3 dcm and –type 2 ccm. Also, in addition to the first resonant peak at $F_s/F_0 = 1$, the second resonant peak at $F_s/F_0 = 1/3$ occurs because of the occurrence of ±type 2 ccm. In general, if $Q1$ and $Q2$ are allowed to conduct at most j number of times then only j resonant peaks occur at F_s/F_0 = 1, 1/3, 1/5,...$1/(2j-1)$ and $C_2(Q_s,2j) = 0$.

This completes the dc analysis of the series resonant converter in the general continuous and discontinuous conduction modes.

3.5 Nonidealities

As in the case of the parallel resonant converter, the only two nonidealities considered in this section are the voltage drop in the output rectifier bridge and the parasitic resistances in the tank and the output filter circuits.

The voltage drop in the output rectifiers is considered first. The two methods of output rectification are shown in Fig. 3.27a and b where the isolation transformer is assumed to be ideal and of unity turns ratio. The nonideal circuit is shown in Fig. 3.28a where the output network is shown reflected to the primary side. All the diodes in this circuit are assumed to be ideal. The voltage drop in the output rectifiers is separated and is represented by a voltage source V_{BD} in series with an ideal diode. For the center-tapped circuit $V_{BD} = V_D$ and for the full-bridge circuit $V_{BD} = 2V_D$. As in the case of the parallel resonant converter, an ideal circuit, shown in Fig. 3.28b, is determined which delivers the same power P_{in}' at the input side of the bridge as the nonideal circuit. The conversion ratio, $M' = V'/V_g$, and the load parameter, $Q_s' = \omega_0 L_0/R'$, of the ideal circuit are related to $M_a = V_0/V_g$ and $Q_s = \omega_0 L_0/R$ of the nonideal circuit by

$$M' = M_a + \frac{V_{BD}}{V_g} = \frac{V_0 + V_{BD}}{V_g} \tag{3.109}$$

$$Q_s' = Q_s\left[1 - \frac{V_{BD}}{M'V_g}\right] \quad \text{or} \quad R' = \frac{R}{1 - V_{BD}/M'V_g} \tag{3.110}$$

The derivation of Eqs. (3.109) and (3.110) is the same as the derivation given in Sec. 2.4 for the parallel resonant converter and will not be

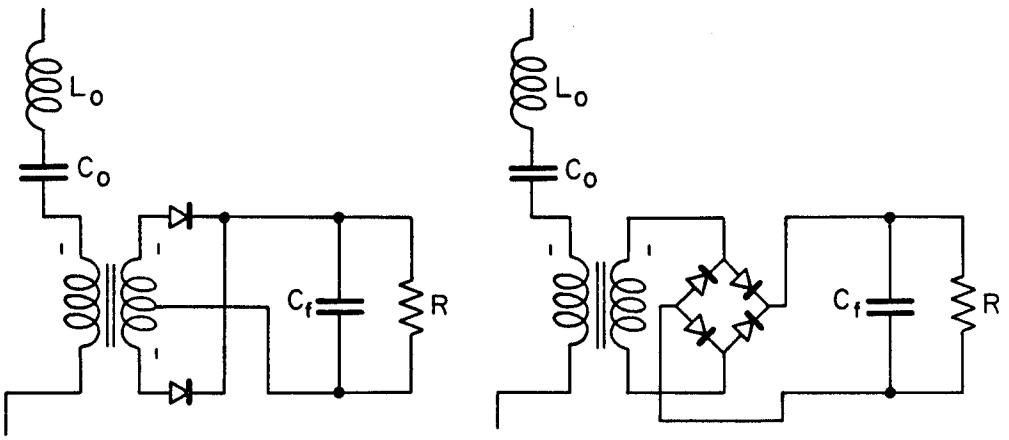

Fig. 3.27 Two methods of implementing the isolation transformer in the series resonant converter. a) Center-tapped and b) full-bridge.

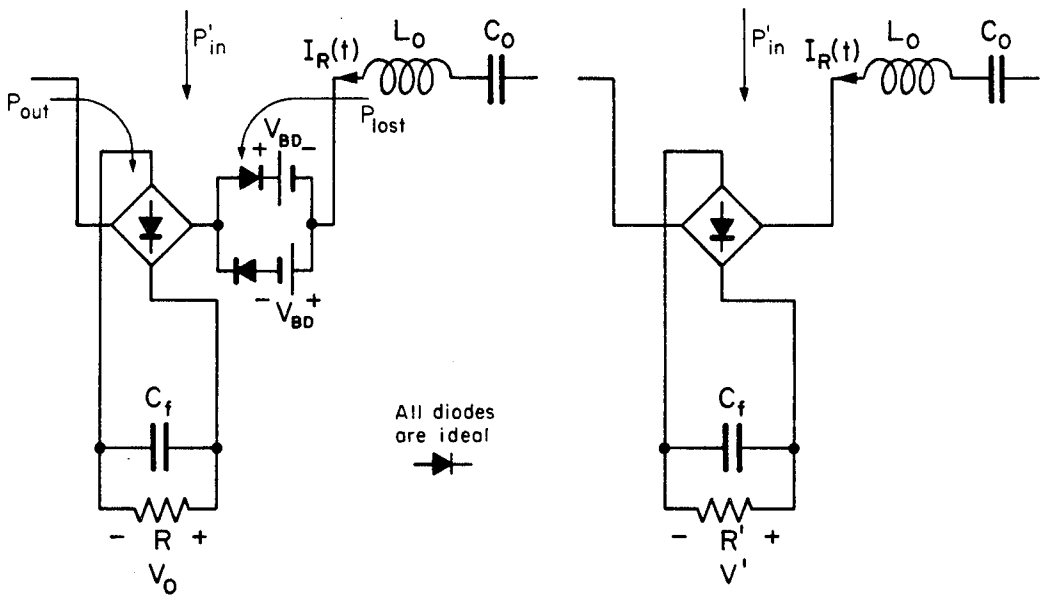

Fig. 3.28 a) Nonideal circuit with voltage drop V_{BD} in the output rectifiers and b) ideal circuit that delivers the same power P_{in}' as the nonideal circuit in a).

repeated here. According to Eq. (3.109) M' can be measured *directly* by measuring the voltage V_B at the input side of the bridge which is a square wave of amplitude $V_0 + V_{BD}$. For the parallel converter M', given by Eq. (2.41), cannot be measured directly. M' is determined from Eqs. (3.64), (3.88), and (3.91) in which K is modified to K' by

$$K' = K\left[1 - \frac{V_{BD}}{M'V_g}\right] = \left[1 - \frac{V_{BD}}{M'V_g}\right]\frac{Q_s\gamma}{2} \tag{3.111}$$

Since for odd type n dcm the conversion ratio is insensitive to the load and control parameters, Eq. (3.68) remains unchanged, and we have

$$M' = \frac{1}{n} \quad \text{or} \quad M_a = \frac{1}{n} - \frac{V_{BD}}{V_g} \tag{3.112}$$

Substitution of Eq. (3.111) in (3.64) gives for even type n dcm

$$M' = \frac{n}{K} + \frac{V_{BD}}{V_g} \quad \text{or} \quad M_a = \frac{n}{K} \tag{3.113}$$

Therefore, the actual conversion ratio for even type n dcm remains unchanged. In Appendix B.6 a numerical method for determining M' and M for continuous conduction mode is discussed. The modification in the boundaries between dcm and ccm are discussed by way of an example in the section on experimental results.

The efficiency due to the losses in the output rectifiers is the same as for all other converters and is given by

$$\eta_R = \frac{1}{1 + V_{BD}/V_0} \tag{3.114}$$

According to Eqs. (3.109) and (3.114) the η_R can be written as

$$\eta_R = 1 - \frac{V_{BD}}{M' V_g} \tag{3.115}$$

The actual conversion ratio can now be written as

$$M_a = \eta_R M' \tag{3.116}$$

Equation (3.115) is plotted in Fig. 3.29 for two different cases of V_{BD}/V_g and Q_s in the range $F_s/F_0 \geq 1/2$. The efficiency near the resonant peak is higher since M is larger near the peak. In a closed loop regulator, for a given output voltage requirement, the efficiency η_R is fixed and is given by Eq. (3.114). The curves shown in Fig. 3.29 do not suggest the converter should be operated near the resonant peak; all they show is the behavior of η_R for an open loop converter. The values of V_{BD}/V_g chosen for the series resonant converter are less than those of the parallel converter (Fig. 2.17) because in the useful range of the operation the conversion ratio of the parallel converter is greater than unity while that of the series resonant converter is always less than unity. Therefore, for a given V_0/V_g the series resonant converter requires a step-up transformer to match the conversion ratio of the parallel converter. Consequently, the reflected value of V_{BD}/V_g will be reduced by the step-up turns ratio. Since M is smaller for larger values of Q_s, the values of V_{BD}/V_g chosen for $Q_s = 10$ are smaller than those chosen for $Q_s = 3$. It should be noted that when the parallel resonant converter is excited well beyond resonance, or if Q_p is selected very small,

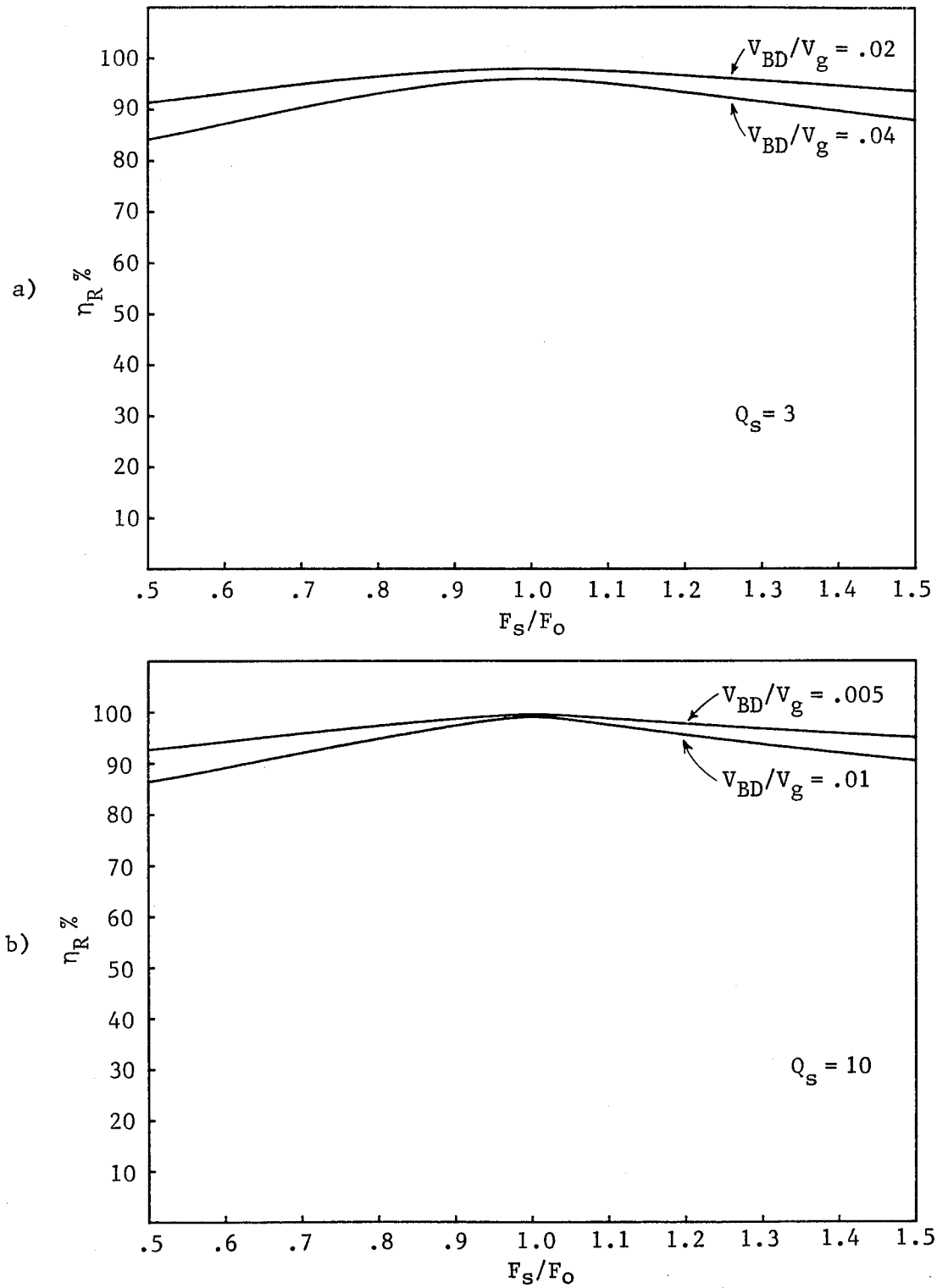

Fig. 3.29 a-b) Efficiency of the series resonant converter due to losses in the output rectifiers for two different values of V_{BD}/V_g and Q_s.

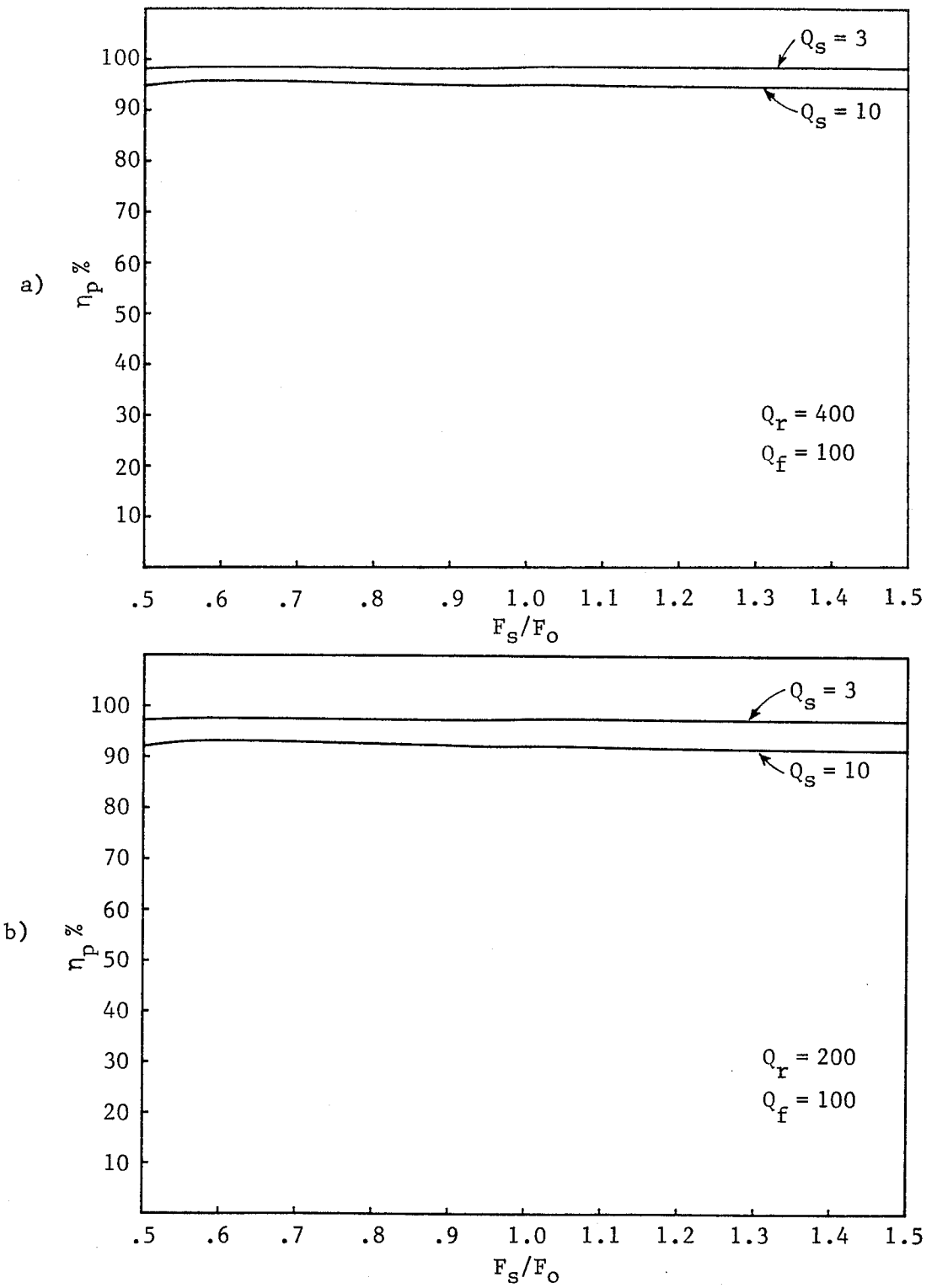

Fig. 3.30 Efficiency of the series resonant converter due to losses in the parasitic resistances. a) $Q_r = 400$ and $Q_f = 100$ and b) $Q_r = 200$ and $Q_f = 100$.

M will be less than unity as in the case of the series resonant converter, but since this type of operation is not useful, the choices of V_{BD}/V_g made were relevant.

The efficiency due to the losses in the parasitic resistances in the tank circuit and the output filter capacitor is given by

$$\eta_p = \frac{1}{1 + \frac{I_r^2}{I_0^2}\frac{r_r}{R} + \frac{I_c^2}{I_0^2}\frac{r_{C_f}}{R}} \tag{3.117}$$

where r_r is the total parasitic resistance in the tank circuit, r_{C_f} is esr of the output filter capacitor C_f, and I_r and I_c are the rms tank current and output capacitor current respectively. As explained earlier in Sec. 2.4, in the presence of the parasitic resistances, the ratios I_r/I_0 and I_c/I_0 are assumed to remain unchanged from the ideal conditions. In Appendix B.7 these rms values are determined and η_p is given by

$$\eta_p = \frac{1}{1 - \frac{Q_s}{Q_f} + \frac{D_r}{M^2 Q_s}\left[\frac{1}{Q_r} + \frac{1}{Q_f}\right]} \tag{3.118}$$

where D_r is given in Appendix B.7 and Q_f and Q_r are the normalized loss parameters defined as

$$Q_f = \frac{\omega_0 L_0}{r_{C_f}} \quad \text{and} \quad Q_r = \frac{\omega_0 L_0}{r_r} \tag{3.119}$$

Equation (3.118) is plotted in Fig. 3.30 for two different cases of Q_r , Q_f, and Q_s.

3.6 Experimental Results

The experimental circuit used is shown in Fig. 3.31. The isolation transformer is eliminated in order to avoid additional losses. The circuit parameters used for the verification of the conversion ratio characteristics are

$$V_g = 19.5V \quad L_0 = .197\text{mH} \quad C_0 = .051\mu\text{F} \quad F_0 = 50.21\text{kHz}$$

The conversion ratio for the various modes of operation is verified in the range $F_s/F_0 \geq 1/4$ as shown in Fig. 3.32a and b. The agreement between the predicted and measured results is generally good except near the resonant peaks at $F_s/F_0 = 1/3$ and $F_s/F_0 = 1$ for high Q_s where the effect of the parasitics is dominant. The only nonideality considered in obtaining the predicted characteristics is the voltage drop in the output rectifiers, which was taken to be .7V, i.e., $V_{BD} = 1.4$. Certainly, an analysis with all the parasitics considered (including core losses) will result in better agreement near the resonant peaks, however, such an analysis would be complicated and unnecessary because it is undesirable to operate this converter near the resonant peak.

Figure 3.33 shows predicted and measured voltage and current waveforms with the following circuit conditions

$$V_g = 19.5V \quad F_s/F_0 = .75 \quad Q_s = 1.94$$

The following table summarizes the results relevant to Fig. 3.33

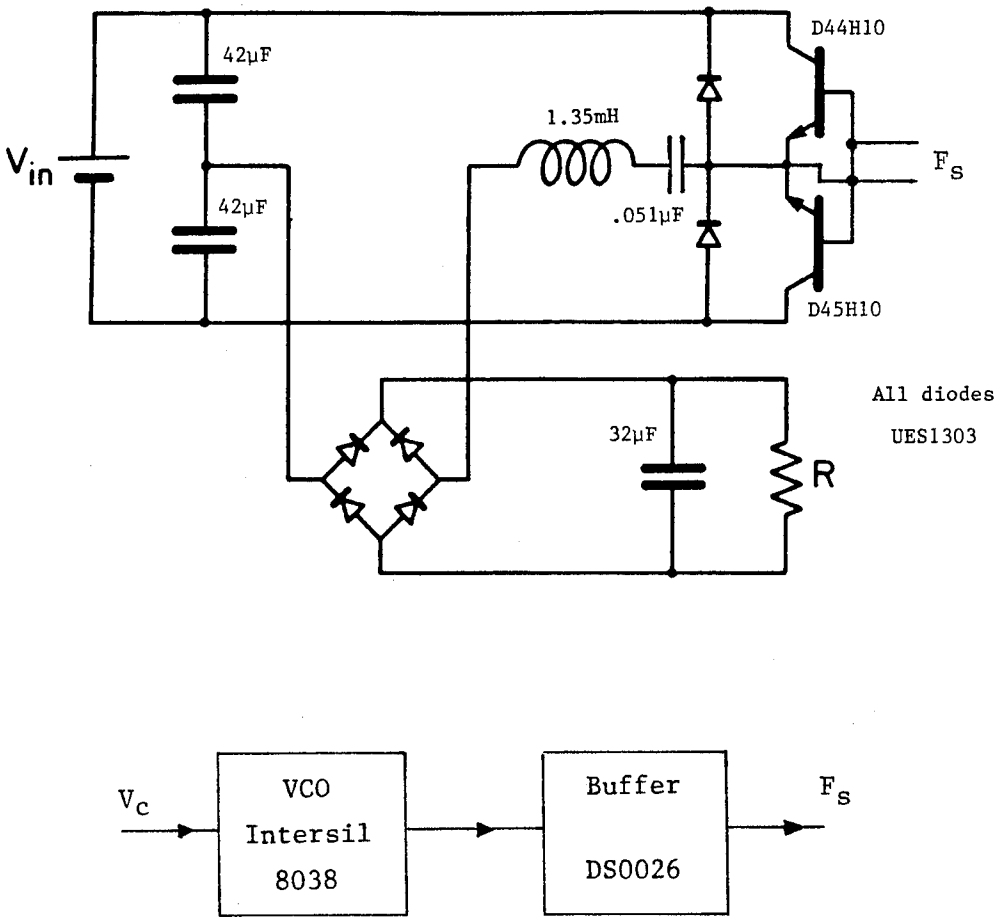

Fig. 3.31 Experimental circuit for the series resonant converter.

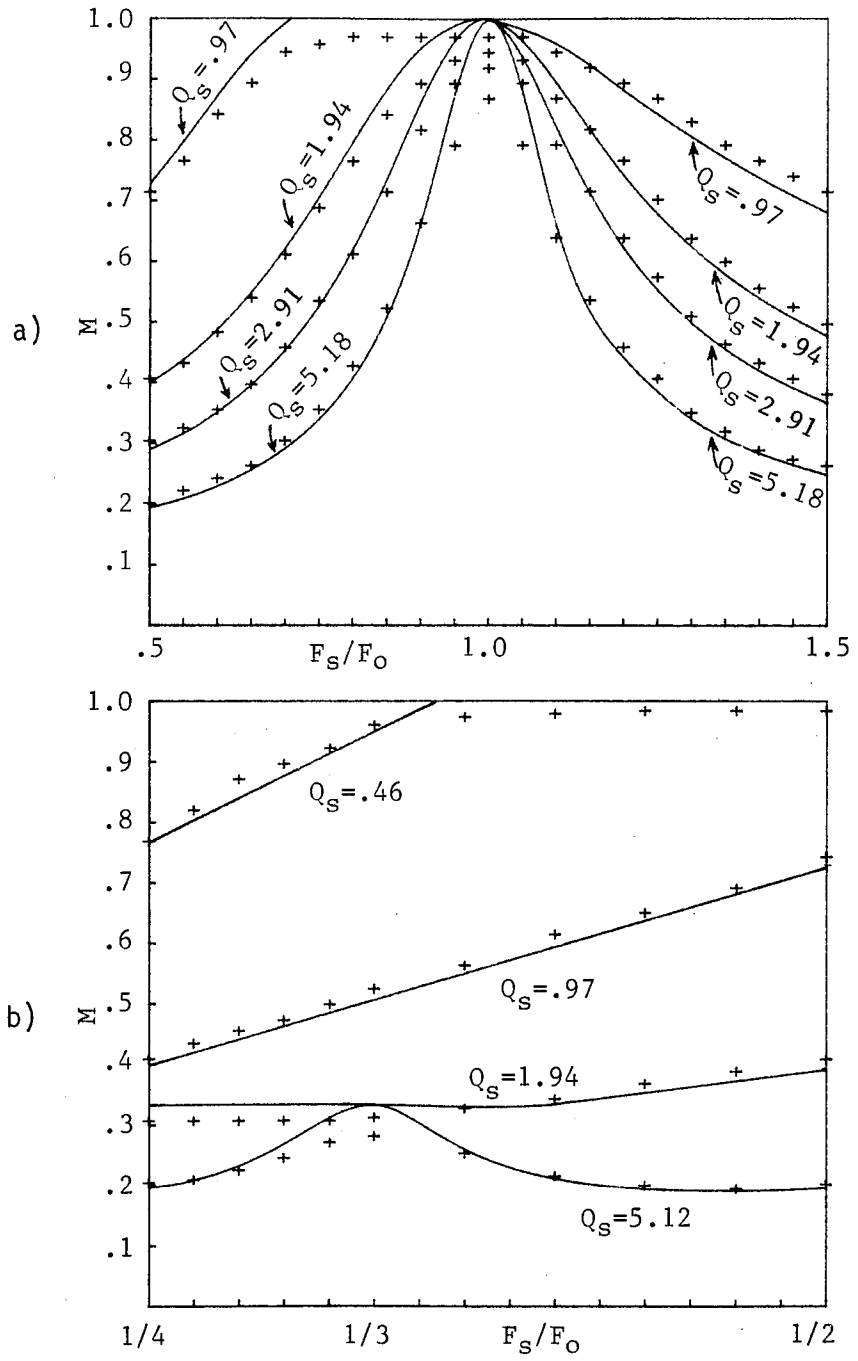

Fig. 3.32 a) Measured and predicted conversion ratio characteristics in the range $1/2 \leq F_s / F_0 \leq 1.5$ *and b) in the range* $1/4 \leq F_s / F_0 \leq 1/2$

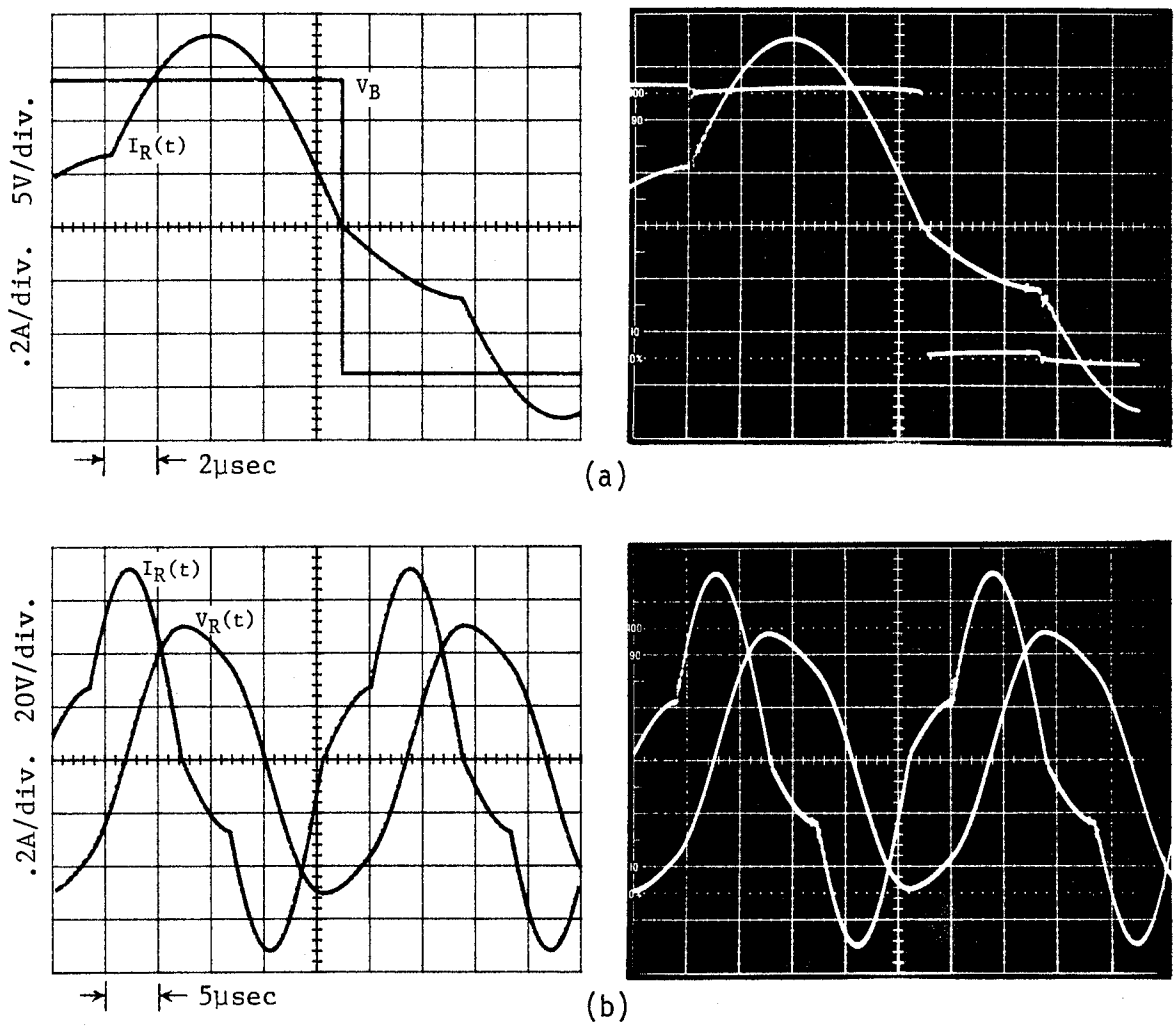

Fig. 3.33 Experimentally measured waveforms, left, and predicted waveforms, right, of the series resonant converter. a) The resonant current, $I_R(t)$, and the voltage, V_B, at the input side of the bridge. b) The resonant capacitor voltage and the resonant current. The circuit parameters are given in the text.

	Predicted	Measured
I_{peak}	.72A	.7A
V_{peak}	50.33V	49V
V_B	13.78V	13V
T_a	8.7μsec	8.9μsec

Figure 3.34 shows how the operation changes from one mode to another for a fixed value of F_s/F_0 as Q_s is varied. The boundaries between the various modes of operation are verified now by way of this example. The circuit parameters for the results in Fig. 3.34 are

$$V_g = 15V \quad F_s/F_0 = .42 \quad Q_s = .49, 1.94, \text{ and } 5.18$$

First, F_s/F_0 = .42 falls in the range

$$\frac{1}{n+1} \leq \frac{F_s}{F_0} \leq \frac{1}{n} \qquad n = 2$$

and consequently, the only allowed modes of operation are –type 2 ccm, type 2 dcm, and type 1 dcm. The occurrence of these modes is verified in Figs. 3.34 a-c. Now we will verify the conditions on Q_s for each of these modes to occur.

According to Eqs. (3.98a-b), –type 2 ccm occurs if

$$Q_s \geq \frac{F_s}{F_0}\frac{12}{\pi} = .42\,\frac{12}{\pi} = 1.6 \qquad (3.120)$$

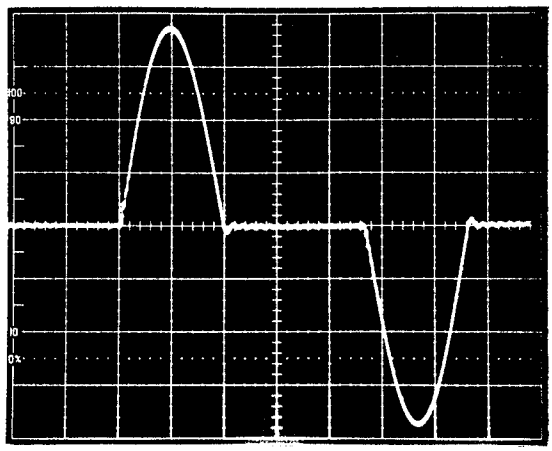

a) .1A/div. 5μsec/div.

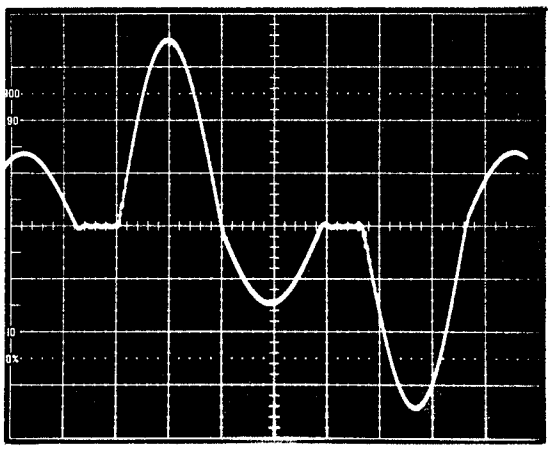

b) .1A/div. 5μsec/div.

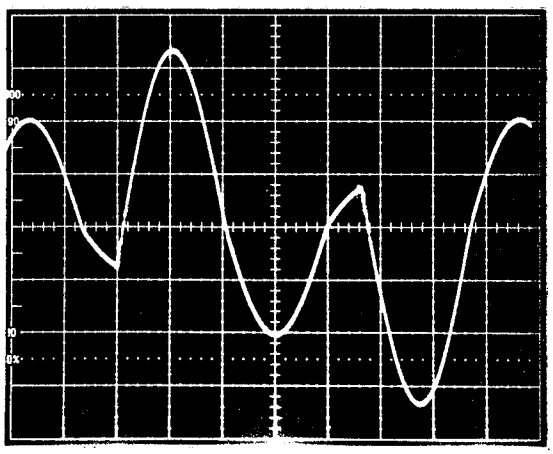

c) .1A/div. 5μsec/div.

Fig. 3.34 Experimental verification of the change of operation of the series resonant converter from a) type 1 dcm to b) type 2 dcm to c) –type 2 ccm as Q_s changes from .49 to 1.94 to 5.18 respectively at $F_s / F_0 = .42$.

If the voltage drop in the output rectifiers is to be considered, then Q_s must be modified according to Eq. (3.110)

$$Q_s' = Q_s\left[1 - \frac{V_{BD}}{M' V_g}\right] \tag{3.121}$$

The value of M' that must be used here is that of the boundary between –type 2 ccm and type 2 dcm which is simply $M' = 1/3$ and we have

$$Q_s' = Q_s\left[1 - \frac{2\times.7}{(1/3)(15)}\right] = Q_s(.72) \tag{3.122}$$

and the condition for –type 2 ccm to occur is modified to

$$Q_s' \geq 1.6 \quad \text{or} \quad Q_s \geq \frac{1.6}{.72} = 2.22 \tag{3.123}$$

Since $Q_s = 5.18$ satisfies this condition, the converter operates in –type 2 ccm for this value of Q_s as shown in Fig.3.34c.

Since $Q_s = 1.94$ does not satisfy the condition in (3.123), for this Q_s the converter operates discontinuous conduction mode. But which type of dcm?. From the value of $F_s/F_0 = .42$ the only two types of dcm possible are type 2 dcm and type 1 dcm. To find out which occurs for a given Q_s we refer to the boundaries between two discontinuous conduction modes discussed earlier in Sec. 3.4.3. According to (3.78) type 2 dcm occurs if

$$\frac{4}{\pi}\frac{F_s}{F_0} \leq Q_s \leq \frac{12}{\pi}\frac{F_s}{F_0} \quad ; \quad \frac{F_s}{F_0} < \frac{1}{2} \tag{3.124}$$

The upper bound of Q_s in (3.124) defines the boundary between –type 2 ccm and type 2 dcm which is in agreement with the condition in (3.120).

The lower bound in (3.124) gives the boundary between type 1 dcm and type 2 dcm. Substitution of $F_s/F_0 = .42$ in (3.124) gives

$$.535 \leq Q_s \leq 1.6 \tag{3.125}$$

If the voltage drop in the output rectifiers is taken into account, then (3.125) must be modified. The upper bound, which is the boundary between –type 2 ccm and type 2 dcm was modified earlier in (3.123). At the lower bound Q_s is modified according to Eq. (3.121), in which this time $M' = 1$ because at the boundary between type 2 dcm and type 1 dcm $M' = 1$. We then have

$$Q_s' = Q_s\left[1 - \frac{1.4}{(1)(15)}\right] = Q_s(.91) \tag{3.126}$$

and consequently, the condition in (3.125) is modified to

$$\frac{.535}{.91} \leq Q_s \leq \frac{1.6}{.72} \quad \text{or} \quad .59 \leq Q_s \leq 2.22 \tag{3.127}$$

$Q_s = 1.94$ satisfies the condition in (3.127) for type 2 dcm to occur which is verified in Fig. 3.34b. Finally, since $Q_s = .49 < .59$ type 1 dcm occurs for this value of Q_s as shown in Fig. 3.34a.

3.7 Conclusion

In this chapter a thorough dc analysis of the series resonant converter is given in terms of the normalized load parameter, Q_s, and the control parameter, F_s/F_0. The various modes of continuous and discontinuous conduction are identified and the conversion ratio in each mode of operation is determined. The boundaries between the various

modes of operation are determined by simple equations.

There are two general types of continuous conduction mode, namely, *+type n* ccm and *−type n* ccm for which the conversion ratio is determined numerically. There are, also, two general types of discontinuous conduction mode defined as *even type n* dcm and *odd type n* dcm. For the even type n dcm the conversion ratio is given by a simple equation which is a linear function of F_s/F_0 and R. Therefore, it is immediately seen that when operating in an even type n dcm the converter behaves as a *true current−fed* converter because the average output current is independent of the load R. The conversion ratio for the odd type n dcm is simply $M = 1/n$ which is *insensitive* to variations in the load and the control parameter.

The most useful range of continuous conduction mode is $1/2 \leq F_s/F_0 \leq 1$ because in this range the switches turn off naturally and the maximum value of M is unity. It is shown that in this range the converter behaves as a current fed converter only away from resonance and for values of Q_s larger than three or four. It is also shown that, in this range type 1 dcm can occur for which M becomes uncontrollable. Therefore, in order to avoid this type of discontinuous conduction mode, a simple boundary equation is given from which Q_s can be chosen properly.

According to the conversion ratio characteristics, this converter is not very well suited for applications that require very large load variations. Other steady-state quantities such as peak stress levels and diode conduction time are determined as well.

CHAPTER 4

SMALL-SIGNAL ANALYSIS OF RESONANT CONVERTERS

4.1 Introduction

This chapter discusses the small-signal response of resonant converters to perturbations in the switching frequency and the input voltage at a given operating point. For the series and parallel resonant converters, the operating point is determined from the dc analysis given in Chapters 2 and 3. In Sec. 4.2 the small-signal analysis of these converters is given only for operation in continuous conduction mode and in the range $F_s/F_0 \geq 1/2$. For the series resonant converter, it was shown if discontinuous conduction mode (type 1 dcm) occurs in the range $1/2 \leq F_s/F_0 \leq 1$, the output becomes uncontrollabe and hence a small-signal analysis would be useless. It was also shown that this type of discontinuity can be avoided in the entire range $1/2 \leq F_s/F_0 \leq 1$ if $Q_s \geq 4/\pi$ (Eq. (3.25a)). For the parallel resonant converter the occurrence of dcm was not analyzed although this mode can occur if Q_p is large enough because L_f/L_0 is finite. For the parallel converter dcm is ignored because it corresponds to very light load conditions. The various modes of operation that occur in the range $F_s/F_0 \leq 1/2$ are ignored as well because the most important range of operation of these converters is $1/2 \leq F_s/F_0 \leq 1$, however, the analysis given is also valid for $F_s/F_0 \geq 1$. The control-to-output transfer function is given in Sec. 4.2.1, the audio susceptibility is

given in Sec. 4.2.2, and the input impedance is given in Sec. 4.2.3. The experimental results given in Sec. 4.3 are in good agreement with the predictions of the analysis.

A block diagram of resonant converters for small-signal perturbations is shown below in Fig. 4.1.

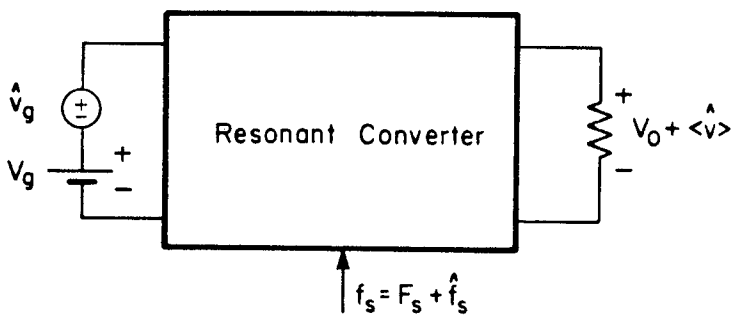

Fig. 4.1 Block diagram of a resonant converter with perturbations in the switching frequency and in the input voltage.

4.2 Analysis in Continuous Conduction Mode and in the Range $F_s/F_0 \geq 1/2$

In this section a systematic method of small-signal analysis of resonant converters in frequency control is outlined in detail. This method employs state-space analysis without the linear ripple approximation, since it is clear that such an approximation is not valid for resonant converters. In this analysis steady-state terms of the form e^{AT} are retained while perturbation terms of the form $e^{A\hat{t}}$, which arise from perturbations in the switching times, are linearized under small-signal assumption. This is summarized by the following equation

$$e^{At} = e^{A(T+\hat{t})} = e^{AT}e^{A\hat{t}} \approx e^{AT}[I + A\hat{t}] \quad ; \quad \hat{t} \ll \lambda_n^{-1}, T \tag{4.1}$$

where λ_n are the eigenvalues of A and T is the steady-state switching time. The justification of the linearization of the perturbation term in the last step, explained in Appendix C.1, requires that $\hat{t}$ be much smaller than T and the time constants of the circuit λ_n^{-1}. Since for resonant converters T cannot be assumed to be much smaller than the circuit time constants λ_n^{-1}, as in the case of PWM converters (buck, boost, Ćuk,...), the linear approximation of e^{AT} is not performed here [8].

Because of the symmetric operation of the circuit over an entire switching interval, as in the case of the dc analysis, the small-signal analysis is carried out over half the switching interval, T_s.

4.2.1 Control-to-output Transfer Function

In this section, the small-signal response of the series and parallel resonant converters to perturbations in the switching frequency is determined. If the switching frequency is perturbed by a small amount $\hat{f}_s(t)$, by injecting a control signal, $\hat{v}_c(t)$, in the voltage-controlled oscillator (VCO), then the switching time $\hat{t}_s(t)$ will be modulated by

$$\hat{t}_s(t) = -\frac{1}{2F_s^2}\hat{f}_s(t) = -\frac{1}{2F_s^2}K_m\hat{v}_c(t) \tag{4.2}$$

The switching interval, however, can only be considered on a *discrete* basis. This does not present a problem, and the connection between the continuous injected signal and the discrete perturbation in the switching interval will be explained presently. Consider the arbitrary switching interval shown in Fig. 4.2a

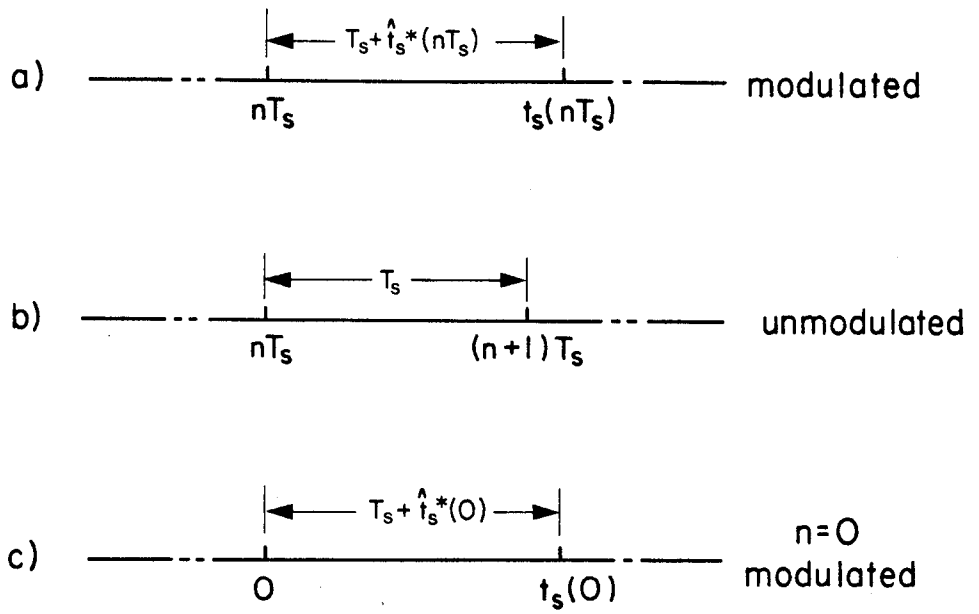

Fig. 4.2 a) An arbitrary modulated switching interval. b) An arbitrary unmodulated switching interval. c) A modulated interval for $n = 0$.

$$nT_s \le t \le t_s(nT_s) \tag{4.3}$$

In the absence of any modulation, as shown in Fig. 4.2b, this interval is given by

$$nT_s \le t \le (n+1)T_s \tag{4.4}$$

In the presence of modulation, the perturbation in the duration of this interval is denoted by $\hat{t}_s{}^*(nT_s)$ and (4.3) is written as

$$nT_s \le t \le (n+1)T_s + \hat{t}_s{}^*(nT_s) \tag{4.5}$$

The time $t_s(nT_s)$ can be summarized by the following equation

$$t_s(nT_s) = \begin{cases} (n+1)T_s & \text{unmodulated} \\ (n+1)T_s + \hat{t}_s{}^*(nT_s) & \text{modulated} \end{cases} \tag{4.6a-b}$$

The discrete perturbation $\hat{t}_s{}^*(nT_s)$ in the switching time is now related to the continuous control signal by

$$\hat{t}_s{}^*(nT_s) = \hat{t}_s(t)\,\delta(t - nT_s) \tag{4.7a}$$

$$= -\frac{\hat{f}_s(t)}{2F_s^2}\delta(t - nT_s) \tag{4.7b}$$

In addition to the switching interval, the output-network switching time, T_a, is modulated as well. In the parallel resonant converter t_a is determined by the zero-crossing of the resonant capacitor voltage while in the series resonant converter t_a is determined by the zero crossing of the resonant current. Since in the presence of modulation these states are

modulated, it follows that the zero-crossing times determined by these states are modulated as well. The perturbation in the zero-crossing time is denoted by $\hat{t}_a^*(nT_s)$ and is considered to be a sampled point of a continuous function $\hat{t}_a(t)$

$$\hat{t}_a^*(nT_s) = \hat{t}_a(t)\,\delta(t-nT_s) \tag{4.8}$$

The switching time $t_a(nT_s)$, inside the interval in (4.3), is given by

$$t_a(nT_s) = nT_s + T_a + \hat{t}_a^*(nT_s) \tag{4.9}$$

Whereas $\hat{t}_s(t)$ is a continuous function that can be related *directly* to the measurable quantity $\hat{v}_c(t)$, $\hat{t}_a(t)$ is just a continuous function with no such physical significance. In step v, the unknown modulation $\hat{t}_a(t)$ is determined in terms of the perturbations in the state vector from a certain constraint.

For conciseness and without loss of generality we let $n=0$ in (4.3) through (4.9). The resonant current waveform for the series resonant converter and the perturbations in the switching times t_s and t_a in the interval $0 \le t \le t_s(0)$ are shown in Fig. 4.3. A similar figure for the parallel resonant converter applies with the resonant current replaced by the resonant capacitor voltage since in this case it is the capacitor voltage that determines the output-network switching time t_a. To simplify the notation further, whenever possible, t_s and t_a will be used instead of $t_s(0)$ and $t_a(0)$.

In what follows the steps of the small-signal analysis are outlined in detail.

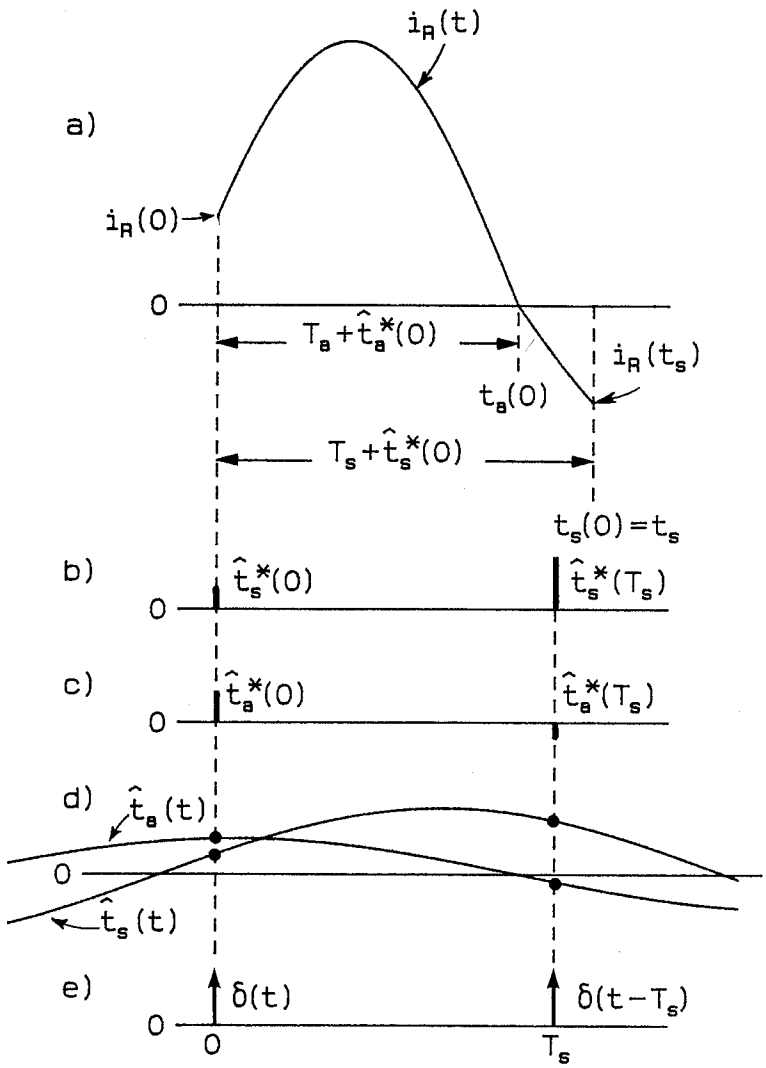

Fig. 4.3 a) The resonant current $i_R(t)$ in the modulated interval $0 \le t \le t_s(0)$. b) The perturbations $\hat{t}_s^*(0)$ in the switching interval and the perturbation $\hat{t}_a^*(0)$ in the zero-crossing time. c) The continuous functions $\hat{t}_s(t)$ and $\hat{t}_a(t)$ which when sampled at $t = nT_s$ give the perturbations in the switching interval $nT_s \le t \le t_s(nT_s)$ and the zero-crossing time $t_a(nT_s)$ in that interval respectively.

i) State Equations

The two switched networks of the series and parallel resonant converters over half the switching interval are shown in Fig. 4.4. For the series resonant converter the sequence of switched networks shown is for the range of operation $1/2 \leq F_s/F_0 \leq 1$, and is reversed in the range $F_s/F_0 \geq 1$, but for the parallel resonant converter the sequence remains the same for all $F_s/F_0 \geq 1/2$. According to Fig. 4.4a the state equations in the interval $0 \leq t \leq t_a$ are

$$\dot{x}(t) = A_1 x(t) + b_1 V_g \tag{4.10}$$

$$v(t) = c_1^T x(t) \tag{4.11}$$

where for the series resonant converter the matrix A_1 and the vectors $x(t)$, b_1 and c_1^T are given by

$$x^T(t) = [i_R(t) \;\; v_R(t) \;\; v_{C_f}(t)]$$

$$A_1 = \begin{bmatrix} -(R \| r_{C_f} + r_0)\dfrac{1}{L_0} & -\dfrac{1}{L_0} & -\dfrac{1}{L_0}\dfrac{1}{1+r_{C_f}/R} \\ \dfrac{1}{C_0} & 0 & 0 \\ \dfrac{1}{C_f}\dfrac{1}{1+r_{C_f}/R} & 0 & -\dfrac{1}{C_f}\dfrac{1}{R+r_{C_f}} \end{bmatrix} \tag{4.12}$$

$$b_1^T = [1/L_0 \;\; 0 \;\; 0] \tag{4.13}$$

$$c_1^T = [R \| r_{C_f} \;\; 0 \;\; 1/(1+r_{C_f}/R)] \tag{4.14}$$

For the parallel resonant converter these are given by

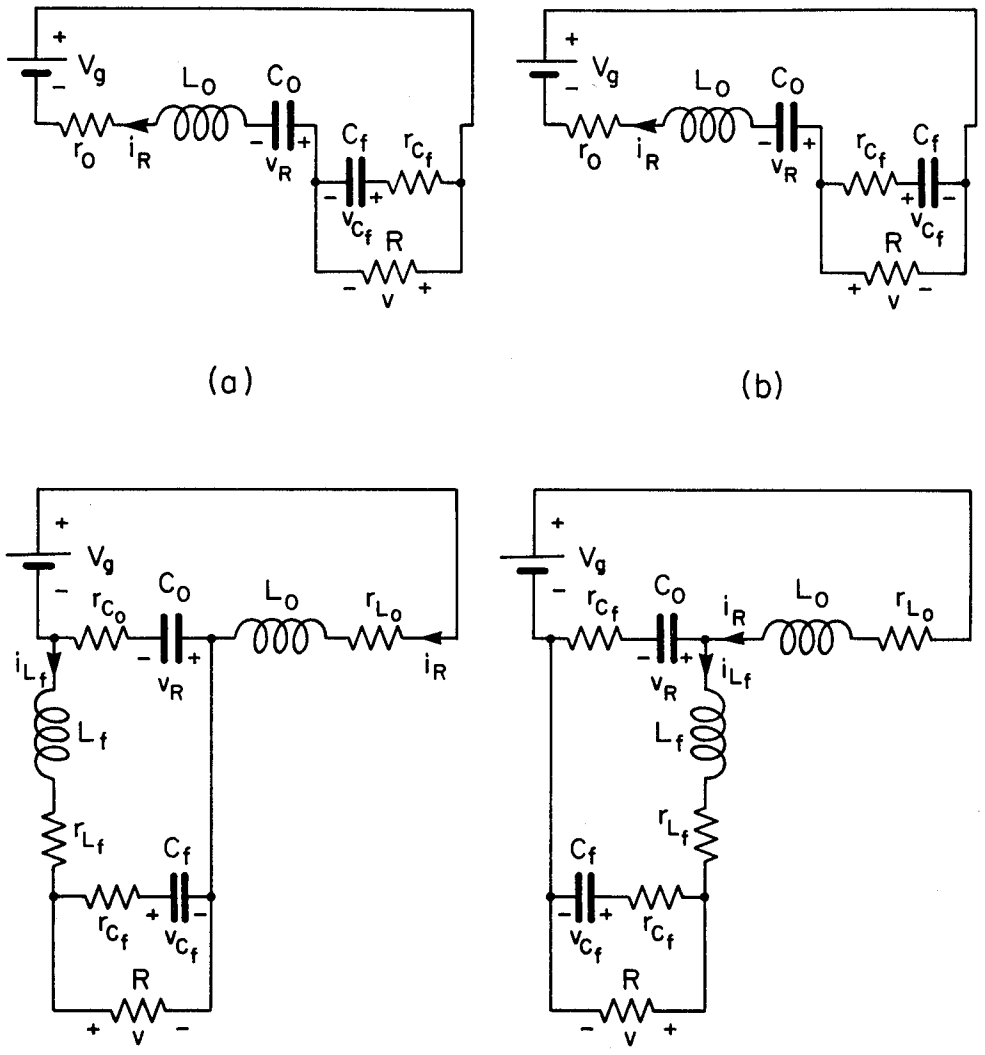

Fig. 4.4 The two switched networks for the series and the parallel resonant converters a) during $0 \le t \le t_a$ and b) during $t_a \le t \le t_s$.

$$x^T = [i_R(t)\ \ v_R(t)\ \ i_{L_f}(t)\ \ v_{C_f}(t)]$$

$$A_1 = \begin{bmatrix} -\frac{(r_{L_0}+r_{C_0})}{L_0} & -\frac{1}{L_0} & -\frac{r_{C_0}}{L_0} & 0 \\ \frac{1}{C_0} & 0 & \frac{1}{C_0} & 0 \\ -\frac{r_{C_0}}{L_f} & -\frac{1}{L_f} & -(r_{L_f}+r_{C_0}+r_{C_f}\|R)\frac{1}{L_f} & -\frac{1}{L_f}\frac{R}{R+r_{C_f}} \\ 0 & 0 & \frac{R}{R+r_{C_f}}\frac{1}{C_f} & -\frac{1}{(R+r_{C_f})C_f} \end{bmatrix}$$

$$b_1^T = [1/L_0\ \ 0\ \ 0\ \ 0] \tag{4.16}$$

$$c_1^T = [0\ \ 0\ \ R\|r_{C_f}\ \ \ 1/(1+r_{C_f}/R)] \tag{4.17}$$

The solution of Eq. (4.10), with the assumption that V_g is constant, is given from linear system theory by

$$x(t) = e^{A_1 t}x(0) + B_1(t)b_1V_g \tag{4.18}$$

where the matrix $B_1(t)$ is given by

$$B_1(t) = \int_0^t e^{A_1(t-\tau)}d\tau = A_1^{-1}[e^{A_1 t} - I] \tag{4.19}$$

According to Fig. 4.4b, the corresponding expressions for the series resonant converter in the interval $t_a \le t \le t_s$ are

$$A_2 = \begin{bmatrix} -(R \| r_{C_f} + r_0)\frac{1}{L_0} & -\frac{1}{L_0} & \frac{1}{L_0}\frac{1}{1+r_{C_f}/R} \\ \frac{1}{C_0} & 0 & 0 \\ -\frac{1}{C_f}\frac{1}{1+r_{C_f}/R} & 0 & -\frac{1}{C_f}\frac{1}{R+r_{C_f}} \end{bmatrix} \tag{4.20}$$

$$b_2 = b_1 \quad ; \quad c_2^T = [-R \| r_{C_f} \;\; 0 \;\; 1/(1+r_{C_f}/R)] \tag{4.21}$$

For the parallel resonant converter these are given by

$$A_2 = \begin{bmatrix} -\frac{(r_{L_0}+r_{C_0})}{L_0} & -\frac{1}{L_0} & \frac{r_{C_0}}{L_0} & 0 \\ \frac{1}{C_0} & 0 & -\frac{1}{C_0} & 0 \\ \frac{r_{C_0}}{L_f} & \frac{1}{L_f} & -(r_{L_f}+r_{C_0}+r_{C_f} \| R)\frac{1}{L_f} & -\frac{1}{L_f}\frac{R}{R+r_{C_f}} \\ 0 & 0 & \frac{R}{R+r_{C_f}}\frac{1}{C_f} & -\frac{1}{(R+r_{C_f})C_f} \end{bmatrix}$$

$$b_2 = b_1 \quad ; \quad c_2^T = c_1^T \tag{4.23}$$

The solution in this interval is given by

$$x(t) = e^{A_2(t-t_a)}x(t_a) + B_2(t-t_a)bV_g \tag{4.24}$$

where the matrix $B_2(t)$ is given by

$$B_2(t-t_a) = \int_{t_a}^{t} e^{A_2(t-\tau)}d\tau = A_2^{-1}[e^{A_2(t-t_a)} - I] \tag{4.25}$$

The evolution of the state vector $x(t)$ over the interval $0 \le t \le t_s$ is obtained by matching the solutions given by Eqs. (4.18) and (4.24) at $t = t_a$. This gives

$$x(t_s) = A\,x(0) + BbV_g \tag{4.26}$$

where the matrices A and B are given by

$$A = e^{A_2(t_s - t_a)}\,e^{A_1 t_a} \tag{4.27}$$

$$B = e^{A_2(t_s - t_a)}\,B_1(t_a) + B_2(t_s - t_a) \tag{4.28}$$

ii) State–Space Averaging

When the system is not perturbed or modulated, the output voltage consists of a dc component and a ripple with a fundamental at twice the switching frequency. Let the steady-state output voltage be denoted by $V(t)$ and defined as follows

$$V(t) \equiv \textit{Steady-state or unmodulated output voltage}$$

This is a periodic waveform of period T_s and is shown in Fig. 4.5a in a thin line. The spectrum of $V(t)$, which consists of a dc component and other harmonics at $2nF_s$, is shown in Fig. 4.6a. The dc component, which is the average output voltage, is determined from the dc analysis discussed in Chapters 2 and 3, and is simply given by

$$V_0 = MV_g \tag{4.29}$$

This can also be written in terms of $V(t)$ as

$$V_0 = \frac{1}{T_s}\int_{nT_s}^{(n+1)T_s} V(t)dt \tag{4.30}$$

V_0 is a constant throughout all the intervals and is shown in Fig. 4.5a with

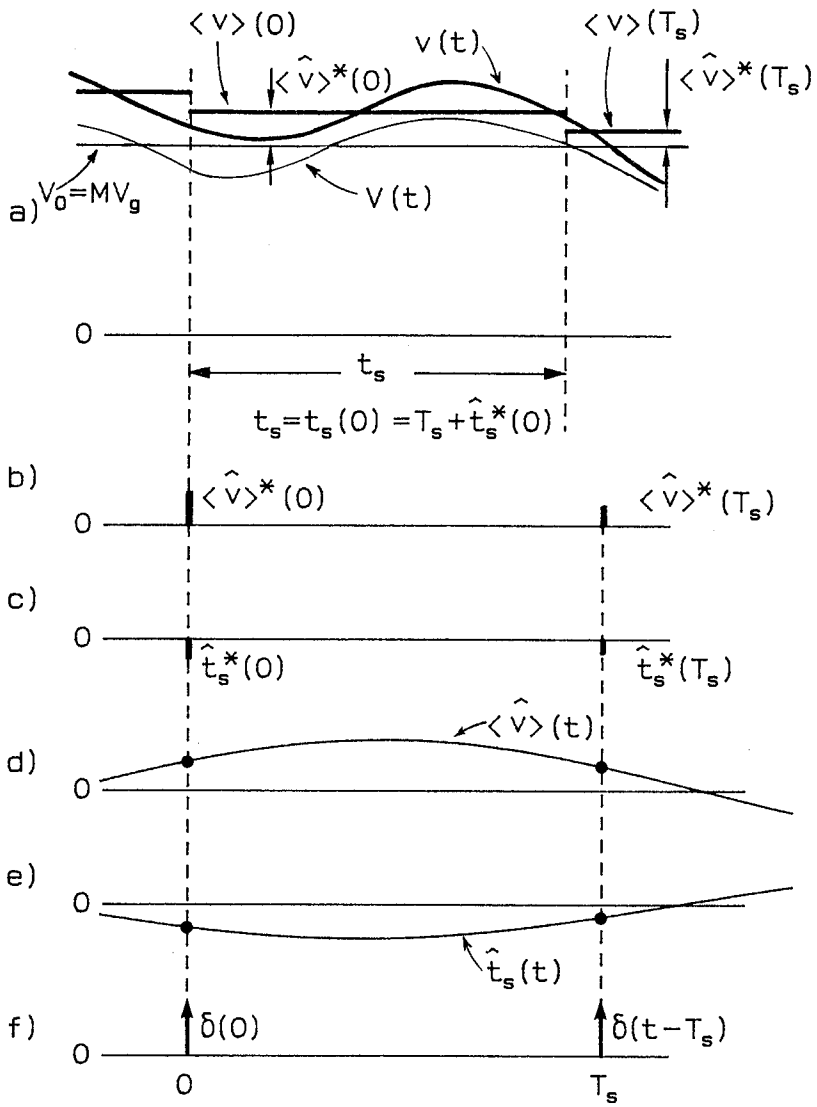

Fig. 4.5 *a) The steady-state or unmodulated output voltage, $V(t)$, and its average value, V_0, are shown in thin lines. The modulated output voltage, $v(t)$, and its average, $\langle v\rangle(nT_s)$, in each interval in the presence of modulation are shown in thick lines. b) Perturbations in the average output voltage, $\langle\hat{v}\rangle^*(nT_s)$, in each interval are shown as sampled points of a continuous function d) $\langle\hat{v}\rangle(t)$ which is the component in the output voltage that has the same frequency as the modulating signal.*

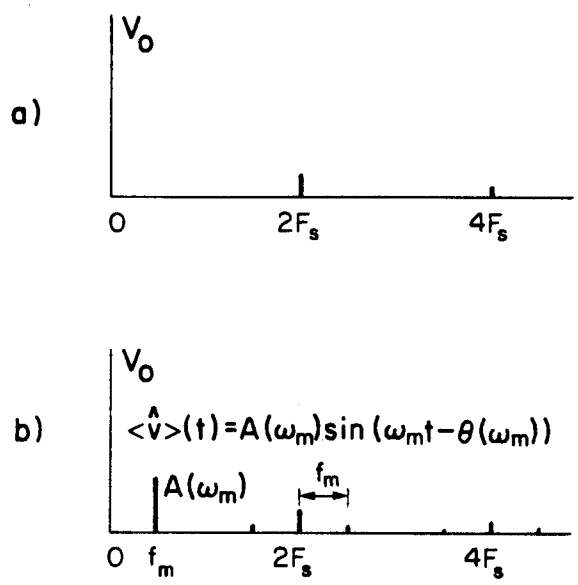

Fig. 4.6 a) The spectrum of the unmodulated or steady-state output voltage, $V(t)$, and b) the spectrum of the modulated output voltage, $v(t)$.

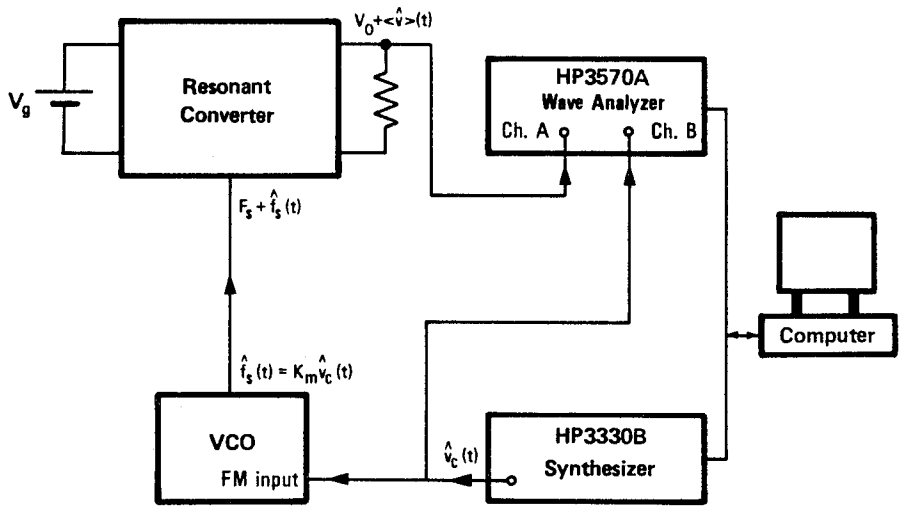

Fig. 4.7 Experimental method of determining the control-to-output transfer function.

a thin straight line.

Let the switching frequency be modulated now by a small amount $\hat{f}_s(t) = \varepsilon \sin\omega_m t$

$$f_s(t) = F_s + \hat{f}_s(t) \tag{4.31}$$

The output voltage, which is a modulated signal now, is denoted by $v(t)$ and defined as follows

$$v(t) \equiv \textit{Modulated output voltage}$$

This is shown in Fig. 4.5a with a thick line, and is no longer a periodic waveform. The spectrum of $v(t)$ is shown in Fig. 4.6b and it consists of, in addition to the dc component and the harmonics of twice the switching frequency, a sideband accompanying the zero frequency component and sidebands around each harmonic. Strictly speaking, $v(t)$ is a demodulated signal since the harmonics of the carrier and their sidebands are well suppressed because of the small ripple requirement on the output. The only component in this spectrum that is of interest to us is the sideband accompanying the zero frequency component because it is the only component which has the same frequency, ω_m, as the modulating signal. This sideband is denoted by $\widehat{<v>}(t)$ and is defined as follows

$$\widehat{<v>}(t) \equiv \textit{Sideband accompanying the zero frequency component of the output voltage which has the same frequency as the modulating signal.}$$

The experimental method used to verify the small-signal transfer functions [9] is shown in Fig. 4.7. At the output, the analyzer searches for that signal which has the same frequency as the injected signal. In other words the transfer function that can be verified experimentally is

$$\frac{\langle\hat{v}\rangle(s)}{\hat{v}_c(s)} = \frac{\langle\hat{v}\rangle(s)}{\hat{f}_s(s)}\frac{\hat{f}_s(s)}{\hat{v}_c(s)} \tag{4.32a}$$

$$= K_m \frac{\langle\hat{v}\rangle(s)}{\hat{f}_s(s)} \tag{4.32b}$$

Our goal, then, is to determine $\langle\hat{v}\rangle(t)$. To do this, first, the average output voltage in *each* interval is determined in the presence of modulation

$$\langle v\rangle(nT_s) = \frac{1}{t_s(nT_s) - nT_s}\int_{nT_s}^{t_s(nT_s)} v(t)dt \tag{4.33}$$

In steady state, this reduces to Eq. (4.30). In the presence of modulation, in each interval, $\langle v\rangle(nT_s)$ differs from V_0 by an amount $\langle\hat{v}\rangle^*(nT_s)$

$$\langle v\rangle(nT_s) = V_0 + \langle\hat{v}\rangle^*(nT_s) \tag{4.34}$$

In Fig. 4.5a, $\langle v\rangle(nT_s)$ is shown in each interval ($n = -1, 0, 1$) by a thick straight line, and the perturbation $\langle\hat{v}\rangle^*(nT_s)$ in each interval is shown in Fig. 4.5b as a sampled data point of the continuous function $\langle\hat{v}\rangle(t)$

$$\langle\hat{v}\rangle^*(nT_s) = \langle\hat{v}\rangle(t)\,\delta(t - nT_s) \tag{4.35}$$

It is, therefore, proposed that $\langle\hat{v}\rangle(t)$, the component of interest to us, be determined from a knowledge of the perturbation in the average output voltage, $\langle\hat{v}\rangle^*(nT_s)$, in each interval. Since the sampled points $\langle\hat{v}\rangle^*(nT_s)$

are spaced at intervals corresponding to twice the switching frequency, $\widehat{<v>}(t)$ can be determined for modulating frequencies reaching near the switching frequency.

Our first task, then, is to determine $<v>(nT_s)$ in Eq. (4.33). Again, without loss of generality, we let $n=0$, so that Eq. (4.33) becomes

$$<v>(0) = \frac{1}{t_s}\left[\int_0^{t_a} c_1^T x(t)dt + \int_{t_a}^{t_s} c_2^T x(t)dt\right] \tag{4.36}$$

This integration is carried out by substituting $x(t)$ from Eqs. (4.18) and (4.24) in the proper appropriate integrands. The result is

$$t_s<v>(0) = c^T x(0) + d^T b V_g \tag{4.37}$$

where the vectors c^T and d^T are given by

$$c^T = c_1^T B_1(t_a) + c_2^T B_2(t_s - t_a)e^{A_1 t_a} \tag{4.38}$$

$$d^T = c_1^T B_1(t_a)A_1^{-1} + c_2^T B_2(t_s - t_a)[B_1(t_a) + A_2^{-1}]$$

$$-c_1^T A_1^{-1} t_a - c_2^T A_2^{-1}(t_s - t_a) \tag{4.39}$$

Equation (4.37) is the statement of state-space averaging, according to which the average output voltage in *each* interval is expressed as a *linear* combination of the states at the beginning of that interval.

iii) Perturbations in $<v>(0)$, $x(0)$, and $x(T_s)$

In the presence of modulation, the switching times $t_s(0)$ and $t_a(0)$ (or t_s and t_a) are perturbed according to Eqs. (4.5) and (4.9)

$$t_s = T_s + \hat{t}_s{}^*(0) = T_s + \hat{t}_s \tag{4.40a}$$

$$t_a = T_a + \hat{t}_a{}^*(0) = T_a + \hat{t}_a \tag{4.40b}$$

When these are substituted in Eq. (4.37), in which the average output voltage in each interval is perturbed by $\langle\hat{v}\rangle^*(nT_s)$, the following is obtained

$$[V_0 + \langle\hat{v}\rangle^*(0)][T_s + \hat{t}_s{}^*(0)] = [c^T + \hat{c}^T][X(0) + \hat{x}^*(0)] + [d^T + \hat{d}^T]bV_g \tag{4.41}$$

The linearization of this equation will be discussed shortly. It is clear from Eq. (4.41) that the dynamics of $\langle\hat{v}\rangle^*(nT_s)$ depends on the dynamics of $\hat{x}^*(nT_s)$, which is pursued next.

The state vector at $t = 0$ is perturbed as follows

$$x(0) = X(0) + \hat{x}^*(0) \tag{4.42}$$

At $t = T_s$, since $i_R(T_s) = -i_R(0)$ and $v_R(T_s) = -v_R(0)$, these states will be perturbed as follows

$$i_R(T_s) = I_R(T_s) - \hat{i}_R{}^*(T_s) \tag{4.43a}$$

$$v_R(T_s) = V_R(T_s) - \hat{v}_R{}^*(T_s) \tag{4.43b}$$

The output capacitor and inductor states, on the other hand, are perturbed as usual

$$i_{L_f}(T_s) = I_{L_f}(T_s) + \hat{i}_{L_f}{}^*(T_s) \tag{4.43c}$$

$$v_{C_f}(T_s) = V_{C_f}(T_s) + \hat{v}_{C_f}{}^*(T_s) \tag{4.43d}$$

Equations (4.43) can be summarized by

$$x(T_s) = X(T_s) + M_r \hat{x}^*(T_s) \tag{4.44}$$

where the matrix M_r for the series resonant converter is given by

$$M_r = \begin{bmatrix} -1 & 0 & 0 \\ 0 & -1 & 0 \\ 0 & 0 & 1 \end{bmatrix} \tag{4.45a}$$

and for the parallel converter it is given by

$$M_r = \begin{bmatrix} -1 & 0 & 0 & 0 \\ 0 & -1 & 0 & 0 \\ 0 & 0 & 1 & 0 \\ 0 & 0 & 0 & 1 \end{bmatrix} \tag{4.45b}$$

It should be noted that, instead of writing $x(T_s)$ and $\hat{x}^*(T_s)$ in Eq. (4.44), one should actually write $x(t_s)$ and $\hat{x}^*(t_s)$, but expanding around T_s we get

$$x(t_s) = x(T_s + \hat{t}_s) = x(T_s) + \frac{\partial x}{\partial \hat{t}_s}\hat{t}_s + \cdots \tag{4.46}$$

Since the second term represents a product of two perturbations, it is ignored and thus

$$x(t_s) \approx x(T_s) \quad \text{and} \quad \hat{x}^*(t_s) \approx \hat{x}^*(T_s) \tag{4.47}$$

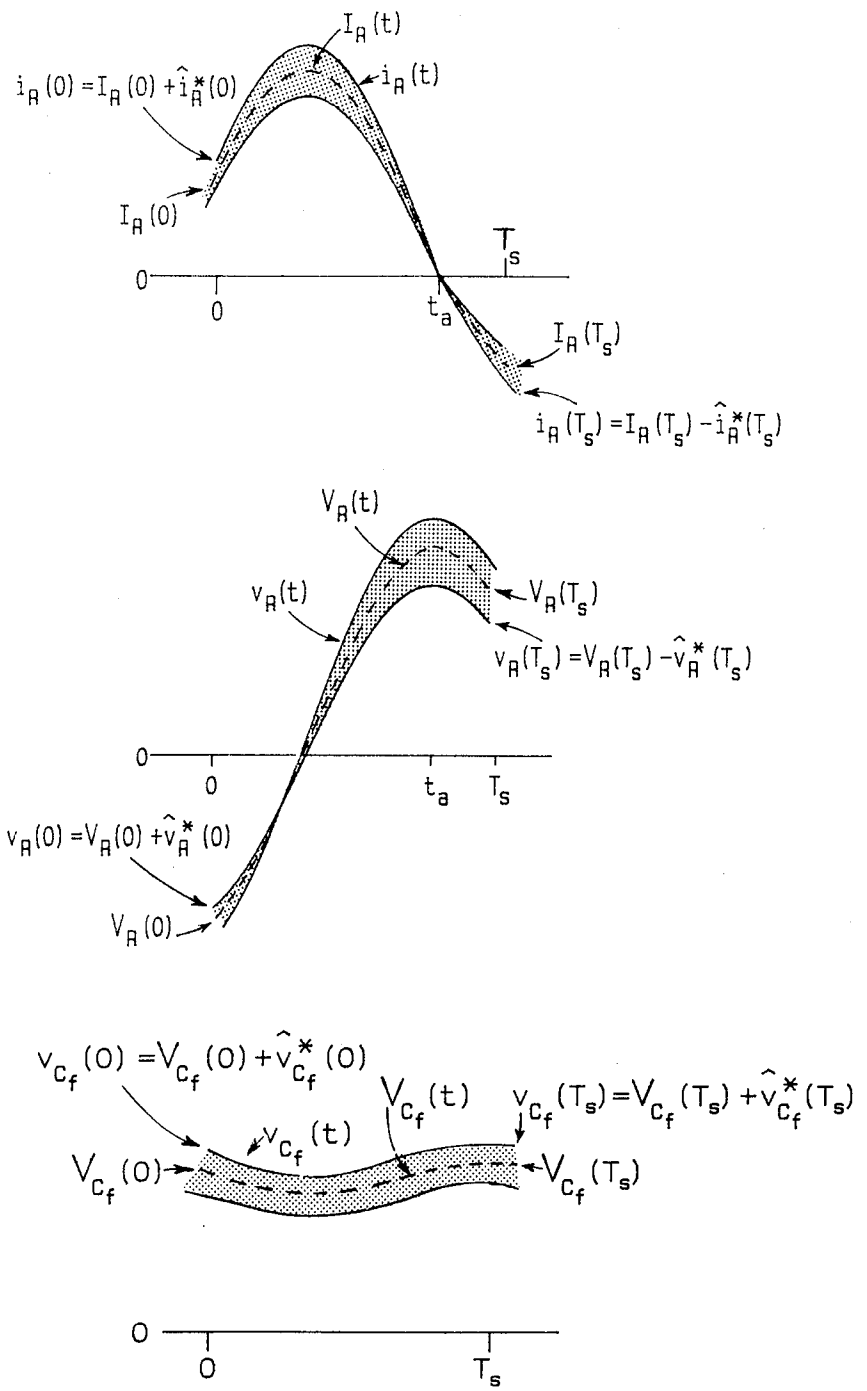

Fig. 4.8 The modulated components of the state vector $x(t)$ of the series resonant converter. The steady-state components are shown in dotted lines inside the envelope of modulation. a) The resonant current, b) the resonant capacitor voltage, and c) the output capacitor voltage.

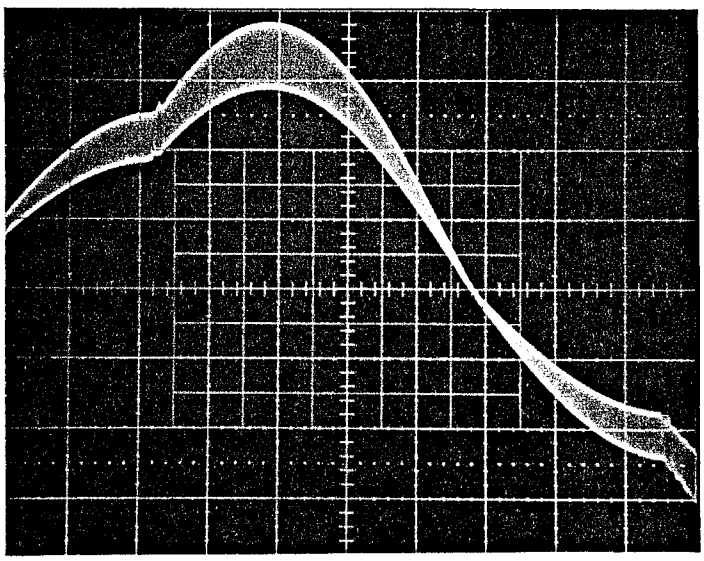

Fig. 4.9 The envelope of the resonant current of the series resonant converter due to modulations in the switching frequency. The triggering level is set such that all the zero-crossings at $t=t_a$ are coincident.

The modulated components of the state vector $x(t)$ for the series resonant converter are shown in Fig. 4.8. The shaded areas represent the envelope of modulation in which the steady-state or unmodulated waveforms are shown in dashed lines. An oscillogram of the envelope of modulation of the resonant current of the series converter, with the trigger adjusted such that all the zero-crossings are coincident, is shown in Fig. 4.9.

Now, when the perturbations in t_s, t_a, $x(0)$ and $x(t_s)$ are substituted in the equation of the evolution of the state vector given by Eq. (4.26), the following is obtained

$$M_T\hat{x}^*(T_s)+X(T_s) = [A+\hat{A}][X(0)+\hat{x}^*(0)] + [B+\hat{B}]bV_g \qquad (4.48)$$

iv) Linearization

Equations (4.41) and (4.48) are now linearized under small-signal assumption using Eq. (4.1). As an example of this linearization, consider the matrix $[A+\hat{A}]$ in Eq. (4.48)

$$A + \hat{A} = e^{A_2(T_s-T_a)}\underbrace{e^{A_2(\hat{t}_s-\hat{t}_a)}}_{\text{linearize}}e^{A_1\hat{t}_a}e^{A_1T_a} \qquad (4.49)$$

The perturbation terms are linearized according to Eq. (4.1) as follows

$$e^{A_2(\hat{t}_s-\hat{t}_a)}e^{A_1\hat{t}_a} \approx [I + A_2(\hat{t}_s-\hat{t}_a)][I + A_1\hat{t}_a]$$

$$\approx I + A_2(\hat{t}_s-\hat{t}_a) + A_1\hat{t}_a \qquad (4.51)$$

where the second line is obtained by neglecting products of two perturbation terms. When Eq. (4.51) is substituted in the Eq. (4.49), the

following is obtained

$$\hat{A} = A_2 A \hat{t}_s + (AA_1 - A_2 A)\hat{t}_a \tag{4.52}$$

where the matrix A is given by

$$A = e^{A_2(T_s - T_a)} e^{A_1 T_a} \tag{4.53}$$

Following the same procedure on the remaining terms in Eq. (4.48), cancelling dc terms, and substituting $\hat{t}_s^*(0) = -\hat{f}_s^*(0)/2F_s^2$ as given by Eq. (4.7b), we get the following linear discrete equation

$$\hat{x}^*(T_s) = M_r A \hat{x}^*(0) + d_a \hat{t}_a^*(0) + d_s \hat{f}_s^*(0) \tag{4.54}$$

The vectors d_a and d_s are given in Appendix C.2. Equation (4.54) is equivalent to the following linear difference equation

$$\hat{x}(t + T_s) = M_r A \hat{x}(t) + d_a \hat{t}_a(t) + d_s \hat{f}_s(t) \tag{4.55}$$

where the continuous perturbation vector is defined as follows

> $\hat{x}(t) \equiv$ *The continuous perturbation vector which has the same frequency as the modulating frequency,* ω_m, *and which when sampled at* $t = nT_s$, *gives the perturbation* $\hat{x}^*(nT_s)$ *on the state vector* $x(nT_s)$. *When sampled at* $t = (n+1)T_s$, $M_r \hat{x}(t)$ *gives the perturbation* $M_r \hat{x}^*((n+1)T_s)$ *on the state vector* $X((n+1)T_s)$.

It should be clear that

$$x(t) \neq X(t) + \hat{x}(t) \tag{4.56}$$

because a modulated signal, in this case $x(t)$, cannot be simply represented by the sum of the unmodulated signal and a signal that has the same frequency as the modulating signal.

Following the same linearization procedure, we obtain from Eq. (4.41)

$$\hat{<v>}(t) = c^T\hat{x}(t) + k_a\hat{t}_a(t) + k_s\hat{f}_s(t) \tag{4.57}$$

where the vector c^T is given by Eq. (4.38), and the constants k_a and k_s are given in Appendix C.2. From this equation it is clear that the dynamics of $\hat{<v>}(t)$ depends *linearly* on the dynamics of the components of $\hat{x}(t)$. Equations (4.55) and (4.57) have an unknown modulation term, $\hat{t}_a(t)$, in them which needs to be resolved. This is explained in the following step.

v) Determination of $\hat{t}_a(t)$ in Terms of $\hat{x}(t)$

Since the time t_a is determined by the zero-crossing of either the resonant inductor current (for the series resonant converter) or the resonant capacitor voltage (parallel resonant converter), the perturbations on these states at $t = t_a$ is *zero* as well. Let $t = t_a$ in Eq. (4.18)

$$x(t_a) = e^{A_1 t_a}x(0) + B_1(t_a)bV_g \tag{4.58}$$

When this equation is perturbed and linearized as explained earlier, the following is obtained

$$\hat{x}^*(T_a) = e^{A_1 T_a}\hat{x}^*(0) + e^{A_1 T_a}[A_1 X(0) + bV_g]\hat{t}_a^*(0) \tag{4.59}$$

The constraint $\hat{i}_R^*(t_a)=0$ gives for the series resonant converter

$$\hat{t}_a^*(0) = -\frac{a_{11}}{k_1}\hat{i}_R^*(0) - \frac{a_{12}}{k_1}\hat{v}_R^*(0) - \frac{a_{13}}{k_1}\hat{v}_{C_f}^*(0) \tag{4.60}$$

For the parallel resonant converter, the constraint $\hat{v}_R^*(t_a)=0$ gives

$$\hat{t}_a^*(0) = -\frac{a_{21}}{k_2}\hat{i}_R^*(0) - \frac{a_{22}}{k_2}\hat{v}_R^*(0) - \frac{a_{23}}{k_2}\hat{i}_{L_f}^*(0) - \frac{a_{24}}{k_2}\hat{v}_{C_f}^*(0) \tag{4.61}$$

The constants a_{ij} are the elements of the matrix $e^{A_1 T_a}$ and the constants k_i are the elements of the vector $e^{A_1 T_a}[A_1 X(0) + bV_g]$

$$[a_{ij}] = e^{A_1 T_a} \qquad \text{and} \qquad [k_i] = e^{A_1 T_a}[A_1 X(0) + bV_g] \tag{4.62a-b}$$

Equations (4.60) and (4.61) can be put in continuous form and summarized as follows

$$\hat{t}_a(t) = V_a^T \hat{x}(t) \tag{4.63}$$

where, for the series resonant converter, the vector V_a^T is given by

$$V_a^T = [-a_{11}/k_1 \;\; -a_{12}/k_1 \;\; -a_{13}/k_1] \tag{4.64a}$$

and for the parallel resonant converter V_a^T is given by

$$V_a^T = [-a_{21}/k_2 \;\; -a_{22}/k_2 \;\; -a_{23}/k_2 \;\; -a_{24}/k_2] \tag{4.64b}$$

When Eq. (4.63) is substituted in Eq. (4.55), the final desired difference equation is obtained for $\hat{x}(t)$

$$\hat{x}(t + T_s) = M_x\hat{x}(t) + d_s\hat{f}_s(t) \tag{4.65}$$

where the matrix M_x is given in Appendix C.2. The equation for $\langle\hat{v}\rangle(t)$ follows after substitution of Eq. (4.63) in Eq. (4.57)

$$\langle\hat{v}\rangle(t) = h^T\hat{x}(t) + k_s\hat{f}_s(t) \tag{4.66}$$

where the constant k_s and the vector h^T are given in Appendix C.2.

vi) The Control–to–Output Transfer Function

The control-to-output transfer function is now easily determined by taking the Laplace transform of Eqs. (4.65) and (4.66)

$$\frac{\langle\hat{v}\rangle(s)}{\hat{f}_s(s)} = h^T\frac{\hat{x}(s)}{\hat{f}_s(s)} + k_s \tag{4.67a}$$

$$\frac{\hat{x}(s)}{\hat{f}_s(s)} = [Ie^{sT_s} - M_x]^{-1}d_s \tag{4.67b}$$

Substitution of Eq. (4.67b) in (4.67a) gives

$$\frac{\langle\hat{v}\rangle(s)}{\hat{f}_s(s)} = h^T[Ie^{sT_s} - M_x]^{-1}d_s + k_s \tag{4.68}$$

This is the control-to-output transfer function. As mentioned earlier, $\hat{f}_s(t)$ is generated via a control signal $\hat{v}_c(t)$ that is fed into the FM input of the VCO. This control-to-output transfer function is given

$$\frac{\langle\hat{v}\rangle(s)}{\hat{v}_c(s)} = \frac{\langle\hat{v}\rangle(s)}{\hat{f}_s(s)}\frac{\hat{f}_s(s)}{\hat{v}_c(s)} \tag{4.69}$$

The particular VCO used for the experimental verification of the control-to-output transfer function was the Intersil 8038 waveform generator for

which $\hat{f}_s(s)/\hat{v}_c(s)$ is frequency independent so that

$$\frac{\langle\hat{v}\rangle(s)}{\hat{v}_c(s)} = K_m \frac{\langle\hat{v}\rangle(s)}{\hat{f}_s(s)} \tag{4.70}$$

where K_m is a constant. Consequently, no other dynamics was observed in the experimental results other than that given by Eq. (4.68).

4.2.2 Audio Susceptibility

In this section the response to small-signal variations in the input voltage is determined. Let the perturbation in V_g be denoted by $\hat{v}_g(t)$

$$v_g(t) = V_g + \hat{v}_g(t) \tag{4.71}$$

If $\hat{v}_g(t)$ varies *slowly* during T_s, then it can be assumed to be constant during this interval and the results in Eqs. (4.18) and (4.24) are still valid. Therefore, unlike the control-to-output transfer function, the line-to-output transfer function determined is valid only for *low frequencies*. The equations for the evolution of the state vector and the average output voltage in each interval is now perturbed for $\hat{v}_g$. First, consider Eq. (4.37) in which in addition to $x(0)$ and V_g, the vectors c^T and d^T are perturbed because they are functions of t_a

$$T_s\langle\hat{v}\rangle^*(0) = c^T\hat{x}^*(0) + \hat{c}^T X(0) + \hat{d}^T b V_g + d^T b\hat{v}_g{}^*(0) \tag{4.72}$$

Let $\hat{c}^T = c'^T\hat{t}_a$ and $\hat{d}^T = d'^T\hat{t}_a$

$$T_s\langle\hat{v}\rangle^*(0) = c^T\hat{x}^*(0) + [c'^T X(0) + d'^T b V_g]\hat{t}_a{}^*(0) + d^T b\hat{v}_g{}^*(0) \tag{4.73}$$

The equation for $\langle\hat{v}\rangle(t)$ follows from the continuous form of this equation

$$T_s\langle\hat{v}\rangle(t) = c^T\hat{x}(t) + [c'^T X(0) + d'^T bV_g]\hat{t}_a(t) + d^T b\hat{v}_g(t) \qquad (4.74)$$

Similarly, for the perturbation vector $\hat{x}(t)$ the following difference equation is obtained

$$M_r\hat{x}(t+T_s) = A\hat{x}(t) + [A'X(0)+B'bV_g]\hat{t}_a(t) + Bb\hat{v}_g(t) \qquad (4.75)$$

The unknown modulation $\hat{t}_a$ can now be determined as before from the requirement that the perturbation on the state that determines t_a be zero at $t = T_a$. Equation (4.58) is repeated here as Eq. (4.76)

$$x(t_a) = e^{A_1 t_a}x(0) + B_1(t_a)bV_g \qquad (4.76)$$

Perturbation of V_g in this equation gives

$$\hat{x}^*(T_a) = e^{A_1 T_a}\hat{x}^*(0) + e^{A_1 T_a}[A_1 X(0) + bV_g]\hat{t}_a{}^*(0) + B_1(T_a)b\hat{v}_g{}^*(0) \qquad (4.77)$$

The constraint $\hat{i}_R{}^*(t_a) = 0$ gives for the series resonant converter

$$\hat{t}_a{}^*(0) = -\frac{a_{11}}{k_1}\hat{i}_R{}^*(0) - \frac{a_{12}}{k_1}\hat{v}_R{}^*(0) - \frac{a_{13}}{k_1}\hat{v}_{C_f}{}^*(0) - \frac{p_1}{k_1}\hat{v}_g{}^*(0) \qquad (4.78)$$

For the parallel resonant converter, the constraint $\hat{v}_R{}^*(t_a) = 0$ gives

$$\hat{t}_a{}^*(0) = -\frac{a_{21}}{k_2}\hat{i}_R{}^*(0) - \frac{a_{22}}{k_2}\hat{v}_R{}^*(0) - \frac{a_{23}}{k_2}\hat{i}_{L_f}{}^*(0) - \frac{a_{24}}{k_2}\hat{v}_{C_f}{}^*(0) - \frac{p_2}{k_2}\hat{v}_g{}^*(0) \qquad (4.79)$$

In Eqs. (4.78) and (4.79) a_{ij} and k_i are given by Eqs. (4.62a-b) and the constants p_1 and p_2 are the elements of the vector $B_1(t_a)b$

$$[p_i] = B_1(T_a)b \tag{4.80}$$

Equations (4.77) and (4.78) can be put in continuous form and summarized as follows

$$\hat{t}_a(t) = V_a^T\hat{x}(t) + k_p\hat{v}_g(t) \tag{4.81}$$

where V_a^T is given by Eqs. (4.64a-b) as before and k_p is given by

$$k_p = \frac{p_i}{k_i} \tag{4.82}$$

where $i=1$ corresponds to the series resonant converter and $i=2$ corresponds to the parallel converter. Substitution of Eq. (4.81) in Eqs. (4.74) and (4.75) gives

$$\langle\hat{v}\rangle(t) = h^T\hat{x}(t) + k_g\hat{v}_g(t) \tag{4.83}$$

$$\hat{x}(t+T_s) = M_x\hat{x}(t) + d_g\hat{v}_g(t) \tag{4.84}$$

where k_g and d_g are given in Appendix C.2 and where h^T and M_x are the same as in Eqs. (4.65) and (4.66) and are also given in Appendix C.2.

The audio susceptibility is now determined by taking the Laplace transform of Eqs. (4.83) and (4.84)

$$\frac{\langle\hat{v}\rangle(s)}{\hat{v}_g(s)} = h^T[Ie^{sT_s} - M_x]^{-1}d_g + k_g \tag{4.85}$$

4.2.3 Input Impedance

The input impedance of a converter is determined by the small-signal response of the *average* input current to perturbations in the input voltage. Because of the various methods of excitation of these converters as shown in Figs. 2.1 and 3.1, the input impedance seen by the source, V_{in}, in each of these converters is different. The ideal equivalent circuits of these converters, shown in Fig. 4.10, relate all these different input impedances to a single input impedance given by

$$Z_{in}(s) = \frac{\hat{v}_g(s)}{\langle \hat{i}_b \rangle(s)} \tag{4.86}$$

where $\langle i_b \rangle$ is the average branch current in Fig. 4.10. It can be easily seen that the input impedance, $Z_{in}'(s)$, seen by the source, V_{in}, for the converters in Figs. 2.1a and 3.1b is related to $Z_{in}(s)$ of Eq. (4.86) by

$$Z_{in}'(s) = 2\,\frac{1}{sC_\infty} \| Z_{in}(s) \tag{4.87}$$

For the converters in Figs. 2.1b and 3.1d, which implement four switches, the input impedance $Z_{in}'(s)$ is given by

$$Z_{in}'(s) = \frac{Z_{in}(s)}{2} \tag{4.88}$$

Finally, for the converters in Figs. 3.1a and c, $Z_{in}'(s)$ is given by

$$Z_{in}'(s) = 2\,Z_{in}(s) \tag{4.89}$$

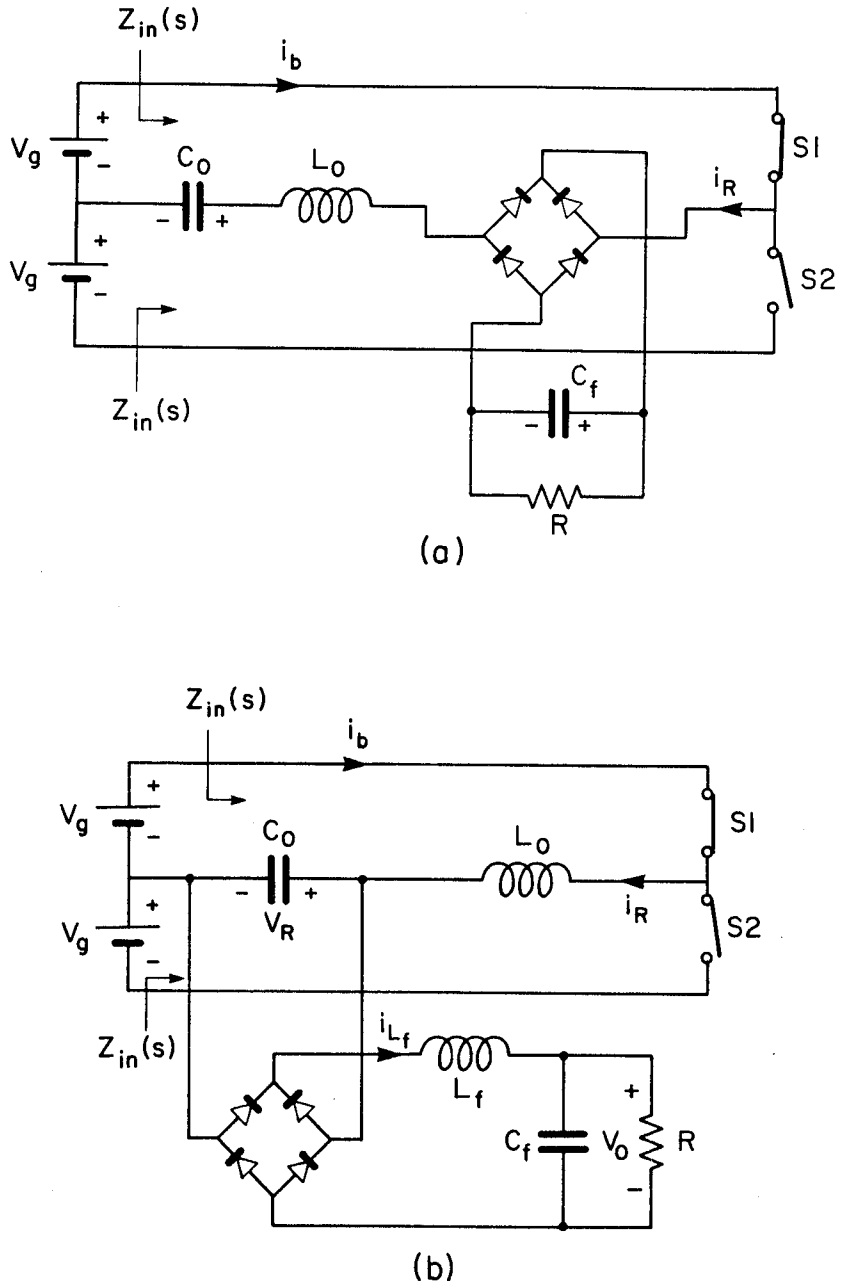

Fig. 4.10 The input impedance, $Z_{in}(s)$, of the ideal equivalent circuit of a) the series resonant converter and b) of the parallel resonant converter.

The branch current i_b is the same as the resonant current $i_R(t)$ during the interval $0 \leq t \leq T_s$ and is zero during the interval $T_s \leq t \leq 2T_s$. The steady-state and modulated waveforms of i_b are shown in Fig. 4.11. Since the first component of the state vector $x^T(t)$ is the resonant current, the average branch current $<i_b>(0)$ in each interval is given by the first component of the average state vector $<x>(0)$

$$<x>(0) = \frac{1}{2T_s}\left[\int_0^{t_a} x(t)dt + \int_{t_a}^{T_s} x(t)dt\right] \tag{4.90}$$

In Eq. (4.90), the averaging interval is taken as $2T_s$ while the integral is taken from 0 to T_s because the branch current is zero during $T_s \leq t \leq 2T_s$. Equation (4.90) gives

$$<x>(0) = A_a\, x(0) + B_b\, bV_g \tag{4.91}$$

where the matrices A_a and B_a are given by

$$A_a = \frac{1}{2T_s}[B_1(t_a) + B_2(T_s - t_a)e^{A_1 t_a}] \tag{4.92}$$

$$B_a = \frac{1}{2T_s}[A_1^{-1}B_1(t_a) + B_2(T_s - t_a)B_1(t_a)$$

$$+ A_2^{-1}B_2(T_s - t_a) - (T_s - t_a)A_2^{-1} - t_a A_1^{-1}] \tag{4.93}$$

The steady-state or unmodulated current, $I_b(t)$, is shown in Fig. 4.11a in a thin line and the modulated current, $i_b(t)$, is shown in a thick line. The steady-state average current, $<I_b>$, shown in a thin straight line throughout all the intervals, can be expressed in terms of $I_b(t)$ and the

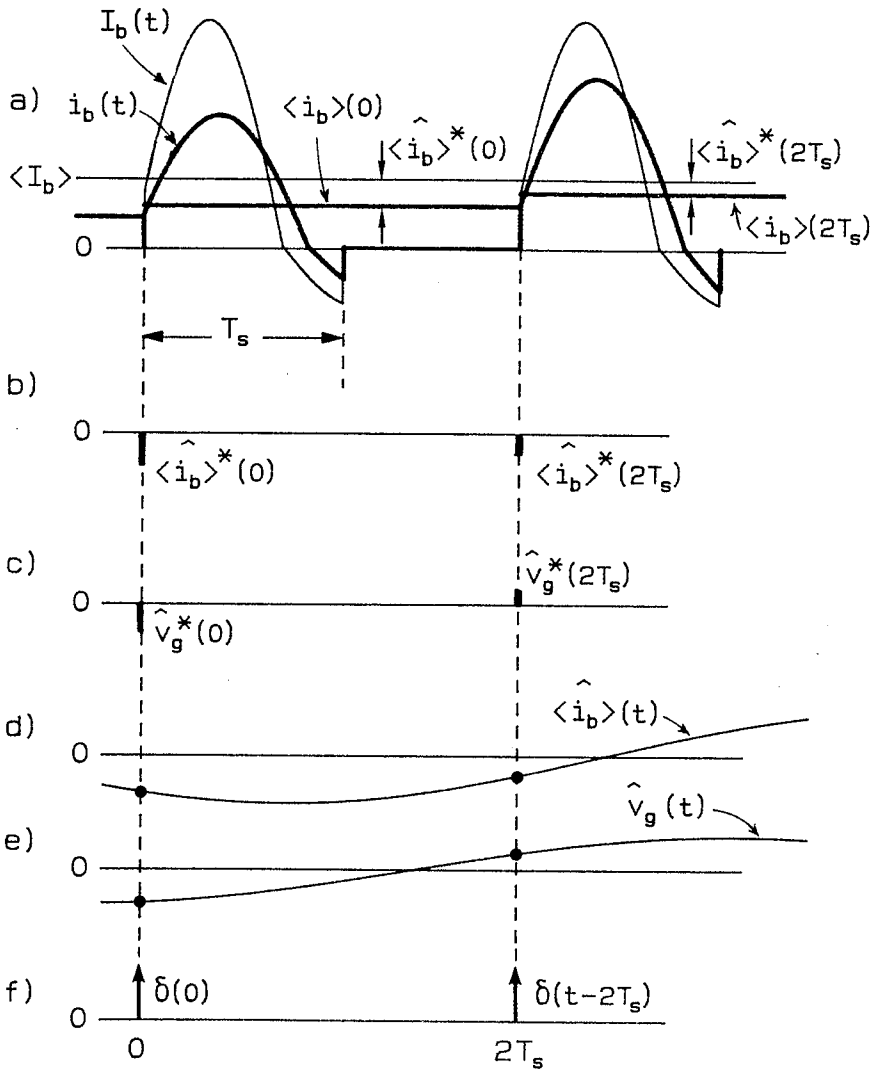

Fig. 4.11 The branch current i_b of Fig. 4.10. a) The unmodulated branch current, $I_b(t)$, and its steady-state average value, $\langle I_b\rangle$, are shown in thin lines. The modulated branch current, $i_b(t)$, and its average, $\langle i_b\rangle(nT_s)$, in each interval are shown in thick lines. b) The perturbations in the average branch current, $\langle \hat{i}_b\rangle^*(nT_s)$, in each interval in the presence of $\hat{v}_g$ are shown as sampled data points of a continuous function d) $\langle \hat{i}_b\rangle(t)$ from which the input impedance, given by Eq. (4.86), *is determined.*

conversion ratio M as

$$<I_b> = \frac{1}{2T_s}\int_0^{T_s} I_b(t)dt = \frac{M^2 V_g}{2R} \tag{4.94}$$

where the last equality is simply obtained from the following dc consideration

$$V_0 I_0 = 2<I_b>V_g \rightarrow \frac{MI_0}{2} = <I_b> \rightarrow \frac{M^2 V_g}{2R} = <I_b> \tag{4.95}$$

From the last equality, it can be seen that the dc input impedance is given by

$$\lim_{s\to 0} Z_{in}(s) = \frac{2R}{M^2} \tag{4.96}$$

The modulated branch current $i_b(t)$, in the presence of modulation of the input voltage, is shown in a thick line and the average branch current in each interval is shown in a thick straight line in that interval. In each interval the modulated average branch current deviates from the steady-state average by $<\hat{i}_b>^*(0)$

$$<\hat{i}_b>^*(0) = <i_b>(0) - <I_b> \tag{4.97}$$

To determine the small-signal perturbations in the average branch current, Eq. (4.91) is perturbed for V_g. This perturbation gives

$$<\hat{x}>(t) = A_a\hat{x}(t) + [A_a'X(0) + B_a'b]\hat{t}_a(t) + B_a b\hat{v}_g(t) \tag{4.98}$$

The perturbation in the evolution of the state vector and the unknown modulation $\hat{t}_a(t)$ are given by Eqs. (4.81) and (4.84) as before. Substituting

Eq. (4.81) in Eq. (4.98) and rewriting Eq. (4.84) as Eq. (4.100) we get

$$<\hat{x}>(t) = A_x \hat{x}(t) + b_g \hat{v}_g(t) \tag{4.99}$$

$$\hat{x}(t + T_s) = M_x \hat{x}(t) + d_g \hat{v}_g(t) \tag{4.100}$$

where the matrix A_x and the vector b_g are given in Appendix C.2. Equations (4.99) and (4.100) are solved by taking their Laplace transform

$$\frac{<\hat{x}>(s)}{\hat{v}_g(s)} = A_x[Ie^{sT_s} - M_x]^{-1} d_g + b_g \tag{4.101}$$

The first component in Eq. (4.101) is the input admittance.

4.3 Experimental Results

In this section the experimental and predicted results of the small-signal response are given with special emphasis on the control-to-output transfer function. The circuit parameters of the series resonant converter are

$$F_0 = 50.2\text{kHz} \quad L_0 = .197\text{mH} \quad C_0 = .051\mu\text{F} \quad C_f = 32\mu\text{F}$$

For the parallel resonant converter, the circuit parameters are

$$F_0 = 38.7\text{kHz} \quad L_0 = 36\mu\text{H} \quad C_0 = .47\mu\text{F} \quad L_f = 1.35\text{mH} \quad C_f = 32\mu\text{F}$$

The control-to-output transfer function for the series resonant converter is shown in Figs. 4.12a-d where it can be seen that predicted and experimental results are in good agreement. In Figs. 4.12a and b the operating point is below resonance and in Figs. 4.12c and d the operating point is above resonance. Comparing the transfer functions below and

above resonance we can see that there is a 180° phase shift in the phase response owing to the reversal of the slope of the conversion ratio characteristics as the point $F_s/F_0=1$ is traversed. An interesting point in these transfer functions is the following: in Fig. 4.12d, for the operating point $Q_s=3$ (or $R=20.7\Omega$) and $F_s/F_0=1.3$, the low-frequency behavior is essentially that of a single pole ($f_p=240\text{Hz}$) at RC_f, which is in agreement with our intuition since the output low-pass network is current fed by the resonant branch. This intuition fails completely for the operating conditions in Figs. 4.12b and c, but the results of the exact analysis are in good agreement with the measurements. If the modulation of the zero-crossing time t_a, determined in step v, is neglected, then this change in the dominant behavior will *not* be predicted properly. Therefore, the dominant behavior of the transfer functions depends on the *modulation of the zero-crossing time* t_a.

An example of a transfer function, shown in Fig. 4.12a, is given for the operating point $Q_s=4$ and $F_s/F_0=.8$

$$\frac{\langle\hat{v}\rangle(s)}{\hat{v}_c(s)} = K\frac{1+a_1z+a_2z^2+a_3z^3}{1+b_1z+b_2z^2+b_3z^3} \quad ; \quad z=e^{sT_s}$$

where the coefficients in the numerator and the denominator are given by

$$a_1=-23.813 \quad a_2=-19.9 \quad a_3=-2.086$$

$$b_1=-2.811 \quad b_2=3.382 \quad b_3=-1.593$$

and the constant K depends on the input voltage, the gain of the VCO, and values of the circuit components.

a)

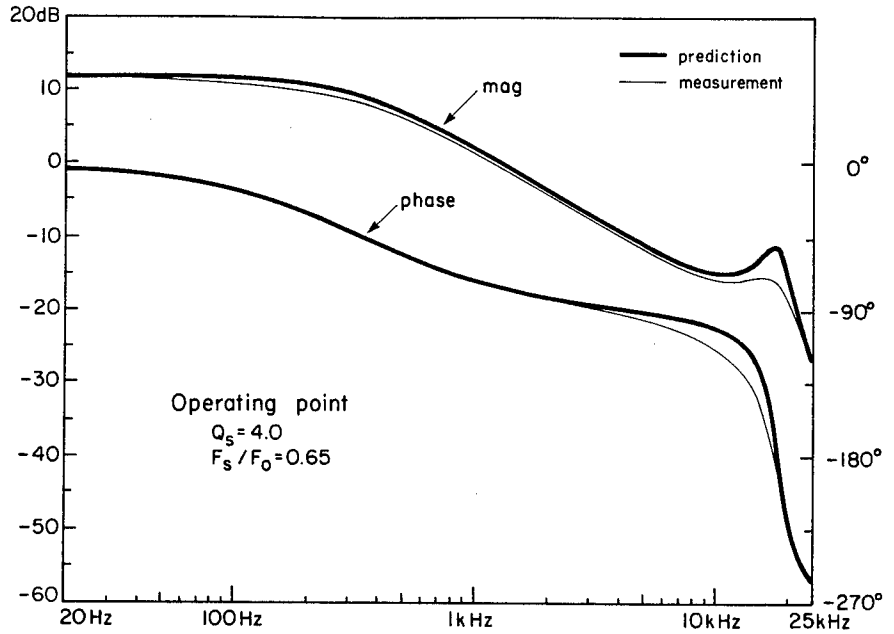
20dB
10
0
-10
-20
-30
-40
-50
-60
0°
-90°
-180°
-270°
prediction
measurement
mag
phase
Operating point
Q_s = 4.0
F_s / F_0 = 0.65
20Hz
100Hz
1kHz
10kHz
25kHz

b)

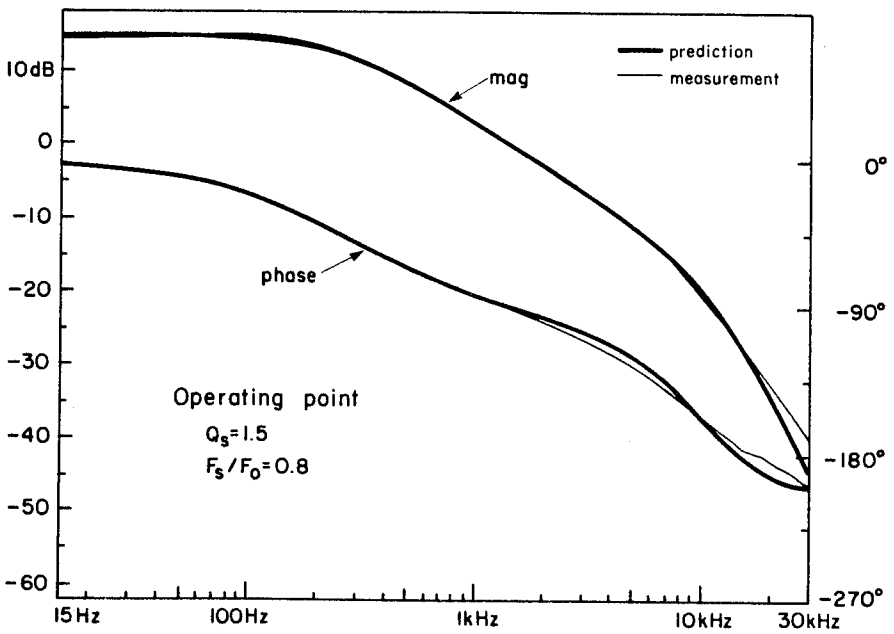
10dB
0
-10
-20
-30
-40
-50
-60
0°
-90°
-180°
-270°
prediction
measurement
mag
phase
Operating point
Q_s = 1.5
F_s / F_0 = 0.8
15Hz
100Hz
1kHz
10kHz
30kHz

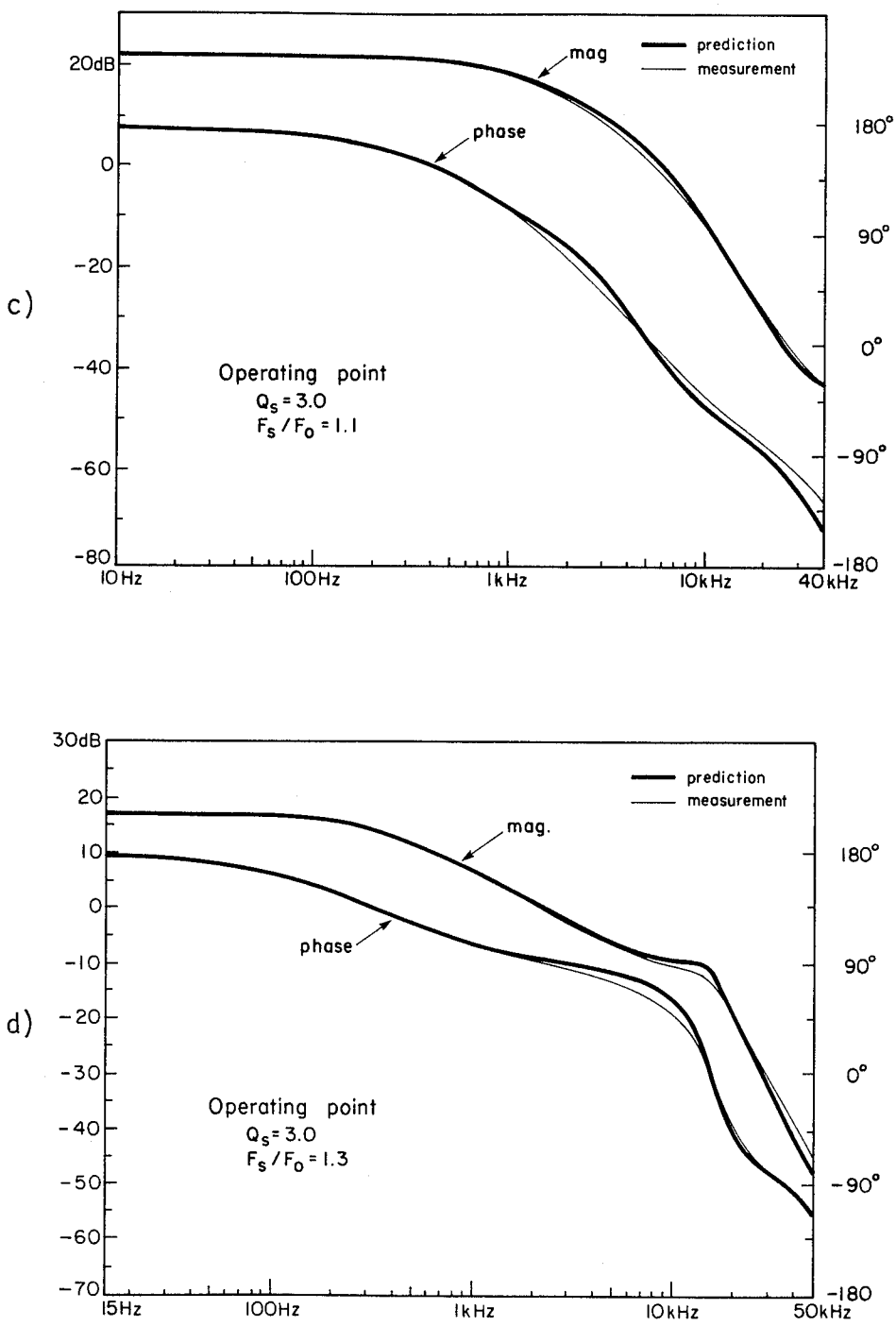

Fig. 4.12 a-d) Experimental and predicted results of the control-to-output transfer functions of the series resonant converter.

a)

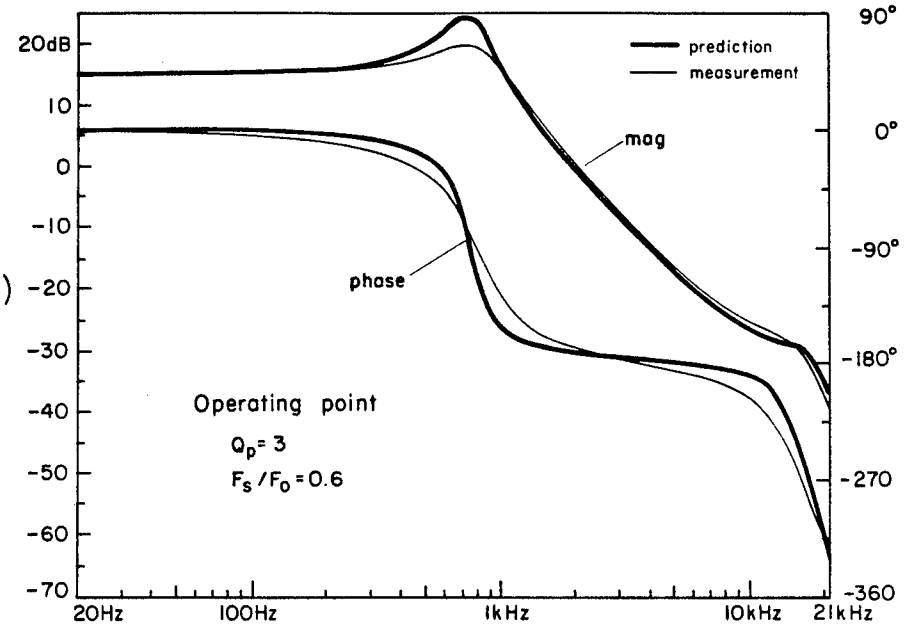
20dB
10
0
-10
-20
-30
-40
-50
-60
-70
90°
0°
-90°
-180°
-270
-360
prediction
measurement
mag
phase
Operating point
Q_p= 3
F_s/F_0=0.6
20Hz
100Hz
1kHz
10kHz
21kHz

b)

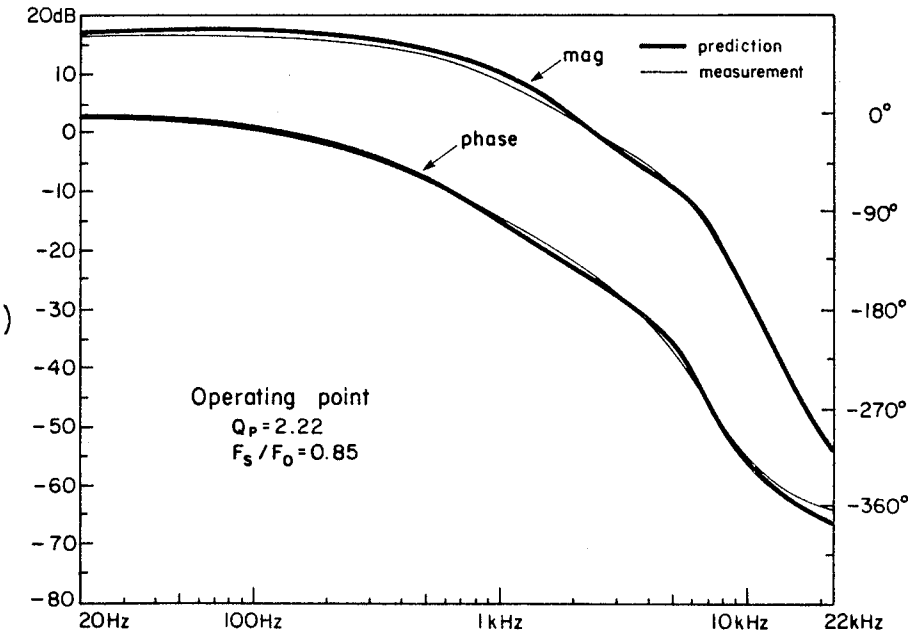
20dB
10
0
-10
-20
-30
-40
-50
-60
-70
-80
0°
-90°
-180°
-270°
-360°
mag
prediction
measurement
phase
Operating point
Q_P=2.22
F_s/F_0=0.85
20Hz
100Hz
1kHz
10kHz
22kHz

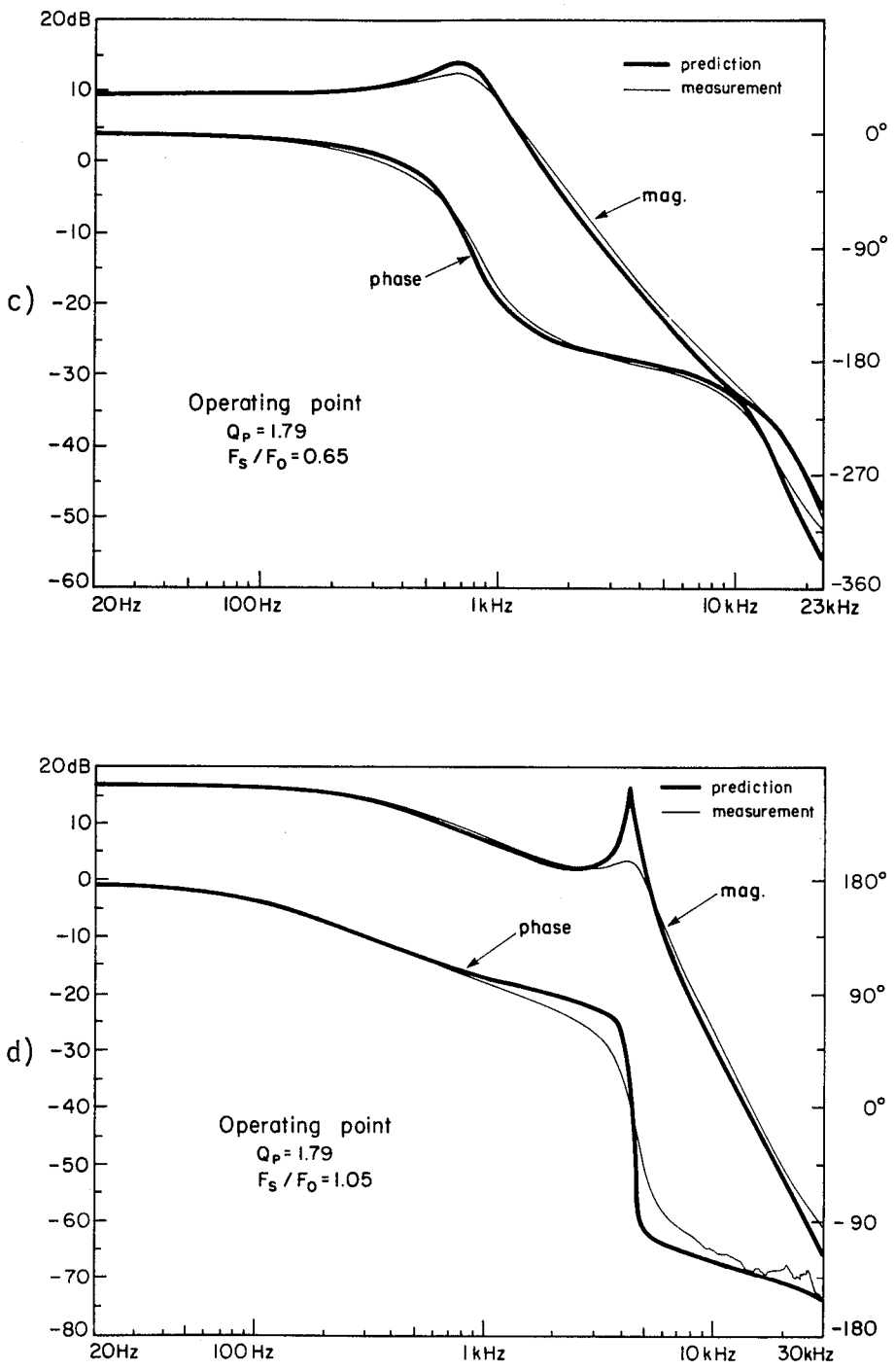

Fig. 4.13 a-d) Experimental and predicted results of the control-to-output transfer functions of the parallel resonant converter.

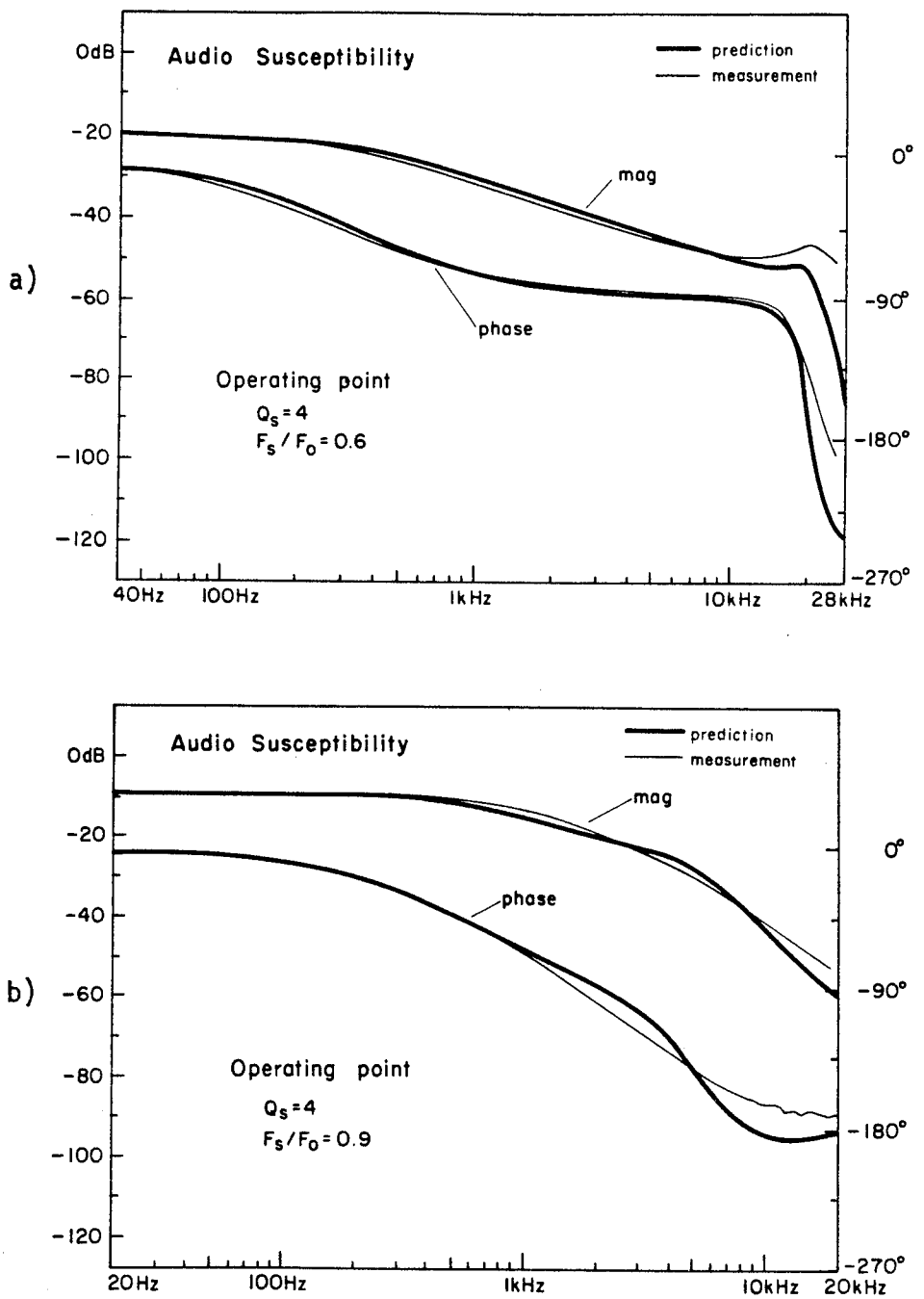

Fig. 4.14 a-b) Experimental and predicted results of the audio susceptibility of the series resonant converter.

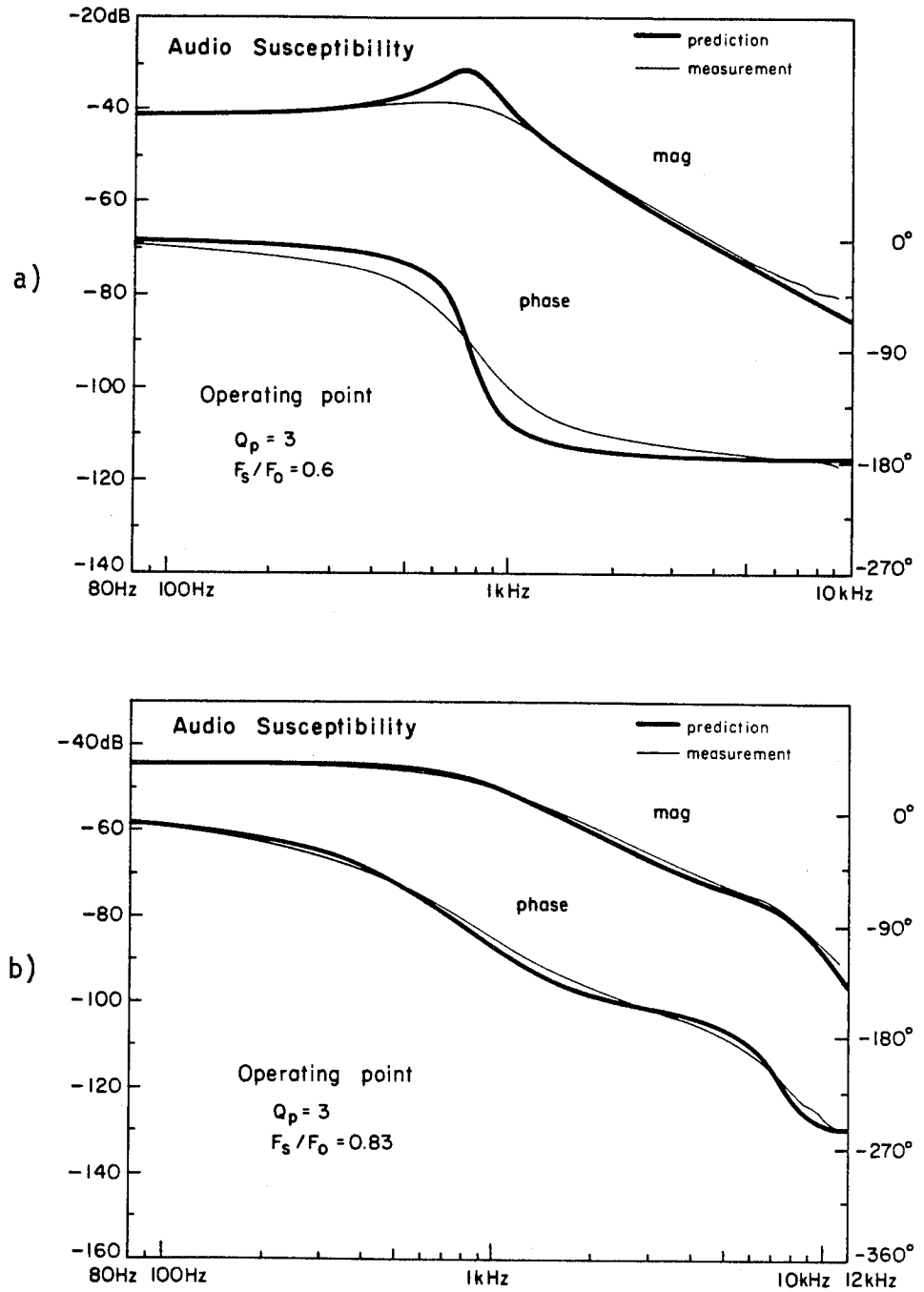

Fig. 4.15 a-b) Experimental and predicted results of the audio susceptibility of the parallel resonant converter.

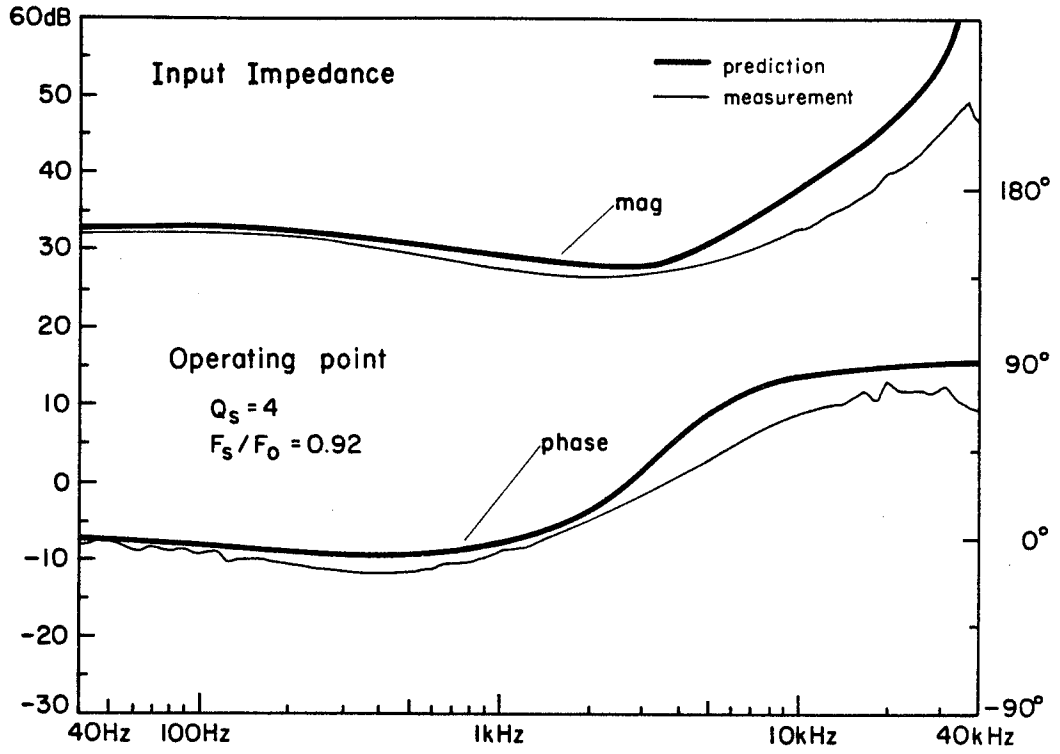

Fig. 4.16 Experimental and predicted results of the input impedance of the series resonant converter.

The control-to-output transfer function for the parallel converter is given in Figs. 4.13a-d.

The audio susceptibility, or the line-to-output transfer function, is shown in Figs. 4.15 and 4.16 and the input impedance is shown in Fig. 4.17. Because of low frequency limitation in the analysis of the response to perturbations in input voltage, there is some discrepancy at high frequencies between predicted and measured results.

4.4 Conclusion

In Chapters 2 and 3 an accurate dc analysis of the series and the parallel resonant converters is given whereby the steady-state vector is determined in terms of Q and F_s / F_0 at a given operating point. In this chapter, a systematic method of small-signal analysis is given whereby the response of resonant converters to perturbations in switching frequency and input voltage is determined. Experimental and predicted results for the parallel and series resonant converters are in good agreement.

In this analysis the *discrete* and *average* small-signal responses are determined. The average response is important because in the experimental verification of the small-signal response the network analyzer searches for that component in the output voltage or the input current which has the same frequency as the modulating signal. This component which the analyzer searches for is determined from a knowledge of the perturbations in the average output voltage or the average input current in *each* interval. The average state in *each* switching interval is determined as a *linear* combination of the initial states at the beginning of that switching interval. Consequently, the average response is determined in

terms of the discrete response of the initial states.

The control-to-output transfer function is valid for modulating frequencies approaching near the switching frequency because the discrete analysis is carried out over half the switching interval which corresponds to a sampling rate of twice the switching frequency. The line-to-output transfer function and the input impedance are valid only for low-frequency variations in the input voltage because the solutions of the differential equations, during each output-network switching time, are obtained assuming slow variations in the input voltage.

The results are determined numerically because of the occurrence of functions of matrices that are difficult to determine in expression form.

CHAPTER 5

HIGH-Q APPROXIMATION

5.1 Introduction

The results of the analysis in the previous chapters were obtained numerically. To gain further insight, an approximate small-signal analysis is given in this chapter assuming high Q and operation away from the resonant peak. It was shown in Chapter 2 that it is desirable to operate the parallel resonant converter with a high Q_p (greater than 3) and below resonance because in this range it behaves like a voltage source (Fig. 2.5). Although this high Q approximation is relevant for the series resonant converter as well, it is slightly restrictive because it is not always necessary to design this converter for $Q_s>3$ provided of course Q_s is not small enough for discontinuous conduction mode to occur in the range $1/2 \leq F_s/F_0 \leq 1$ ($Q_s \geq 4/\pi$ as given by Eq. (3.25a)). Therefore, improved approximate results, valid over a wider range of Q_s are given for the series resonant converter. The results of the approximate and exact analysis are in good agreement over the range of interest.

5.2 Approximate Analysis

In this section, an intuitive rather a formal approximation of the exact analysis is given. An inspection of the Bode plots of the control-to-output transfer functions given in the previous chapter shows that for the series resonant converter the dominant behavior is given by a single-pole and the high-frequency behavior is given by a quadratic

$$\frac{\hat{<v>}(s)}{\hat{f}_s(s)} = \frac{A}{\left[1+\frac{s}{\omega_{fs}}\right]\left[1+\frac{s}{\omega_{s0}Q_s}+\frac{s^2}{{\omega_{s0}}^2}\right]} \tag{5.1}$$

For the parallel resonant converter a similar observation leads to

$$\frac{\hat{<v>}(s)}{\hat{f}_s(s)} = \frac{A}{\left[1+\frac{s}{\omega_{fp}Q_f}+\frac{s^2}{{\omega_{fp}}^2}\right]\left[1+\frac{s}{\omega_{s0}Q_s}+\frac{s^2}{{\omega_{s0}}^2}\right]} \tag{5.2}$$

The low-frequency gain, A, in both of these transfer functions is proportional to the slope of the conversion ratio characteristics, A_0, which is determined numerically and plotted in Fig. 5.1a and b. A is given by

$$A = A_0 \frac{V_g}{F_0} \tag{5.3}$$

where A_0 is obtained from Fig. 5.1 and is equal to the slope of M

$$A_0 = \frac{dM}{d(F_s/F_0)} \tag{5.4}$$

Next, the dominant behavior of these transfer functions is determined. For the series resonant converter, it can be seen from Fig. 3.9 that the average output current is almost independent of the load for high

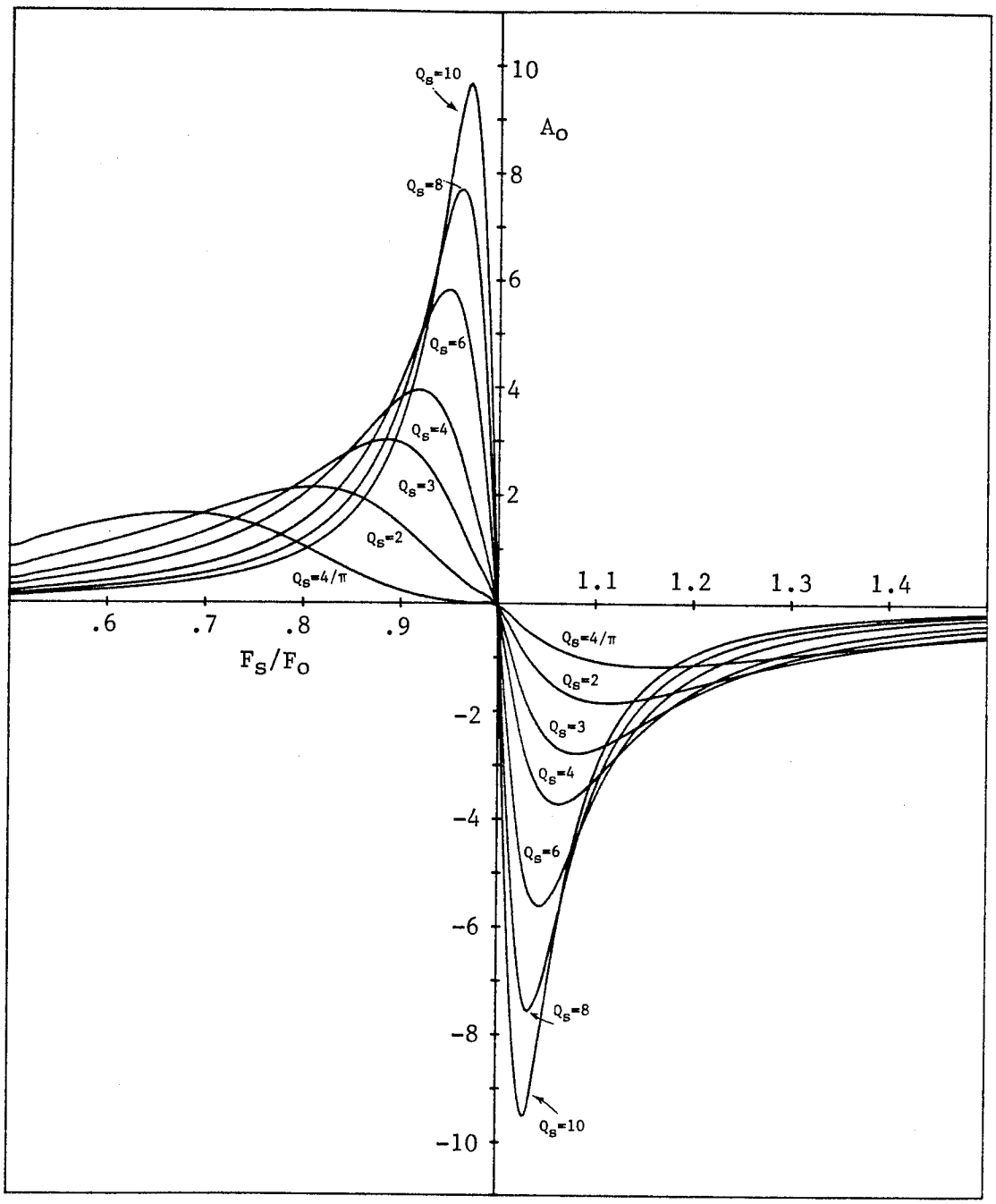

Fig. 5.1a Slope of the conversion ratio characteristics of the series resonant converter in continuous conduction mode.

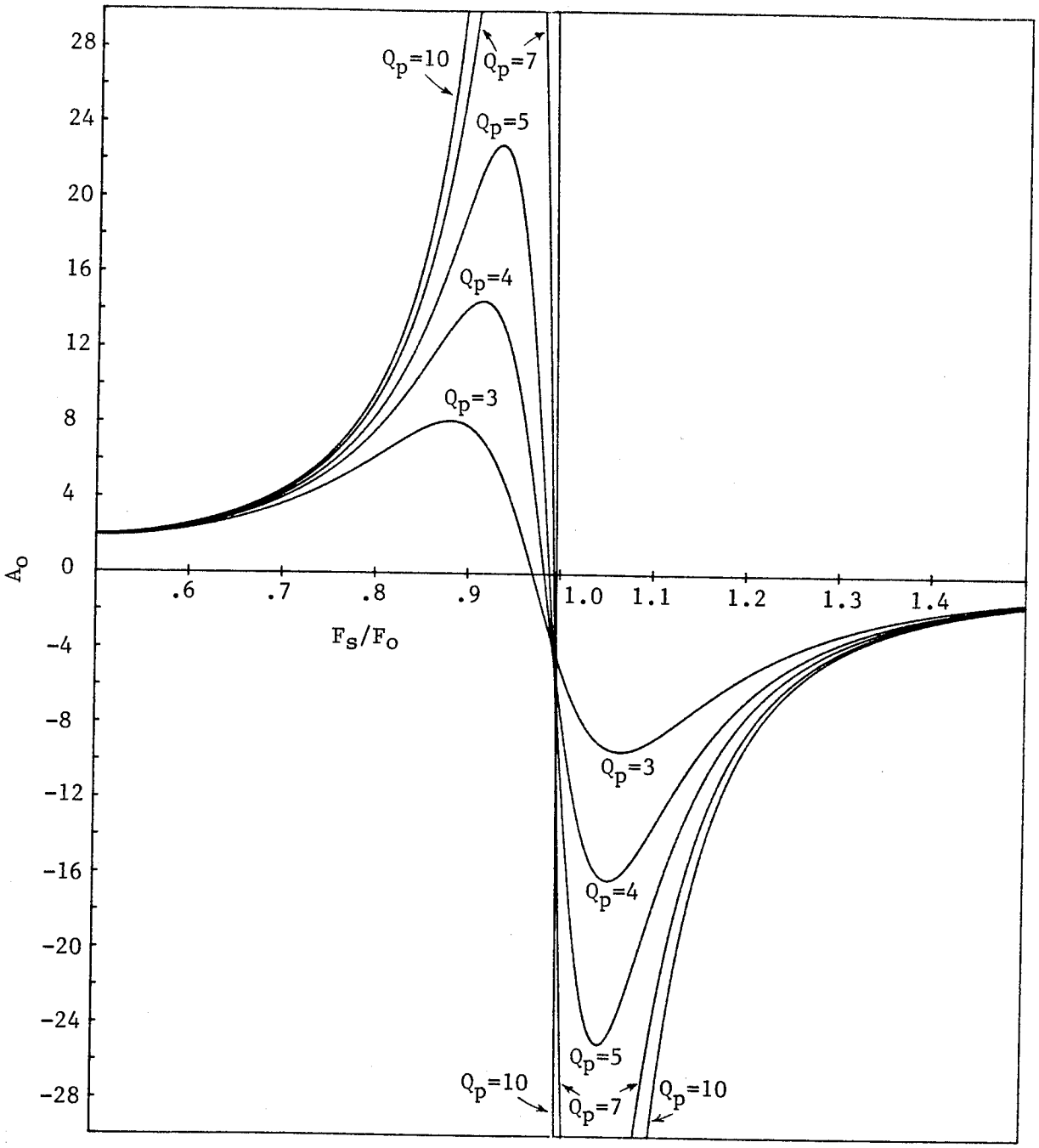

Fig. 5.1b Slope of the conversion ratio characteristics of the parallel resonant converter in continuous conduction mode.

Q_s and away from the resonant peak. A circuit that represents this approximation is shown in Fig. 5.2b where the average rectified current $|I_R|$ is represented by a stiff current source. It is clear from this circuit and Fig. 3.9 that small variations in F_s will cause the output voltage to vary with a single-pole frequency dependence. Therefore, ω_{fs} in Eq. (5.1) is given by

$$\omega_{fs} = \frac{1}{RC_f} \tag{5.5}$$

For the parallel resonant converter, the dominant behavior is determined by referring to the conversion ratio characteristics given in Fig. 2.5 whence it can be seen that for high Q and away from the resonant peak – specially below resonance – the output voltage is almost independent of the load. This is shown in Fig. 5.3b where the rectified capacitor voltage $|V_R|$ is represented by a stiff voltage source. From this circuit and the conversion ratio characteristics it is clear that the dominant behavior of the transfer function in Eq. (5.2) is given by the output low-pass filter and hence

$$\omega_{fp} = \frac{1}{\sqrt{L_f C_f}} \quad \text{and} \quad Q_f = \frac{R}{\omega_{fp} L_f} \tag{5.6a-b}$$

The high-frequency quadratic behavior of these transfer functions is determined next. In Figs. 5.2a and 5.3a, the resonant converter is viewed as a circuit driven by a square voltage voltage, V_s, with Fourier components at F_s, $2F_s$,...,nF_s as shown in Fig. 5.4a. When the frequency, or the amplitude, of V_s is small-signal modulated, its spectrum will contain sidebands around each Fourier component. The most important sidebands

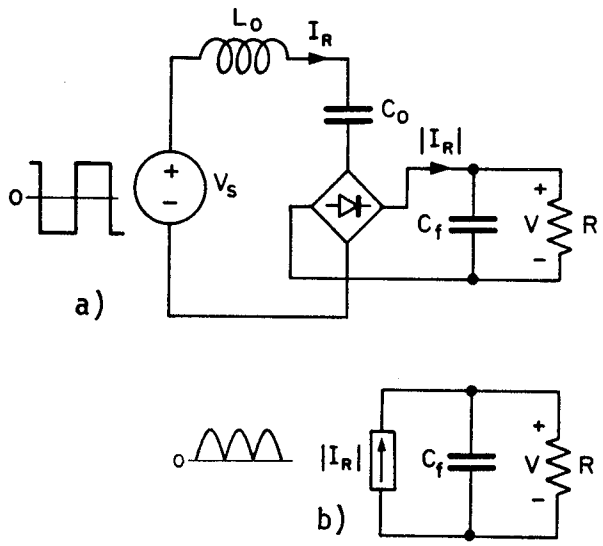

Fig. 5.2 a) The series resonant converter viewed as a circuit driven by a square voltage source, V_s, and b) an approximate circuit valid for high Q and away from the resonant peak.

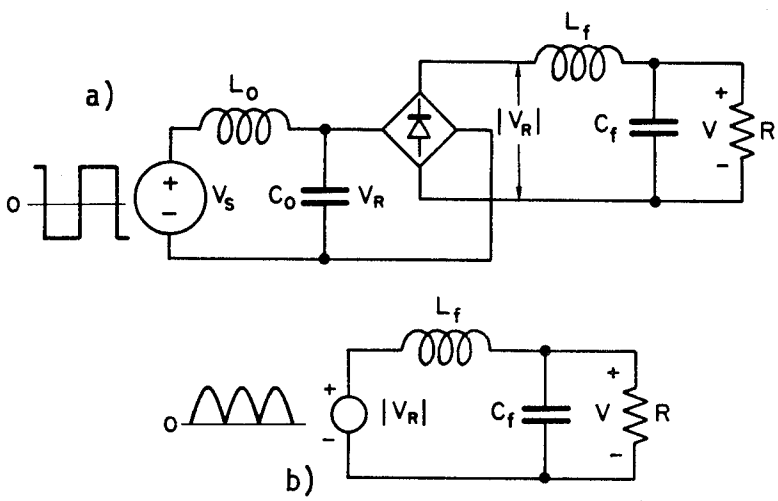

Fig. 5.3 a) The parallel resonant converter viewed as a circuit driven by a square voltage source, V_s, and b) an approximate circuit valid for high Q and away from the resonant peak.

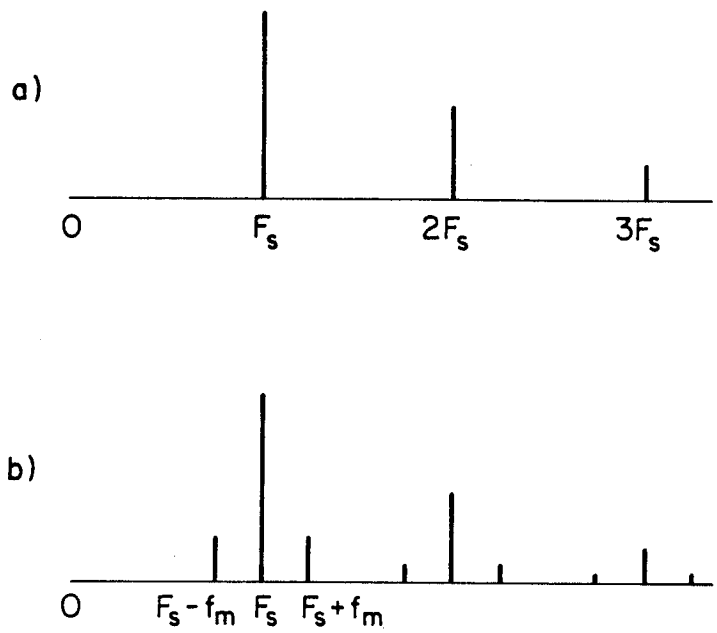

Fig. 5.4 The spectrum of the voltage source, V_s, in Fig. 5.3, a) when unmodulated and b) when small-signal amplitude or frequency modulated.

are $F_s + f_m$ and $F_s - f_m$. When either circuit is excited below resonance, the response of the resonant branch to the modulation is strongest when the frequency of the sideband at $F_s + f_m$ is equal to the resonant frequency

$$F_s + f_m = F_0 \quad \text{or} \quad f_m = F_0 - F_s \tag{5.7}$$

and when excited above resonance, the response is strongest when the sideband at $F_s - f_m$ is equal to the resonant frequency

$$F_s - f_m = F_0 \quad \text{or} \quad f_m = F_s - F_0 \tag{5.8}$$

Since the voltage and current sources, shown in Figs. 5.2b and 5.3b, are determined by the resonant branch, their response to the modulating signal is strongest when the frequency of the sideband is equal to the resonant frequency. This explains the high-frequency quadratic behavior in these transfer functions. The modulating frequency for which Eqs. (5.7) and (5.8) are satisfied is denoted by ω_{s0} and is the frequency in the quadratic factor in Eqs (5.1) and (5.2). This is summarized as follows

$$\omega_{s0} = \begin{cases} \omega_0 - \omega_s & F_s < F_0 \\ \omega_s - \omega_0 & F_s > F_0 \end{cases} \tag{5.9}$$

The Q in this quadratic factor is the same as the original resonant Q

$$Q_s = \frac{\omega_0 L_0}{R} \quad \text{and} \quad Q_p = \frac{R}{\omega_0 L_0} \tag{5.10}$$

Equations (5.1) and (5.2) are now compared to the results of the exact analysis in Figs. 5.5 and 5.6. These results are in good agreement for high Q and operation away from the resonant peak. The values of the circuit components, used in determining these transfer functions, for the series resonant converter are

$$L_0 = .197\text{mH} \qquad C_0 = .051\mu\text{F} \qquad C_f = 32\mu\text{F}$$

For the parallel resonant converter, the values of these components are

$$L_0 = 36\mu\text{H} \qquad C_0 = .47\mu\text{F} \qquad L_f = 1.35\text{mH} \qquad C_f = 32\mu\text{F}$$

These are the same values used in the experimental circuits in the previous chapter.

Equations (5.1) and (5.2) break down as the operating point gets closer to the resonant peak as shown in Fig. 5.7a and b. These figures are the same as Figs. 4.12b and 4.13b where the results of the exact analysis and measurements are given. The degree of closeness to the peak is dependent on the Q; the higher the Q the closer the operating point can get to the peak before the approximate results begin to deteriorate. For the parallel converter this does not present a serious problem since as explained earlier it is desirable to operate this converter for $Q_p > 3$ and below resonance. For the series resonant converter, this high Q assumption must be relaxed since there is no apparent advantage in designing this converter for high Q provided of course, that the Q is not selected low enough for discontinuous conduction mode to occur (Eq. (3.25a)). For example, according to the conversion ratio characteristics in Fig. 3.8, $Q_s = 1.5$ and $F_s / F_0 = .8$ is a reasonable point to operate at, and it

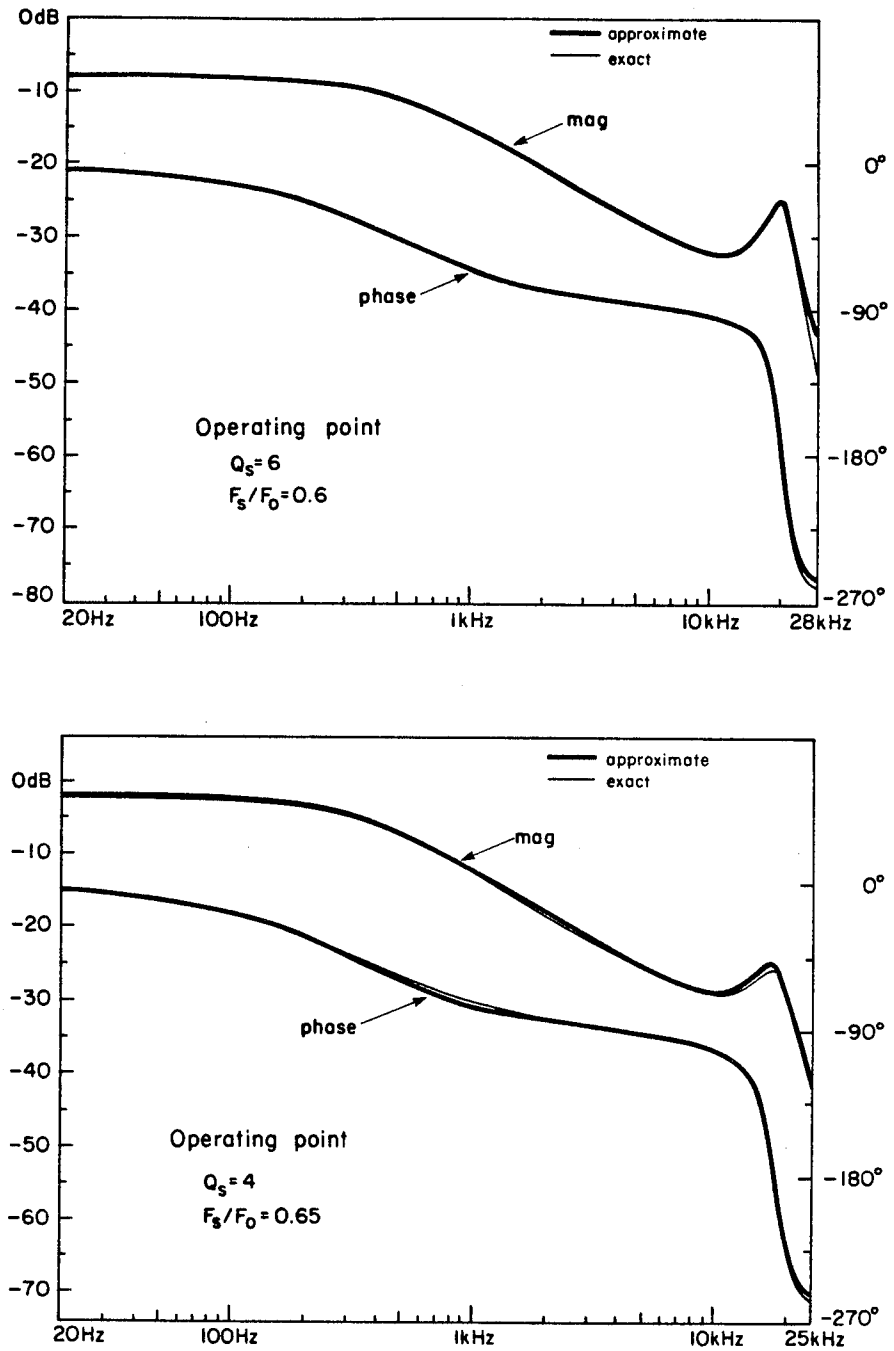

Fig. 5.5 Comparison of approximate and exact control-to-output transfer functions of the series resonant converter for high Q and operation away from the resonant peak.

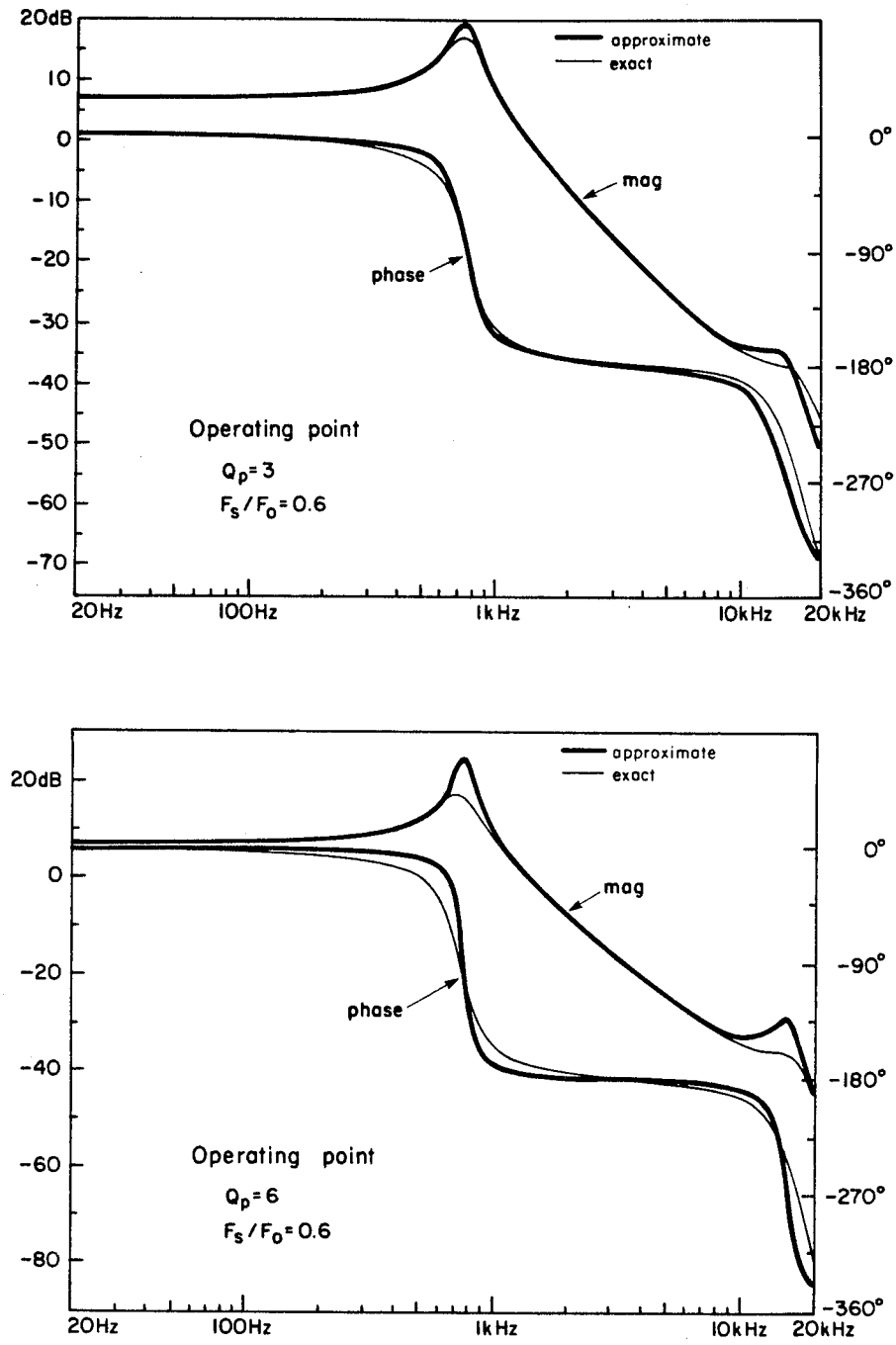

Fig. 5.6 Comparison of approximate and exact control-to-output transfer functions of the parallel resonant converter for high Q and operation away from the resonant peak.

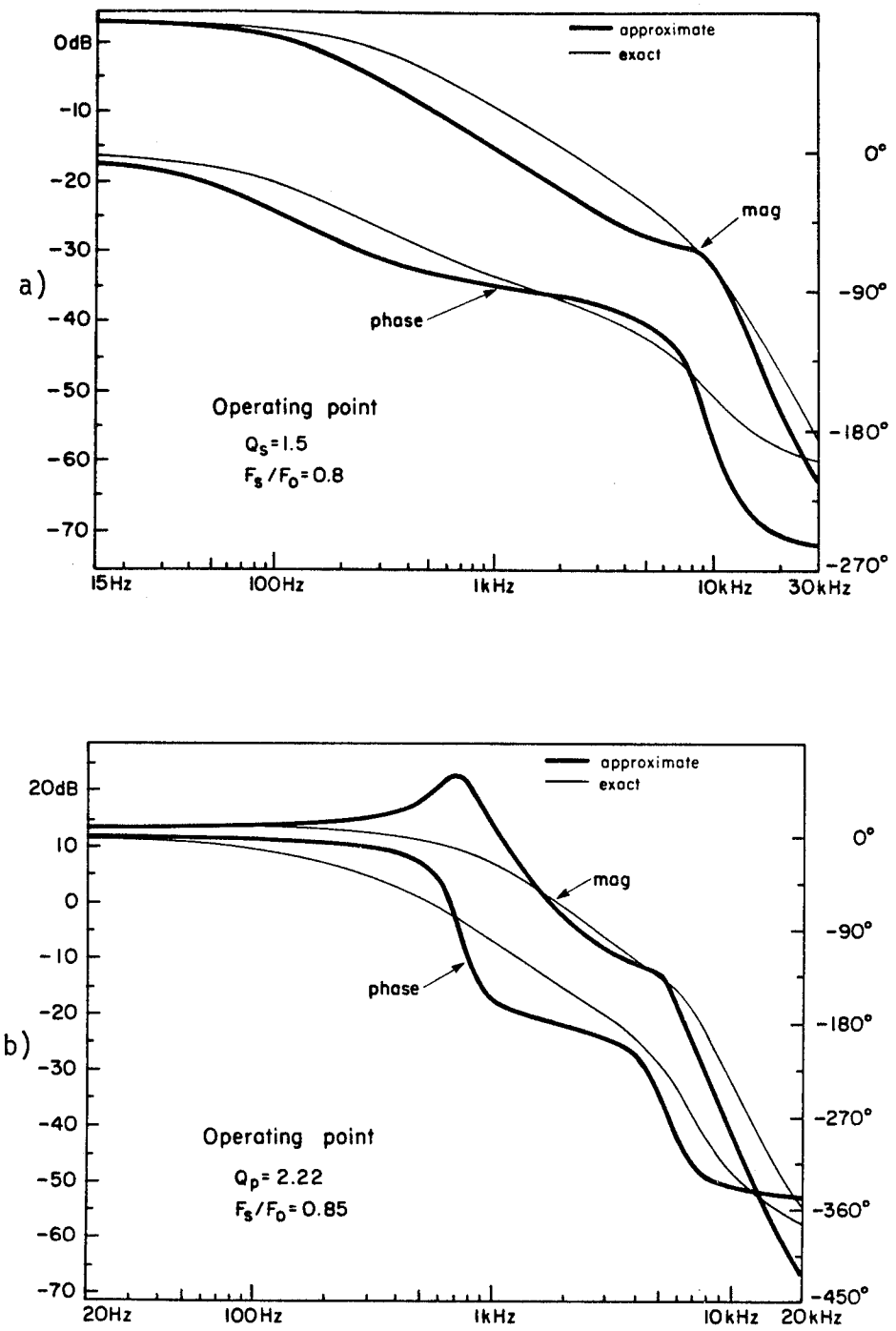

Fig. 5.7 Breakdown of approximate control-to-output transfer functions for operating points close to the resonant peak and low Q: a) for the series resonant converter and b) for the parallel resonant converter.

would be nice if the results of the approximation could be improved for this converter.

According to Fig. 5.7b the discrepancy between the exact and the approximate analysis is in the position of the dominant pole. As the operating point moves towards the peak, the dominant pole begins to move forward and is no longer given by Eq. (5.5). For $Q_s = 1.5$ and $F_s / F_0 = .8$ the dominant pole is already at twice the pole given by Eq. (5.5). This new pole that must be determined is given by

$$\omega_{fs}' = \kappa \omega_{fs} \quad ; \quad \omega_{fs} = \frac{1}{RC_f} \tag{5.11}$$

The modification factor κ is shown in Fig. 5.8 and is determined by a low-frequency numerical approximation of the exact transfer functions. The form of the transfer function given by Eq. (4.68) is

$$\frac{\langle \hat{v} \rangle (s)}{\hat{f}_s(s)} = \frac{\sum_{n=0}^{3} a_n e^{nsT_s}}{\sum_{n=0}^{3} b_n e^{nsT_s}} \quad ; \quad T_s = \frac{1}{2F_s} \tag{5.12}$$

If we let $e^{sT_s} \approx 1 + sT_s$ in $\sum_{n=0}^{3} b_n e^{nsT_s}$ then the real root of

$$\sum_{n=0}^{3} b_n (1 + sT_s)^n = 0 \tag{5.13}$$

corresponds to the dominant pole ω_{fs}' in Eq. (5.11) from which κ is determined and plotted in Fig. 5.8. It should be pointed out that the quadratic factor in Eq. (5.13) does *not* correspond to the quadratic factor in Eqs. (5.1) and (5.2) determined earlier. Also, a heuristic modification of

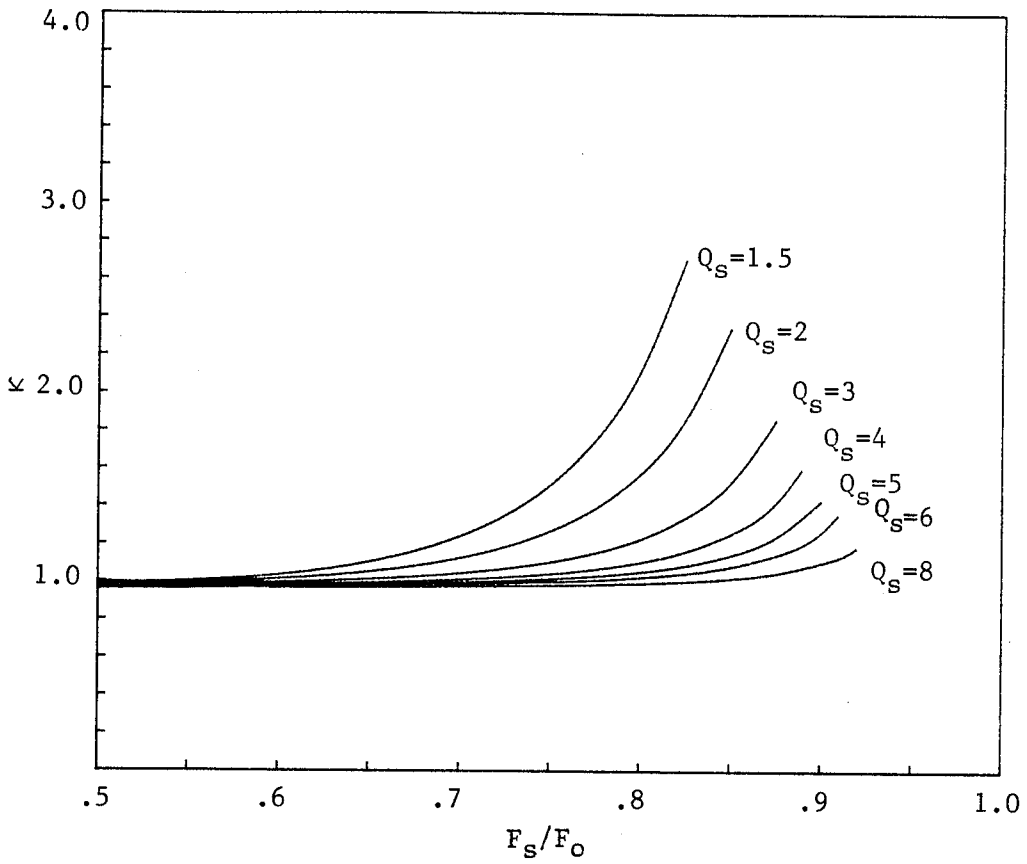

Fig. 5.8 The dominant pole modification factor, κ, of the series resonant converter.

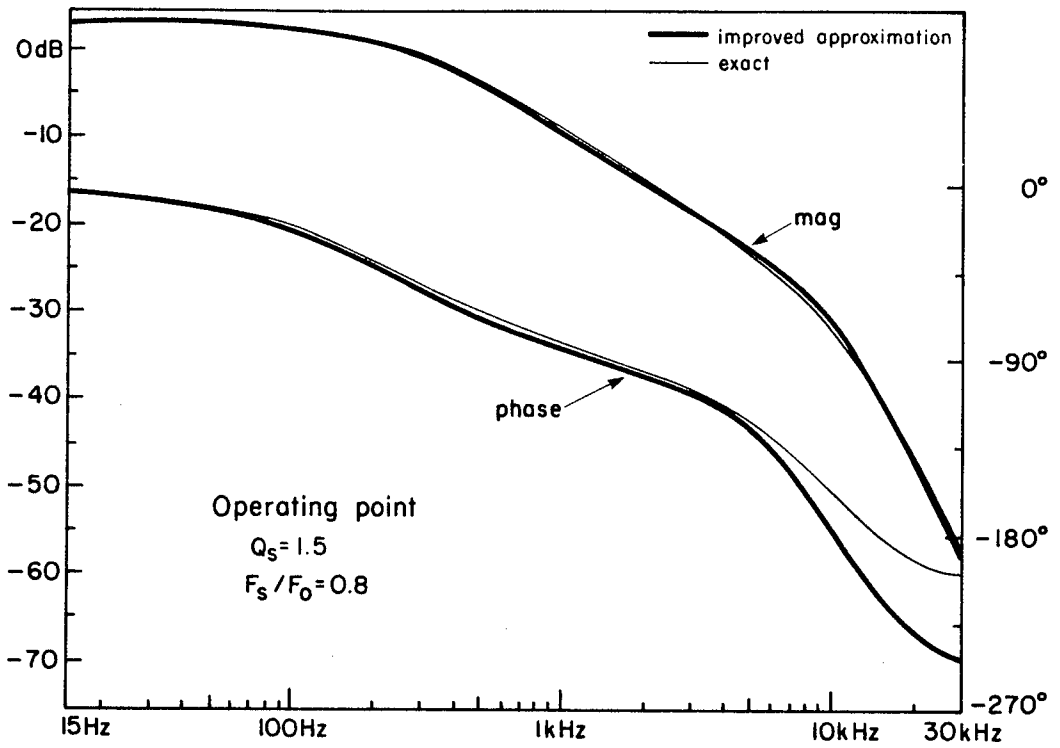

Fig. 5.9 Improved approximate control-to-output transfer function for the series resonant converter, given by Eq. (5.15), *after modification of the dominant pole and the Q by* κ.

Q_s is given by

$$Q_s' = \frac{Q_s}{\kappa} \tag{5.14}$$

where κ is the same pole modification factor shown in Fig. 5.8. The modified transfer function for the series resonant converter can now be written as

$$\frac{\hat{<v>}(s)}{\hat{f}_s(s)} = \frac{A}{\left(1+\frac{s}{\kappa\omega_{fs}}\right)\left(1+\frac{s}{\omega_{s0}}\frac{\kappa}{Q_s}+\frac{s^2}{{\omega_{s0}}^2}\right)} \tag{5.15}$$

This improved result is shown in Fig. 5.9 where it can be seen that the magnitude now is excellent agreement but there is still some discrepancy in the phase.

The approximate line-to-output transfer function is obtained by an entirely similar argument. These approximate transfer functions are the same as the control-to-output transfer functions except for the low frequency gain, which in this case is given by the conversion ratio M. For the parallel resonant converter the approximate line-to-ouput transfer function is given by

$$\frac{\hat{<v>}(s)}{\hat{v}_g(s)} = \frac{M}{\left(1+\frac{s}{\omega_{fp}Q_f}+\frac{s^2}{{\omega_{fp}}^2}\right)\left(1+\frac{s}{\omega_{s0}Q_s}+\frac{s^2}{{\omega_{s0}}^2}\right)} \tag{5.16}$$

For the series resonant converter the approximate line-to-output transfer function is given by

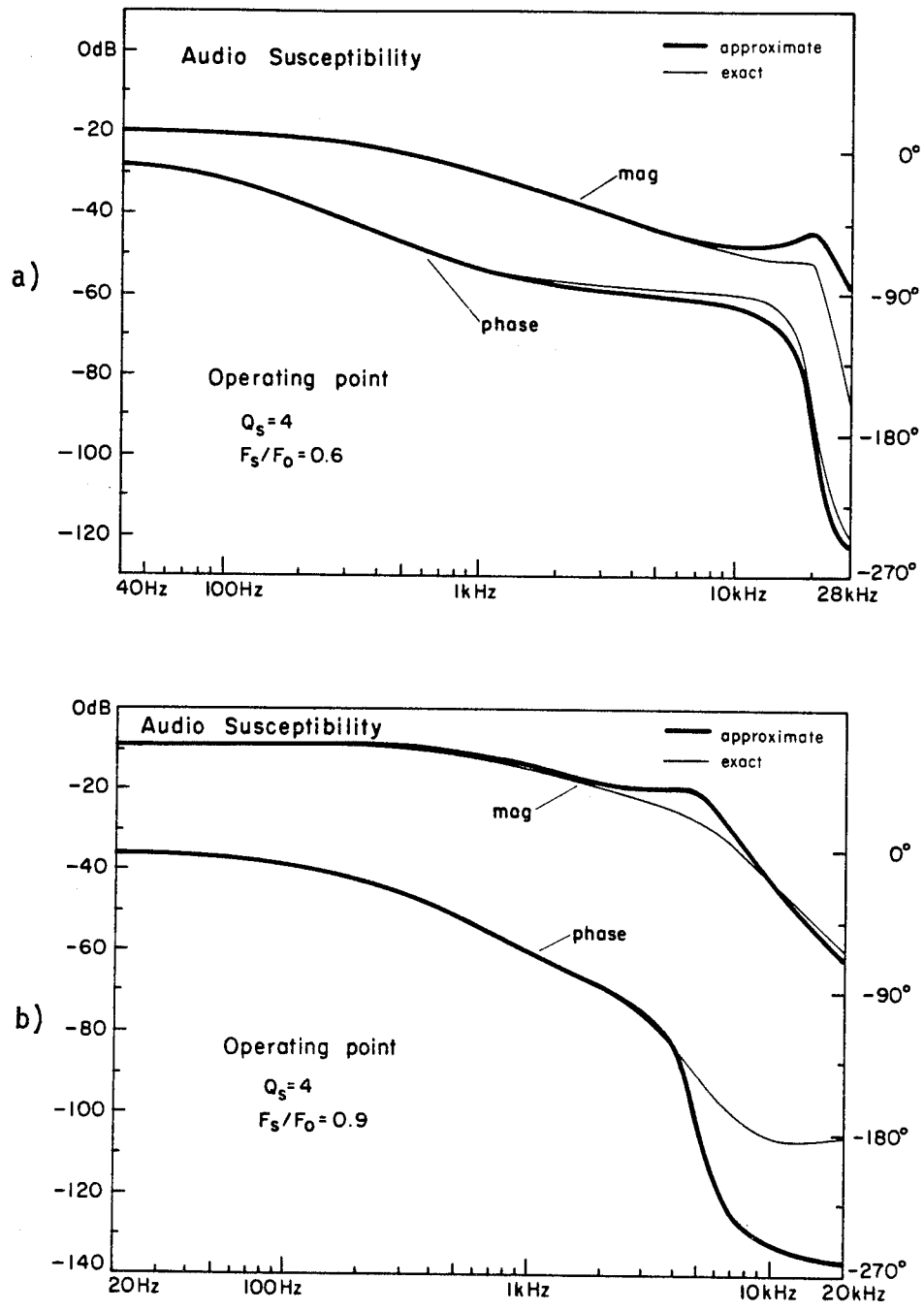

Fig. 5.10a-b Approximate and exact line-to-output transfer functions of the series resonant converter.

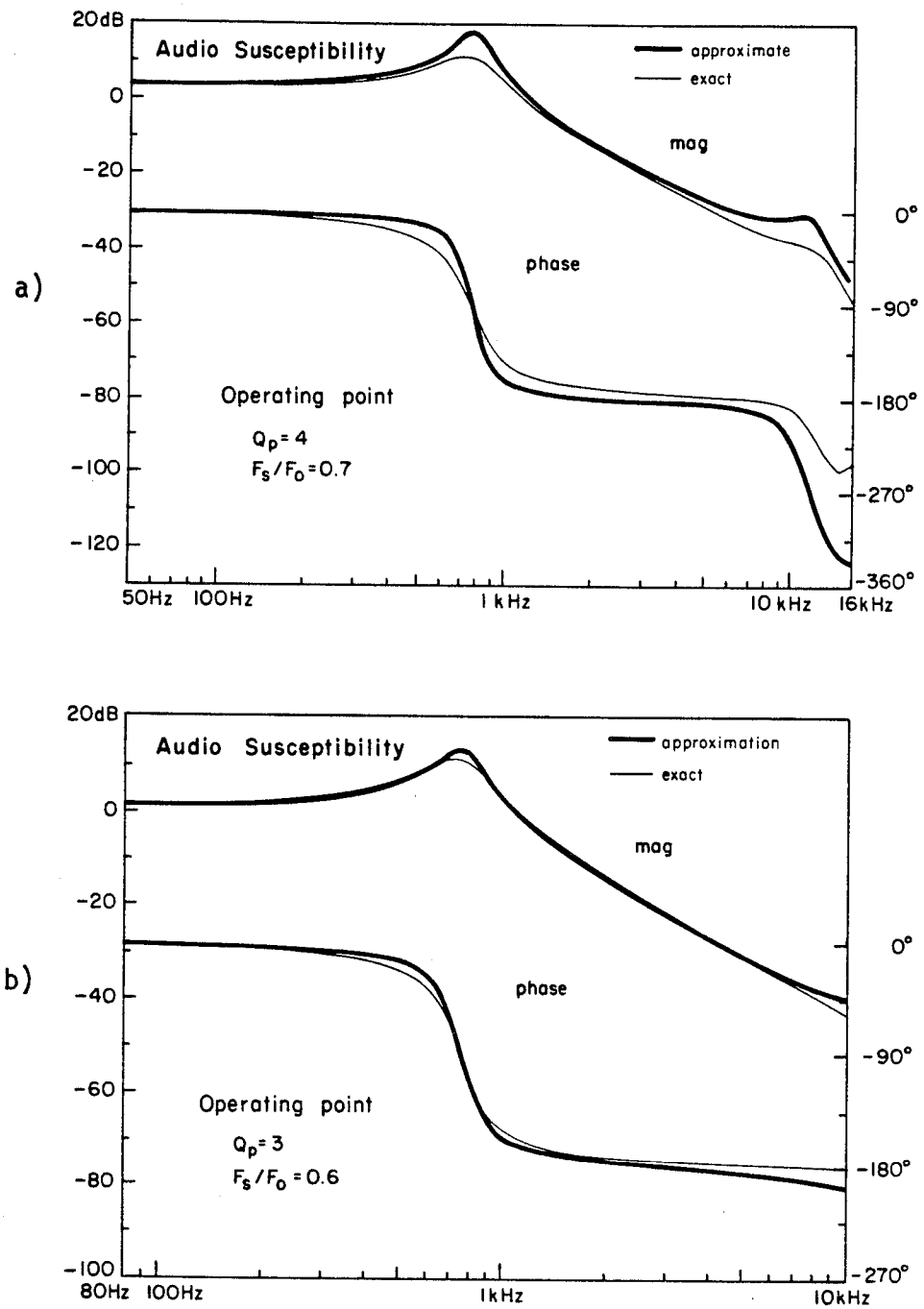

Fig. 5.11a-b Approximate and exact line-to-output transfer functions of the parallel resonant converter.

$$\frac{\hat{<v>}(s)}{\hat{v}_g(s)} = \frac{M}{\left[1+\frac{s}{\kappa\omega_{fs}}\right]\left[1+\frac{s}{\omega_{s0}}\frac{\kappa}{Q_s}+\frac{s^2}{{\omega_{s0}}^2}\right]} \tag{5.17}$$

The approximate and exact line-to-output transfer functions are compared in Figs. 5.10 and 5.11 using the same circuit values as before. Note that for the series resonant converter, the pole position in Fig. 5.10b has been modified by the factor $\kappa = 1.73$.

5.3 Conclusion

In this short chapter approximate transfer functions of the series and parallel resonant converters are given for high Q and operating points away from the resonant peak. It is shown that the dominant behavior of these transfer functions is determined by the output low-pass filter while the high-frequency behavior is given by a second order response in the denominator whose frequency is at the difference between the switching and the resonant frequency and whose Q is the same as the original resonant Q. These approximations break down for lower Q and operating points near the resonant peak. For the parallel resonant converter this breakdown of the approximate results can be ignored since this converter operates satisfactorily for $Q_p \geq 3$ and below resonance ($F_s / F_0 \leq .8$). For the series resonant converter the results are improved for lower Q since it may still be desirable to operate this converter for Q_s in the range 1.5 to 2.5. The results of the approximate and the exact analyses are in good agreement.

CHAPTER 6

CONCLUSIONS

Resonant converters belong to a class of dc-to-dc switching converters in which the circuit time constants are comparable to the switching time. For this reason their analysis is tedious and has often been neglected or given in limited and nonilluminating form. In this thesis, the load parameter, Q, and the ratio of switching frequency to the resonant frequency, F_s / F_0, are considered as the only two parameters required to characterize the operation of these converters.

The dc and small-signal ac analyses are given. In the dc analysis, the conversion ratio characteristics, peak stresses, and diode conduction time are determined in terms of Q and F_s / F_0 for the series and parallel resonant converters. In the small-signal analysis, the control-to-output transfer function, audio susceptibility, and input impedance are determined at a given operating point (Q, F_s / F_0) determined from the dc analysis.

Most of the results are obtained numerically. For the dc analysis, the only numerical routine required is a root finder, which today can be found in hand-held calculators. The results obtained are plotted in numerous useful graphs to help the engineer design as well as evaluate the performance of these converters for any specific application. In the small-signal analysis, the coefficients in the numerator and the denominator of the transfer functions are determined numerically using a root finder and a matrix multiplication routine.

To gain further insight simple and approximate transfer functions are obtained under high Q assumption.

APPENDICES

APPENDIX A

A.1 Determination of The RMS Values of the Resonant Inductor and Capacitor Currents of the Parallel Resonant Converter

The square of the rms value of the resonant current is given by

$$I_r^2 = \frac{1}{T_s}\left[\int_0^{T_a} I_R^2(t)dt + \int_{T_a}^{T_s} I_R^2(t)dt\right] \tag{A.1}$$

The resonant current in the interval $0 \leq t \leq T_a$ is given by Eq. (2.3a) which can be rewritten as

$$\frac{\omega_0 L_0}{V_g} I_R(t) = -\frac{M}{Q_p} + \sec(\omega_0\beta)\left[1 - \frac{V_R(0)}{V_g}\right]\sin\omega_0(t-\beta) \tag{A.2}$$

where β is given by Eq. (2.29). In the interval $T_a \leq t \leq T_s$, $I_R(t)$ is given by Eq. (2.29)

$$\frac{\omega_0 L_0}{V_g} I_R(t) = -\frac{M}{Q_p} + \sec(\omega_0\alpha)\sin\omega_0(t - T_a + \alpha) \tag{A.3}$$

where α is given by Eq. (2.14). Integration in Eq. (A.1) gives

$$I_r^2 = \frac{{V_g}^2}{{\omega_0}^2 {L_0}^2} B_r \tag{A.4}$$

where B_r is given by

$$B_r = A^2 + \frac{B^2}{2} + (C^2 - B^2)\frac{\omega_0 T_a}{2\gamma}$$

$$+\frac{2A}{\gamma}\left[C(\cos\omega_0(T_a-\beta)-\cos\omega_0\beta) - B(\cos(\gamma-\omega_0 T_a+\omega_0\alpha)-\cos\omega_0\alpha)\right]$$

$$-\frac{1}{4\gamma}\left[C^2(\sin2\omega_0(T_a-\beta)+\sin2\omega_0\beta)+B^2(\sin2(\gamma-\omega_0 T_a+\omega_0\alpha)-\sin2\omega_0\alpha)\right] \tag{A.5}$$

where

$$A = \frac{M}{Q_p} \tag{A.6}$$

$$B = \sec\omega_0\alpha \tag{A.7}$$

$$C = \sec\omega_0\beta\left[1-\frac{V_R(0)}{V_g}\right] \tag{A.8}$$

The current through the resonant capacitor, $I_c(t)$, is equal to the difference between the resonant inductor current and the reflected load current. In the interval $0 \le t \le T_a$, $I_c(t)$ is given by

$$I_c(t) = \sec(\omega_0\beta)\left[1-\frac{V_R(0)}{V_g}\right]\sin\omega_0(t-\beta) \tag{A.9}$$

and in the interval $T_a \le t \le T_s$, $I_c(t)$ is given by

$$I_c(t) = \sec(\omega_0\alpha)\sin\omega_0(t-T_a+\alpha) \tag{A.10}$$

The rms square value is then given by

$$I_c^2 = \frac{V_g^2}{\omega_0^2 L_0^2} B_c \tag{A.11}$$

where B_c is given by

$$B_c = \frac{B^2}{2} + (C^2 - B^2)\frac{\omega_0 T_a}{2\gamma}$$

$$-\frac{1}{4\gamma}\left[C^2(\sin 2\omega_0(T_a - \beta) + \sin 2\omega_0\beta) + B^2(\sin 2(\gamma - \omega_0 T_a + \omega_0\alpha) - \sin 2\omega_0\alpha)\right] \tag{A.12}$$

APPENDIX B

B.1 Determination of $G_s(M,Q_s,\gamma)=0$ in the Range $1/2 \le F_s/F_0 \le 1$

Expansion of Eq. (3.18) gives

$$\cos\gamma\cos\omega_0 T_a + \sin\gamma\sin\omega_0 T_a = \frac{1+M-M^2K}{1+M-MK} \tag{B.1}$$

The resonant current, $I_R(t)$, in the interval $0 \le t \le T_a$ is given by Eq. (3.5a) which, after substitution of $V_R(0)$ and $I_R(0)$ given by Eqs. (3.15) and (3.16) respectively, is rewritten here as

$$I_R(t) = \omega_0 C_0 V_g \frac{1-M+M^2K}{\cos\omega_0 T_a}\sin\omega_0(t-T_a) \tag{B.2}$$

Similarly, the current in the interval $T_a \le t \le T_s$, given by Eq. (3.6a), is rewritten after substitution of $V_R(T_a)$, given by Eq. (3.13), as

$$I_R(t) = \omega_0 C_0 V_g [1+M-MK]\sin\omega_0(t-T_a) \tag{B.3}$$

The positive areas A_1 and A_2, shown in Fig. 3.3, are determined by integration of Eqs. (B.2) and (B.3).

$$A_1 = \int_0^{T_a} I_R(t)dt = C_0 V_g (1-M+M^2K)(1-\sec\omega_0 T_a) \tag{B.4}$$

$$A_2 = -\int_{T_a}^{T_s} I_R(t)dt = C_0 V_g (1+M-MK)(\cos(\gamma-\omega_0 T_a)-1) \tag{B.5}$$

Substitution of $\cos(\gamma-\omega_0 T_a)$ from Eq. (3.18) in Eq. (B.5) gives

$$A_2 = C_0 V_g MK(1-M) \tag{B.6}$$

From Eqs. (3.11) and (3.13) we have

$$A_1 + A_2 = C_0 V_g 2MK \tag{B.7}$$

Substitution of Eqs. (B.4), (B.6), and (B.7) gives

$$\cos\omega_0 T_a = \frac{1-M+M^2K}{1-M-MK} \tag{B.8}$$

The expression for $\sin\omega_0 T_a$ follows from Eq. (B.8)

$$\sin\omega_0 T_a = \frac{\sqrt{(1-M^2)(MK-2)MK}}{MK+M-1} \tag{B.9}$$

Substitution of Eqs. (B.8) and (B.9) in Eq. (B.1) gives the implicit equation $G_s(M,Q_s,\gamma)=0$ in Eq. 3.19 from which the conversion ratio is determined for a given Q_s and F_s/F_0.

In deriving Eq. (B.9) from Eq. (B.8), we made sure that the sign of the denominator was positive because $\sin\omega_0 T_a \geq 0$. For operation in the range $1/2 \leq F_s/F_0 \leq 1$, it is important to note that the range of $\omega_0 T_a$ is given by

$$\frac{\pi}{2} \leq \omega_0 T_a \leq \pi \tag{B.10}$$

which implies

$$\cos\omega_0 T_a \leq 0 \quad \text{and} \quad \sin\omega_0 T_a \geq 0 \tag{B.11}$$

In [6] and [7] it is assumed that the range of $\omega_0 T_a$ is given by $0 < \omega_0 T_a \leq \pi$, which does not restrict the range of $\omega_0 T_a$ properly. It should be clear from

Fig. B.1, that if $\omega_0 T_a \leq \pi/2$ then $A_1 - A_2 \leq 0$ which implies negative conversion ratio. Hence the proper range of $\omega_0 T_a$, when the converter is operating in the range $1/2 \leq F_s / F_0 \leq 1$, is given by Eq. (B.10).

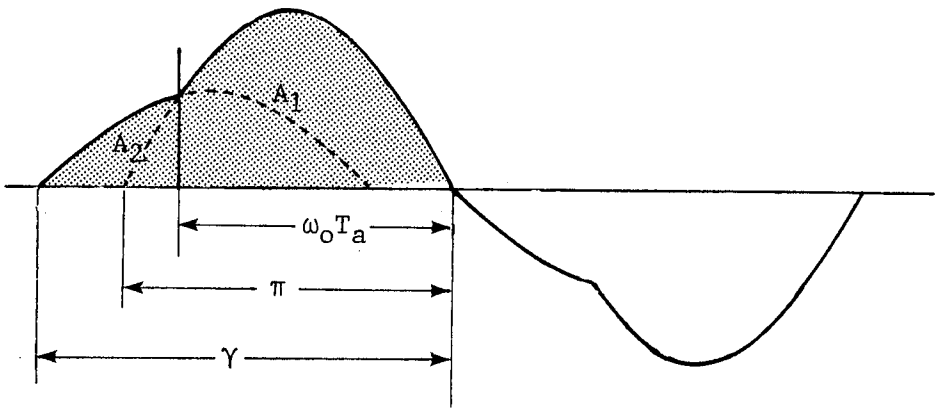

Fig. B.1 The resonant current of the series resonant converter in the range $1/2 \leq F_s / F_0 \leq 1$. $\omega_0 T_a$ is always larger than $\pi/2$ and less than π, otherwise if $\omega_0 T_a < \pi/2$ then $A_1 - A_2 \leq 0$ and the conversion ratio will be negative which is impossible.

B.2 Determination of $G_s(M, Q_s, \gamma) = 0$ in the Range $F_s / F_0 \geq 1$

It can be seen that in this range of operation, M, V_{peak}, and $V_R(0)$ are still given by Eqs. (3.9), (3.11), (3.13), and (3.15) as in the case of operation in the range $1/2 \leq F_s / F_0 \leq 1$.

$$M = \frac{A_1 - A_2}{A_1 + A_2} \tag{B.12}$$

$$V_{peak} = V_R(T_a) = \frac{1}{C_0} \frac{A_1 + A_2}{2} = MKV_g \tag{B.13}$$

$$V_R(0) = -M^2 K V_g \tag{B.14}$$

The resonant current in the interval $0 \leq t \leq T_a$ is given by

$$I_R(t) = \omega_0 C_0 [V_g + V_0 - V_R(0)] \sin\omega_0 t + I_R(0)\cos\omega_0 t \tag{B.15}$$

and in the interval $T_a \leq t \leq T_s$, $I_R(t)$ is given by

$$I_R(t) = \omega_0 C_0 [V_g - V_0 + V_R(T_a)] \sin\omega_0 (t - T_a) \tag{B.16}$$

Substitution of $V_R(0)$ and $V_R(T_a)$ gives for $I_R(t)$ in the interval $0 \leq t \leq T_a$

$$I_R(t) = \omega_0 C_0 V_g [1 + M + M^2 K] \sin\omega_0 t + I_R(0)\cos\omega_0 t \tag{B.17}$$

and for the interval $T_a \leq t \leq T_s$

$$I_R(t) = \omega_0 C_0 V_g [1 - M + MK] \sin\omega_0 (t - T_a) \tag{B.18}$$

The requirement $I_R(T_a) = 0$ in Eq. (B.17) gives

$$I_R(0) = -\omega_0 C_0 V_g [1 + M + M^2 K] \tan\omega_0 T_a \tag{B.19}$$

which when substituted in Eq. (B.17) gives

$$I_R(t) = \omega_0 C_0 V_g \frac{1 + M + M^2 K}{\cos\omega_0 T_a} \sin\omega_0 (t - T_a) \tag{B.20}$$

Similarly the equations for $V_R(t)$, given by Eqs. (3.40b) and (3.41b), are obtained. The requirements $V_R(0) = -V_R(T_s)$ and $I_R(0) = -I_R(T_s)$ gives

$$\sin(\gamma - \omega_0 T_a) = \frac{1 + M + M^2 K}{1 - M + MK} \tan\omega_0 T_a \tag{B.21}$$

$$\cos(\gamma-\omega_0 T_a) = \frac{1-M-M^2K}{1-M+MK} \tag{B.22}$$

Expansion of Eq. (B.22) gives

$$\cos\gamma\cos\omega_0 T_a + \sin\gamma\sin\omega_0 T_a = \frac{1-M-M^2K}{1-M+MK} \tag{B.23}$$

Next, the angle $\omega_0 T_a$ is determined. The positive areas A_1 and A_2, shown in Fig. 3.13, are determined by integration of $I_R(t)$.

$$A_2 = -\int_0^{T_a} I_R(t)dt = C_0 V_g [1+M+M^2K][\sec\omega_0 T_a - 1] \tag{B.24}$$

$$A_1 = \int_{T_a}^{T_s} I_R(t)dt = C_0 V_g [1-M+MK][1-\cos(\gamma-\omega_0 T_a)] \tag{B.25}$$

Substitution of Eq. (B.22) in Eq. (B.25) gives

$$A_1 = C_0 V_g MK[1+M] \tag{B.26}$$

Substitution of Eqs. (B.13), (B.24), and (B.26) in Eq. (B.12) gives

$$\cos\omega_0 T_a = \frac{1+M+M^2K}{M(K+1)+1} \tag{B.27}$$

The expression for $\sin\omega_0 T_a$ follows immediately from Eq. (B.27)

$$\sin\omega_0 T_a = \frac{\sqrt{(1-M^2)(MK+2)MK}}{1+M(K+1)} \tag{B.28}$$

Substitution of Eqs. (B.27) and (B.28) in Eq. (B.23) gives the implicit Equation (3.38), $G_s(M,Q_s,\gamma)=0$, from which the conversion ratio M is determined for a given Q_s and F_s/F_0.

When the converter is operating in the range $F_s / F_0 \geq 1$, it is important to note that the range of $\omega_0 T_a$ is given by

$$0 \leq \omega_0 T_a \leq \frac{\pi}{2} \tag{B.29}$$

which implies that

$$\sin\omega_0 T_a \geq 0 \quad \text{and} \quad \cos\omega_0 T_a \geq 0 \tag{B.30}$$

The range given in Eq. (B.29) ensures that $A_1 - A_2 \geq 0$ so that the conversion ratio M is always positive. It is clear from Fig. B.2 that if $\omega_0 T_a \geq \pi/2$, then $A_1 - A_2 \leq 0$ which implies negative conversion ratio which of course is impossible.

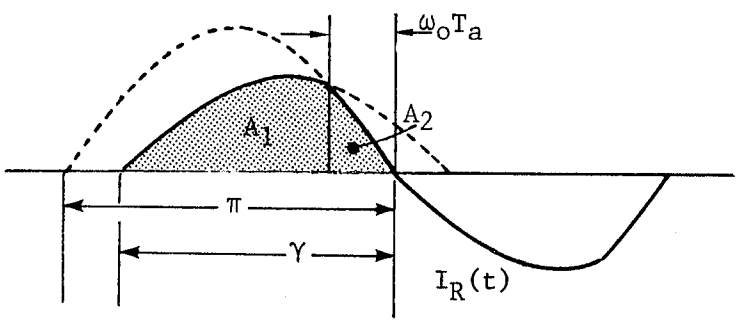

Fig. B.2 The resonant current of the series resonant converter in the range $F_s / F_0 \geq 1$. In this case $\omega_0 T_a$ is always less than $\pi/2$, otherwise if $\omega_0 T_a > \pi/2$ then $A_1 - A_2 \leq 0$ and the conversion ratio will be negative which is impossible.

B.3 Derivation of the Equations in Discontinuous Conduction Mode

Equations (3.54), (3.61), and (3.62) are repeated here

$$A_m = 2C_0[V_g + (-1)^m V_0 - V_{cm}](-1)^{m+1} \tag{B.31}$$

$$V_{cm} = V_{cm-1} + (-1)^m \frac{A_{m-1}}{C_0} \tag{B.32}$$

$$V_{c1} = -MKV_0 = -M^2KV_g \tag{B.33}$$

A recurrence expression for A_m is obtained now by writing the first few terms of A_m. For $m=1$, A_1 is given by

$$A_1 = 2C_0[V_g - V_0 - V_{c1}] \tag{B.34}$$

Substitution of Eq. (B.33) in Eq. (B.34) gives

$$A_1 = 2C_0V_g[1 - M + M^2K] \tag{B.35}$$

From Eq. (B.32) V_{c2} is determined next

$$V_{c2} = V_{c1} + \frac{A_1}{C_0} = 2V_g[1 - M + \frac{M^2K}{2}] \tag{B.36}$$

From Eq. (B.31) A_2 is given by

$$A_2 = -2C_0[V_g + V_0 - V_{c2}] \tag{B.37}$$

Substitution of Eq. (B.36) in Eq. (B.37) gives

$$A_2 = 2C_0V_g[1 - 3M + M^2K] \tag{B.38}$$

When V_{c3}, determined by substitution of Eqs. (B.36) and (B.38) in Eq. (B.32),

is substituted in Eq. (B.31) the expression for A_3 is obtained

$$A_3 = 2C_0V_g[1-5M+M^2K] \tag{B.39}$$

From Eqs. (B.35), (B.38), and (B.39) the recurrence relation for A_m, given by Eq. (3.63), becomes clear

$$A_m = 2C_0V_g[1-(2m-1)M+M^2K] \tag{B.40}$$

The summation in Eq. (3.59) is written as

$$S_n = \sum_{m=1}^{n} A_m(-1)^{m+1} \tag{B.41}$$

The sequence of partial sums S_n for even n are computed as

$$S_2 = A_1 - A_2 = 2C_0V_g(2M) \tag{B.42a}$$

$$S_4 = S_2 + A_3 - A_4 = 2C_0V_g(4M) \tag{B.42b}$$

$$\vdots$$

$$S_n = S_{n-2} + A_{n-1} - A_n = 2C_0V_g(nM) \tag{B.42c}$$

Substitution of Eq. (B.42c) in Eq. (3.59) gives the conversion ratio of even type n dcm

$$M = \frac{n}{K} \tag{B.43}$$

To determine the conversion ratio for odd type n dcm, the summation in Eq. (3.59) is computed for odd n. The sequence of partial sums, S_n, for odd n is given by

$$S_1 = A_1 = 2C_0V_g[1-M+M^2K] \tag{B.44a}$$

$$S_3 = A_1-A_2+A_3 = 2C_0V_g[1-3M+M^2K] \tag{B.44b}$$

$$\vdots$$

$$S_n = S_{n-2}-A_{n-1}+A_n = 2C_0V_g[1-nM+M^2K] \tag{B.44c}$$

Substitution of Eq. (B.44c) in Eq. (3.59) gives the conversion ratio for odd type n dcm

$$M = \frac{1}{n} \tag{B.45}$$

The peak stresses are now easily determined. Since $V_{peak} = V_{c2}$, substitution of Eq. (B.43) in Eq. (B.36) gives Eq. (3.66) and substitution of Eq. (B.45) in Eq. (B.36) gives Eq. (3.69). The peak resonant current is given by the amplitude of $i_1(t)$ in Eq. (3.53)

$$\omega_0C_0V_g[1-M-\frac{V_{c1}}{V_g}] = \omega_0C_0V_g[1-M+M^2K] \tag{B.46}$$

in which if M is substituted for odd and even type n dcm the corresponding expressions for I_{peak} are obtained.

B.4 Derivation of the Equations for +type n ccm

The area under each complete half-cycle of the resonant current, $i_m(t)$, is given by

$$A_m = \int_0^{T_0/2} |i_m(t)|\,dt = 2C_0[V_g + V_0(-1)^{m+1} - V_{cm}](-1)^m \qquad \text{(B.47)}$$

The recursive relation for A_m, given by Eq. (3.82), is determined next. From Eq. (B.47) we have for m = 1 and 2

$$A_1 = -2C_0[V_g + V_0 - V_{c1}] \qquad \text{(B.48)}$$

$$A_2 = 2C_0[V_g - V_0 - V_{c2}] \qquad \text{(B.49)}$$

V_{c1} is related to V_{c2} by

$$V_{c2} = V_{c1} - \frac{A_1}{C_0} \qquad \text{(B.50)}$$

Substitution of Eqs. (B.48) and (B.50) in Eq. (B.49) gives

$$A_2 = 2C_0[V_{c1} - 3V_0 - V_g] \qquad \text{(B.51)}$$

Following the same procedure we get for m = 3

$$A_3 = 2C_0[V_{c1} - 5V_0 - V_g] \qquad \text{(B.52)}$$

From Eqs. (B.48), (B.51) and (B.52), the recursive relation of A_m, given by Eq. (3.82), becomes apparent

$$A_m = 2C_0[V_{c1} - (2m-1)V_0 - V_g] \qquad \text{(B.53)}$$

The summation in the numerator of Eq. (3.80) is determined next. This summation is denoted by S_n

$$S_n = \sum_{m=1}^{n} A_m(-1)^m \tag{B.54}$$

The recursive expression for S_n, given in Eq. (3.83), follows from the expressions of the first few terms of Eq. (B.54) given by

$$S_2 = -A_1 + A_2 = -2C_0(2V_0) \tag{B.55a}$$

$$S_4 = S_2 - A_3 + A_4 = -2C_0(4V_0) \tag{B.55b}$$

$$\vdots$$

$$S_n = S_{n-2} - A_{n-1} + A_n = -2C_0(nV_0) \tag{B.55c}$$

The currents $i_{01}(t)$ and $i_{02}(t)$, shown in Figs. 3.19a and 3.20a are given by

$$i_{01}(t) = I_R(0)\cos\omega_0 t + (V_g - V_0 - V_R(0))\omega_0 C_0 \sin\omega_0 t \tag{B.56a}$$

$$i_{02}(t) = \omega_0 C_0[-V_g - V_0 - V_R(-T_b)]\sin\omega_0(t + T_b) \tag{B.56b}$$

The initial capacitor voltage, $V_R(0)$, is determined as follows

$$V_R(T_s) = V_R(0) + \frac{1}{C_0}\left[A_{01} + \sum_{m=1}^{n} A_m(-1)^m - A_{02}\right] \tag{B.57}$$

Since $V_R(0) = -V_R(T_s)$, we get from Eq. (B.57)

$$-2V_R(0) = \frac{1}{C_0}\left[\sum_{m=1}^{n} A_m(-1)^m + A_{01} - A_{02}\right] \tag{B.58}$$

Substitution of Eq. (3.79) in Eq. (3.80) gives

$$\sum_{m=1}^{n} A_m(-1)^m + A_{01} - A_{02} = 2MC_0V_0K = 2C_0V_gM^2K \tag{B.59}$$

Substitution of Eq. (B.59) in (B.58) gives

$$V_R(0) = -M^2KV_g \tag{B.60}$$

Substitution of Eq. (B.60) in (B.56a) and the requirement $i_{01}(T_a)=0$ gives

$$I_R(0) = -\omega_0C_0V_g[1-M+M^2K]\tan\omega_0T_a \tag{B.61}$$

Substitution of Eqs. (B.61) and (B.60) in Eq. (B.56a) gives

$$i_{01}(t) = \omega_0C_0V_g\frac{1-M+M^2K}{\cos\omega_0T_a}\sin(\omega_0t-\omega_0T_a) \tag{B.62}$$

which is Eq. (3.84). The area, A_{01}, is given by

$$A_{01} = \int_0^{T_a} = C_0V_g[1-M+M^2K][1-\sec\omega_0T_a] \tag{B.63}$$

The area, A_{02}, is given by integrating Eq. (B.56b)

$$A_{02} = \int_{-T_b}^{0} i_{02}(t)dt = C_0[V_g+V_0+V_R(-T_b)][\cos\omega_0T_b-1] \tag{B.64}$$

$V_R(-T_b)$ is related to $V_R(0)$ by

$$V_R(-T_b) = V_R(0) - \frac{A_{02}}{C_0} = -M^2KV_g - \frac{A_{02}}{C_0} \tag{B.65}$$

Substitution of Eq. (B.65) in Eq. (B.64) gives for A_{02}

$$A_{02} = C_0V_g[M^2K-M-1][\sec\omega_0T_b-1] \tag{B.66}$$

Since $T_b = T_s - \frac{nT_0}{2} - T_a$ we have

$$\cos\omega_0 T_b = \cos(\gamma - n\pi - \omega_0 T_a) = \cos(\gamma - \omega_0 T_a) \qquad n = 0,2,4,6,... \qquad (B.67)$$

The area, A_{02}, is now rewritten as

$$A_{02} = C_0 V_g [M^2 K - M - 1][\sec(\gamma - \omega_0 T_a) - 1] \qquad (B.68)$$

Substitution of Eq. (B.68) in (B.65) gives

$$V_R(-T_b) = -MV_g - V_g - V_g [M^2 K - M - 1]\sec(\gamma - \omega_0 T_a) \qquad (B.69)$$

Substitution of Eq. (B.69) in Eq. (B.56b) gives Eq. (3.85) for $i_{02}(t)$

$$i_{02}(t) = \omega_0 C_0 V_g \frac{M^2 K - M - 1}{\cos(\gamma - \omega_0 T_a)} \sin(\omega_0 t - \omega_0 T_a + \gamma) \qquad (B.70)$$

Substitution of Eq. (3.83), or Eq. (B.55c), and Eq. (3.79) in Eq. (3.80) gives

$$M = \frac{-2nC_0 V_0 + A_{01} - A_{02}}{2V_0 C_0 K} \qquad (B.71)$$

Substitution of A_{01} and A_{02} from Eqs. (B.63) and (B.68) in Eq. (B.71) gives

$$2M(n+1) = [1 + M - M^2 K]\sec(\gamma - \omega_0 T_a) - [1 - M + M^2 K]\sec\omega_0 T_a \qquad (B.72)$$

Also the requirement $i_{01}(0) = i_{02}(0)$ gives

$$\tan(\gamma - \omega_0 T_a) = \frac{1 - M + M^2 K}{1 + M - M^2 K} \tan\omega_0 T_a \qquad (B.73)$$

Equations (B.72) and (B.73) are solved simultaneously as follows. In Eqs. (B.72) and (B.73) let

$$C = 1 + M - M^2K \quad \text{and} \quad D = 1 - M + M^2K \tag{B.74}$$

Equations (B.72) and (B.73) can be written as

$$\sec(\gamma - \omega_0 T_a) = \frac{D}{C}\sec\omega_0 T_a + \frac{2M(n+1)}{C} \tag{B.75}$$

$$\tan(\gamma - \omega_0 T_a) = \frac{D}{C}\tan\omega_0 T_a \tag{B.76}$$

Squaring both sides of Eq. (B.76) and using the identity $tn^2 = sc^2 - 1$ we get

$$\sec^2(\gamma - \omega_0 T_a) = \frac{D^2}{C^2}(\sec^2\omega_0 T_a - 1) + 1 \tag{B.77}$$

Squaring both sides of Eq. (B.75)

$$\sec^2(\gamma - \omega_0 T_a) = \frac{D^2}{C^2}\sec^2\omega_0 T_a + 4M^2\frac{(n+1)^2}{C^2} + 4MD\frac{n+1}{C^2}\sec\omega_0 T_a \tag{B.78}$$

Equating Eqs. (B.78) and (B.77) we get

$$\cos\omega_0 T_a = \frac{1 - M + M^2K}{1 - M(n+1)^2 - MK}(n+1) \tag{B.79}$$

$\sin\omega_0 T_a$ follows from Eq. (B.79)

$$\sin\omega_0 T_a = \frac{\sqrt{[MK + n][M^2(n+1)^2 - 1][n + 2 - MK]}}{MK + M(n+1)^2 - 1} \tag{B.80}$$

In obtaining Eq. (B.80) from Eq. (B.79) we made sure the sign of the denominator was positive by realizing that $M \geq 1/(n+1)$ because $\sin\omega_0 T_a$ must be positive. Substitution of Eq. (B.79) in Eq. (B.72) gives

$$\cos(\gamma-\omega_0 T_a) = \frac{1+M-M^2K}{1+M(n+1)^2-MK}(n+1) \tag{B.81}$$

which upon expansion gives

$$\cos\gamma\cos\omega_0 T_a + \sin\gamma\sin\omega_0 T_a = \frac{1+M-M^2K}{1+M(n+1)^2-MK}(n+1) \tag{B.82}$$

Substitution of Eqs. (B.79) and (B.80) in Eq. (B.82) gives the implicit equation $G_{s+}(M,Q_s,\gamma,n)=0$ in Eq. (3.88).

The peak stresses are easily determined now. According to Fig. 3.19a V_{peak} is given by

$$V_{peak} = V_{c1} = V_R(0)+\frac{A_{01}}{C_0} \tag{B.83}$$

Substitution of Eqs. (B.60), (B.63) and (B.79) in Eq. (B.83) gives Eq. (3.89). The peak resonant current, I_{peak}, according to Fig. 3.19a, is given by the amplitude of $i_{01}(t)$ which from Eq. (B.62) is given by

$$I_{peak} = \omega_0 C_0 V_g \left| \frac{1-M+M^2K}{\cos\omega_0 T_a} \right| \tag{B.84}$$

Substitution of Eq. (B.79) in Eq. (B.84) gives Eq. (3.90).

B.5 Derivation of The Equations For –type n ccm

Since the analysis of –type n ccm is very similar to the analysis of +type n ccm, given in the previous section, only the key equations are given in this section. Referring to Fig. 3.19b we proceed as before by equating input and output powers and obtain

$$M = \frac{-\sum_{m=1}^{n} A_m(-1)^m + A_{01} - A_{02}}{\sum_{m=1}^{n} A_m + A_{01} + A_{02}} \tag{B.85}$$

The output voltage is given by the product of the average rectified resonant current and the load R

$$V_0 = <|I_R(t)|>R = \frac{R}{T_s}\left(\sum_{m=1}^{n} A_m + A_{01} + A_{02}\right) \tag{B.86}$$

The recursive relation for areas, A_m, under each complete half-cycle is determined exactly as before and is given by

$$A_m = 2C_0[V_g - (2m-1)V_0 - V_{c1}] \tag{B.87}$$

where V_{c1}, shown in Fig. 3.19b, is the resonant capacitor voltage at the beginning of the first complete half-cycle. The summation in the numerator of Eq. (B.85) is determined using Eq. (B.87) which for even n gives

$$\sum_{m=1}^{n} A_m(-1)^m = -2nC_0V_0 \qquad n = 0,2,4,6,.... \tag{B.88}$$

Substitution of Eqs. (B.88) and (B.86) in Eq. (B.85) gives

$$M = \frac{2nC_0V_0 + A_{01} - A_{02}}{2C_0V_0K} \tag{B.89}$$

To complete the analysis, the currents $i_{01}(t)$ and $i_{02}(t)$ must be determined. These are easily given by

$$i_{01}(t) = \omega_0 C_0 V_g \frac{1-M-M^2K}{\cos(\gamma-\omega_0 T_a)} \sin\omega_0 t \tag{B.90}$$

$$i_{02}(t) = \omega_0 C_0 V_g \frac{1+M+M^2K}{\cos\omega_0 T_a} \sin(\gamma-\omega_0 t) \tag{B.91}$$

where the time origin for these equations has been shifted to the beginning of $i_{01}(t)$ as shown in Fig. 3.20b. The areas A_{01} and A_{02} are given by

$$A_{01} = C_0 V_g [1-M-M^2K][\sec(\gamma-\omega_0 T_a)-1] \tag{B.92}$$

$$A_{02} = C_0 V_g [1+M+M^2K][\sec\omega_0 T_a - 1] \tag{B.93}$$

Substitution of A_{01} and A_{02} in Eq. (B.89) gives

$$2M(\mathrm{n}+1) = (1+M+M^2K)\sec\omega_0 T_a - (1-M-M^2K)\sec(\gamma-\omega_0 T_a) \tag{B.94}$$

The requirement $i_{01}(T_b) = i_{02}(T_b)$ and use of $T_b = T_s - \frac{\mathrm{n}T_0}{2} - T_a$ give

$$\frac{1+M+M^2K}{1-M-M^2K} \tan\omega_0 T_a = \tan(\gamma-\omega_0 T_a) \tag{B.95}$$

Equations (B.94) and (B.95) are solved simultaneously to eliminate $\omega_0 T_a$. We then have

$$\cos\omega_0 T_a = \frac{1+M+M^2K}{1+M(\mathrm{n}+1)^2+MK}(\mathrm{n}+1) \tag{B.96}$$

$$\sin\omega_0 T_a = \frac{\sqrt{[MK-\mathrm{n}][1-M^2(\mathrm{n}+1)^2][\mathrm{n}+2+MK]}}{1+M(\mathrm{n}+1)^2+MK} \tag{B.97}$$

$$\cos(\gamma-\omega_0 T_a) = \frac{1-M-M^2K}{1-M(\mathrm{n}+1)^2+MK}(\mathrm{n}+1) \tag{B.98}$$

Substitution of Eqs. (B.96) and (B.97) in the expansion of Eq. (B.98) gives

the implicit equation $G_{s-}(M,Q_s,\gamma,\mathrm{n})=0$ in Eq. (3.91).

B.6 Numerical Methods of Solving $G_{s\pm}(M,Q_s,\gamma,\mathrm{n})=0$

Equations (3.88) and (3.91) are solved numerically for a given Q_s, γ and n. These equations have only one root that lies in the range $0<M\leq 1/(\mathrm{n}+1)$. There are several numerical routines available for solving such implicit equations, even some that can be found on hand-held calculators. The particular numerical routine used in this work was the "BISECT" method available on Hewlett-Packard System 45 [10]. These equations can also be solved using a polynomial root-finder routine (subroutine "SILJACK" [10]) if they are put in polynomial form. The polynomial that correspond to these implicit equations is given by

$$\sum_{l=0}^{6}(\alpha M)^l P_l(Q_s,\gamma,\mathrm{n}) = 0 \qquad \text{(B.99)}$$

where $\alpha=1$ corresponds to $G_{s+}(M,Q_s,\gamma,\mathrm{n})=0$ and $\alpha=-1$ corresponds $G_{s-}(M,Q_s,\gamma,\mathrm{n})=0$. The coefficients P_l are given by

$$P_0=2\mathrm{m}^2(1-\cos\gamma)-\sin^2\gamma$$

$$P_1=4K[\sin^2\gamma+\mathrm{m}^2(\cos\gamma-1)]$$

$$P_2=2(\mathrm{m}^4-3K^2)\sin^2\gamma-2(K^2-\mathrm{m}^4-1)\mathrm{m}^2\cos\gamma+2\mathrm{m}^2(K^2+\mathrm{m}^4-4\mathrm{m}^2+1)$$

$$P_3=4K(K^2-\mathrm{m}^4)\sin^2\gamma-8K\mathrm{m}^2\cos\gamma+8K\mathrm{m}^2(2\mathrm{m}^2-1)$$

$$P_4=-(K^2-\mathrm{m}^4)^2\sin^2\gamma+(6K^2-\mathrm{m}^4)2\mathrm{m}^2\cos\gamma+2\mathrm{m}^2(6K^2+\mathrm{m}^4-4K^2\mathrm{m}^2)$$

$$P_5 = -4Km^2[2K^2 + m^4 + (2K^2 - m^4)\cos\gamma]$$

$$P_6 = 2K^2m^2[K^2 + m^4 + (K^2 - m^4)\cos\gamma] \qquad \text{(B.100a-b)}$$

where

$$m = n + 1 \qquad \text{(B.101)}$$

Of all six roots only that which satisfies the original equation, Eq. (3.88) or Eq. (3.91), is accepted.

In the presence of diode voltage drops, Q_s is modified according to Eq. (3.110). If Eqs. (3.88) and (3.91) are modified with this change in Q_s, they can still be solved numerically using the subroutine "BISECT" to obtain the value of M'. The polynomial method in this case must also be modified. One method is to find a new polynomial which corresponds to either Eq. (3.88) or Eq. (3.91) in which Q_s has been modified, or an iterative method can be employed without changing the polynomial in Eq. (B.99) as shown in the diagram. Normally, five to six iterations are sufficient. Of course, if in the range of interest $V_{BD}/MV_g << 1$, this correction for Q_s is not necessary.

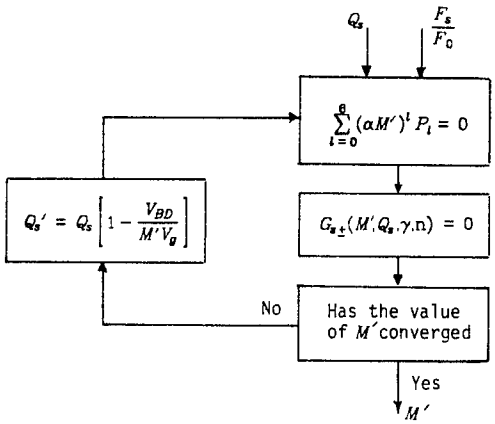

Fig. B.3 An iterative method for the determination of M' of the series resonant converter when taking into account the voltage drop in the output rectifiers. This refinement can be ignored if $V_{BD}/V_0 \ll 1$.

B.7 Determination of the RMS Values of the Resonant Current and the Output Filter Capacitor Current of the Series Resonant Converter in the Range $F_s/F_0 \geq 1/2$

In the range $1/2 \leq F_s/F_0 \leq 1$ the resonant current in the interval $0 \leq t \leq T_a$ is given by Eq. (B.2) in which substitution of Eq. (B.8) gives

$$I_R(t) = \omega_0 C_0 V_g (1 - M - MK) \sin\omega_0 (t - T_a) \tag{B.102}$$

In the interval $T_a \leq t \leq T_s$, $I_R(t)$ is given by Eq. (B.3). The rms square value of $I_R(t)$ is given by

$$I_r^2 = \frac{1}{T_s}\left[\int_0^{T_a} I_R^2(t)dt + \int_{T_a}^{T_s} I_R^2(t)dt\right] \tag{B.103}$$

Integration in Eq. (B.103) gives

$$I_r^2 = \omega_0^2 C_0^2 V_g^2 D_r \tag{B.104}$$

where

$$D_r = \frac{(1-M-MK)^2}{2}\left[\frac{T_a}{T_s} - \frac{1}{2\gamma}\sin 2\omega_0 T_a\right]$$

$$+\frac{(1+M-MK)^2}{2}\left[1 - \frac{T_a}{T_s} - \frac{1}{2\gamma}\sin 2(\gamma - \omega_0 T_a)\right] \tag{B.105}$$

A similar computation gives for D_r in the range $F_s/F_0 \geq 1$

$$D_r = \frac{(1+M+MK)^2}{2}\left[\frac{T_a}{T_s} - \frac{1}{2\gamma}\sin 2\omega_0 T_a\right]$$

$$+\frac{(1-M+MK)^2}{2}\left[1-\frac{T_a}{T_s}-\frac{1}{2\gamma}\sin 2(\gamma-\omega_0 T_a)\right] \qquad \text{(B.106)}$$

Note that eq. (B.106) can be obtained form Eq. (B.105) by changing M to $-M$.

The current through the output filter capacitor is given by

$$I_c = |I_R(t)| - I_0 \qquad \text{(B.107)}$$

The rms square value of I_c is then given by

$$I_c^2 = <(|I_R(t)| - I_0)^2> = I_r^2 - I_0^2 \qquad \text{(B.108)}$$

where I_r^2 is given by Eq. (B.104). Substitution of Eqs. (B.108) and (B.104) in Eq. (3.117) gives Eq. (3.118).

APPENDIX C

C.1 Small-Signal Approximation of $e^{A\hat{t}}$

If A is diagonalizable (A has distinct eigenvalues or is Hermitian) then $f(A)$ is given by

$$f(A) = Tf(\Lambda)T^{-1} = \sum_{i=1}^{n} f(\lambda_i)x_i r_i^T \tag{C.1}$$

where x_i and λ_i are the eigenvectors and the eigenvalues of A, and the matrix T is given by

$$T = [x_1 | x_2 | \cdots | x_n] \tag{C.2}$$

$$T^{-1} = [r_1 | r_2 | \cdots | r_n]^T \tag{C.3}$$

Let $f(\lambda) = e^{\lambda\hat{t}}$ and $g(\lambda) = 1 + \lambda\hat{t}$ and assume that $\lambda_i\hat{t} \ll 1$ so that

$$f(\lambda_i) = e^{\lambda_i\hat{t}} \approx 1 + \lambda_i\hat{t} = g(\lambda_i) \tag{C.4}$$

From Eq. (C.1) we have

$$f(A) = \sum f(\lambda_i)x_i r_i^T \approx \sum g(\lambda_i)x_i r_i^T = g(A) \tag{C.5}$$

which gives

$$f(A) \approx g(A) \quad \text{or} \quad e^{A\hat{t}} \approx I + A\hat{t} \tag{C.6}$$

A similar argument applies for an arbitrary square matrix A for which $f(A) = Tf(J)T^{-1}$ where J is the Jordan form A. In this case, in addition to $f(\lambda_i)$, the derivatives of $f(\lambda_i)$ are considered while still (C.4) is satisfied.

C.2 Matrices, Vectors, and Constants Occurring in Chapter 4

Some of the vectors and matrices in Chapter 4 are redefined here for conciseness. These are

$$\varphi_1 = e^{A_1 T_a} \qquad \varphi_2 = e^{A_2(T_s - T_a)} \tag{C.7}$$

$$B_1 = B_1(T_a) \qquad B_2 = B_2(T_s - T_a) \tag{C.8}$$

The vectors in Eqs. (4.54) and (4.55) are given by

$$d_a = M_r[(AA_1 - A_2A)X(0) + \varphi_2(\varphi_1 - A_2B_1 - I)bV_g] \tag{C.9}$$

$$d_s = -M_r[A_2AX(0) + \varphi_2(A_2B_1 + I)bV_g](1/2F_s^2) \tag{C.10}$$

where $A = \varphi_2\varphi_1$ as given by Eq. (4.27).

The constants k_a and k_s in Eq. (4.57) are given by

$$k_a = \frac{1}{T_s}[c_1^T\varphi_1 + c_2^T(B_2\varphi_1A_1 - A)]X(0)$$

$$+ \frac{1}{T_s}[c_1^TB_1 + c_2^T(B_2A_1 - \varphi_2)B_1]bV_g \tag{C.11}$$

$$k_s = -c_2^T[AX(0) + (\varphi_2(B_1 + A_2^{-1}) - A_2^{-1})bV_g]2T_s + 2T_sV_0 \tag{C.12}$$

The matrix M_x in Eq. (4.65) is given by

$$M_x = M_r A + d_a V_a^T \tag{C.13}$$

where V_a^T is the vector given by Eqs. (4.64).

The vector h^T in Eq. (4.66) is given by

$$h^T = c^T + k_a V_a^T \tag{C.14}$$

where the vector c^T is given by Eq. (4.38).

The constant k_g in Eq. (4.83) is given by

$$k_g = k_p k_a + d^T b \tag{C.15}$$

where k_p is given by Eq. (4.82) and d^T is given by Eq. (4.39).

The vector d_g in Eq. (4.84) is given by

$$d_g = k_p d_a + Bb \tag{C.16}$$

where $B = \varphi_2 B_1 + B_2$ as given by Eq. (4.28).

The matrix A_x and the vector b_g in Eq. (4.99) are given by

$$A_x = A_a + g_a V_a^T \tag{C.17}$$

$$b_g = k_p g_a + B_a b \tag{C.18}$$

where the matrices A_a and B_a are given by Eqs. (4.92) and (4.93) respectively and the vector g_a is given by

$$g_a = \frac{1}{2T_s}[I + B_2 A_1 - \varphi_2]\varphi_1 X(0) + \frac{1}{2T_s}[I + B_2 A_1 - \varphi_2]B_1 b V_g \tag{C.19}$$

REFERENCES

[1] Dilip A. Amin, "Applying Sinewave Power Switching Techniques to the Design of High-Frequency Off-line Converters," Proc. of the Seventh National Solid-State Power Conversion Conference (Powercon 7), March 1980, pp. A1.1-A1.7

[2] Richard Myers and Robert D. Peck, "200 khz Power Technology in New Modular Power Supplies," Hewlett-Packard Journal, Aug. 1981, pp. 3-10

[3] V.T. Ranganathan, Phoivos D. Ziogas, Victor Stefanovic, " A Regulated Dc-Dc Voltage Source Inverter Converter Using a High Frequency Link," IEEE Transactions on Industry and Applications, vol. IA-18, No. 3, May/June 1982, pp. 279-287.

[4] Slobodan Ćuk, "Modeling, Analysis and Design of Switching Converters," Ph.D. Thesis, California Institute of Technology, pp. 49-44, Nov. 1976.

[5] F.C. Schwarz, "A Method of Resonant Current Pulse Modulation for Power Converters," IEEE Transactions on Industrial Electronics and Control Instrumentation, vol. IECI-17, No. 3, pp.209-221, May 1970.

[6] F.C. Schwarz, "An Improved Method of Resonant Current Pulse Modulation for Power Converters," IEEE Power Elecronics Specialists Conference, 1975 Record, pp. 194-204 (IEEE Publication 75CH0965-4 AES); also IEEE Transactions on Industrial Electronics and Instrumentation, vol.IECI-23, pp. 134-141. May 1976.

[7] R. King and T.A. Stuart, "A Normalized Model for the Half-Bridge Series Resonant Converter," IEEE Transactions on Aerospace and Electronic Systems, vol. AES-17, No. 2, pp. 190-198. March 1981.

[8] R.D. Middlebrook and Slobodan Ćuk, "A General Unified Approach to Modelling Switching-Converter Power Stages," IEEE Power Electronics Specialists Conference, 1976 Record, pp. 18-34, (IEEE Publication 76CH1084-3 AES); also International J. of Electronics, vol. 40, no. 1, pp. 1-4, Jan. 1976.

[9] Farhad Barzegar, "Problems in Switched-mode DC and AC Power Conversion," Ph.D Thesis, California Institute of Technology, pp. 38-49, May 1983.

[10] Hewlett-Packard System 45 General Utility Routines.